Advanced Signal Processing Concepts for Multi-Dimensional Communication Systems

Sher Ali Cheema

ILMENAU UNIVERSITY OF TECHNOLOGY

Fakultät für Elektrotechnik und Informationstechnik
der Technischen Universität Ilmenau
Fachgebiet Nachrichtentechnik

Advanced Signal Processing Concepts for Multi-Dimensional Communication Systems

May 22, 2018

Sher Ali Cheema

Anfertigung im:	Fachgebiet Nachrichtentechnik
	Institut für Informationstechnik
	Fakultät für Elektrotechnik und Informationstechnik
Gutachter:	Univ.-Prof. Dr.-Ing. Martin Haardt
	Univ.-Prof. Dr. Mario Huemer, University of Linz, Austria
	Univ.-Prof. Dr.-Ing. Eduard Jorswieck, Technische Universität Dresden
Vorgelegt am:	11.12.2017
Verteidigt am:	23.04.2018
Verf.-Nr.:	EI432

urn:nbn:de:gbv:ilm1-2018000145
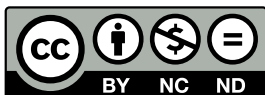
Acknowledgements

The work presented in this thesis would not have been possible without the tremendous support of so many people who deserve a deep sense of my gratitude.

First of all, I would like to pay my deepest regards to my supervisor and mentor Prof. Martin Haardt for giving me opportunity to work under his supervision and able guidance. I have no words to thank him for all his efforts and time in training me to be independent, for supporting and encouraging me in all difficult times, and also for giving me numerous ideas to pursue the doctoral studies. His own zeal for perfection, passion, unflinching courage and conviction has always inspired me to do more. Especially, the joy and enthusiasm he has for his research was contagious and motivational for me, even during tough times in the Ph.D. pursuit.

I would also like to express my gratitude to Prof. Mario Huemer for all of the fruitful discussions and ideas he gave me over the past years. All of these discussions were really helpful in further improving my research work. I would also like to thank Prof. Eduard Jorswieck and Prof. Mario Huemer for volunteering to review the thesis.

I also owe a lot of tributes to Dr. Mike Wolf for teaching me the basics of optical communication, for providing me better insights to the future research directions, and also helping me out at numerous occasions whenever I was stuck at some point. This thesis would not have been possible without his tremendous support and guidance. I also owe a debt of gratitude to my colleagues as well. Over the last years, they have always supported me and shared with me their knowledge and skills. I was lucky to have such friendly and helpful colleagues. Therefore, I would like to say special thanks to Kristina Noskovska, Jianshu Zhang, Jens Steinwandt, Yao Cheng, Mikus Grasis, Marko Hennhöfer, and Bilal Zafar. I really appreciate every technical or private discussion and exchange of ideas we had over the past years. I would also like to thank my former students. Their enthusiasm, energy, and optimism was always a motivating factor for me. In particular, I would like to thank Emilio Rafael Balda for working with me over the span of two years and also for being a good friend. No research is possible without infrastructure and requisite materials and resource. For this I extend thanks to Ms. Christina Patotschka and Mr. Wolfgang Erdtmann for always providing me the administrative help with a smile.

Last but not the least, I would like to thank my family. None of all this would have been possible without the tremendous support of my family. I feel a deep sense of gratitude for my grand parents, mother, father, who formed part of my vision and taught me good things that really matter in life. Their infallible love and support has always been my strength. Their patience and sacrifice will remain my inspiration throughout my life. I would also like to express my deep appreciation to my beloved wife for her eternal support and understanding of my goals and aspirations. Her patience and sacrifice will remain my inspiration throughout my life. Without her help, I would not have been able to complete much of what I have done and become who I am. A special thanks to my brother, sister, and brother in law for their unconditional love, affection, and encouragements. I would like to mention my elder cousin Mohammad Omer who was the first to motivate me for pursuing my doctoral studies. Finally, a few compliments to my one year old son Ahmed Ali Cheema. His innocent smile and cute little gestures

have brought so much happiness and joy in my life.

Abstract

The widespread use of mobile internet and smart applications has led to an explosive growth in mobile data traffic. With the rise of smart homes, smart buildings, and smart cities, this demand is ever growing since future communication systems will require the integration of multiple networks serving diverse sectors, domains and applications, such as multimedia, virtual or augmented reality, machine-to-machine (M2M) communication / the Internet of things (IoT), automotive applications, and many more. Therefore, in the future, the communication systems will not only be required to provide Gbps wireless connectivity but also fulfill other requirements such as low latency and massive machine type connectivity while ensuring the quality of service. Without significant technological advances to increase the system capacity, the existing telecommunications infrastructure will be unable to support these multi-dimensional requirements. This poses an important demand for suitable waveforms with improved spectral characteristics and signal processing solutions with an increased flexibility. Moreover, future wireless networks will be required to exploit several frequency bands, such as lower frequency bands (typically with frequencies below 10 GHz), mm-wave bands (few hundred GHz at the most), and THz bands. Many alternative technologies such as optical wireless communication (OWC), dynamic radio systems, and cellular radar should also be investigated to assess their true potential. Especially, OWC offers a large but as yet unexploited optical band in the visible spectrum that uses light as a means to carry information. Therefore, future communication systems can be seen as composite hybrid networks that consist of a number of different wireless networks based on radio and optical access. On the other hand, it poses a significant challenge to come up with advanced signal processing solutions in multiple areas of communication systems. This thesis contributes to this goal by demonstrating methods for finding efficient algebraic solutions to various applications of multi-channel digital signal processing. In particular, we contribute to three different scientific fields, i.e., waveforms, optical wireless systems, and multi-dimensional signal processing.

Currently, cyclic prefix orthogonal frequency division multiplexing (CP-OFDM) is the widely adopted multicarrier technique for most of the communication systems. However, to overcome the CP-OFDM demerits in terms of poor spectral containment, poor robustness in highly asynchronous environments, and inflexibility of parameter choice, many alternative waveforms have been proposed. Such multicarrier waveforms include filter bank multicarrier (FBMC), generalized frequency division multiplexing (GFDM), universal filter multicarrier (UFMC), and unique word orthogonal frequency division multiplexing (UW-OFDM). These new air interface schemes take different approaches to overcome some of the inherent deficiencies in CP-OFDM. Some of these waveforms have been well investigated while others are still in its infancy. Specifically, the integration of multiple-input multiple-output (MIMO) concepts with UW-OFDM and UFMC is still at an early stage of research.

Therefore, in the *first* part of this thesis, we propose novel linear and successive interference cancellation techniques for MIMO UW-OFDM systems. The design of these techniques is aimed to result in receivers with a low computational complexity. Another focus area is the applicability of space-time block codes (STBCs) to UW-OFDM and UFMC waveforms. For this purpose, we present novel tech-

niques along with detection procedures. We also compare the performance of these waveforms with our proposed techniques to the other state-of-the-art waveforms that has been proposed in the literature. We demonstrate that space-time block coded UW-OFDM systems with the proposed methods not only outperform other waveforms significantly but also result in receivers with a low computational complexity.

The *second* application area comprises of optical systems in the visible band (390-700 nm) that can be utilized in plastic optical fibers (POFs), multimode fibers or OWC systems such as visible light communication (VLC). VLC can provide solutions for a number of applications including wireless local, personal, and body area networks (WLAN, WPAN, and WBANs), indoor localization and navigation, vehicular networks, underground and underwater networks, offering a range of data rates from a few Mbps to 10 Gbps. VLC takes full advantage of visible light emitting diodes (LEDs) for the dual purpose of illumination and data communications at very high speeds. Because of the incoherent nature of the LED sources, such systems employ intensity modulation and direct detection (IM/DD), thus demanding that the transmit signal should be real-valued and positive. This also implies that the conventional waveforms designed for the radio frequency (RF) communication cannot be directly used. For example, a Hermitian symmetry has to be applied to the CP-OFDM spectrum to obtain a real-valued signal (often referred to as discrete multitone transmission (DMT)) that in return reduces the bandwidth efficiency. Moreover, the LED/LED driver combination limits the electrical bandwidth. All these factors require the use of spectrally efficient transmission schemes along with robust equalization schemes to achieve high data rates. Therefore, in the second part of the thesis, we propose transmission schemes that are best suited for such optical systems. Specifically, we demonstrate the performance of PAM block transmission with frequency domain equalization. We show that this scheme is not only more power efficient but also outperforms all of the state-of-the-art schemes such as CP-DMT schemes. We also propose novel UW-DMT schemes that are derived from the UW-OFDM concept. These schemes also show a superior bit error ratio (BER) performance over the conventional CP-DMT schemes.

The *third* application area focuses on multi-dimensional signal processing techniques. With the use of MIMO, STBCs, multi-user processing, and multicarrier waveforms in wireless communications, the received signal is multidimensional in nature and may exhibit a multilinear structure. In this context, signal processing techniques based on a tensor model can simultaneously benefit from multiple forms of diversity to perform multi-user signal separation/equalization and channel estimation. This advantage is a direct consequence of the essential uniqueness property that is not available for matrix based approaches. Tensor decompositions such as the higher order singular value decomposition (HOSVD) and the canonical polyadic decomposition (CPD) are widely recommended for performing these tasks. The performance of these techniques is often evaluated using time consuming Monte-Carlo trials. In the last part of the thesis, we perform a first-order perturbation analysis of the truncated HOSVD and the SEmi-algebraic framework for approximate Canonical polyadic decompositions via SImultaneous matrix diagonalizations (SECSI). The SECSI framework is an efficient tool for the computation of the approximate CPD of a low-rank noise corrupted tensor. Especially, the SECSI framework shows a significantly improved performance and comparatively low-complexity as compared to the conventional algorithms such as alternative least squares (ALS). Moreover, it also facilitates the implementation on a parallel hardware architecture. The obtained analytical expressions for both algorithms are formulated in terms

of the second-order moments of the noise, such that apart from a zero-mean, no assumptions on the noise statistics are required. We demonstrate that the derived analytical results exhibit an excellent match to the Monte-Carlo simulations.

Abstract

Zusammenfassung

Die zunehmende Nutzung des mobilem Internets und die wachsende Verbreitung intelligenter Anwendungen hat zu einem explosionsartigen Anstieg des mobilen Datenverkehrs geführt. Mit der Einführung intelligenter Häuser, intelligenter Gebäude und dem Heranwachsen intelligenter Städte wird der mobile Datenverkehr immer weiter steigen. Zukünftige Kommunikationssysteme erfordern dabei die Integration verschiedenartiger Netzwerke, welche unterschiedliche Sektoren, Domänen und Anwendungen bedienen, wie beispielsweise Multimedia, virtuelle oder erweiterte Realität, Maschine-zu-Maschine (M2M) -Kommunikation, Internet of Things (IoT), Automobilanwendungen und vieles mehr. Daher werden Kommunikationssysteme zukünftig nicht nur drahtlose Gbps-Verbindungen bereitstellen müssen, sondern auch andere Anforderungen wie niedrige Latenzzeiten oder eine massive Maschinentyp-Konnektivität erfüllen müssen, während die Dienstqualität sichergestellt wird. Ohne bedeutende technologische Fortschritte zur Erhöhung der Systemkapazität wird die bestehende Telekommunikationsinfrastruktur diese vielfältigen Anforderungen nicht unterstützen können. Damit stellt sich einerseits die Frage nach Wellenformen mit verbesserten spektralen Eigenschaften und andererseits nach Signalverarbeitungslösungen mit erhöhter Flexibilität. Zudem werden zukünftige drahtlose Netzwerke mehrere Frequenzbänder nutzen und dabei auch den mm-Wellen- und THz-Bereich unterstützen müssen. Viele alternative Ansätze wie Optical Wireless Communication (OWC), dynamische Funksysteme oder zellulares Radar sollten ebenfalls untersucht werden, um ihr tatsächliches Potenzial abzuschätzen. Insbesondere bietet die OWC auf der Basis sichtbaren Lichts die Möglichkeit, einen sehr großen zusätzlichen Spektralbereich zu nutzen. Hierbei wird die Beleuchtung mit der Kommunikation kombiniert. Zukünftige Kommunikationssysteme können demnach als Hybridnetzwerke angesehen werden, welche aus verschiedenen drahtlosen Netzwerken bestehen. Es ist eine große Herausforderung, fortschrittliche Signalverarbeitungslösungen für solch heterogene Systeme zu entwickeln. Die vorliegende Arbeit soll zu dieser Entwicklung beitragen, indem effiziente algebraische Lösungen für verschiedene Anwendungen der digitalen Mehrkanal-Signalverarbeitung entwickelt und evaluiert werden. Konkrete wird zu drei verschiedenen Forschungsgebieten beigetragen: Wellenformen, OWC und mehrdimensionale Signalverarbeitung.

Gegenwärtig ist das orthogonale Frequenzmultiplexverfahren OFDM (Orthogonal Frequency Division Multiplexing) auf der Basis eines zyklischen Präfix (CP, Cyclic Prefix) die am weitesten verbreitete Mehrträgertechnik für Kommunikationssysteme. Um jedoch die Nachteile des CP-OFDM-Verfahrens — schlechte spektrale Begrenzung sowie geringe Flexibilität bei der Parameterwahl — zu überwinden und die Robustheit in hoch asynchronen Umgebungen zu erhöhen, wurden viele alternative Wellenformen vorgeschlagen. Zu solchen Mehrträgertechniken gehören FBMC (Filter Bank Multicarrier), GFDM (Generalized Frequency Division Multiplexing), UFMC (Universal Filter Multicarrier) und OFDM auf der Basis des Unique Words (UW-OFDM). Diese neuen Verfahren für die Luftschnittstelle verwenden verschiedene Ansätze, um einige der inhärenten Mängel des CP-OFDM zu vermeiden. Einige dieser Ansätze wurden in der Vergangenheit intensiv untersucht, andere sind noch im Anfangsstadium der Entwicklung. Insbesondere befindet sich die Integration von Multiple-Input-Multiple-Output (MIMO) -Konzepten mit UW-OFDM oder UFMC noch in einem frühen Forschungsstadium.

Daher schlagen wir im *ersten Teil dieser Arbeit* neuartige lineare und sukzessive Interferenzunter-drückungsverfahren für MIMO UW-OFDM-Systeme vor. Die neuen Techniken zielen unter anderem auf Empfänger mit geringer Rechenkomplexität ab. Ein weiterer Schwerpunkt im ersten Teil dieser Arbeit ist die Anwendbarkeit von Space-Time Block Codes (STBCs) in Verbindung mit den UW-OFDM- und UFMC-Wellenformen. Zu diesem Zweck stellen wir die neuen Techniken und Wellenformen in Verbindung mit geeigneten Detektionsverfahren vor und vergleichen ihr Potential mit dem der Wellenformen, die bisher in der Literatur diskutiert wurden. Wir zeigen, dass die neuartigen Raum- und Zeit- blockkodierten UW-OFDM-Ansätze die bisher vorgeschlagenen Methoden in ihrer Leistungsfähigkeit nicht nur signifikant übertreffen, sondern auch zu Empfängern mit geringer Rechenkomplexität führen.

Der *zweite in der vorliegenden Arbeit adressierte Forschungsbereich* umfasst optische Systeme, die mit Wellenlängen im sichtbaren Bereich (390-700 nm) arbeiten. Dazu gehören neben — drahtlosen — VLC-Systemen (VLC: Visible Light Communication) auch drahtgebundene optische Systeme auf der Basis von Multimode-Fasern. VLC kann Lösungen für eine Reihe von Anwendungen bieten. Das beinhaltet WBANs, WPANs und WLANs (Wireless Body Area Networks, Wireless Personal Area Networks, Wireless Local Area Networks), die Lokalisierung und -navigation im Gebäudeinneren, Fahrzeugnetze, U-Bahn-Kommunikationsnetze und sogar die Unterwasserkommunikation. Die Datenraten können dabei zwischen von wenigen Mbps bis zu etwa 10 Gbps reichen. VLC nutzt die Tatsache, sich sich LED-Lampen (LED: Light Emitting Diode) nicht nur für den Zweck der Beleuchtung, sondern auch für die hochbitratige Datenkommunikation einsetzen lassen. Aufgrund der inkohärenten Natur von LED-Licht basieren solche Systeme auf Intensitätsmodulation und Direktempfang (IM/DD: Intensity Modulation / Direct Detection), was impliziert, dass das Signal zur Modulation des Diodenstroms reellwertig und positiv sein muss. Das bedeutet aber auch, dass die herkömmlichen Wellenformen, die für die Radio Frequency (RF) -Kommunikation mit Modulation auf Feldebene ausgelegt sind, nicht direkt verwendet werden können. Zum Beispiel muss das CP-OFDM-Spektrum eine hermitesche Symmetrie aufweisen, damit ein reellwertiges, d.h. eindimensionales Zeitsignal erhalten wird. In diesem Zusammenhang wird häufig von Discrete Multitone Transmission (DMT) gesprochen. Gegenüber Systemen mit Modulation auf Feldebene und der Möglichkeit einer Quadrature-Upconversion eines komplexen, d.h. zweidimensionalen Signals, halbiert sich so die Bandbreiteeffizienz. Darüber hinaus begrenzt die LED / LED-Treiberkombination die mögliche elektrische Modulationsbandbreite. Alle diese Faktoren erfordern die Verwendung spektral effizienter Übertragungsverfahren zusammen mit robusten Entzerrungsschemata, damit hohe Datenraten erreicht werden können. Deshalb schlagen wir im zweiten Teil der Arbeit Übertragungsverfahren vor, die für solche optischen Systeme am besten geeignet sind. Insbesondere demonstrieren wir die Leistungsfähigkeit der PAM-Blockübertragung mit Frequenzbereichsentzerrung. Wir zeigen, dass dieses Verfahren am leistungsstärksten ist und auch modernen Techniken wie CP-DMT übertrifft. Wir schlagen zudem neue UW-DMT-Verfahren vor, die vom UW-OFDM-Konzept abgeleitet sind und zeigen, dass diese herkömmlichen CP-DMT-Techniken überlegen sind.

Der *dritte Teil der Arbeit* konzentriert sich auf mehrdimensionale Signalverarbeitungstechniken. Bei der Verwendung von MIMO, STBCs, Mehrbenutzerverarbeitung und Mehrträgerwellenformen zur drahtlosen Kommunikation ist das empfangene Signal mehrdimensional und kann eine multilineare Struktur aufweisen. In diesem Zusammenhang können Signalverarbeitungstechniken, die auf einem Tensor-Modell basieren, gleichzeitig von mehreren Formen von Diversität profitieren, um Mehrbenutzer-Signaltrennung

/ -entzerrung und Kanalschätzung durchzuführen. Dieser Vorteil ist eine direkte Konsequenz der Eigenschaft der wesentlichen Eindeutigkeit, die für Matrix-basierende Ansätze nicht verfügbar ist. Eine Tensor-Zerlegung wie die HOSVD (Higher Order Singular Value Decomposition) und die CPD (Canonical Polyadic Decomposition) werden weithin zur Durchführung dieser Aufgaben empfohlen. Die Leistung dieser Techniken wird oft mit zeitraubenden Monte-Carlo-Versuchen bewertet. Im letzten Teil der Arbeit führen wir für diese Tensor-Zerlegungsmethoden eine Störungsanalyse erster Ordnung durch. Insbesondere führen wir eine analytische Leistungsfähigkeitsanalyse des SECSI (SEmialgebraischen Frameworks für approximative Canonical polyadic decompositions via SImultaneous matrix diagonalizations) durch. Das SECSI-Framework ist ein effizientes Werkzeug zur Berechnung der CPD eines verrauschten Tensors mit niedrigem Rang. Darüber hinaus werden die erhaltenen analytischen Ausdrücke in Bezug auf die Momente zweiter Ordnung des Rauschens formuliert, so dass, abgesehen von einem verschwindenden Erwartungswert, keine weiteren Annahmen bzgl. der Rauschstatistik erforderlich sind. Wir zeigen, dass die abgeleiteten analytischen Ergebnisse eine ausgezeichnete Übereinstimmung mit den Monte-Carlo-Simulationen aufweisen.

Contents

List of Figures

List of Tables

1. Introduction and scope of the thesis

Signals play a vital role in our daily life. They convey information about the state or behavior of a physical system such as sound, images, and biological measurements. A signal is typically a function of independent variables such as time, distance, position, temperature, and pressure. Signals may have to be transformed in order to carry out some specific tasks such as to amplify or filter out embedded information, to detect patterns, to prepare the signal to survive a transmission channel, to undo distortions contributed by a transmission channel, and to find information encoded in a different domain. This is achieved by employing signal processing techniques that use some methods to measure, characterize, model, and simulate signals. Especially, signals in digital form provide us with a very convenient abstract representation which is both simple and powerful. Therefore, digital signal processing techniques are used in a variety of application fields such as communication systems, consumer electronics, music, medical diagnostics, geophysics, astronomy, experimental physics, aviation, control systems, pattern recognition, and many more.

Digital signal processing techniques have played the most important role in the development of modern communication systems. Specifically, they have reshaped modern wireless communications starting from the second generation (2G) cellular systems to the current fourth generation (4G) cellular systems. Each generation has a development cycle of about ten years and is defined by an air interface and a corresponding standout signal processing technology, i.e., time division multiple access (TDMA) for 2G, code division multiple access (CDMA) for 3G, and orthogonal frequency division multiple access (OFDMA) for 4G, that represents the most important advancement in that generation. However, the number of devices that require digital signal processing techniques has grown manifold over the recent years. The computing prowess of these devices can range from simple, e.g., wireless sensors, to mid-range, e.g., laptops and smart phones, to very complicated, e.g., medical resonance imaging machines and systems for industrial control. The large number of these devices and their respective capabilities, such as computing power and smart functions, pose a challenge as well as an opportunity for further developments in the field of digital signal processing. The large number of devices also provides an unprecedented amount of data, computing power, and the opportunity for inter-device collaboration to help us tackle problems that were considered intractable before.

The challenges are manifold. The growing number of devices is putting an enormous demand on the capabilities of network providers to guarantee high data rates for future communication systems. This has led to an increased focus on the development of new signal processing techniques for different air interfaces, especially for fifth Generation (5G) cellular systems. These techniques are expected to meet requirements such as low latency transmissions for long and short data bursts, fast switching between uplink and downlink for time division duplex systems, and handling high data rates that require a wide bandwidth. Moreover, new spatial domain signal processing techniques such as multiple-input multiple-output (MIMO) concepts, beamforming techniques, and antenna diversity schemes have to be developed for these new air interface proposals.

With the ever growing popularity of data heavy wireless communications, the demand for RF spectrum
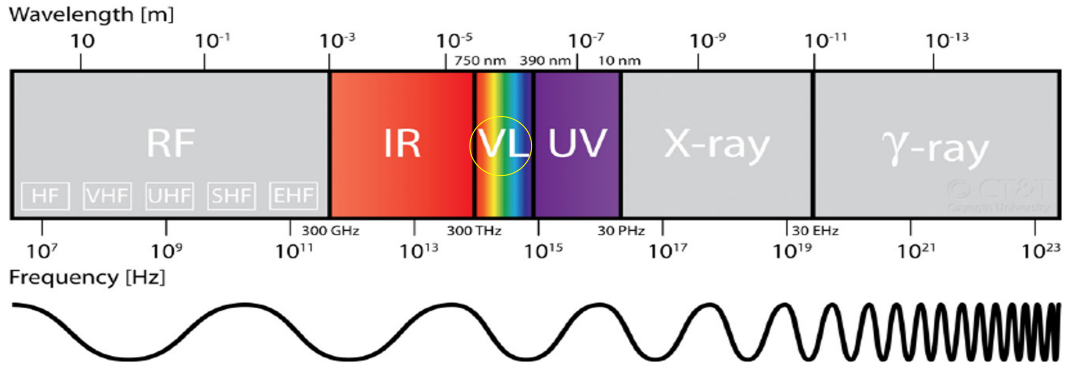
Figure 1.1.: Visible light spectrum (marked with a yellow circle)

is outstripping supply. This has led researchers to explore more and more innovative solutions for 5G wireless communication systems and beyond. One such solution could consider wireless communications in the visible optical band, as shown in Fig. 1.1. Such a utilization of the optical band of the electromagnetic spectrum for wireless transmissions opens doors of opportunities in areas as yet largely unexplored. It is estimated that more than 70 % of the wireless traffic takes place in an indoor environment, i.e., home, office, etc. In that case, optical wireless technologies such as visible light communication (VLC) can be a suitable alternative. In many aspects, optical wireless technology is still in its infancy and calls for consolidated efforts to harness its enormous potential.

The amount of new devices, the widespread use of multi-sensor technology, and the emergence of big data sets also create new problems in the areas of computational complexity, security, energy consumption, and privacy. Moreover, these factors also result in an increased dimensionality of the data sets. For example, in a multicarrier transmission system with multiple transmit and receive antennas, the received signal is multi-dimensional in nature, i.e., time, frequency, as well as space at the transmitter and the receiver side. In most of the cases, the multi-dimensional data is reformatted as a matrix and resorted to signal processing approaches developed for classical matrix (two-way) analysis. However, the rigid assumptions inherent in matrix analysis are not always a good match for multi-dimensional (tensor) data. It is only through higher-order tensor decompositions that we can handle data and extract more information from it. Therefore, tensor decomposition techniques are gaining a lot of popularity and importance for wireless communication systems.

In order to address these multi-dimensional issues related to modern communication systems, we focus on three different application areas. We devise not only new methods for these application fields but also show how existing algebraic solutions can be applied by simple algebraic modifications. To enhance the overall structure of the thesis, we present each application area in a separate part of the thesis which can be read independently of the other. In the following sections, we provide a brief motivation for the different parts and also briefly describe some of the preliminary definitions and multi-linear concepts that would be helpful in understanding the rest of the thesis. We also provide a detailed introduction at the beginning of each part/chapter separately.

1.1. Part I: MIMO Concepts for UW-OFDM Systems

The principle concept of orthogonal frequency division multiplexing (OFDM) stems from the mid 1960s that is based on the multicarrier modulation techniques used in the high frequency military radio [Cha66, Sal67]. The idea of using a discrete Fourier transform (DFT) for the implementation of the generation and reception of OFDM signals was introduced in [WE71]. It eliminated the requirement for banks of analog subcarrier oscillators, thus presenting an opportunity for an easy implementation of OFDM, especially with the use of fast Fourier transform (FFT), which is an efficient implementation of the DFT. Moreover, in OFDM, a time domain guard interval or a cyclic prefix (CP) is inserted between OFDM symbols (blocks) to avoid intersymbol interference (ISI). Therefore, in the literature, it is also referred as CP-OFDM. Countless efforts have been put into investigating CP-OFDM and, as a consequence, a vast amount of knowledge is available on this topic [Hir81, BDH99, WCLM99, LWS02, SPSH04]. The intriguing features of coded CP-OFDM include a great robustness against multi-path fading, an efficient implementation, and the capability of turning the frequency selective channel into parallel flat fading subchannels such that sophisticated receiver designs are avoided. Consequently, CP-OFDM has been adopted in a variety of wired and wireless communication standards and products. Prominent examples include dynamic subscriber line (DSL), power line communication (PLC), most of the IEEE 802.11 specifications (802.11), long term evolution (LTE) downlink, terrestrial digital video broadcasting (DVB-T), and terrestrial integrated services digital broadcasting (ISDB-T). Nevertheless, CP-OFDM has also many shortcomings. For example, CP-OFDM signals require a high linearity of the output power amplifiers due to their high peak to average power ratio (PAPR). As a result, the power amplifier efficiency is low, increasing the user equipment (UE) battery power consumption. CP-OFDM signals also suffer from high out-of-band (OOB) leakage due to the use of a rectangular pulse in the time domain. Moreover, the insertion of a CP reduces the spectral efficiency of CP-OFDM systems. Furthermore, CP-OFDM is sensitive to synchronization errors. It is thus not an efficient multicarrier modulation scheme for communication scenarios where perfect synchronization is hardly guaranteed, e.g., the uplink of multi-user MIMO systems.

Although widely deployed in various state-of-the-art communication standards, these issues with CP-OFDM give rise to the trend of the development of new advanced multicarrier modulation schemes such as unique word orthogonal frequency division multiplexing (UW-OFDM) [HHH10b, OH10], filter bank multicarrier (FBMC) [Bel10b, PNCZ+16], generalized frequency division multiplex (GFDM) [MMG+14, NCE+17], and universal filter multicarrier (UFMC) [SWC14]. These new waveforms aim at solving some of these issues by adopting different approaches. Still, CP-OFDM and many newly proposed block based transmission techniques require the insertion of guard intervals to eliminate ISI. Typically, a guard interval length of up to 25 % of the transmit symbol duration is inserted which is a rather wasteful consumer of transmit time. This reduces the bandwidth efficiency significantly and also wastes transmit energy, an aspect which gets more dominant for battery-driven devices. UW-OFDM is one of the novel variants of CP-OFDM signaling that aim at utilizing this guard interval in an efficient manner. It may act as a promising candidate for future wireless, wireline, and optical communication systems [HHH10b, HHOH14]. For example, approaches based on UW-OFDM are currently part of on-going standardization discussions for 5G millimeter wave systems [IKN+15]. In UW-OFDM, the time domain guard interval is

filled with an arbitrary deterministic sequence, the so-called "unique word" (UW), instead of a random CP. This sequence provides the same advantages as a CP (no intersymbol interference and diagonalization of the channel matrix), but can additionally be designed to optimally meet the synchronization and channel estimation tasks, as known from the single carrier systems [CSBM06, WMP$^+$03]. To fill the time domain guard interval, zeros are generated at the output of the inverse discrete Fourier transform (IDFT). Then, the UW is added in the time domain. Ensuring such time domain properties entails the introduction of a certain redundancy in the frequency domain. This redundancy is added with the help of a code generator matrix and can be exploited beneficially to enhance the range, reliability, capacity or battery life span. In this sense, UW-OFDM transforms the usually disregarded guard interval into a multi-purpose sequence, thus tackling the well-known inefficiency problem of guard intervals in current communication systems. Since the guard interval in UW-OFDM is a part of the DFT interval, varying the length of the UW and therefore the guard interval length to different channel conditions will not impact the DFT length and thus keeps the relevant processing chain structures untouched. Hence, UW-OFDM allows supporting a wide range of communication scenarios (different channel conditions, lower OOB emissions, etc.,) while still ensuring high efficiency. Moreover, the generation of the UW within the DFT interval introduces correlations in the frequency domain which can beneficially be exploited by the receiver to improve the bit error ratio (BER) performance. The simulation results investigated for single-input single-output (SISO) systems show that UW-OFDM has a superior BER performance over CP-OFDM [HOH11, Oni13]. Moreover, it is also shown that the design of the code generator matrix is not unique and different code generator matrices yield different BER performances [HHH12]. Another advantage of UW-OFDM over CP-OFDM is the superior spectral containment of the generated waveform [HHH12, RSK13]. Specifically, the desired sidelobe suppression can be achieved by designing the code generator matrix without the need for any extra processing [RKS14], which is in contrast to most of the sidelobe suppression methods proposed for the CP-OFDM system.

Multiple-input multiple-output (MIMO) systems have become an integral part of modern wireless communication systems due to their inherent advantages such as array gain, interference reduction, and diversity gain. MIMO systems can exploit not only the transmit and receive multi-antenna benefits simultaneously but they also offer something new compared to traditional antenna array systems, i.e., a spatial multiplexing gain. However, a compromise between diversity and multiplexing has to be made since it is not possible to exploit both maximum diversity gain and maximum multiplexing gain at the same time [ZT03]. One of the reasons for the popularity of CP-OFDM is its easy integration with MIMO technology. A lot of research has been carried out in this regard for CP-OFDM [LWS02, SPSH04]. But to date, a limited research has been carried out for the integration of MIMO systems with some newly proposed waveforms. For example, so far UW-OFDM has been investigated from various aspects for SISO systems only [OH10, HHH12, RSK13, HHOH14]. In the first part of the thesis, we expand these investigations to MIMO UW-OFDM systems.

1.1.1. Major Contributions

In the literature, all the investigations regarding UW-OFDM have been carried out for SISO systems only. Therefore, almost all of the presented techniques/results for the integration of MIMO to UW-OFDM

are novel. The major contributions of this part are as follows:

- *Design of low-complexity linear and non-linear detection schemes for MIMO UW-OFDM systems*

  We start this part of the thesis by discussing detection schemes for MIMO UW-OFDM systems in Chapter 2. In UW-OFDM, the generation of a UW within the DFT interval introduces redundancy in the frequency domain. This redundancy is added with the help of a code generator matrix and introduces correlation in the frequency domain. For SISO systems, it has been shown in [HOH11, Oni13] that sophisticated receivers are required to beneficially exploit this correlation. This results in a superior BER performance of UW-OFDM over CP-OFDM, but at the expense of higher computational complexity. We expand these investigations to MIMO systems by first presenting a joint detection method which is a direct extension of the SISO model. This method results in a much better BER performance for MIMO UW-OFDM systems over MIMO CP-OFDM systems, but also suffers from a much higher computational complexity. Alternatively, we present another approach, namely a two step detection method, which has the same BER performance as joint detection but has a much lower computational complexity. We also present successive interference cancellation (SIC) based non-linear detection schemes for MIMO UW-OFDM systems. UW-OFDM systems with the SIC schemes outperform the UW-OFDM with the linear detection schemes significantly but also have a very high computational complexity, thus making it unsuitable for practical implementations. Therefore, we propose a hybrid detection scheme where a combination of linear subcarrier-wise detection is performed in the first step and SIC based code generator demodulation is performed in the second step. This hybrid scheme has a lower complexity and shows a better BER performance than the linear detection schemes but worse than the SIC schemes. Thus it offers a trade-off between performance and computational complexity.

- *Design of techniques to integrate space-time block codes to MIMO UW-OFDM systems*

  When channel state information (CSI) is not available at the transmitter, space-time block codes (STBCs) are widely recommended for MIMO systems to achieve the maximum diversity gain. In space-time block coding, the information is coded across transmit antennas and time slots in a way that the receiver can reliably extract the information and exploit spatial diversity. Today, STBCs form an integral part of modern wireless communication standards such as LTE, LTE-A, and WLAN and are expected to be a part of future wireless communication systems. Therefore, in Chapter 3, we discuss space-time block coded UW-OFDM systems. In the last couple of decades, many space-time block coding techniques have been presented in the literature. Specifically, orthogonal STBCs (OSTBCs) are the most frequently used technique due to the implementation of simple linear decoding at the receiver. The main focus of this chapter is to devise methods to apply existing OSTBCs to MIMO UW-OFDM systems. In this regard, we propose two methods, namely a frequency domain space-time block code and a time-reversal space-time code (TR-STC). Frequency domain space-time block coding techniques are the extension of the orthogonal space-frequency block codes (SFBCs) that are used for CP-OFDM. We show that this approach results in much more complex receivers and a simple linear receiver as of SFBCs in CP-OFDM is not possible. However, when TR-STCs are used, a simple linear decoding technique such as maximum

ration combing (MRC) can be employed while achieving the similar performance.

- *Design of space-time block coded UFMC systems and performance comparison of 5G air interface proposals*

  We further continue the discussion from Chapter 3 to other newly proposed waveforms in Chapter 4. Currently, a lot of effort is being carried out to integrate space-time block coding for FBMC and GFDM [ZL13, MMF14, MMG$^+$15]. However, a limited knowledge is available in the literature for MIMO UFMC systems. Therefore, we first investigate space-time block coded UFMC systems. In contrast to CP-OFDM, where only DFT filtering is applied at the transmitter, an additional filtering is used in UFMC to suppress OOB emissions [SWC14]. Therefore, the transceiver chain of UFMC is different from the conventional CP-OFDM transceiver. Especially at the receiver, different types of receive filtering methods such as matched filtering, zero forcing (ZF), minimum mean square error (MMSE) filtering, and FFT based filtering can be employed. In this work, we show that the integration of the available STBC methods to UFMC is possible, but it strongly depends on the type of receive filtering methods employed. In the literature, the performance of these new waveforms is only compared with CP-OFDM which is often misleading. A fair comparison of these waveforms is particularly important to facilitate the selection of a waveform for any particular requirement. Therefore, after proposing the methods to employ STBCs for UFMC, we compare the performance of space-time block coded UFMC, UW-OFDM, FBMC, and GFDM systems. The results show that space-time block coded UW-OFDM systems not only result in a superior BER performance as compared to competing schemes, but also have a receiver architecture with a lower complexity.

1.2. Part II: Transmission Strategies for Optical Systems with Intensity Modulation and Direct Detection

In this part, we focus on the transmission schemes for optical systems that employ intensity modulation (IM) and direct detection (DD). The most widely used examples of such systems are plastic optical fibers (POFs), multimode fibers, and wireless optical transmission such as visible light communication (VLC). VLC is an attractive choice in many application scenarios, where either the RF communication has the spectrum congestion problem, i.e., indoor wireless communication and car to car or car to infrastructure communication, or RF communication does not work, i.e., underwater communication. VLC is based on smart lighting that integrates the functions of illumination, communications, and even positioning [EMH09, ASN13, PFHM15]. It becomes possible since the light emitting diode (LED) lighting sources, which have become a standard in illumination, can be modulated with several tens of MHz bandwidth. Specifically, in an indoor environment a wireless link can greatly benefit from the high signal-to-noise ratio offered by the LEDs (that are used to illuminate the room) instead of using a high power RF based outdoor base station to provide services. Therefore, VLC is often considered as a WiFi complement and the term LiFi is used to describe such networks [HYWC16]. In comparison to the RF counterparts, VLC enjoys superior features such as ultra-high optical bandwidth, robustness to electromagnetic interference, a high degree of spatial confinement bringing virtually unlimited frequency

(or wavelength) reuse, and inherent physical security [BST$^+$14, TVH15]. Similarly, POFs are popular
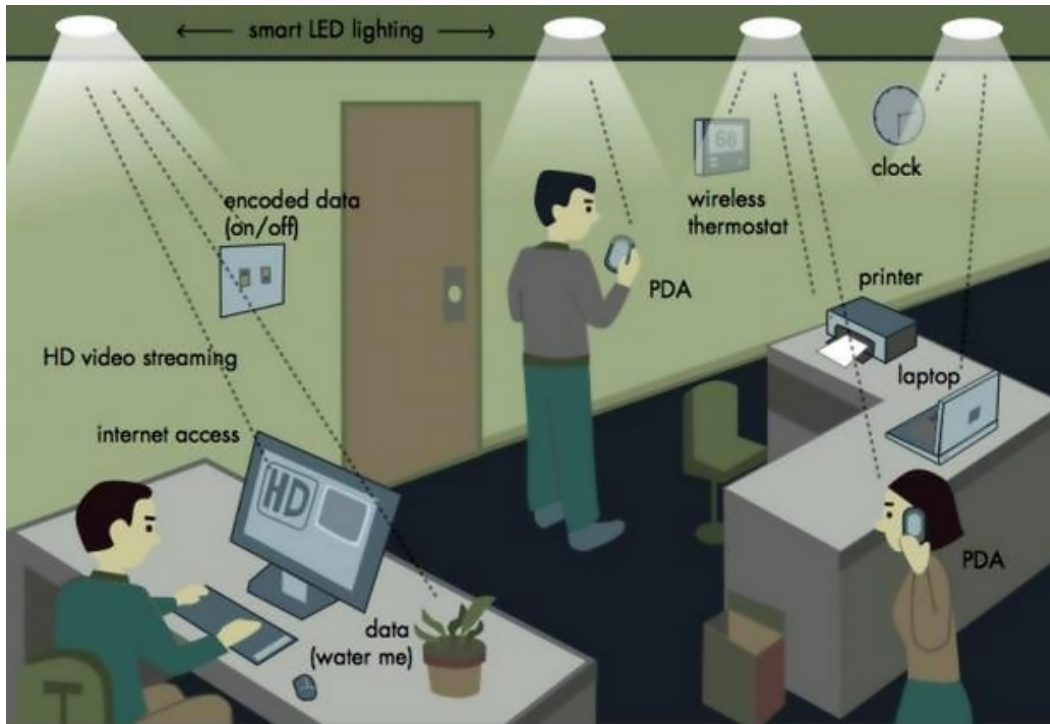
Figure 1.2.: An illustration of indoor VLC system.

low-cost solutions for short-distance applications in digital car networks, industrial networks, and home networks as well as appliances. Specifically, POF has been used in automotive networking systems since 1998 after the successful introduction of the media oriented systems transport (MOST) standard [MOS10, Grz11]. POFs are manufactured from low-cost plastics, i.e., polymethyl methacrylate (PMMA), commonly known as acrylic or polystyrene, whereas the traditional glass fiber optic are constructed from tiny strands of glass that are bundled together inside an application-specific sheath. In general, POFs use a large core step-index fiber with a typical diameter of 1 mm. This large size makes it easy to couple lot of light from sources, and the connectors do not need to have a high precision. Therefore, in comparison with glass fibers, POFs offer easy and cost-efficient processing since the fiber and the associated optical links, connectors, and installations are all inexpensive. Moreover, POFs are more flexible for plug interconnections. The main advantage of using glass fibers is their low attenuation, which is below 0.5 dB/km in the infrared range [Kei08]. This makes them ideal for long distance communications. In contrast to the glass fiber, POFs provide acceptable attenuation only in the visible spectrum from 450 nm up to 750 nm, where the minimum attenuation is about 85 dB/km at approximately 570 nm [ZKZD02]. Thus, light emitting diodes (LEDs) or laser diodes can be used as a source. Due to this relatively low attenuation in the visible band, POFs can be efficiently used only for short distance communication, i.e., up to 100 m.

To achieve high data rates, these optical systems have to use advanced transmission techniques which offer robustness against dispersion in the time domain. This is due to the fact that both POF and VLC systems generally employ low cost LEDs as a source which have limited temporal and spatial

coherence. For POFs, the multipath propagation channel causes bandwidth limitations as it acts as a low pass filter for transmitted signals. Therefore, the multipath dispersion in POFs increases with the fiber length [PHH13]. Although a VLC system may also suffer from multipath dispersion when a wide field-of-view (FOV) detector is used instead of an imaging or angle diversity receiver [KB97], in general the primary source of this dispersion is the high-power LED itself unless a micro-LED is used. The LED output signal, if considered from the field perspective, appears like broadband noise, i.e., a random signal. Therefore, intensity modulation needs to be used and the optical channel is consequently modeled with respect to the instantaneous optical power/intensity. The corresponding signals are baseband signals and not passband signals, and pulse-amplitude modulation (PAM) and on-off keying (OOK) relying on baseband pulses are obvious ways for modulation. It is also possible to modulate the LED intensity by means of biased or half-wave rectified sinusoidal electrical signals. In this case, we use the terminologies single or multiple subcarrier modulation as in [KB97, CK96] but not the single-carrier or multi-carrier modulation as suggested in many other publications, e.g., [HYWC16] [1]. Two important examples of multiple subcarrier modulation schemes, which have been investigated intensively for these optical systems, are DC-biased discrete multi-tone transmission (DC-DMT) and asymmetrically clipped DMT (AC-DMT), where AC-DMT uses half-wave rectifying pulses [CK96, AS08]. DMT refers to the real-valued version of the CP-OFDM scheme. This clearly distinguishes such multiple subcarrier schemes from coherent OFDM approaches with a complex-valued IDFT output signal that is used for a two-dimensional field modulation of an optical carrier. Since subcarrier channel gains are mainly determined by deterministic low-pass transfer functions of the LEDs, in general optical transmission with IM and DD does not suffer from channel frequency selectivity at optical frequencies. In order to compensate the increasing loss at higher subcarrier frequencies, DMT is often combined with bit-loading when channel state information (CSI) is available at the transmitter [WCHG14].

Note that one of the advantages of CP-OFDM in RF communication is its simple per-subcarrier signal processing, which is a consequence of the diagonalization of a circulant matrix using the DFT. This simple frequency domain equalization (FDE) can also be achieved by using CP or UW based PAM block transmission. The insertion of a CP ensures that the received symbol appears as a cyclic signal within the DFT window. Compared to DMT, PAM block transmission offers two significant advantages. Firstly, the necessity of a real-valued IDFT output at the DMT transmitter annuls the bandwidth advantage compared to baseband PAM [WH12]. This is due to the fact that the necessity of a real-valued IFFT output imposes that the FFT-spectrum must have a complex conjugated symmetry. As a result, at least half of the complex subcarriers are basically redundant, since they are just required to ensure a real-valued time domain signal. For the same modulation order, this reduces the bandwidth efficiency of the DMT schemes compared to CP-OFDM with field modulation by a factor of two for DC-Biased DMT and by a factor of 4 for AC-DMT. Secondly, a DMT signal has a large peak-to-average power ratio (PAPR) and thus it requires a correspondingly large dynamic range of the LED driver. In contrast, the PAM transmission based on rectangular pulses exhibits only a few discrete amplitude levels, which are equal to the modulation order, and the optical PAPR is only 3 dB if the non-return-to-zero (NRZ) format is used [WCH16a]. In particular, since typical LED light devices consist of multiple LEDs, the

---

[1]Unlike in RF communications, where single or multiple high-frequency sinusoidal carriers are used for up-conversion, coherent optical carriers do not exist for LEDs. Hence, the terms 'single-carrier' and 'multi-carrier' can cause misunderstandings.

M different power levels of such a multilevel PAM signal can be realized by simply switching different LEDs in one LED device on and off, which is the most energy efficient way of LED driving. Most of the existing literature on optical systems with IM/DD use or recommend DMT schemes. Their main motivation for the use of DMT schemes comes from the success of CP-OFDM in RF communications. However, all the above mentioned factors motivate us to investigate alternative transmission strategies that are best suited to achieve high data rates for optical systems with IM/DD.

1.2.1. Major Contributions

The major contributions of this part are as follows:

- *Investigation of block transmission with frequency domain equalization for optical systems with intensity modulation and direct detection*

  In Chapter 5, we mainly focus on block transmission schemes that can be combined with frequency domain equalization. We investigate the performance of these schemes for both VLC and POF systems. Specifically, we show that PAM block transmission combined with FDE is a very good alternative to DMT schemes. We contribute in this chapter from various aspects. We investigate the performance of PAM block transmission combined with a non-return-to-zero (NRZ) or a return-to-zero (RZ) transmit filter and also with symbol-spaced or fractionally-spaced linear FDE for POF and VLC systems. VLC systems require DC-balanced schemes to avoid the flickering of light. PAM does not provide a DC-balance. Therefore we propose line coding techniques for PAM transmission. We also propose novel single subcarrier (SSC) modulation schemes. We further show that the existing SSC schemes in the literature can be combined with block transmission and FDE. Finally, we propose bit-loading techniques for DMT schemes and do a comprehensive comparison of these schemes.

- *Non-linear equalization and precoding techniques for PAM transmission*

  The dispersive nature of the optical channel in these systems results in pre-cursor and post-cursor inter symbol interference (ISI). Although linear FDE can fully compensate for ISI but it suffers from noise enhancement. Therefore, non-linear equalization and precoding techniques such as decision feedback equalization (DFE) and Tomlinson-Harashima precoding (THP) are attractive choices to achieve a better performance. However, this better performance comes at the expense of a higher computational complexity. In Chapter 6, we discuss the performance of PAM transmission with different transceiver concepts and compare it with the other transmission schemes. Specifically, a low computationally complex transceiver architecture for PAM block transmission is proposed where a linear FDE along with a time domain feedback equalizer is employed. This scheme has the same performance as the DFE and THP, but requires a much lower computational complexity.

- *Design of novel unique word DMT schemes that are derived from UW-OFDM*

  The conventional DMT schemes that satisfy the non-negativity constraint include AC-DMT, DC-biased DMT, and PAM DMT. These schemes have been thoroughly investigated in the literature [AS08, EMH09, WH12]. In Part 1, it has been shown that UW-OFDM shows a superior bit

error ratio (BER) performance over CP-OFDM especially for highly frequency selective channels. In Chapter 7, we propose novel unique word DMT (UW-DMT) schemes that use complex-valued and real-valued modulation formats. The concept of these UW-DMT schemes is derived from UW-OFDM. But it differs from UW-OFDM because of two reasons. Firstly, a Hermitian symmetry has to be enforced in the frequency domain to obtain a real-valued signal that imposes an additional constraint on the design of the code generator matrix. Secondly, we need to derive new approaches to design the code generator matrix while keeping this additional constraint (non-negativity constraint) in mind. Hence, the code generator matrices derived for UW-OFDM cannot be used. Therefore, we derive new code generator matrix designs for these schemes. Moreover, the design of the code generator is different for real-valued and complex-valued constellation formats. The results show that these schemes outperform the conventional CP-DMT schemes.

1.3. Part III: Analytical Performance Analysis of Multi-linear (tensor) Algebraic Concepts

Tensors, which are multi-dimensional generalizations of matrices, are adopted in diverse branches of science such as image processing [KB09, Cic13, DLS$^+$15], signal processing for telecommunications [dAFM07, dLC07], array signal processing [SGB00, RHDG14], psychometrics [Tuc64, CC70], quantum chemistry [SBG05], arithmetic complexity [Kru77, BCS10], and biomedical signal processing [MHH$^+$06, VdLV$^+$07, WRH$^+$09]. Tensors provide a useful representation of multi-dimensional data and enables us to exploit the rich multi-dimensional structure that often results in a benefit such as improved estimation accuracy or lower complexity. Specifically tensor decompositions that decompose data tensors in factor matrices are very attractive from a signal processing and data analysis point of view. The popularity is due to the fact they take into account spatial, temporal, and spectral information. Moreover, they provide links among various data and extracted factors or hidden components with physical or physiological meaning and interpretations. In most of the above mentioned applications, we would like to estimate the factor matrices that have some physical meaning. The decomposition of a tensor into a sum of rank-one terms allows to solve this problem, provided that the decomposition can be shown to be essentially unique. The main difficulty stems from the fact that actual tensors may not exactly satisfy the expected model due to additive noise, so that the problem is eventually an approximation rather than an exact decomposition.

Although there exist many models for tensor decompositions, but the most basic and widely used ones are the higher-order singular value decomposition (HOSVD) and the canonical polyadic decomposition (CPD). The HOSVD decomposes a tensor into a core tensor and unitary factor matrices. The core tensor itself satisfies the so-called all-orthogonality condition, i.e., all of its unfoldings are row-orthogonal matrices. In many applications, low-rank approximations are required to suppress the additive noise of a low-rank desired signal component from a noisy observation. However, the HOSVD does not provide the best low-rank approximation in some norm as the truncated SVD provides the best low-rank approximation in the Frobenius norm for matrices [GVL13]. There exist many algorithms [dLdMV00a] that provide a good low-rank approximation, but are not optimal. Still, the truncated HOSVD is asymptotically optimal in the high signal to noise ratio (SNR) [dLdMV00a] and thus can be used as a

starting point for any algorithm such as higher order orthogonal iterations (HOOI) which computes the best approximation.

Another widely adopted tensor decomposition method is the CPD, also referred as canonical decomposition (CANDECOMP) or parallel factor (PARAFAC) analysis. It allows to decompose a tensor into a sum of rank-one components. The biggest advantage of the CPD comes from the fact that the factor matrices are essentially unique under mild conditions, which makes it very useful, also in cases when no or only very limited a priori information is available. Therefore, the CPD has been recognized as a basic tool for signal separation and data analysis, with many concrete applications in telecommunication, array processing, and machine learning [CMdL+15, CJ10, SdLF+17]. The CPD can be viewed as another extension of the matrix SVD to higher orders, with the difference that the factor matrices are generally non-orthogonal and the core tensor is an identity tensor.

In most of the data driven applications, we only have a noise corrupted version of the low-rank noiseless tensor. The main goal in such applications is to compute the approximate CPD of this noisy tensor. To solve CPD problems, iterative alternating least squares (ALS) methods are widely employed [CC70, Har70]. However, these methods are not efficient since they may require a large number of iterations to converge and are not guaranteed to reach the global optimum. Therefore, these methods are computationally expensive. Alternatively, semi-algebraic solutions such as the Semi-Algebraic canonicaL decomposiTion (SALT) [LA11] and the SEmi-algebraic Canonical polyadic decomposition via SImultaneous matrix diagonalizationn (SECSI) [RH13] have been proposed in the literature. By exploiting the structure of the tensor, the SECSI framework identifies the whole set of joint eigenvalue decompositions (JEVDs) (also called simultaneous matrix diagonalizations (SMDs)) [RH13]. Solving all of the JEVD problems yields several estimates of the factor matrices. In the final step of the SECSI framework, an appropriate solution is selected that results in a more robust algorithm with an improved performance. Moreover, in contrast to ALS, the SECSI framework facilitates the implementation on a parallel hardware architecture.

1.3.1. Major Contributions

In this part of the thesis, we focus on deriving analytical expressions for the first-order perturbation analysis of the truncated HOSVD and the SECSI framework that is used to compute the approximate CPD of a noise corrupted low-rank tensor. The results of a perturbation analysis for these decompositions are of major importance when analyzing the tensor based algorithms that use these decompositions. Moreover, a perturbation analysis of these decompositions allows us to simulate the behavior of these algorithms, in different scenarios, without the need of computationally expensive Monte-Carlo trials. To the best of our knowledge, there exists no such analytical assessments in the literature. The main contributions of this part are as follows:

- *First-order perturbation analysis of the truncated HOSVD*

  The HOSVD was first introduced in [dLdMV00b], as the generalization of the SVD for the multlilinear case. Later, the truncated HOSVD was investigated in [dLdMV00a] as an alternative for low-rank approximation. In that work, it has been shown that the truncated HOSVD is not the optimal low-rank approximation in the multi-dimensional case. However, iterative algorithms such

as the HOOI [dLdMV00a] can be used to obtain a better approximation. But the improvement in terms of reconstruction error from using the HOOI algorithm instead of the truncated HOSVD is only marginal in the low SNR regime and negligible for high SNRs [Roe12]. A perturbation analysis of the truncated HOSVD as low-rank approximation of a tensor was presented in [dL04]. But the results are shown in terms of a known noise tensor and no closed-form mean square error (MSE) expressions in term of the noise statistics are derived. In Chapter 8, we present a first-order perturbation analysis of the truncated HOSVD where we derive closed-form MSE expressions in terms of the noise statistics. We evaluate the performance of our analytical results not only on computer generated data but also on some images. The simulation results show an excellent match between the derived expressions and the empirical results.

- *First-order perturbation analysis of the SECSI framework for the approximate CPD*

  The SECSI framework performs three distinct steps to compute the approximate CPD of a noisy low-rank tensor. In the first step, the truncated HOSVD is used to suppress the noise. In the second step, the whole set of JEVDs is constructed from the truncated core tensor that results in several estimates of the factor matrices. Finally, the best factor matrices are selected from these estimates by using an appropriate selection strategy as presented in [RH13]. Depending on the chosen strategy, a performance complexity trade-off can be obtained. To compute a first-order perturbation analysis of the SECSI framework, we need a perturbation analysis for each of the steps. We have performed a first-order perturbation analysis of the JEVD algorithms which are based on the indirect least squares (LS) cost function in [BCW+17]. The indirect LS cost function based JEVD algorithms are generally employed in the SECSI framework. Using the results presented in Chapter 8 and in [BCW+17] (also summarized in Appendix D.1), we perform a first-order perturbation analysis of the SECSI framework for the approximate CPD of a noisy low-rank 3-way tensor in Chapter 9. In this work, apart from zero-mean and finite second order moments, no assumptions about the noise are required. In the 3-way case, we can construct up to 6 JEVD problems in the SECSI framework that result in multiple estimates for each factor matrices (one factor matrix estimate from each JEVD). In [RH13], an exhaustive search based best matching scheme and also heuristic selection schemes with a reduced computational complexity are proposed to select the final matrix estimates. In Chapter 9, we propose a new selection scheme that is based on the performance analysis results. We show that this new scheme outperforms the existing schemes especially at high SNR values.

1.4. Preliminary Definitions and Concepts

In this section, we define the notation and some necessary fundamental concepts which are used in this thesis. We summarize these properties/definitions in a compact and systematic form so that the following chapters can be easily understood without the need to search these properties/concepts in various references. We first define the general notation that is used in the thesis. We also review some of the matrix properties/concepts that already exist in the literature and are used in the rest of the thesis. Since in Part 3 of this thesis we focus on the first-order perturbation analysis of tensor based algorithms,

we review some of the basic algebraic tools for tensors and also state some useful tensor properties.

1.4.1. Notation and Matrix-Properties

We use the formulations a, $\mathbf{a}$, $\boldsymbol{A}$, and $\boldsymbol{\mathcal{A}}$ for a scalar, column vector, matrix, and tensor variables respectively. Furthermore, $\boldsymbol{\mathcal{A}}(i, j, k)$ will be the element (i, j, k) of a tensor $\boldsymbol{\mathcal{A}}$. The same applies for $\boldsymbol{A}(i, j)$ and $\mathbf{a}(i)$ in the matrix and vector cases, respectively. The superscripts $^{-1}$, $^{+}$, *, $^{\mathrm{T}}$, $^{\mathrm{H}}$ denote the matrix inverse, Moore-Penrose pseudo inverse, conjugate, transposition, and conjugate transposition, respectively. Also, we will use the notation $\mathbb{E}\{\cdot\}$, $\mathrm{tr}[\cdot]$, $\otimes$, $\|\cdot\|_{\mathrm{F}}$, $\|\cdot\|_2$ for the expectation, trace, Kronecker product, Frobenius norm, and 2-norm operators. Some of the Kronecker product related properties that are used in this thesis are summarized as

$$(\boldsymbol{A} \otimes \boldsymbol{B})^H = \boldsymbol{A}^H \otimes \boldsymbol{B}^H \tag{1.1}$$

$$(\boldsymbol{A} \otimes \boldsymbol{B})^+ = \boldsymbol{A}^+ \otimes \boldsymbol{B}^+ \tag{1.2}$$

$$\|\boldsymbol{A} \otimes \boldsymbol{B}\|_F = \|\boldsymbol{A}\|_F \cdot \|\boldsymbol{B}\|_F \tag{1.3}$$

$$(\boldsymbol{A} \otimes \boldsymbol{B}) \cdot (\boldsymbol{C} \otimes \boldsymbol{D}) = (\boldsymbol{A} \cdot \boldsymbol{C}) \otimes (\boldsymbol{B} \cdot \boldsymbol{D}), \tag{1.4}$$

where $\boldsymbol{A} \in \mathbb{C}^{N \times M}$, $\boldsymbol{B} \in \mathbb{C}^{P \times Q}$, $\boldsymbol{C} \in \mathbb{C}^{M \times R}$, and $\boldsymbol{D} \in \mathbb{C}^{Q \times R}$.

For a matrix $\boldsymbol{A} = [\mathbf{a}_1, \mathbf{a}_2, \ldots, \mathbf{a}_M] \in \mathbb{C}^{N \times M}$, where $\mathbf{a}_1, \mathbf{a}_2, \ldots, \mathbf{a}_M$ are its columns, the operator $\mathrm{vec}\{\cdot\}$ denotes the vectorization operation that is defined as

$$\mathrm{vec}\{\boldsymbol{A}\}^{\mathrm{T}} = [\mathbf{a}_1^{\mathrm{T}}, \mathbf{a}_2^{\mathrm{T}}, \ldots, \mathbf{a}_M^{\mathrm{T}}].$$

This operator has the following properties

$$\mathrm{vec}\{\boldsymbol{A} \cdot \boldsymbol{X} \cdot \boldsymbol{B}\} = (\boldsymbol{B}^{\mathrm{T}} \otimes \boldsymbol{A}) \cdot \mathrm{vec}\{\boldsymbol{X}\} \tag{1.5}$$

$$\mathrm{vec}\{\boldsymbol{A} \cdot \boldsymbol{B}\} = (\boldsymbol{I} \otimes \boldsymbol{A}) \cdot \mathrm{vec}\{\boldsymbol{B}\} = (\boldsymbol{B}^{\mathrm{T}} \otimes \boldsymbol{I}) \cdot \mathrm{vec}\{\boldsymbol{A}\} \tag{1.6}$$

where $\boldsymbol{A}$, $\boldsymbol{X}$, $\boldsymbol{B}$ are matrices with the corresponding dimensions. Moreover, we define the $\mathrm{unvec}\{\cdot\}$ operator that stands for the inverse operation of $\mathrm{vec}\{\cdot\}$. In this work, we also use the trace operator which has the following properties

$$\mathrm{tr}(\boldsymbol{A} \cdot \boldsymbol{B}) = \mathrm{tr}(\boldsymbol{B} \cdot \boldsymbol{A}) = \mathrm{vec}(\boldsymbol{A}^{\mathrm{T}})^{\mathrm{T}} \cdot \mathrm{vec}\{\boldsymbol{B}\} \tag{1.7}$$

$$\mathrm{tr}(\boldsymbol{A} \cdot \boldsymbol{B} \cdot \boldsymbol{C} \cdot \boldsymbol{D}) = \mathrm{tr}(\boldsymbol{B} \cdot \boldsymbol{C} \cdot \boldsymbol{D} \cdot \boldsymbol{A}) = \mathrm{tr}(\boldsymbol{C} \cdot \boldsymbol{D} \cdot \boldsymbol{A} \cdot \boldsymbol{B}) = \mathrm{tr}(\boldsymbol{D} \cdot \boldsymbol{A} \cdot \boldsymbol{B} \cdot \boldsymbol{C}) \tag{1.8}$$

$$\mathrm{tr}(\boldsymbol{A} \otimes \boldsymbol{B}) = \mathrm{tr}(\boldsymbol{A}) \cdot \mathrm{tr}(\boldsymbol{B}) \tag{1.9}$$

$$\mathrm{tr}(\boldsymbol{A} \cdot \boldsymbol{B} \cdot \boldsymbol{C}) = \mathrm{vec}(\boldsymbol{A}^{\mathrm{T}})^{\mathrm{T}} \cdot (\boldsymbol{I} \otimes \boldsymbol{B}) \cdot \mathrm{vec}(\boldsymbol{C}) \tag{1.10}$$

$$\mathrm{tr}(\boldsymbol{B} \cdot \boldsymbol{X} \cdot \boldsymbol{B}^{\mathrm{H}}) = \mathrm{vec}(\boldsymbol{B})^{\mathrm{H}} \cdot (\boldsymbol{X}^{\mathrm{T}} \otimes \boldsymbol{I}) \cdot \mathrm{vec}(\boldsymbol{B}) \tag{1.11}$$

where $\boldsymbol{A} \in \mathbb{C}^{N \times M}$ and $\boldsymbol{B} \in \mathbb{C}^{M \times N}$.

Moreover, we define the diagonalization operator $\mathrm{diag}(\cdot)$ as in Matlab. Note that, when this operator is applied to a vector, the output is a diagonal matrix, and when applied to a matrix, the output is a

column vector. Therefore, for the sake of clarity, we use the notation $\text{Diag}(\cdot)$ when applying this operator to a vector, and $\text{diag}(\cdot)$ when applying it to a matrix. Furthermore we define the operators $\text{Ddiag}(\cdot)$ and $\text{Off}(\cdot)$ as

$$\text{Ddiag}(\boldsymbol{X}) = \text{Diag}(\text{diag}(\boldsymbol{X})) \in \mathbb{C}^{N \times N}$$
$$\text{Off}(\boldsymbol{X}) = \boldsymbol{X} - \text{Diag}(\text{diag}(\boldsymbol{X})) \in \mathbb{C}^{N \times N},$$

where $\boldsymbol{X}$ is a square matrix matrix of size $N \times N$. Note that the $\text{Ddiag}(\cdot)$ operator sets to zero all the off-diagonal elements of $\boldsymbol{X}$, while the $\text{Off}(\cdot)$ operator sets to zero the diagonal elements of $\boldsymbol{X}$.

Finally, we frequently use the following property

$$(\boldsymbol{Y} + \Delta \boldsymbol{Y})^{-1} = \boldsymbol{Y}^{-1} - \boldsymbol{Y}^{-1} \cdot \Delta \boldsymbol{Y} \cdot \boldsymbol{Y}^{-1} + \mathcal{O}(\Delta^2), \tag{1.12}$$

where $\boldsymbol{Y}$ is a square invertible matrix and $\Delta \boldsymbol{Y}$ is a square matrix as well as a first-order term. This property can be proven by making use of a theorem that was introduced by Carl Newman in 1877 [Neu77]. According to this theorem

$$(\boldsymbol{I}_d + \Delta \boldsymbol{X})^{-1} = \boldsymbol{I}_d - \Delta \boldsymbol{X} + (\Delta \boldsymbol{X})^2 - (\Delta \boldsymbol{X})^3 + \cdots,$$

for any $\Delta \boldsymbol{X} \in \mathbb{C}^{d \times d}$ with Frobenius norm smaller than one. Since, $\boldsymbol{Y}$ is invertible we can reformulate $(\boldsymbol{Y} + \Delta \boldsymbol{Y})^{-1}$ as $\boldsymbol{Y}^{-1} \cdot (\boldsymbol{I}_d + \Delta \boldsymbol{Y} \cdot \boldsymbol{Y}^{-1})^{-1}$. By using the above theorem, we get the following expression

$$
\begin{aligned}
(\boldsymbol{Y} + \Delta \boldsymbol{Y})^{-1} &= \boldsymbol{Y}^{-1} \cdot (\boldsymbol{I}_d + \Delta \boldsymbol{Y} \cdot \boldsymbol{Y}^{-1})^{-1} \\
&= \boldsymbol{Y}^{-1} \cdot \left(\boldsymbol{I}_d - (\Delta \boldsymbol{Y} \cdot \boldsymbol{Y}^{-1}) + (\Delta \boldsymbol{Y} \cdot \boldsymbol{Y}^{-1})^2 - (\Delta \boldsymbol{Y} \cdot \boldsymbol{Y}^{-1})^3 + \cdots \right) \\
&= \boldsymbol{Y}^{-1} \cdot \left(\boldsymbol{I}_d - (\Delta \boldsymbol{Y} \cdot \boldsymbol{Y}^{-1}) + \mathcal{O}(\Delta^2) \right) \\
&= \boldsymbol{Y}^{-1} - \boldsymbol{Y}^{-1} \cdot \Delta \boldsymbol{Y} \cdot \boldsymbol{Y}^{-1} + \mathcal{O}(\Delta^2),
\end{aligned}
$$

which proves this relation.

1.4.2. Tensor Algebra - Definitions and Properties

In many signal processing applications, the term tensor is used synonymously with the term multi-way array. In this case, an R-D tensor which is defined by a collection of numbers referenced by R indices. Therefore, up to $R = 2$ tensors are no different from matrices. However, for $R > 2$ new operations are needed.

Let $\boldsymbol{\mathcal{A}} \in \mathbb{C}^{M_1 \times M_2 \times \cdots \times M_R}$ be an R-D tensor or R-way array, where M_r is the size along the r-th dimension for $r = 1, 2, \cdots, R$. The r-mode vectors of a tensor are the vectors we obtain if the r-th index is varied and all other indices are kept fixed. They represent the generalization of row vectors and column vectors of matrices. Moreover, an $M_r \times \frac{M}{M_r}$ matrix containing all r-mode vectors as its column is called the r-mode unfolding of $\boldsymbol{\mathcal{A}}$ where $M = \prod_{r=1}^{R} M_r$. The ordering of the columns in the r-mode unfolding defines how to arrange the remaining $R-1$ indices. There exist many choices for this ordering but two of the most popular choices are

1. Reverse cyclical: This way of unfolding was introduced in [dLdMV00b] and has become the standard practice in the community. In this ordering, we first vary the $(r-1)$th index, then the $(r-2)$th, and continue up to the 1st, then we start over with the Rth index, the $(R-1)$th, and continue up to the $(r+1)$th index. An r-mode unfolding achieved in this way is denoted as $[\boldsymbol{\mathcal{A}}]_{(r)}$. As an example, the r-mode vectors of a three-way tensor $\boldsymbol{\mathcal{X}} \in \mathbb{C}^{4 \times 5 \times 3}$ are shown in Fig. 1.3.

2. Forward column ordering: In this ordering of the columns of the r-mode unfolding, we always start with the first index and keep increasing to the Rth by leaving out the rth index. It is, for instance, the column ordering that we get by using the "permute" and "reshape" commands in MATLAB.
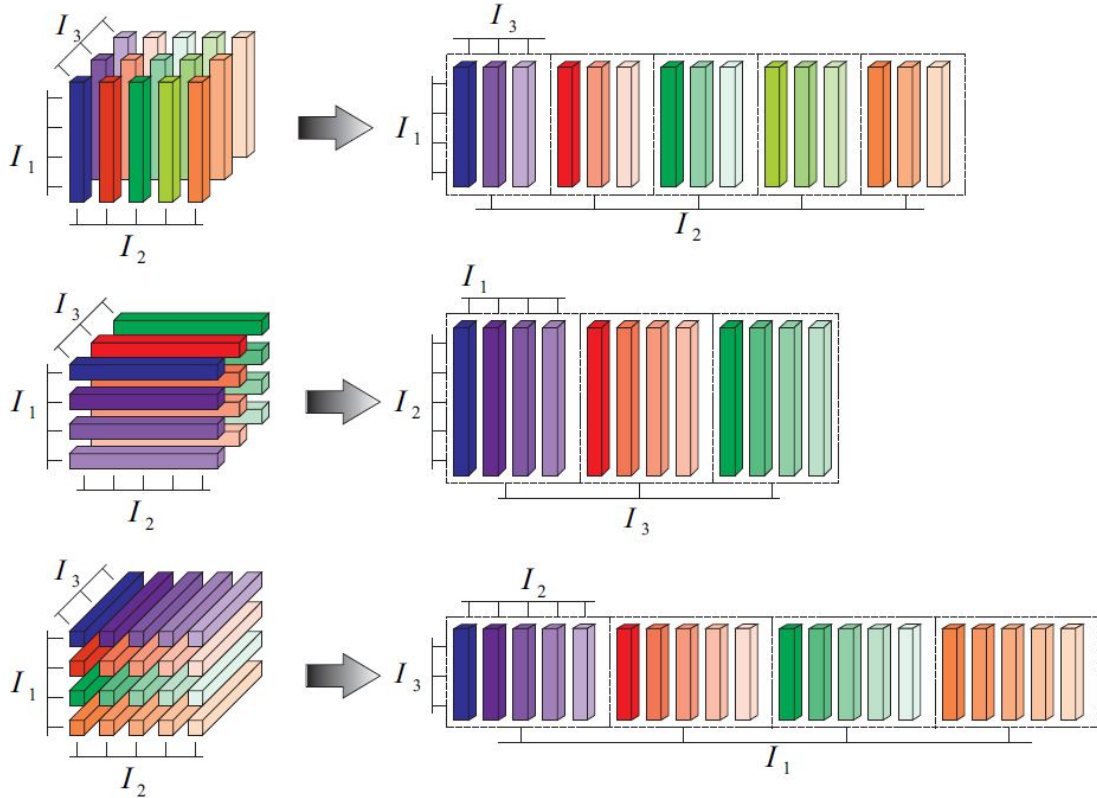
Figure 1.3.: Graphical representation, from [HC15], of the reverse cyclical unfoldings of a $\boldsymbol{\mathcal{X}} \in \mathbb{C}^{4 \times 5 \times 3}$ tensor.

The r-mode product of a tensor $\boldsymbol{\mathcal{A}}$ with a matrix $\boldsymbol{B} \in \mathbb{C}^{N \times M_r}$ (i.e., $\boldsymbol{\mathcal{A}} \times_r \boldsymbol{B}$) is defined as

$$\boldsymbol{\mathcal{C}} = \boldsymbol{\mathcal{A}} \times_r \boldsymbol{B} \iff [\boldsymbol{\mathcal{C}}]_{(r)} = \boldsymbol{B} \cdot [\boldsymbol{\mathcal{A}}]_{(r)},$$

where $\boldsymbol{\mathcal{C}}$ is a tensor with the corresponding dimensions. This can be interpreted as an r-linear transformation, i.e., a transformation which is linear in the r-th mode which can be expressed via the multiplication of all r-mode vectors by a matrix $\boldsymbol{B}$ from the left. Moreover, the r-mode product also has the property: if $\boldsymbol{\mathcal{C}} = \boldsymbol{\mathcal{A}} \times_1 \boldsymbol{X}^{(1)} \times_2 \boldsymbol{X}^{(2)} \times_3 \cdots \times_R \boldsymbol{X}^{(R)}$, then

$$[\boldsymbol{\mathcal{C}}]_{(r)} = \boldsymbol{X}^{(r)} \cdot [\boldsymbol{\mathcal{A}}]_{(r)} \cdot \left(\boldsymbol{X}^{(r+1)} \otimes \boldsymbol{X}^{(r+2)} \otimes \cdots \boldsymbol{X}^{(R)} \otimes \boldsymbol{X}^{(1)} \otimes \boldsymbol{X}^{(2)} \otimes \cdots \otimes \boldsymbol{X}^{(r-1)} \right)^{\mathrm{T}}, \tag{1.13}$$

where $\boldsymbol{X}^{(r)}, \forall r = 1, 2, \ldots, R$ are matrices with the corresponding dimensions. Moreover, the order of the matrices in the Kronecker product is a direct consequence of the reverse cyclical column ordering that was chosen for the r-mode unfolding. Similarly, r-mode products and r-mode unfoldings satisfy the following properties.

$$\boldsymbol{\mathcal{A}} \times_r \boldsymbol{X}^{(r)} \times_p \boldsymbol{X}^{(p)} = \boldsymbol{\mathcal{A}} \times_p \boldsymbol{X}^{(p)} \times_r \boldsymbol{X}^{(r)} \qquad \text{where } r \neq p \tag{1.14}$$

$$\boldsymbol{\mathcal{A}} \times_r \boldsymbol{X}^{(r)} \times_r \boldsymbol{Y}^{(r)} = \boldsymbol{\mathcal{A}} \times_r (\boldsymbol{Y}^{(r)} \cdot \boldsymbol{X}^{(r)}), \tag{1.15}$$

where $r, p \in \{1, 2, \cdots, R\}$ and the dimensions of tensors and matrices are $\boldsymbol{\mathcal{A}} \in \mathbb{C}^{M_1 \times M_2 \times \cdots \times M_R}$, $\boldsymbol{X}^{(r)} \in \mathbb{C}^{N_r \times M_r}$, and $\boldsymbol{Y}^{(r)} \in \mathbb{C}^{P_r \times N_r}$. Furthermore, for the sake of notational simplicity, we define the following short-hand notation for multiple Kronecker and r-mode products as

$$\bigotimes_{r=1}^{R} \boldsymbol{X}^{(r)} = \boldsymbol{X}_1 \otimes \boldsymbol{X}^{(2)} \otimes \cdots \otimes \boldsymbol{X}^{(R)}$$

$$\boldsymbol{\mathcal{A}} \bigtimes_{r=1}^{R} \boldsymbol{X}^{(r)} = \boldsymbol{\mathcal{A}} \times_1 \boldsymbol{X}^{(1)} \times_2 \boldsymbol{X}^{(2)} \times_3 \cdots \times_R \boldsymbol{X}^{(R)}$$

$$\boldsymbol{\mathcal{A}} \bigtimes_{\substack{r=1 \\ r \neq j}}^{R} \boldsymbol{X}^{(r)} = \boldsymbol{\mathcal{A}} \times_1 \boldsymbol{X}^{(1)} \times_2 \cdots \times_{j-1} \boldsymbol{X}^{(j-1)} \times_{j+1} \boldsymbol{X}^{(j+1)} \times_{j+2} \cdots \times_R \boldsymbol{X}^{(R)}.$$

Eq. (1.13) suggests that the r-mode multiplication can be easily transformed into a matrix multiplication via the r-mode unfolding. However, the vectorized versions of different unfoldings contain the same elements in a different order. The correct ordering can be restored by defining permutation matrices. For every tensor $\boldsymbol{\mathcal{A}} \in \mathbb{C}^{M_1 \times M_2 \times \cdots \times M_R}$, there exists a unique set of permutation matrices $\boldsymbol{P}^{(r)}_{M_1, M_2 \cdots M_R} \forall r = 1, 2, \cdots, R$ such that

$$\text{vec}\{\boldsymbol{\mathcal{A}}\} = \boldsymbol{P}^{(r)}_{M_1, M_2 \cdots M_R} \cdot \text{vec}\{[\boldsymbol{\mathcal{A}}]_{(r)}\}. \tag{1.16}$$

The space spanned by the r-mode vectors is termed as r-space of $\boldsymbol{\mathcal{A}}$, whereas the dimension of this vector space refers to the r-rank of $\boldsymbol{\mathcal{A}}$ (the rank of the r-mode unfolding). Note that in general, the r-ranks (also referred to as the multilinear ranks) of a tensor $\boldsymbol{\mathcal{A}}$ can all be different. Since a matrix of rank r can be constructed as a sum of r rank-one matrices, in the same manner, a tensor of rank r can be constructed as a sum of r rank-one tensors. Therefore, tensor rank refers to the smallest possible r such that a tensor can be written as a sum of r rank-one tensors. More importantly, the tensor rank is not directly related to the r-rank, it only provides an upper bound, i.e., $\text{rank}(\boldsymbol{\mathcal{A}}) \geq r\text{-rank}(\boldsymbol{\mathcal{A}})$, $\forall r = 1, 2, \cdots, R$.

Lastly, the higher order norm $\| \cdot \|_{\text{H}}$ of a tensor is defined as

$$\|\boldsymbol{\mathcal{A}}\|_{\text{H}} = \|[\boldsymbol{\mathcal{A}}]_{(r)}\|_{\text{F}} = \|\text{vec}\{[\boldsymbol{\mathcal{A}}]_{(r)}\}\|_2 \quad \forall r = 1, 2, \ldots, R,$$

which is nothing else but a higher-order extension of the Frobenius norm. Therefore, like the Frobenius norm of a matrix, it is defined as the square-root of the sum of the squared magnitude of all its elements.

Part I.

MIMO Concepts for UW-OFDM Systems

In this part of the thesis we focus on MIMO concepts for UW-OFDM. UW-OFDM is a relatively new signaling concept which has been introduced in 2010. So far, this signaling concept has been well investigated in the literature only for single-input single-output (SISO) systems. One attractive method for satisfying the growing demand for higher data rates while ensuring the quality of service is to employ additional antennas at the transmitter and/or at the receiver side and/or at the relays. By using more antennas, we can extract the benefits of the MIMO channels and increase the throughput of the transmission. Therefore, the aim of this part is to investigate MIMO concepts for UW-OFDM systems.

In UW-OFDM, a code generator matrix is used at the transmitter to generate zero unique words at the output of the IDFT. This code generator matrix is known both at the transmitter and the receiver. So far it has been shown for SISO systems that if this code generator matrix is efficiently utilized at the receiver in the estimation process, UW-OFDM shows a superior bit error ratio performance over CP-OFDM. Therefore, in Chapter 2, we expand these investigations to MIMO systems and propose novel linear and non-linear detection schemes for MIMO UW-OFDM systems where the knowledge of the code generator matrix is efficiently used in the estimation process. Major parts of this chapter have been published in two conference papers [CZHH16, CZHH17b].

If channel knowledge is not available at the transmitter, space-time block codes (STBCs) can be used to extract the diversity of the fading channel. Therefore, Chapter 3 is devoted to the applicability of STBCs to UW-OFDM systems. Various types of STBCs have been well investigated in the literature. The main aim of this chapter is to present transceiver designs to apply existing STBCs to UW-OFDM systems. For this purpose, we develop two novel approaches for UW-OFDM systems, namely a frequency domain space-time block code and a time-reversal space-time code (TR-STC). The former one is an extension of the traditional space-frequency block codes for CP-OFDM systems to UW-OFDM systems while the latter one exploits the frame structure of the UW-OFDM symbols to achieve a low complexity decoder. We also develop suitable detection procedures for these approaches. The results of this chapter have been published in [CZHH17a].

5th Generation (5G) cellular systems are expected to meet requirements such as low latency transmissions for long and short data bursts, fast switching between uplink and downlink for time division duplex systems, and handling high data rate wide bandwidth signals. Therefore, many new air interfaces such as filter bank multicarrier (FBMC), universal filtered multicarrier (UFMC), and generalized frequency division multiplex (GFDM) have been proposed to meet these requirements. MIMO systems are expected to be an integral part of 5G systems. Hence, these waveforms need to be well investigated for MIMO systems. In Chapter 4, we focus on space-time block coded UFMC systems. We propose two different approaches to apply STBCs to UFMC systems. The performance of these 5G air proposals is often not compared between each other. Therefore, to facilitate the air interface selection for future cellular systems, we compare the performance of 5G air interface proposals with STBCs using LTE-A parameters. We also compare their performance with UW-OFDM. Parts of this chapter has already been published in the conference paper [CNA+16].

2. Detection Schemes for MIMO UW-OFDM Systems

This chapter is devoted to the detection schemes for MIMO UW-OFDM systems. We introduce the UW-OFDM signaling concept in Section 2.2. A brief overview of the procedures to derive the code generator matrix is also discussed. Then, the linear detection procedures for MIMO UW-OFDM are presented in Section 2.3 where two detection approaches are proposed. Similar to CP-OFDM, a subcarrier wise detection is also possible for UW-OFDM. But in addition an efficient code generator demodulator is required to take advantage of the correlation introduced in the data symbols. Then in the second part of the chapter, we present non-linear equalization techniques in Section 2.4. Moreover, we discuss different successive interference cancellation (SIC) schemes for UW-OFDM. These SIC schemes outperform the linear detection schemes significantly, but have a higher computational complexity. Therefore, a novel hybrid detection scheme is presented in Section 2.4.3. In this scheme, linear detection is employed in the first step and a SIC based code generator demodulation is performed in the second step. The computational complexity of the proposed linear and non-linear detection schemes is analyzed in Section 2.5. The simulation results are presented in Section 2.6. Finally, the contributions are summarized at the end in Section 2.7.

2.1. Introduction

Orthogonal frequency division multiplexing (OFDM) is a popular transmission approach in modern communication systems due to its robustness against frequency selective environments, its simple implementation, and its bandwidth efficiency. A cyclic prefix (CP) is inserted periodically in OFDM. Therefore, within the receivers correlation interval, the linear convolution with the channel impulse response appears as a cyclic convolution. It enables a fast Fourier transform (FFT) based processing of the received signal such that only a simple one tap equalization is needed on each subcarrier in the frequency domain. Since the CP is data dependent and varies from symbol to symbol, it cannot be utilized for any other purposes.

Many alternative concepts have been introduced in RF communication where the conventional CP is replaced by a fixed data independent sequence which still maintains the cyclicity. A well discussed scheme is known symbol padding (KSP) OFDM [CM01]. Recently a new OFDM signaling concept, called unique word (UW) OFDM, has been introduced in [HHH10b, OH10, HHOH14] which is different from CP- or KSP-OFDM. Unlike the CP and KSP cases, the UW forms a part of the DFT-interval as shown in Fig. 2.1. Hence, the most important difference between UW- and KSP-OFDM is the fact that the UW is part of the DFT interval, whereas the known symbol (KS) in KSP is not. As a result of the insertion of the UW in the DFT interval, redundancy is introduced in the frequency domain, which can advantageously be exploited by the receiver to improve the bit error ratio (BER) performance. This redundancy is added in the frequency domain with the help of a code generator matrix. It has been shown in [OH10, HHH10a, HHH10b, HHOH14] that UW-OFDM has a superior BER performance over classical CP-OFDM in frequency selective environments. Moreover, whereas the CP is a random

sequence, the UW or the KS is deterministic. Since the KS and the UW are deterministic, the UW or KS can optimally be designed for particular needs such as synchronization and/or system parameter estimation purposes at the receiver side.

(a) Data structure using CPs

(b) Data structure using KSP

(c) Data structure using UWs
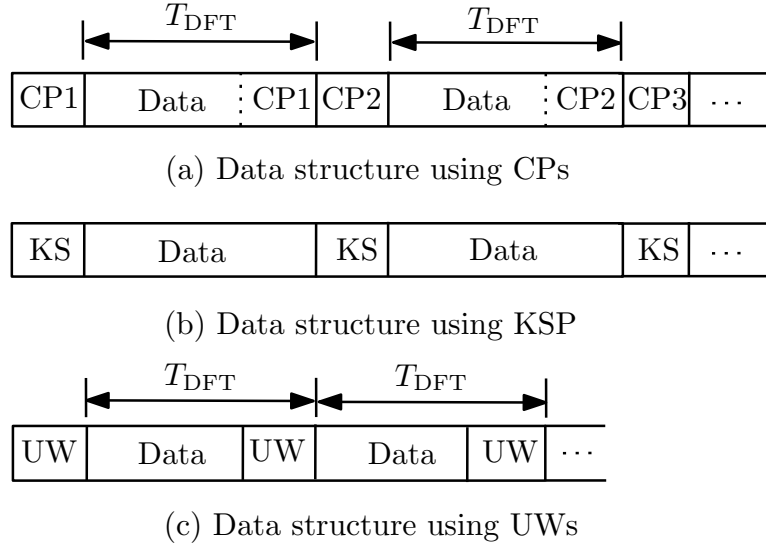
Figure 2.1.: Transmit structure using (a) a CP, (b) a KS or (c) a UW.

In the initial concept described in [HHH10b, OH10], it was suggested to generate UW-OFDM symbols by appropriately loading so-called redundant subcarriers. It turned out that the energy contribution of the redundant subcarriers has a significant impact on the UW-OFDM performance. Moreover, the choice of their positions has a significant influence on the redundant energy. Therefore, in [HHOH14], the authors proposed a heuristic method to calculate the optimum or near optimum redundant subcarrier positions. However, even with the best choice, this so called systematic approach suffers from a high energy contribution of the redundant subcarriers. Hence, in [HHH12], the authors introduced a non-systematic approach where the idea of the dedicated redundant subcarriers is abandoned, and the redundancy is distributed across all subcarriers. The results show that UW-OFDM based on the non-systematic approach not only outperforms the systematic UW-OFDM but also the conventional CP-OFDM [HHH12]. This improved performance is achieved by exploiting the redundancy in the receiver design [Oni13].

One of the reasons for the popularity of CP-OFDM is its simple and low complex frequency domain equalization where usually a single-tap equalization is applied on each subcarrier. Since the code generator matrix in UW-OFDM introduces correlation between the subcarriers, more sophisticated detection schemes are required for UW-OFDM. Various linear and non-linear detection schemes have been studied for UW-OFDM in [Oni13, HOH11]. These detection procedures have been well investigated for single-input single-output (SISO) systems. In wireless communication systems multiple-input multiple-output (MIMO), techniques are widely used to improve the overall spectral and energy efficiency by exploiting the multiple antennas. Therefore, MIMO is an integral part of many modern communication standards such as WLAN, LTE, LTE-A, etc. In this work, we extend our investigations of UW-OFDM to MIMO systems. To achieve an improved performance for UW-OFDM, the code generator matrix has to be efficiently used in the receiver design. Therefore, the conventional detection schemes for CP-OFDM

MIMO systems need to be modified for UW-OFDM systems. The main contribution of this work is to propose detection schemes for MIMO UW-OFDM.

After introducing the UW-OFDM signaling scheme, we propose linear detection schemes in the first part of this chapter in Section 2.3. For this purpose, we propose two approaches where we take advantage of the correlation among the data symbols in the frequency domain introduced by the code generator matrix. In the first approach, we present a model to employ joint detection which is a direct extension of the SISO model in [HOH11], but requires a high computational complexity. In the second approach, we propose a two step procedure where a subcarrier-wise equalization is performed in the first step and in the second step, a code generator demodulator matrix is employed. This approach has the same BER performance as joint detection but a very low computational complexity as compared to the joint detection approach.

In general, the performance of the nonlinear detection schemes is much better than that of linear detection schemes but at the cost of a higher computational complexity. However, the successive interference cancellation (SIC) method offers improved performance without increasing the complexity significantly. It consists of a bank of linear receivers, each of which detects one of the parallel data streams, with the detected signal components successively canceled from the received signal at each stage. Therefore, in the second part of this chapter, the investigation are extended to SIC detection schemes for MIMO UW-OFDM systems. Zero-forcing and QR decomposition based SIC detection schemes are investigated for UW-OFDM. These schemes are based on the linear model that is presented for the joint detection scheme in Section 2.3.1. The MIMO UW-OFDM system employing these SIC schemes results in a significantly superior BER performance but suffers from a higher computational complexity. As compared to the linear two step detection scheme, a hybrid detection scheme is proposed where a combination of subcarrier-wise linear detection is performed in the first step and QR-SIC demodulation is performed in the second step. It offers a trade-off between performance and computational complexity. The performance of this scheme is better than the linear scheme but worse than the SIC schemes.

2.2. The Unique Word OFDM Signaling Scheme

In the following, we briefly review the UW-OFDM symbol generation concept [HHH10b,OH10,HHOH14]. Let $\mathbf{x}_u \in \mathbb{C}^{N_u \times 1}$ be a unique word of length N_u which shall be generated at the tail of a time domain UW-OFDM symbol. In [OH10, HHH10b], it has been suggested to generate a UW-OFDM symbol $\mathbf{x} = \begin{bmatrix} \mathbf{x}_d^T & \mathbf{0} \end{bmatrix}^T$ with a zero-UW in a first step as shown in Fig. 2.2, and to add the desired UW in the time domain in a second step:

$$ \boldsymbol{x}' = \begin{bmatrix} \boldsymbol{x}_d \\ \mathbf{0} \end{bmatrix} + \begin{bmatrix} \mathbf{0} \\ \boldsymbol{x}_u \end{bmatrix} = \begin{bmatrix} \boldsymbol{x}_d \\ \boldsymbol{x}_u \end{bmatrix} \in \mathbb{C}^{N \times 1}. \tag{2.1} $$

The UW-OFDM symbol $\boldsymbol{x}$ with a zero UW is obtained by introducing redundancy in the frequency domain. This is achieved by defining codewords with the help of an appropriate complex-valued code generator matrix $\boldsymbol{G} \in \mathbb{C}^{N_m \times N_d}$ with $N_m = N_d + N_r$ where N_r is the number of additionally required (redundant) subcarriers and $N_r = N_u$.

(a) UW-OFDM symbol generation using systematic method

(b) UW-OFDM symbol generation using non-systematic method
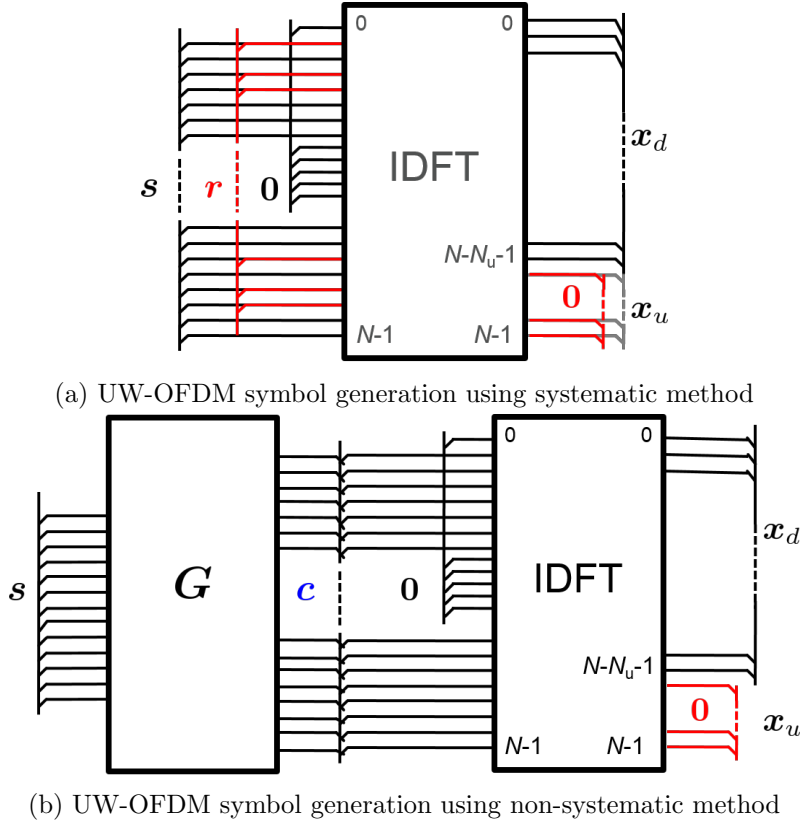
Figure 2.2.: UW-OFDM symbol generation using systematic and non-systematic methods

Let $\boldsymbol{s} \in \mathbb{C}^{N_d \times 1}$ represent the complex data symbols in the frequency domain for N_d data subcarriers. In the UW-OFDM symbol generation, the data symbols $\boldsymbol{s}$ are first fed to the code generator matrix $\boldsymbol{G}$. Then the resulting coded symbols are mapped to the corresponding data subcarriers by a mapping matrix $\boldsymbol{B} \in \{0, 1\}^{N \times N_m}$, which consists of zero rows at the positions of the zero subcarriers and elsewhere unit row vectors. Thereafter, the resulting frequency domain signal is modulated on the subcarriers using the IDFT to obtain the time domain samples $\boldsymbol{x}$, as given by

$$\boldsymbol{x} = \boldsymbol{F}_N^{-1} \boldsymbol{B} \boldsymbol{G} \boldsymbol{s} = \begin{bmatrix} \boldsymbol{x}_d \\ \boldsymbol{0} \end{bmatrix}. \tag{2.2}$$

In order to obtain a zero word UW in the time domain, a valid code generator matrix has to fulfill the following constraints

$$\boldsymbol{F}_N^{-1} \boldsymbol{B} \boldsymbol{G} = \begin{bmatrix} * \\ \boldsymbol{0} \end{bmatrix}, \tag{2.3}$$

where $\boldsymbol{F}_N$ is the N-point DFT matrix with its elements $[\boldsymbol{F}_N]_{k,l} = \frac{1}{\sqrt{N}} e^{-j\frac{2\pi}{N}kl}$ for $k, l = 0, 1, 2, \dots, N-1$.

Note that the UW-OFDM symbol construction can also be interpreted as a codeword generation process, with the codeword $\boldsymbol{c}$ defined by $\boldsymbol{c} = \boldsymbol{G}\boldsymbol{s}$, as shown in Fig. 2.2b. Similar to block codes, two types of code generator matrices, namely systematic $\boldsymbol{G}_{\text{sys}}$ and non-systematic $\boldsymbol{G}_{\text{Nsys}}$ generator matrices, are

defined [HHH12]. In the systematic approach, the UW-OFDM symbols are generated by appropriately loading so-called redundant subcarriers. The energy contribution of the redundant subcarriers plays an important role on its performance. The positions of the redundant subcarriers are chosen such that the redundant energy becomes as small as possible [HHOH14]. Even with the best position of the redundant subcarrier symbols, the mean power of the redundant subcarrier symbols is still considerably higher than that of the data symbols. Therefore, in the non-systematic approach, the idea of the dedicated subcarriers is abandoned, and the redundancy is distributed over all the subcarriers. The two code generator matrices $\boldsymbol{G}_{\mathrm{Sys}}$ and $\boldsymbol{G}_{\mathrm{Nsys}}$ can be chosen as

$$\boldsymbol{G}_{\mathrm{Sys}} = \boldsymbol{P} \begin{bmatrix} \boldsymbol{I} \\ \boldsymbol{T} \end{bmatrix}; \qquad \boldsymbol{G}_{\mathrm{Nsys}} = \boldsymbol{A} \begin{bmatrix} \boldsymbol{I} \\ \boldsymbol{T} \end{bmatrix}. \qquad (2.4)$$

The matrix $\boldsymbol{P} \in \{0,1\}^{N_m \times N_m}$ is a permutation matrix [Ste13b, HHH10b] which is designed for the optimal position of the redundant subcarriers and $\boldsymbol{A} \in \mathbb{R}^{N_m \times N_m}$ is an arbitrary non-singular matrix. Note that the matrices $\boldsymbol{P}$ and $\boldsymbol{A}$ can be selected freely and thus offer the degree of freedom for optimizing $\boldsymbol{G}$ towards certain cost functions (e.g., minimizing the trace of the error covariance matrix [HHH12], maximizing the minimum Euclidean distance at the transmitter or receiver [Ste14] or minimizing the out of band (OOB) radiation [RNSK14]). Once the matrices $\boldsymbol{P}$ and $\boldsymbol{A}$ are chosen, the matrix $\boldsymbol{T}$ can be derived uniquely from the condition (2.2). In contrast to CP-OFDM, where precoding is required to achieve full diversity, it is shown in [Ste13b] that UW-OFDM offers full diversity as long as the matrices $\boldsymbol{P}$ and $\boldsymbol{A}$ have full rank.

Note that these $\boldsymbol{G}$ matrices are designed for UW-OFDM SISO systems, but the same matrices can also be utilized for MIMO systems. The choice of the $\boldsymbol{G}$ matrix plays an important role with respect to the performance of UW-OFDM, and different $\boldsymbol{G}$ matrices yield different BER-performances [HHH12]. It has also been shown in [HHH12] that the $\boldsymbol{G}$ matrices based on the non-systematic approach show a better performance over flat and frequency selective SISO channels. This is due the fact that the systematic approach suffers from the high contribution of the energy of the redundant subcarriers whereas the redundancy is distributed over all subcarriers in the non-systematic approach. Therefore, in this work, we have used $\boldsymbol{G}$ matrices based on the non-systematic approach. In the following, we briefly discuss the design of these code generator matrices that are used in this work.

The constraint in Eq. (2.2) has to be fulfilled for any code matrix to obtain a valid UW-OFDM symbol. Let $\boldsymbol{U} = \left[\boldsymbol{F}_N^{-1} \boldsymbol{B} \right]_{\mathrm{last}\ N_r\ \mathrm{rows}}$ be the $N_r \times N_m$ matrix containing the N_r last rows of $\boldsymbol{F}_N^{-1} \boldsymbol{B}$. Then the constraint in (2.2) can be reformulated as

$$\boldsymbol{U}\boldsymbol{G} = \boldsymbol{0}, \qquad (2.5)$$

which implies that the columns of $\boldsymbol{G}$ must be in the null space of the matrix $\boldsymbol{U}$. One solution can be a matrix that contains an orthonormal basis of the null space. This can be achieved by computing the singular value decomposition (SVD) of $\boldsymbol{U}$. In this work, we denote the code matrix as $\boldsymbol{G}'$ which is computed in this way.

In [HHH12], it is suggested to derive optimum code generator matrices by minimizing the trace of the error covariance matrices of the best linear unbiased estimator (BLUE) and the linear minimum mean square error (LMMSE) estimator in the AWGN channel for a fixed signal-to-noise ratio (SNR). These

(a) Transceiver architecture with joint detection

(b) Two step detection approach
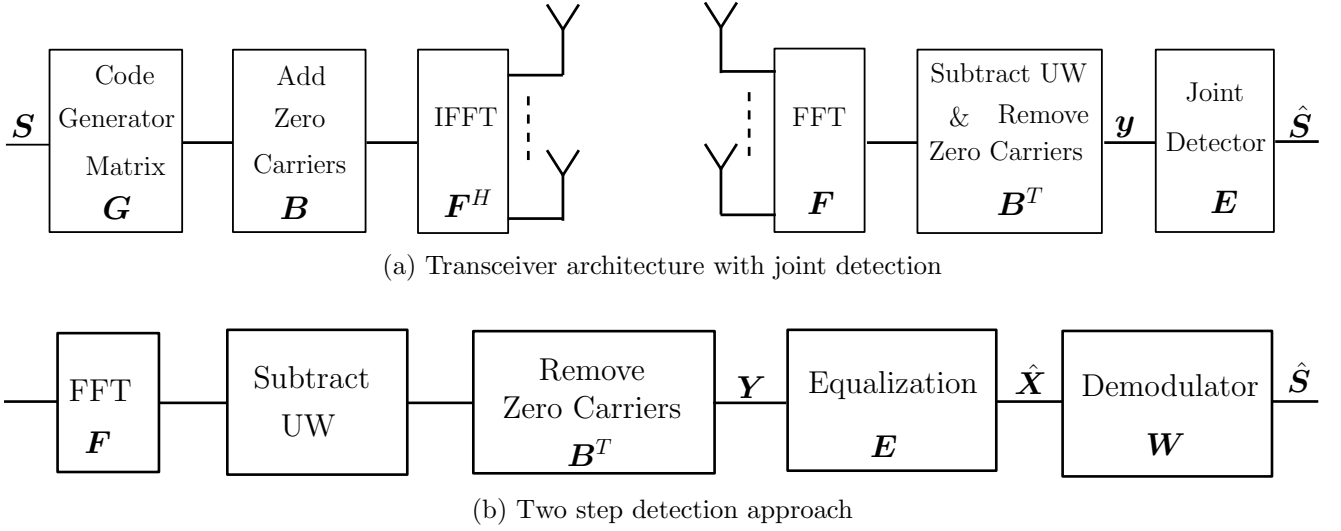
Figure 2.3.: Transceiver architecture with linear detection schemes for MIMO UW-OFDM

cost functions are given as

$$J_{\text{BLUE}} = \frac{\sigma_d^2}{cN_d}\text{tr}\left\{\breve{\boldsymbol{G}}^H\breve{\boldsymbol{G}}\right\}\text{tr}\left\{(\breve{\boldsymbol{G}}^H\breve{\boldsymbol{G}})^{-1}\right\} \tag{2.6}$$

$$J_{\text{LMMSE}} = \sigma_d^2\text{tr}\left\{\left(\frac{cN_d}{\text{tr}\left\{\breve{\boldsymbol{G}}^H\breve{\boldsymbol{G}}\right\}}\breve{\boldsymbol{G}}^H\breve{\boldsymbol{G}} + \boldsymbol{I}_{N_d}\right)^{-1}\right\}, \tag{2.7}$$

where $c = E_s/N_0$ is the SNR, E_s is the mean energy of the individual QAM data symbols, N_0 is the noise spectral density, σ_d^2 is the data variance, and $\breve{\boldsymbol{G}}$ is an arbitrary code generator. The optimization problems are

$$\breve{\boldsymbol{G}}_{\text{BLUE}} = \text{argmin}\{J_{\text{BLUE}}\} \quad \text{s.t.} \quad \boldsymbol{F}_N^{-1}\boldsymbol{B}\boldsymbol{G} = \begin{bmatrix} * \\ \boldsymbol{0} \end{bmatrix} \tag{2.8}$$

$$\breve{\boldsymbol{G}}_{\text{LMMSE}} = \text{argmin}\{J_{\text{LMMSE}}\} \quad \text{s.t.} \quad \boldsymbol{F}_N^{-1}\boldsymbol{B}\boldsymbol{G} = \begin{bmatrix} * \\ \boldsymbol{0} \end{bmatrix}. \tag{2.9}$$

It is also shown in [HHH12] that these optimization problems can be converted to unconstrained problems which can numerically be solved, e.g., by using the steepest descent method. Moreover, different initializations to solve these problems result in different code generator matrices for the same problem [HHH12]. Thus, the solution of these optimization problems are not unique, but all solutions fulfill $\boldsymbol{G}^H\boldsymbol{G} = \alpha^2\boldsymbol{I}_{N_d}$ with α denoting all the identical singular values and $\boldsymbol{I}_{N_d}$ is the identity matrix. In this work, we use a generator matrix $\boldsymbol{G}''$ which has been obtained by a random initialization and by solving the optimization problem defined in Eq. (2.9) for a fixed SNR.

2.3. Linear Detection Schemes

The introduction of redundancy during the UW-OFDM symbol generation can be exploited at the receiver to get better estimates of the data vectors. This has been well investigated for SISO systems in [Oni13], where it has been shown that more sophisticated linear estimators, which are based on joint detection, are required to exploit the benefits of this redundancy. This is in contrast to CP-OFDM where a single-tap estimator is usually employed. In the following, two approaches for MIMO UW-OFDM are developed, as shown in Fig. 2.3. In the first scheme, it is shown that the same linear estimators obtained for SISO systems can be employed for MIMO UW-OFDM by using joint detection. But they suffer from a high computation complexity. In the second scheme, it is shown that a subcarrier-wise detection is also possible where the redundancy in the frequency domain is advantageously exploited by using an LMMSE based code generator demodulator. A MIMO system with M_T transmit antennas and M_R receive antennas is considered where $\boldsymbol{S} \in \mathbb{C}^{N_d \times M_T}$ contains the $N_d \times M_T$ data symbols to be transmitted from M_T transmit antennas. The data symbols are assumed to be zero-mean i.i.d. with variance σ_s^2. The time domain signal is given by

$$\boldsymbol{X} = \boldsymbol{F}_N^H \boldsymbol{B} \boldsymbol{G} \boldsymbol{S} \in \mathbb{C}^{N \times M_T} \tag{2.10}$$

2.3.1. Approach 1 (Joint Detection)

The data received by the ith receive antenna in the frequency domain after subtracting the UW and removing the zero carriers is given by

$$\boldsymbol{y}_i = \sum_{j=1}^{M_T} \boldsymbol{B}^T \boldsymbol{F}_N \boldsymbol{H}_{i,j} \boldsymbol{F}_N^H \boldsymbol{B} \boldsymbol{G} \boldsymbol{s}_j + \boldsymbol{n}_i$$

$$= \sum_{j=1}^{M_T} \hat{\boldsymbol{H}}_{i,j} \boldsymbol{G} \boldsymbol{s}_j + \boldsymbol{n}_i \quad \forall \quad i = 1, \dots, M_R \tag{2.11}$$

where $\boldsymbol{H}_{i,j}$ is the circulant channel convolution matrix containing the channel impulse response, $\hat{\boldsymbol{H}}_{i,j} = \boldsymbol{B}^T \boldsymbol{F}_N \boldsymbol{H}_{i,j} \boldsymbol{F}_N^H \boldsymbol{B} \in \mathbb{C}^{N_m \times N_m}$ is a diagonal matrix containing the channel frequency response from the jth transmit antenna to the ith receive antenna on its main diagonal. The data received over all antennas can be written as

$$\boldsymbol{y} = \begin{bmatrix} \boldsymbol{y}_1 \\ \vdots \\ \boldsymbol{y}_{M_R} \end{bmatrix} = \begin{bmatrix} \hat{\boldsymbol{H}}_{1,1} & \cdots & \hat{\boldsymbol{H}}_{1,M_T} \\ \vdots & \ddots & \vdots \\ \hat{\boldsymbol{H}}_{M_R,1} & \cdots & \hat{\boldsymbol{H}}_{M_R,M_T} \end{bmatrix} \left(\boldsymbol{I}_{M_T} \otimes \boldsymbol{G} \right) \begin{bmatrix} \boldsymbol{s}_1 \\ \vdots \\ \boldsymbol{s}_{M_T} \end{bmatrix} + \begin{bmatrix} \boldsymbol{n}_1 \\ \vdots \\ \boldsymbol{n}_{M_R} \end{bmatrix}. \tag{2.12}$$

Note that the same model can be applied to CP-OFDM where $\boldsymbol{G}$ is an identity matrix for CP-OFDM. We can rewrite the above equation as

$$\boldsymbol{y} = \boldsymbol{H}_{\text{eff}} \boldsymbol{G}_{\text{eff}} \tilde{\boldsymbol{s}} + \boldsymbol{n} \in \mathbb{C}^{(N_m \cdot M_R) \times 1}, \tag{2.13}$$

where $\boldsymbol{H}_{\text{eff}} \in \mathbb{C}^{(N_m \cdot M_R) \times (N_m \cdot M_T)}$ contains the overall channel frequency response as shown in Eq. (2.12), $\boldsymbol{G}_{\text{eff}} = \boldsymbol{I}_{M_T} \otimes \boldsymbol{G} \in \mathbb{C}^{(N_m \cdot M_T) \times (N_d \cdot M_T)}$ is the modified code generator matrix with a block diagonal structure, and $\tilde{\boldsymbol{s}} \in \mathbb{C}^{(N_d \cdot M_T) \times 1}$ contains the transmitted data symbols and is related to $\boldsymbol{S}$ in Eq. (2.10) via $\tilde{\boldsymbol{s}} = \text{vec}(\boldsymbol{S})$. The noise is assumed to be i.i.d. zero-mean circularly symmetric complex Gaussian (ZMCSCG) distributed with variance σ_n^2. The optimum linear estimators such as BLUE or LMMSE can be used to estimate the data symbols by extending the SISO solution in [HOH11]. These equalizer weight matrices are calculated as

$$\boldsymbol{E}_{\text{BLUE}} = \left(\boldsymbol{G}_{\text{eff}}^H \boldsymbol{H}_{\text{eff}}^H \boldsymbol{H}_{\text{eff}} \boldsymbol{G}_{\text{eff}}\right)^{-1} \boldsymbol{G}_{\text{eff}}^H \boldsymbol{H}_{\text{eff}}^H,$$

$$\boldsymbol{E}_{\text{MMSE}} = \left(\boldsymbol{G}_{\text{eff}}^H \boldsymbol{H}_{\text{eff}}^H \boldsymbol{H}_{\text{eff}} \boldsymbol{G}_{\text{eff}} + \frac{\sigma_n^2}{\sigma_d^2} \boldsymbol{I}_{(N_d \cdot M_T)}\right)^{-1} \boldsymbol{G}_{\text{eff}}^H \boldsymbol{H}_{\text{eff}}^H,$$

with $\boldsymbol{E} \in \mathbb{C}^{(N_d \cdot M_T) \times (N_m \cdot M_R)}$, $\boldsymbol{I}_{(N_d \cdot M_T)}$ is the identity matrix of size $N_d \cdot M_T \times N_d \cdot M_T$, σ_n^2 is the variance of the noise samples, and σ_d^2 is the variance of the data symbols. Note that the computational complexity increases significantly with an increased number of transmit antennas since a square matrix of size $N_d \cdot M_T$ has to be inverted. The estimated data symbols are then obtained from

$$\hat{\boldsymbol{S}} = \text{unvec}(\boldsymbol{E}\boldsymbol{y}) \in \mathbb{C}^{N_d \times M_T}. \tag{2.14}$$

2.3.2. Approach 2 (Subcarrier-wise Detection)

The simplicity of CP-OFDM comes from per subcarrier operations where each data subcarrier is treated as a single narrowband carrier in the frequency domain. Since the $\boldsymbol{G}$ matrix introduces correlation between the data symbols by adding redundancy, it is difficult to relate the actual data symbols to the output of the $\boldsymbol{G}$ matrix. Therefore, a two step detection procedure for UW-OFDM is proposed where in the first step, similar to CP-OFDM, a subcarrier-wise linear estimator can be employed. In the second step, a code generator demodulator is used as shown in Fig. 2.3b.

After taking the DFT, subtracting the UW, and removing the zero carriers, the received signal on the lth subcarrier is given as

$$\boldsymbol{y}_l = \boldsymbol{H}_l \boldsymbol{S}^T [\boldsymbol{G}^T]_l + \boldsymbol{n}_l \in \mathbb{C}^{M_R \times 1}, \qquad l = 1, ..., N_m \tag{2.15}$$

where $\boldsymbol{H}_l \in \mathbb{C}^{M_R \times M_T}$ is the channel matrix of the lth subcarrier in the frequency domain and $[\boldsymbol{G}^T]_l$ is the lth column of the matrix $\boldsymbol{G}^T$. Moreover, the noise is assumed to be i.i.d. ZMCSCG distributed with variance σ_n^2. Let $\boldsymbol{c}_l = \boldsymbol{S}^T [\boldsymbol{G}^T]_l \in \mathbb{C}^{M_T \times 1}$ represent the transmit signal on lth subcarrier, then

$$\boldsymbol{y}_l = \boldsymbol{H}_l \boldsymbol{c}_l + \boldsymbol{n}_l \in \mathbb{C}^{M_R \times 1}. \tag{2.16}$$

2.3.2.1. Linear Detectors

We first equalize the channel on the lth subcarrier by performing,

$$\hat{\boldsymbol{c}}_l = \boldsymbol{E}_l \boldsymbol{y}_l \in \mathbb{C}^{M_T \times 1}, \tag{2.17}$$

where $\boldsymbol{E}_l \in \mathbb{C}^{M_T \times M_R}$ contains the equalizer filter weights and can be calculated using the zero forcing (ZF) or the LMMSE criterion.

2.3.2.1.1. ZF Detector   The goal is to find $\hat{\boldsymbol{c}}_l$ such that the reconstruction error is minimized,

$$\text{minimize} \quad \parallel \boldsymbol{y}_l - \boldsymbol{H}_l \hat{\boldsymbol{c}}_l \parallel^2, \tag{2.18}$$

We get the same solution as in CP-OFDM which is given by

$$\boldsymbol{E}_{l,\text{ZF}} = (\boldsymbol{H}_l^H \boldsymbol{H}_l)^{-1} \boldsymbol{H}_l^H. \tag{2.19}$$

2.3.2.1.2. LMMSE Detector   Since ZF receivers are known for their noise amplification at low SNRs, a linear MMSE estimator can be employed which avoids this problem. The filter weights using the MMSE criterion are calculated for the following unconstrained problem

$$\text{minimize} \quad \mathbb{E} \left\{ \parallel \boldsymbol{E}_l \boldsymbol{y}_l - \boldsymbol{c}_l \parallel^2 \right\}, \tag{2.20}$$

where $\mathbb{E}$ is the expectation operator. This leads to the solution

$$\boldsymbol{E}_{l,\text{MMSE}} = \boldsymbol{R}_{c_l c_l} \boldsymbol{H}_l^H (\boldsymbol{H}_l \boldsymbol{R}_{c_l c_l} \boldsymbol{H}_l^H + \boldsymbol{R}_{n_l n_l})^{-1}, \tag{2.21}$$

where $\boldsymbol{R}_{n_l n_l}$ is the noise covariance matrix and $\boldsymbol{R}_{c_l c_l}$ is given as

$$
\begin{aligned}
\boldsymbol{R}_{c_l c_l} &= \mathbb{E} \left\{ \boldsymbol{c}_l \boldsymbol{c}_l^H \right\} \\
&= \mathbb{E} \left\{ (\boldsymbol{S}^T [\boldsymbol{G}^T]_l)(\boldsymbol{S}^T [\boldsymbol{G}^T]_l)^H \right\} \\
&= \mathbb{E}\{ (([\boldsymbol{G}^T]_l^T \otimes \boldsymbol{I}_{M_T}) \text{vec}(\boldsymbol{S}^T))(([\boldsymbol{G}^T]_l^T \otimes \boldsymbol{I}_{M_T}) \text{vec}(\boldsymbol{S}^T))^H \} \\
&= ([\boldsymbol{G}^T]_l^T \otimes \boldsymbol{I}_{M_T}) \mathbb{E} \left\{ \text{vec}(\boldsymbol{S}^T) \text{vec}(\boldsymbol{S}^T)^H \right\} ([\boldsymbol{G}^T]_l^T \otimes \boldsymbol{I}_{M_T})^H \\
&= \sigma_d^2 ([\boldsymbol{G}^T]_l^T \otimes \boldsymbol{I}_{M_T}) \boldsymbol{I}_{M_T N_d} ([\boldsymbol{G}^T]_l^T \otimes \boldsymbol{I}_{M_T})^H \\
&= \sigma_d^2 ([\boldsymbol{G}^T]_l^T [\boldsymbol{G}^T]_l^*) \otimes \boldsymbol{I}_{M_T} \\
&= \sigma_d^2 \parallel [\boldsymbol{G}^T]_l \parallel_2^2 \boldsymbol{I}_{M_T} \\
&= \sigma_d^2 \beta_l \boldsymbol{I}_{M_T},
\end{aligned}
$$

where β_l is the norm of the lth row of the $\boldsymbol{G}$ matrix and can be precalculated. By inserting these values and by applying the matrix inversion lemma [Kay93], it can be easily shown that

$$\boldsymbol{E}_{l,\text{MMSE}} = (\boldsymbol{H}_l^H \boldsymbol{H}_l + \sigma_n^2 / (\sigma_d^2 \beta_l) \boldsymbol{I}_{M_T})^{-1} \boldsymbol{H}_l^H. \tag{2.22}$$

2.3.2.2. Code Generator Demodulator Matrix

In the second step, all equalized symbols are jointly multiplied by a code generator demodulator matrix to get the estimated data symbols

$$\hat{\boldsymbol{S}} = \boldsymbol{W} \hat{\boldsymbol{C}} \in \mathbb{C}^{N_d \times M_T}, \tag{2.23}$$

where $\hat{\boldsymbol{C}} = [\hat{\boldsymbol{c}}_1, ..., \hat{\boldsymbol{c}}_{N_m}]^T \in \mathbb{C}^{N_m \times M_T}$ i.e., rows of $\hat{\boldsymbol{C}}$ are the estimates obtained from Eq. (2.17), and $\boldsymbol{W}$ is the code generator demodulator matrix. Various type of demodulator matrices are defined below.

2.3.2.2.1. Matched Filter based Demodulator A matched filter based demodulator offers the simplest solution since the used code generator matrices fulfill the property $\boldsymbol{G}^H \boldsymbol{G} = \boldsymbol{I}_{N_d}$. Therefore, a matched filter based demodulator is given by

$$\boldsymbol{W}_{\mathrm{MF}} = \boldsymbol{G}^H. \tag{2.24}$$

2.3.2.2.2. LMMSE based Demodulator A subcarrier-wise estimation does not take full advantage of the correlation introduced by the $\boldsymbol{G}$ matrix if detection is used in conjunction with a matched filter based demodulator. Assuming that the propagation channel is perfectly equalized ($\boldsymbol{E}_l \boldsymbol{H}_l = \boldsymbol{I}_{M_T}$), which is exactly true if Eq. (2.19) is used and approximately true if Eq. (2.22) is used, $\hat{\boldsymbol{C}}$ in Eq. (2.23) can be written as

$$\hat{\boldsymbol{C}} = \boldsymbol{G}\boldsymbol{S} + \hat{\boldsymbol{N}}, \tag{2.25}$$

where

$$\hat{\boldsymbol{N}} = \begin{bmatrix} \boldsymbol{n}_1^T \boldsymbol{E}_1^T \\ \vdots \\ \boldsymbol{n}_{N_m}^T \boldsymbol{E}_{N_m}^T \end{bmatrix} \tag{2.26}$$

Note that the noise at the output of the equalizer is not white anymore. It depends upon the equalizer weights and differs for all transmit layers. Ideally, a demodulator matrix for each of the transmit layer is required for optimal demodulation but it also increases the overall complexity of the system because an inverse of a large matrix has to be calculated for each transmit layer. Therefore, in the following we present two solutions for the LMMSE based demodulator. In the first solution, we calculate the demodulation matrix for each transmit layer while in the second solution, we present a combined demodulation matrix for all of the layers.

Solution 1 - Per Transmit Antenna Demodulation: We can rewrite Eq. (2.25) for the received coded symbols $\hat{\boldsymbol{c}}_j \in \mathbb{C}^{N_m \times 1}$ for each jth transmit layer as

$$[\hat{\boldsymbol{c}}_1 \cdots \hat{\boldsymbol{c}}_{M_T}] = \boldsymbol{G} \cdot [\boldsymbol{s}_1 \cdots \boldsymbol{s}_{M_T}] + [\hat{\boldsymbol{n}}_1 \cdots \hat{\boldsymbol{n}}_{M_T}]. \tag{2.27}$$

Let $\boldsymbol{e}_{l,j}^T = \boldsymbol{E}_l(j,:) \in \mathbb{C}^{1 \times M_R}$ be the equalizer weights for the jth transmit layer. Then the noise is

$$\hat{\boldsymbol{n}}_j = \begin{bmatrix} \boldsymbol{n}_1^T \boldsymbol{e}_{1,j} \\ \vdots \\ \boldsymbol{n}_{N_m}^T \boldsymbol{e}_{N_m,j} \end{bmatrix}. \tag{2.28}$$

Now we stack the matrices again to vectors such that

$$\mathrm{vec}(\hat{\boldsymbol{C}}) = \begin{bmatrix} \hat{\boldsymbol{c}}_1 \\ \vdots \\ \hat{\boldsymbol{c}}_{M_T} \end{bmatrix} = (\boldsymbol{I}_{M_T} \otimes \boldsymbol{G}) \cdot \begin{bmatrix} \boldsymbol{s}_1 \\ \vdots \\ \boldsymbol{s}_{M_T} \end{bmatrix} + \begin{bmatrix} \hat{\boldsymbol{n}}_1 \\ \vdots \\ \hat{\boldsymbol{n}}_{M_T} \end{bmatrix}. \tag{2.29}$$

The covariance matrix of this long noise vector has the form

$$\boldsymbol{R}_{\hat{n}\hat{n}} = \begin{bmatrix} \boldsymbol{R}_{11} & \cdots & \boldsymbol{R}_{1M_T} \\ \vdots & \ddots & \vdots \\ \boldsymbol{R}_{M_T 1} & \cdots & \boldsymbol{R}_{M_T M_T} \end{bmatrix}, \tag{2.30}$$

where all individual sub-matrices are diagonal. The autocovariance matrices on the diagonal of $\boldsymbol{R}_{\hat{n}\hat{n}}$ are given as

$$\begin{aligned} [\boldsymbol{R}_{j,j}]_{l,l} &= \mathbb{E}\left[(\boldsymbol{n}_l^T \boldsymbol{e}_{l,j})(\boldsymbol{n}_l^T \boldsymbol{e}_{l,j})^H\right] \\ &= \mathbb{E}\left[(\boldsymbol{n}_l^T \boldsymbol{e}_{l,j})(\boldsymbol{e}_{l,j}^H \boldsymbol{n}_l^*)\right] \\ &= \mathbb{E}\left[(\boldsymbol{e}_{l,j}^H \boldsymbol{n}_l^*)(\boldsymbol{n}_l^T \boldsymbol{e}_{l,j})\right] \\ &= \sigma_n^2 \boldsymbol{e}_{l,j}^H \boldsymbol{e}_{l,j}. \end{aligned}$$

The non-diagonal covariance matrices are given as $[\boldsymbol{R}_{1,j}]_{l,l} = \boldsymbol{0}$, since noise is assumed to be uncorrelated, therefore, $\mathbb{E}\left[\boldsymbol{n}_{l,1}^T \boldsymbol{n}_{l,j}^*\right] = 0$. The LMMSE estimator follows to

$$\begin{bmatrix} \hat{\boldsymbol{s}}_1 \\ \vdots \\ \hat{\boldsymbol{s}}_{M_T} \end{bmatrix} = \sigma_d^2 \left(\boldsymbol{I}_{M_T} \otimes \boldsymbol{G}^H\right) \cdot \left(\sigma_d^2 \left(\boldsymbol{I}_{M_T} \otimes \boldsymbol{G}\right) \cdot \left(\boldsymbol{I}_{M_T} \otimes \boldsymbol{G}^H\right) + \boldsymbol{R}_{\hat{n}\hat{n}}\right)^{-1} \begin{bmatrix} \hat{\boldsymbol{c}}_1 \\ \vdots \\ \hat{\boldsymbol{c}}_{M_T} \end{bmatrix}$$

$$= \sigma_d^2 \left(\boldsymbol{I}_{M_T} \otimes \boldsymbol{G}^H\right) \cdot \left(\sigma_d^2 \left(\boldsymbol{I}_{M_T} \otimes \boldsymbol{G}\boldsymbol{G}^H\right) + \boldsymbol{R}_{\hat{n}\hat{n}}\right)^{-1} \begin{bmatrix} \hat{\boldsymbol{c}}_1 \\ \vdots \\ \hat{\boldsymbol{c}}_{M_T} \end{bmatrix}$$

$$= \sigma_d^2 \begin{bmatrix} \boldsymbol{G}^H & \cdots & \boldsymbol{0} \\ \vdots & \ddots & \vdots \\ \boldsymbol{0} & \cdots & \boldsymbol{G}^H \end{bmatrix} \cdot \begin{bmatrix} (\sigma_d^2 \boldsymbol{G}\boldsymbol{G}^H + \boldsymbol{R}_{11})^{-1} & \cdots & \boldsymbol{0} \\ \vdots & \ddots & \vdots \\ \boldsymbol{0} & \cdots & (\sigma_d^2 \boldsymbol{G}\boldsymbol{G}^H + \boldsymbol{R}_{M_T M_T})^{-1} \end{bmatrix} \begin{bmatrix} \hat{\boldsymbol{c}}_1 \\ \vdots \\ \hat{\boldsymbol{c}}_{M_T} \end{bmatrix}.$$

We can now separate the solutions for the jth transmit layer

$$\hat{\boldsymbol{s}}_j = \sigma_d^2 \boldsymbol{G}^H (\sigma_d^2 \boldsymbol{G}\boldsymbol{G}^H + \boldsymbol{R}_{jj})^{-1} \hat{\boldsymbol{c}}_j = \boldsymbol{W}_j \hat{\boldsymbol{c}}_j, \tag{2.31}$$

where $\boldsymbol{R}_{jj} \in \mathbb{R}^{N_m \times N_m}$ is a diagonal matrix and contains $\sigma_n^2 \boldsymbol{e}_{l,j}^H \boldsymbol{e}_{l,j} \quad \forall \quad l = 1, \ldots, N_m$ for the jth transmit antenna on its diagonal.

Solution 2 - Combined Demodulation: In this section, we present an alternative approach to derive a combined LMMSE demodulation matrix for all transmit layers. The LMMSE based optimization problem to calculate the demodulator filter weights for the equalized data symbols (as defined by Eq. (2.25)) can be written as

$$\text{minimize} \quad \mathbb{E}\left\{\parallel \boldsymbol{W}\hat{\boldsymbol{C}} - \boldsymbol{S} \parallel_{\text{F}}^2\right\}. \tag{2.32}$$

Using the orthogonality principle [Say03]

$$\mathbb{E}\left\{(\boldsymbol{W}\hat{\boldsymbol{C}} - \boldsymbol{S})\hat{\boldsymbol{C}}^H\right\} = \boldsymbol{0}$$

$$\mathbb{E}\left\{\boldsymbol{W}\hat{\boldsymbol{C}}\hat{\boldsymbol{C}}^H - \boldsymbol{S}\hat{\boldsymbol{C}}^H\right\} = \boldsymbol{0}$$

$$\mathbb{E}\left\{\boldsymbol{W}\hat{\boldsymbol{C}}\hat{\boldsymbol{C}}^H\right\} - \mathbb{E}\left\{\boldsymbol{S}\hat{\boldsymbol{C}}^H\right\} = \boldsymbol{0}$$

$$\mathbb{E}\left\{\boldsymbol{W}(\boldsymbol{GS} + \hat{\boldsymbol{N}})(\boldsymbol{GS} + \hat{\boldsymbol{N}})^H\right\} - \mathbb{E}\left\{\boldsymbol{S}(\boldsymbol{GS} + \hat{\boldsymbol{N}})^H\right\} = \boldsymbol{0}$$

Assuming that the signal and the noise are uncorrelated

$$\boldsymbol{W}(\boldsymbol{GG}^H\sigma_d^2 + \mathbb{E}\left\{\hat{\boldsymbol{N}}\hat{\boldsymbol{N}}^H\right\}) - \sigma_d^2\boldsymbol{G}^H = \boldsymbol{0}$$

$$\boldsymbol{W}(\boldsymbol{GG}^H\sigma_d^2 + \mathbb{E}\left\{\hat{\boldsymbol{N}}\hat{\boldsymbol{N}}^H\right\}) = \sigma_d^2\boldsymbol{G}^H \tag{2.33}$$

Using the noise definition in Eq. (2.26), we write

$$\hat{\boldsymbol{N}}\hat{\boldsymbol{N}}^H = \begin{bmatrix} \boldsymbol{n}_1^T\boldsymbol{E}_1^T\boldsymbol{E}_1^*\boldsymbol{n}_1^* & \cdots & \boldsymbol{n}_1^T\boldsymbol{E}_1^T\boldsymbol{E}_{N_m}^*\boldsymbol{n}_{N_m}^* \\ \vdots & \ddots & \vdots \\ \boldsymbol{n}_{N_m}^T\boldsymbol{E}_{N_m}^T\boldsymbol{E}_1^*\boldsymbol{n}_1^* & \cdots & \boldsymbol{n}_{N_m}^T\boldsymbol{E}_{N_m}^T\boldsymbol{E}_{N_m}^*\boldsymbol{n}_{N_m}^* \end{bmatrix} \tag{2.34}$$

Since the noise is uncorrelated, therefore, $\mathbb{E}\left[\boldsymbol{n}_m^T\boldsymbol{n}_l^*\right] = 0$ for $m \neq l$ and $m, l = 1, \cdots, N_m$. The expected value of the diagonal elements is

$$\begin{aligned} \mathbb{E}\left\{\boldsymbol{n}_l^T\boldsymbol{E}_l^T\boldsymbol{E}_l^*\boldsymbol{n}_l^*\right\} &= \mathbb{E}\left\{\mathrm{tr}(\boldsymbol{n}_l^T\boldsymbol{E}_l^T\boldsymbol{E}_l^*\boldsymbol{n}_l^*)\right\} \\ &= \mathbb{E}\left\{\mathrm{tr}(\boldsymbol{E}_l^T\boldsymbol{E}_l^*\boldsymbol{n}_l^*\boldsymbol{n}_l^T)\right\} \\ &= \mathrm{tr}(\boldsymbol{E}_l^T\boldsymbol{E}_l^*\mathbb{E}\left\{\boldsymbol{n}_l^*\boldsymbol{n}_l^T\right\}) \\ &= \mathrm{tr}(\boldsymbol{E}_l^T\boldsymbol{E}_l^*\sigma_n^2\boldsymbol{I}_{M_R}) \\ &= \sigma_n^2\mathrm{tr}(\boldsymbol{E}_l^T\boldsymbol{E}_l^*) \end{aligned}$$

Therefore, $\mathbb{E}\left\{\hat{\boldsymbol{N}}\hat{\boldsymbol{N}}^H\right\} = \sigma_n^2\boldsymbol{Z}$ where $\boldsymbol{Z} \in \mathbb{R}^{N_m \times N_m}$ is a diagonal matrix and contains $[\boldsymbol{Z}]_{l,l} = \mathrm{tr}(\boldsymbol{E}_l^T\boldsymbol{E}_l^*)$ $\forall \quad l = 1, \ldots, N_m$ on its diagonal. Note that the equalizer weights $\boldsymbol{E}_l$ are already calculated in the first step. We can now further simplify Eq. (2.33) as

$$\boldsymbol{W}(\boldsymbol{GG}^H\sigma_d^2 + \sigma_n^2\boldsymbol{Z}) = \sigma_d^2\boldsymbol{G}^H$$

$$\boldsymbol{W}(\boldsymbol{GG}^H + \frac{\sigma_n^2}{\sigma_d^2}\boldsymbol{Z}) = \boldsymbol{G}^H$$

$$\boldsymbol{W} = \boldsymbol{G}^H(\boldsymbol{GG}^H + \frac{\sigma_n^2}{\sigma_d^2}\boldsymbol{Z})^{-1}$$

Finally, the data symbols at the kth subcarrier can also be represented as

$$\hat{\boldsymbol{S}}(k,:) = \boldsymbol{W}(k,:)\hat{\boldsymbol{C}} \qquad k = 1,...,N_d, \tag{2.35}$$

where $\hat{\boldsymbol{S}}(k,:)$ and $\boldsymbol{W}(k,:)$ denotes the k-th row of $\hat{\boldsymbol{S}}$ and $\boldsymbol{W}$, respectively.

2.3.3. Performance Evaluation
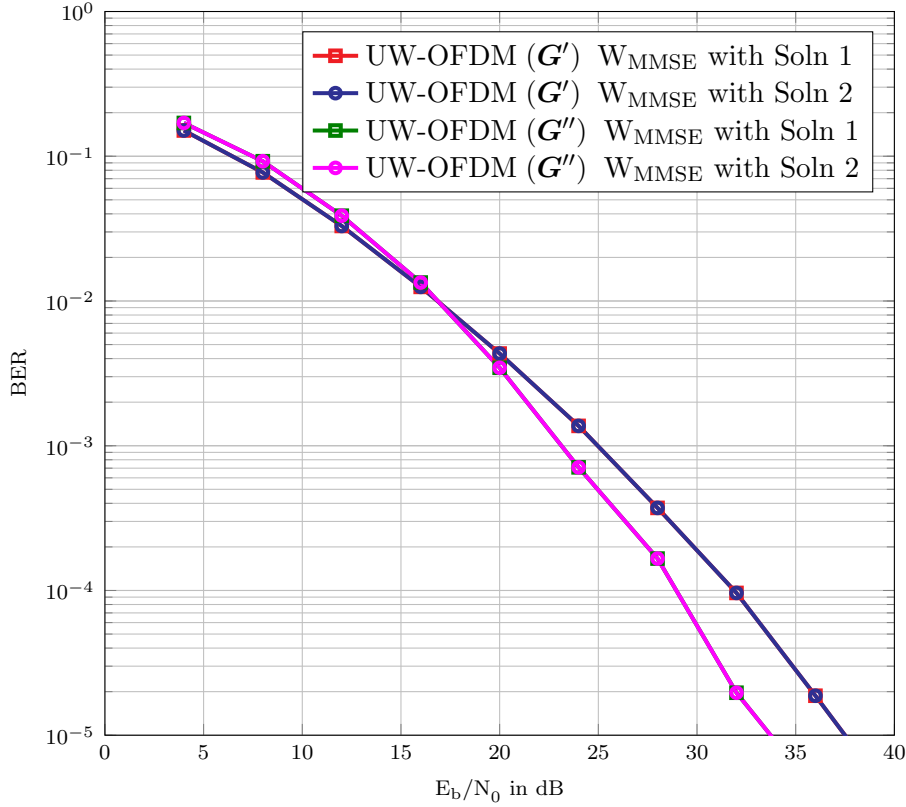
Figure 2.4.: UW-OFDM with two step detection procedure and employing LMMSE demodulation

In this section, the performance of both linear detection approaches is evaluated for UW-OFDM. Moreover, the performance of UW-OFDM with CP-OFDM is also compared. To this end, the IEEE 802.11n parameters for a 40 MHz bandwidth are used, as shown in Table 2.1. The symbol duration of UW-OFDM is 3.2 μs while CP-OFDM has a duration of 4 μs. This is due to the fact that the guard interval in UW-OFDM is a part of the FFT interval. Moreover, the IEEE 802.11n channel model B is used for the simulations. A perfect synchronization and channel state information at the receiver is assumed in this work.

First, we compare the performance of UW-OFDM with the two step approach using both solutions for the LMMSE demodulator, as shown in Fig. 2.4. The results show that the suboptimal LMMSE combined demodulation approach has a similar performance as the per transmit antenna demodulation approach for both generator matrices. Note that the combined demodulator has much less complexity as an inverse of a matrix of size $N_m \times N_m$ has to be calculated only one time. This is really important for

	CP-OFDM	UW-OFDM
Modulation Scheme	QPSK	
Bandwidth	40 MHz	
M_T	2	
M_R	2	
Data Carriers (N_d)	108	82
FFT length (N)	128	
CP/UW duration	800 ns	
DFT Period	3.2 μs	
Total Symbol Period	4 μs	3.2 μs
Channel	IEEE 802.11n Channel B	

Table 2.1.: Simulation parameters

higher order MIMO systems when the number of spatial streams is high. In this case, the demodulation matrix is calculated only once which reduces the overall complexity of the system significantly. In the following, we show results for UW-OFDM with an LMMSE code generator demodulator using the combined demodulation approach solution 2.

The performance of both linear detection approaches for two code generator matrices ($\boldsymbol{G}', \boldsymbol{G}''$) is compared as shown in Fig. 2.5a. The results are shown with LMMSE equalization. Moreover, this LMMSE equalization is combined with a matched filter or an LMMSE based combined code generator demodulator for approach 2. Since the correlation is efficiently exploited in joint detection, it provides the best performance at the cost of a higher computational complexity. A subcarrier-wise detection does not match the performance of joint detection, if the equalization is performed in conjunction with a matched filter based demodulator. But when it is combined with an LMMSE based code generator demodulator, it practically matches the performance of joint detection. This is due to the fact that a matched filter based demodulator does not exploit the statistics of the noise at the output of the equalizer which is not white any more. Clearly a subcarrier-wise detection using an LMMSE based demodulator is a better option than the joint detection because of its lower complexity. However, it has a higher complexity compared to CP-OFDM because we have to calculate an $N_m \times N_m$ code generator demodulator matrix inverse (e.g., once per burst in WLAN systems) and have to apply $\boldsymbol{W}$ for every UW-OFDM symbol. Furthermore, we also observe that the two $\boldsymbol{G}$ matrices yield different results where UW-OFDM with $\boldsymbol{G}''$ outperforms the $\boldsymbol{G}'$ matrix. Note that $\boldsymbol{G}''$ has been optimized for the LMMSE cost function assuming an AWGN channel while $\boldsymbol{G}'$ has been calculated by computing the SVD of $\boldsymbol{U}$. Although both generator matrices form an orthonormal basis of the null space of $\boldsymbol{U}$, this does not necessarily mean that they perform equally well in frequency selective environments. However, they should perform equally well in AWGN environments. In Fig. 2.5b, we show the results for different combinations of equalization and code generator demodulation techniques for the $\boldsymbol{G}''$ matrix using approach 2. The results show that when a ZF estimator is employed in conjunction with a matched filter, it has the worst performance but it still matches the performance of CP-OFDM. We get a performance enhancement if we use an LMMSE estimator even with a matched filter based demodulator. The best performance is achieved when an LMMSE based demodulator is used. Clearly, UW-OFDM with the $\boldsymbol{G}''$ matrix and an LMMSE based demodulator outperforms CP-OFDM significantly. This is also in line with [Ste13a] where it has
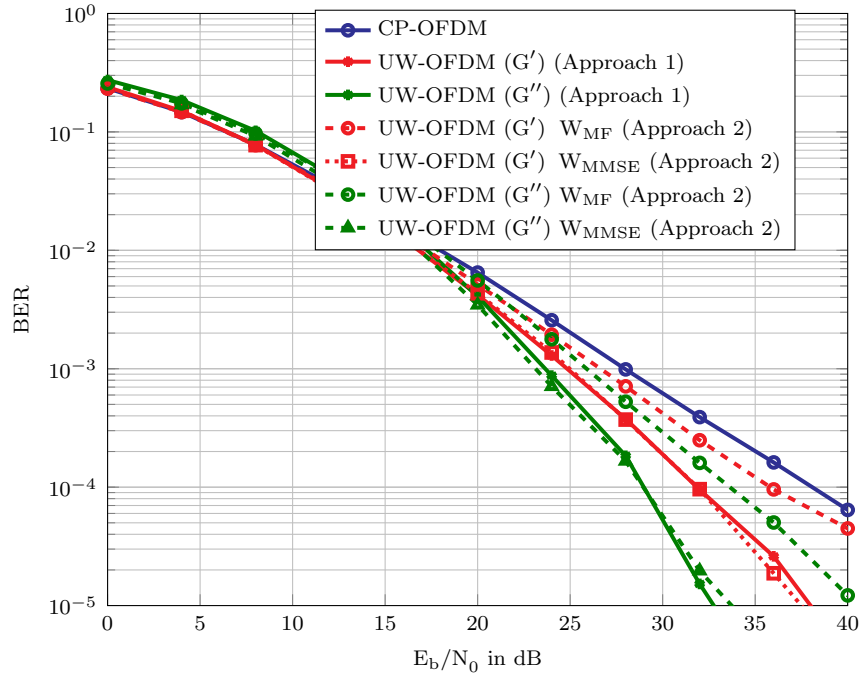
(a) Comparison of both approaches using MMSE equalization
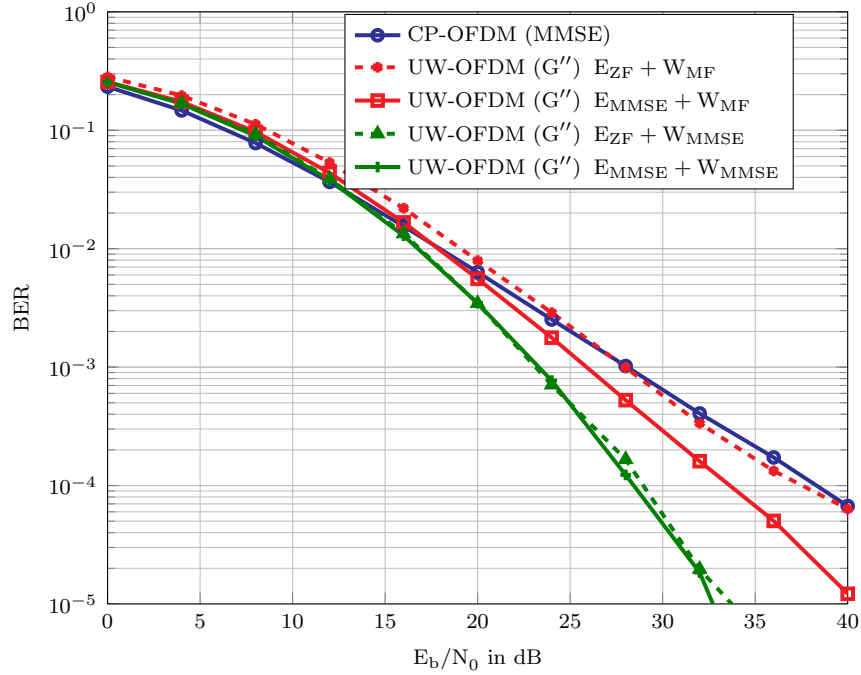
(b) Different combinations of equalizer and demodulator for subcarrier wise detection

Figure 2.5.: Performance comparison of MIMO UW-OFDM with linear detection schemes. The combination of a subcarrier-wise detection and an MMSE based code generator demodulation achieves a similar performance of joint detection but with reduce complexity.

been shown analytically for a SISO system that UW-OFDM achieves the maximum diversity order if $\mathrm{rank}(\boldsymbol{BG}) = N_d$ while CP-OFDM requires precoding to achieve the maximum diversity. Note that there is no performance difference between ZF or LMMSE estimators if they are used in conjunction with an

LMMSE based demodulator.

2.4. Successive Interference Cancellation Schemes

In the last section, we have focused only on linear detection schemes for MIMO UW-OFDM. It is well known in the literature that linear estimators do not fully eliminate the interference which is caused by the multiple-antenna systems or by the multiple-users. Therefore, interference cancellation schemes are recommended to be used in rich scattering environments to exploit the capacity advantage of multiple antenna systems but at the cost of higher complexity [MV13]. The successive interference cancellation (SIC) method represents the most effective interference cancellation based reception technique in terms of BER performance and provides some system robustness. SIC detection schemes based on the ZF or the MMSE criteria are widely discussed schemes [MV13]. These detection schemes require multiple calculations of pseudo-inverses which is a computationally expensive task. This complexity is reduced by using the QR decomposition of the channel and successive decoding of the symbols [HT10]. These SIC detection schemes have been well investigated for CP-OFDM [MV13]. The goal of this section is to expand our investigations to SIC detection schemes for MIMO UW-OFDM systems. Specifically, we propose a hybrid detection scheme with a low complexity where a combination of linear detection and non-linear demodulation is applied.

2.4.1. ZF based successive interference cancellation (ZF-SIC) Detection

In [Oni13], a ZF-SIC was presented for SISO UW-OFDM systems. We employ the same procedure for MIMO where we use the linear model in Eq. (2.13). According to this model,

$$\boldsymbol{y} = \underbrace{\boldsymbol{H}_{\text{eff}}\boldsymbol{G}_{\text{eff}}}_{\boldsymbol{M}} \tilde{\boldsymbol{s}} + \boldsymbol{n} \in \mathbb{C}^{(N_m . M_R) \times 1}$$

$$= \boldsymbol{m}_0 s_0 + \boldsymbol{m}_1 s_1 + \cdots + \boldsymbol{m}_{(N_d \cdot M_t)-1} s_{(N_d \cdot M_t)-1} + \boldsymbol{n},$$

where $\boldsymbol{M} = \boldsymbol{H}_{\text{eff}}\boldsymbol{G}_{\text{eff}} \in \mathbb{C}^{(N_m \cdot M_R) \times (N_d \cdot M_T)}$ and $\boldsymbol{m}_k$ is the kth column of $\boldsymbol{M}$. The impact of the symbol decision is subtracted from the received signal iteratively. Such an iterative equalizer outperforms the linear equalization schemes but it has a very high computational complexity. Specifically for UW-OFDM, this complexity is much higher than for CP-OFDM since we have to consider the $\boldsymbol{M}$ matrix which has large dimensions, whereas in CP-OFDM the matrix dimensions are significantly smaller since a subcarrier wise detection is carried out.

2.4.2. QR decomposition based successive interference cancellation (QR-SIC) Detection

It has been shown in the literature [Kim14, WBKK03] that the ZF-SIC can be restated with the help of a QR decomposition of the effective channel matrix $\boldsymbol{M}$, given as

$$\boldsymbol{M} = \boldsymbol{Q}\bar{\boldsymbol{R}} = \boldsymbol{Q} \begin{bmatrix} \boldsymbol{R} \\ \boldsymbol{0} \end{bmatrix}, \tag{2.36}$$

where $\boldsymbol{Q} \in \mathbb{C}^{(N_m \cdot M_R) \times (N_m \cdot M_R)}$ is a unitary matrix and $\bar{\boldsymbol{R}}$ contains an upper triangular matrix $\boldsymbol{R} \in \mathbb{C}^{(N_d \cdot M_T) \times (N_d \cdot M_T)}$ and a zero matrix $\boldsymbol{0} \in \mathbb{R}^{(N_r \cdot M_T) \times (N_d \cdot M_T)}$. Multiplying the received signal $\boldsymbol{y}$ with $\boldsymbol{Q}^H$, the resulting signal is

$$\bar{\boldsymbol{s}} = \boldsymbol{Q}^H \boldsymbol{y} = \bar{\boldsymbol{R}} \tilde{\boldsymbol{s}} + \bar{\boldsymbol{n}}, \tag{2.37}$$

where $\bar{\boldsymbol{n}} = \boldsymbol{Q}^H \boldsymbol{n}$. As $\boldsymbol{Q}$ is a unitary matrix, the statistical properties of $\boldsymbol{n}$ and $\bar{\boldsymbol{n}}$ are the same. In the next step, a symbol wise detection is carried out. Since $\boldsymbol{R}$ has an upper triangular structure, the interference from other transmit layers and also from data symbols can be removed in a sequential manner. Various methods for the QR decomposition have been proposed in the literature. In this work, we employ a Gram-Schmidt based QR decomposition [Gan80].
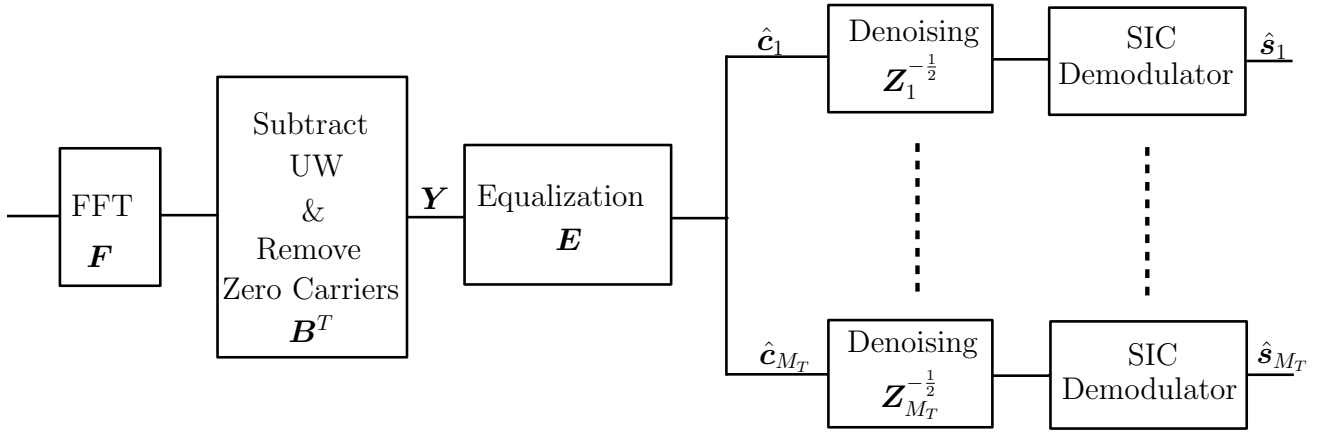
Figure 2.6.: Receiver architecture using hybrid detection

2.4.3. Hybrid Detection

In Section 2.3.2, it is shown that a two step linear detection procedure has a significantly less computational complexity than joint detection. In this procedure, a subcarrier-wise detection is performed in the first step while in the second step an LMMSE based code generator demodulator is used to achieve a similar performance as achieved by joint detection. In this section, we propose a new strategy where a QR decomposition based code generator demodulation is employed, as shown in Fig. 2.6.

After taking the DFT, subtracting the UW, and removing the zero carriers, the received signal on the lth subcarrier is given as

$$\boldsymbol{y}_l = \boldsymbol{H}_l \boldsymbol{c}_l + \boldsymbol{n}_l \in \mathbb{C}^{M_R \times 1}, \qquad l = 1, ..., N_m \tag{2.38}$$

where $\boldsymbol{H}_l \in \mathbb{C}^{M_R \times M_T}$ is the channel matrix of the lth subcarrier in the frequency domain and $\boldsymbol{c}_l = \boldsymbol{S}^T [\boldsymbol{G}^T]_l \in \mathbb{C}^{M_T \times 1}$ represents the transmit signal on the lth subcarrier. Here $[\boldsymbol{G}^T]_l$ is the lth column of the matrix $\boldsymbol{G}^T$.

In the first step, we apply linear equalization on each subcarrier. The output of the equalizer is given by

$$\hat{\boldsymbol{c}}_l = \boldsymbol{E}_l \boldsymbol{y}_l \in \mathbb{C}^{M_T \times 1}, \tag{2.39}$$

where $\boldsymbol{E}_l \in \mathbb{C}^{M_T \times M_R}$ contains the equalizer filter weights and can be calculated using the zero forc-

ing (ZF) or the MMSE criterion. These equalizer weights are calculated according to Eq. (2.19) and Eq. (2.22).

In Section 2.3, it is also shown that when a linear code generator demodulation matrix based on the LMMSE criterion is applied in the second step, this provides a similar performance as joint detection. Here, a QR-SIC based code generator demodulation is applied in the second step on the equalized symbols for each transmit antenna layer. Assuming that the propagation channel is perfectly equalized ($\boldsymbol{E}_l \boldsymbol{H}_l = \boldsymbol{I}_{M_T}$), which is exactly true if Eq. (2.19) is used and approximately true if Eq. (2.22) is used, the equalized symbols for the jth transmit antenna layer are given as

$$\hat{\boldsymbol{c}}_j = \boldsymbol{G}\boldsymbol{s}_j + \hat{\boldsymbol{n}}_j, \tag{2.40}$$

where $\hat{\boldsymbol{C}} = [\hat{\boldsymbol{c}}_1, ..., \hat{\boldsymbol{c}}_{N_m}]^T \in \mathbb{C}^{N_m \times M_T}$, $\hat{\boldsymbol{c}}_j$ is the jth column of $\hat{\boldsymbol{C}}$, and

$$\hat{\boldsymbol{n}}_j = [\boldsymbol{E}_1(j,:)\boldsymbol{n}_1, ..., \boldsymbol{E}_{N_m}(j,:)\boldsymbol{n}_{N_m}]^T \in \mathbb{C}^{N_m \times 1}$$

is the noise at the output of the detector. Here $\boldsymbol{E}_l(j,:)$ denotes the jth row of the matrix $\boldsymbol{E}_l$. Since the output noise is not white, we need to carry out a denoising step. To this end, the noise covariance matrix for each transmit layer is

$$\mathbb{E}\left\{\hat{\boldsymbol{n}}_j \hat{\boldsymbol{n}}_j^H\right\} = \sigma_n^2 \boldsymbol{Z}_j,$$

where $\boldsymbol{Z}_j \in \mathbb{R}^{N_m \times N_m}$ is a diagonal matrix and contains $\boldsymbol{E}_l(j,:)[\boldsymbol{E}_l(j,:)]^H \quad \forall \quad l = 1, \ldots, N_m$ on its diagonal. The equalized symbols $\hat{\boldsymbol{c}}_j$ are first pre-multiplied by $\boldsymbol{Z}_j^{-\frac{1}{2}}$ which results in

$$\bar{\boldsymbol{c}} = \boldsymbol{Z}_j^{-\frac{1}{2}}\hat{\boldsymbol{c}}_j = \boldsymbol{Z}_j^{-\frac{1}{2}}\boldsymbol{G}\boldsymbol{s}_j + \boldsymbol{Z}_j^{-\frac{1}{2}}\hat{\boldsymbol{n}}_j. \tag{2.41}$$

Then we compute the QR-decomposition of $\boldsymbol{Z}_j^{-\frac{1}{2}}\boldsymbol{G}$ as

$$\boldsymbol{Z}_j^{-\frac{1}{2}}\boldsymbol{G} = \boldsymbol{Q}\bar{\boldsymbol{R}}, \tag{2.42}$$

where $\boldsymbol{Q} \in \mathbb{C}^{N_m \times N_m}$ is a unitary matrix and $\bar{\boldsymbol{R}} = \begin{bmatrix} \boldsymbol{R} \\ \boldsymbol{0} \end{bmatrix} \in \mathbb{C}^{N_m \times N_d}$ with $\boldsymbol{R} \in \mathbb{C}^{N_d \times N_d}$ being an upper triangular matrix. The denoised signal $\bar{\boldsymbol{c}} = \boldsymbol{Z}_j^{-\frac{1}{2}}\hat{\boldsymbol{c}}_j$ is filtered with $\boldsymbol{Q}^H$, as given by

$$\boldsymbol{Q}^H\bar{\boldsymbol{c}} = \bar{\boldsymbol{R}}\boldsymbol{S}_j + \bar{\boldsymbol{n}}, \tag{2.43}$$

where $\bar{\boldsymbol{n}} = \boldsymbol{Q}^H\boldsymbol{Z}_j^{-\frac{1}{2}}\hat{\boldsymbol{n}}_j$. Since $\boldsymbol{Q}$ is a unitary matrix, the variance of the noise term remains unaffected. Then we start the sequential decoding and remove the interference from other symbols sequentially. Due to the upper triangular structure of $\boldsymbol{R}$, the estimated signals on the M_T layers are free from interference.

2.5. Complexity Analysis

In this section we perform a computational complexity analysis of the proposed linear and non-linear detection schemes for UW-OFDM. Let $\boldsymbol{A} \in \mathbb{C}^{m \times n}$ be a complex matrix, then a QR decomposition of $\boldsymbol{A}$ has an approximate complexity of mn^2 flops [GVL13]. The inverse of a square matrix $\boldsymbol{A}$ ($m = n$) has an approximate complexity of n^3 flops [GVL13]. In this work, we use these definitions to calculate the approximate number of complex multiplications required by each detection scheme as summarized in Table 2.3.

As seen from Table 2.3, the linear and non-linear detection schemes, which are based on joint detection (utilize $\boldsymbol{H}_{\text{eff}}$ and $\boldsymbol{G}_{\text{eff}}$ in the detection procedure), have the highest computational complexity. The two step approach using linear estimators and a linear code generator demodulation matrix reduces the complexity significantly. The proposed hybrid detection scheme has a slightly lower complexity than the linear two step detection approach. This is true if the channel is time varying. But in practice, the channel is assumed to be constant during the coherence time (for a burst of data in WLAN or for one subframe in LTE-A). Therefore, the coefficients of the linear filters are calculated once for this time while the hybrid detection scheme requires an additional $N_m^2 + \frac{N_d(N_d-1)}{2}$ flops for each symbol during the coherence time of the channel.

2.6. Simulation Results

In this section, we investigate the performance of UW-OFDM in terms of the BER using the proposed detection schemes. We also compare it with CP-OFDM. We have used LTE-A parameters for a 3 MHz bandwidth in our simulations, as described in Table 2.2. The 3GPP channel models Extended Pedestrian A (EPA) and Extended Vehicular A (EVA) are used for the simulations. The EPA channel model has a much lower frequency selectivity than the EVA channel model. All the simulation results are averaged over 10,000 channel realizations.

	CP-OFDM	**UW-OFDM**
Modulation Scheme	QPSK	
Bandwidth	3 MHz	
Data Carriers (N_d)	180	162
Redundant Carriers (N_r)		18
FFT length (N)	256	
CP/UW duration	4.69 μs	
Channel	EPA and EVA	
MIMO Configuration $M_R \times M_T$	2×2, 4×4	

Table 2.2.: Simulation parameters

		Number of flops during coherence time of the channel	Number of flops for each symbol operation
UW-OFDM	Linear Joint Detectors	$N_m^2 N_d M_T^2 M_R + 2N_d^2 N_m M_T^2 M_R + N_d^3 M_T^3$	$N_m^2 N_d M_T^2 M_R + 2N_d^2 N_m M_T^2 M_R + N_d^3 M_T^3 + N_m N_d M_T M_R$
	Two Step Approach	$(2M_T^2 M_R + M_T^3)N_m + 2N_m^2 N_d + N_m^3$	$(2M_T^2 M_R + M_T^3)N_m + 2N_m^2 N_d + N_m^3 + N_m N_d M_T$
	QR-SIC	$2N_d^2 N_m M_T^2 M_R$	$2N_d^2 N_m M_T^2 M_R + N_m^2 M_R^2 + \frac{N_d M_T(N_d M_T-1)}{2}$
	Hybrid Detection	$(2M_T^2 M_R + M_T^3)N_m + 2N_m^2 N_d$	$(2M_T^2 M_R + M_T^3 M_R)N_m + 2N_m^2 N_d + N_m^2 + \frac{N_d(N_d-1)}{2}$
CP-OFDM	Linear Detectors	$(2M_T^2 M_R + M_T^3)N_m$	$(2M_T^2 M_R + M_T^3 M_R)N_m$
	QR-SIC	$2M_T^2 M_R N_m$	$(M_T^2 M_R + 2M_R^2 + \frac{M_T(M_T-1)}{2})N_m$

Table 2.3.: Computational complexity comparison of different estimation techniques in flops

We have chosen two scenarios to show the performance of UW-OFDM with linear and non-linear detection schemes. In the first scenario, we have a 2×2 MIMO system and low frequency selectivity (EPA). We refer to this scenario as "mild scenario". In the second scenario, we have more interference from the antennas (4×4 MIMO) and very high frequency selectivity (EVA). We refer to this scenario as "harsh scenario".

The results show that UW-OFDM with QR-SIC outperforms the linear equalization schemes significantly in both scenarios, as shown in Fig. 2.7. It is also interesting to observe that the proposed hybrid scheme outperforms the linear equalization significantly. The performance of the hybrid scheme is slightly worse than QR-SIC since we still employ linear equalization in the first step. The performance of UW-OFDM differs for both scenarios and we observe huge gains for UW-OFDM with linear and non-linear detection schemes over CP-OFDM in the harsh scenario. However, in the mild scenario the performance difference between UW-OFDM and CP-OFDM is reduced and we observe only a slight gain for UW-OFDM with linear equalization in the high SNRs regime. But still, UW-OFDM with hybrid detection has a considerable gain. Moreover, even UW-OFDM with linear equalization outperforms CP-OFDM with QR-SIC at high SNRs in both scenarios. Furthermore, the gain achieved by successive interference cancellation is not significant for CP-OFDM as compared to UW-OFDM.

2.7. Conclusion

In the UW-OFDM signaling concept, redundancy is introduced in the frequency domain at the transmitter to generate a valid UW-OFDM symbol. It has been shown in the literature for SISO systems that this redundancy can be exploited by a clever estimator design. Specifically, the SISO receiver based on the joint detection exploits this redundancy in an efficient manner [Oni13]. Therefore, after introducing the UW-OFDM signaling concept, two linear detection schemes for MIMO UW-OFDM are proposed in the first part of this chapter. In the first approach, the joint detection based design for SISO systems is extended to a MIMO UW-OFDM system. Although this approach outperforms CP-OFDM significantly, it has a significantly higher computational complexity since a square matrix of size $N_d \cdot M_T \times N_d \cdot M_T$ has to be inverted. Hence, an alternative scheme is proposed where the detection is performed in two steps. In the first step a subcarrier-wise equalization is performed while in the subsequent step a matched filter or LMMSE based code generator demodulator is employed. The results show that subcarrier-wise detection with an LMMSE based demodulator practically matches the performance of joint detection but with a considerably reduced computational complexity. It has also been shown that a combined demodulation matrix results practically in the same performance as of per antenna demodulation. This in return further reduces the computational complexity of two step approach.

In the second part of this chapter, the performance of UW-OFDM with SIC receivers has been investigated. Specifically a new hybrid detection scheme is proposed where a linear equalization is performed in the first step and a SIC code generator demodulation is used in the second step. Moreover, the complexity analysis of the linear and SIC detection schemes is also performed where it has been shown that the proposed hybrid scheme has a significantly lower complexity than the SIC receiver. UW-OFDM with SIC receivers shows a high performance gain in terms of the BER but at the cost of a much higher computational complexity. Note that UW-OFDM with the proposed hybrid equalization provides a
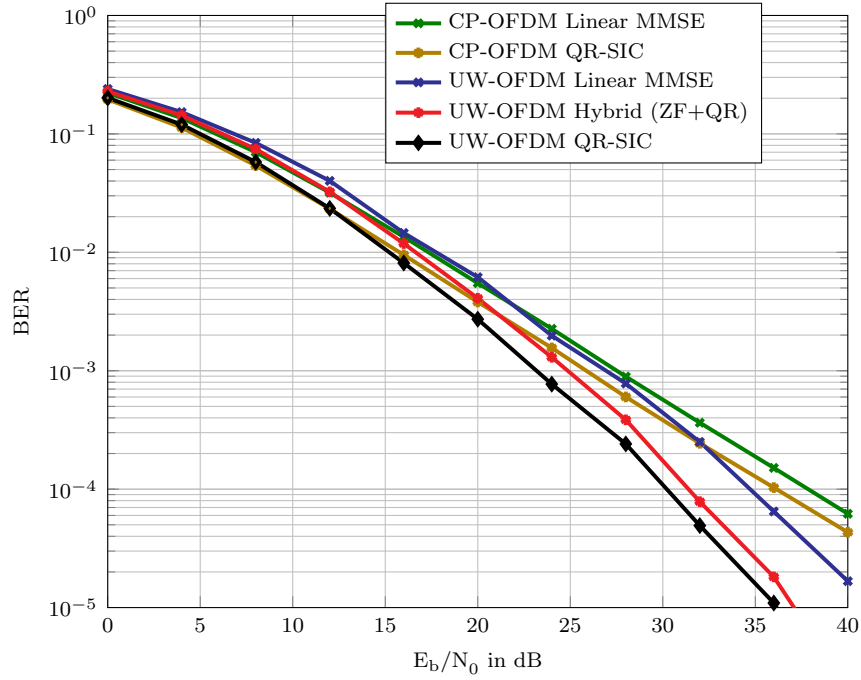
(a) 2×2 MIMO and EPA channel model
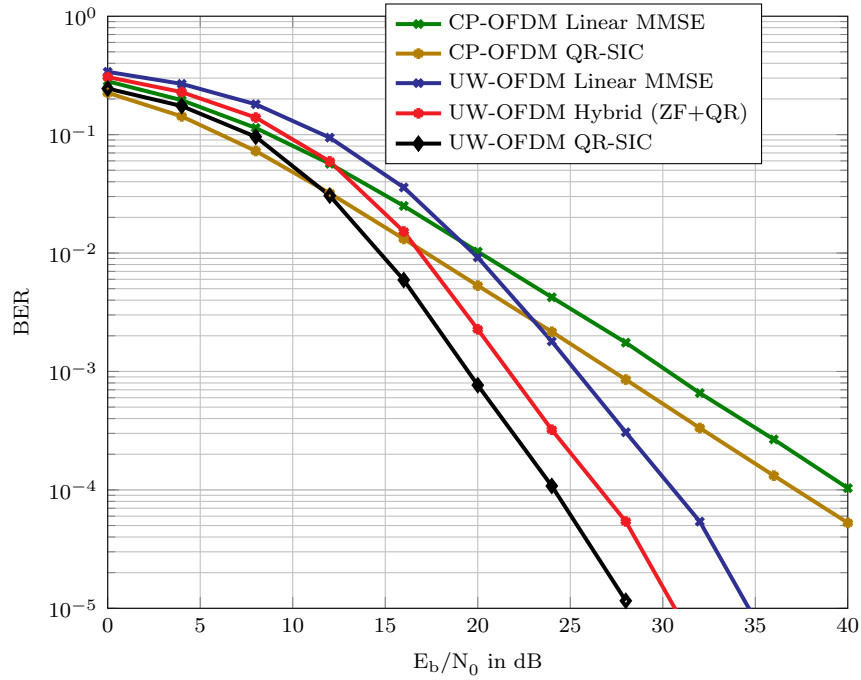
(b) 4×4 MIMO and EVA channel model

Figure 2.7.: Comparison of different detection schemes. UW-OFDM performance improves in high frequency selective environments. Moreover, UW-OFDM with SIC detection outperforms UW-OFDM with linear receivers and CP-OFDM significantly. The proposed hybrid equalizer provides a trade-off between performance and complexity.

trade-off between performance and computational complexity. It shows a better BER performance than

the linear detection schemes but the BER is slightly worse than for SIC receivers.

3. Space-Time Block Codes for UW-OFDM Systems

Orthogonal space-time block codes (OSTBCs) are widely used in modern communication systems when no channel state information (CSI) is available at the transmitter. One of the main reasons for the popularity of OSTBCs is the availability of low complexity optimal detection algorithms such as maximum ratio combining (MRC) at the receiver. The application of these STBCs to CP-OFDM is straightforward, since the detection is performed on each subcarrier separately. However, this is different for UW-OFDM since the code generator matrix introduces correlation among the data symbols which need to be efficiently utilized at the receiver to get a better performance. So far, UW-OFDM has been well investigated from various points of view for single-input single-output (SISO) systems, where it was shown that a joint detection fully exploits this correlation. In the previous chapters, it has been shown that a subcarrier-wise detection is also possible for MIMO UW-OFDM. It has also been shown that a similar performance to that of joint detection can be achieved if equalization combined with an MMSE based code generator demodulation is performed.

The main goal of this chapter is to present techniques to use existing OSTBCs for UW-OFDM systems. For this purpose, we propose two approaches to apply STBCs to UW-OFDM. In the first approach, we exploit STBCs in the frequency domain which is an extension of space-frequency block codes for CP-OFDM. But for UW-OFDM, this approach has a much higher decoding complexity since detection based on maximum ratio combining (MRC) is not feasible. Alternatively, in the second approach, we use STBCs in the time domain with a slight modification of the conventional UW-OFDM frame structure. We show that this approach results in a decoding procedure with a very low complexity. Moreover, a matched filter (MF) based demodulation can also be applied. In case of CP-OFDM, different types of STBCs have been investigated and recommended for different MIMO dimensions [LW00, LXG02]. In this chapter, we have chosen Alamouti based OSTBCs as an example. Other higher-order STBCs such as Tarokh STBCs [TJC99] and quasi orthogonal STBCs [Jaf01] can also be utilized for UW-OFDM, but the application and detection procedures will not change significantly.

The organization of the remaining chapter is as follows. In Section 3.1, STBCs for UW-OFDM are presented. We discuss two approaches to implement STBCs for UW-OFDM. We also propose appropriate detection schemes for these approaches. Section 3.2 shows the simulation results and quantifies the system performance in terms of the BER. The performance is also compared with CP-OFDM. The chapter is summarized at the end in Section 3.3.

3.1. Space-Time Block Codes

In this section, we investigate space-time block codes for UW-OFDM and propose new transceiver architectures for UW-OFDM with STBCs. We discuss two approaches for realizing OSTBCs in UW-OFDM. For the sake of simplicity, we consider Alamouti based STBCs, but the same approaches can be applied to higher MIMO dimensions. The conventional Alamouti STBCs were designed for flat fading channels and the encoding rule was applied to two consecutive symbols instead of applying it to blocks
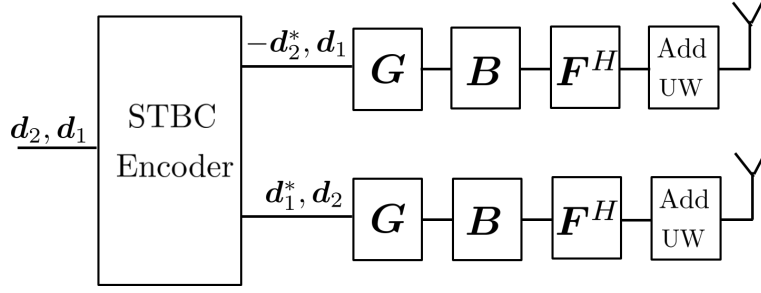
Figure 3.1.: Space-time encoder in the frequency domain

of data. Later on, in [BP00], Alamouti-based space-frequency coding was proposed for CP-OFDM. Here we propose two approaches to apply Alamouti-based STBCs to UW-OFDM systems and design the corresponding receiver.

3.1.1. Space-time encoder in the frequency domain

We consider a system with $M_T = 2$ antennas at the transmitter and M_R receive antennas. In the first approach, we use space-time encoding in the frequency domain, as shown in Fig. 3.1. The modulated data symbols $\boldsymbol{d}_1 \in \mathbb{C}^{N_d \times 1}$ and $\boldsymbol{d}_2 \in \mathbb{C}^{N_d \times 1}$ are processed by the space-time encoder to produce signals $\boldsymbol{s}_1$ and $\boldsymbol{s}_2$ for two transmit antennas in two successive time frames as shown in Table 3.1. The two data vectors at the output of the space-time encoder are independently multiplied with the code generator matrix. Then after applying the IFFT and adding the UW, they are transmitted by the two antennas.

	Antenna 1	Antenna 2
Time frame 1	$\boldsymbol{s}_{1,1} = \boldsymbol{d}_1$	$\boldsymbol{s}_{1,2} = \boldsymbol{d}_2$
Time frame 2	$\boldsymbol{s}_{2,1} = -\boldsymbol{d}_2^*$	$\boldsymbol{s}_{2,2} = \boldsymbol{d}_1^*$

Table 3.1.: STBC encoder for $M_T = 2$ with $\boldsymbol{d}_1,\ \boldsymbol{d}_2 \in \mathbb{C}^{N_d \times 1}$

The received signal at the jth receive antenna for the time frames $(t = 1, 2)$ is given by

$$\boldsymbol{y}_{t,j} = \sum_{i=1}^{M_T} \boldsymbol{H}_{j,i} \boldsymbol{F}_N^{-1} (\boldsymbol{B}\boldsymbol{G}\boldsymbol{s}_{t,i} + \tilde{\boldsymbol{x}}_u) + \boldsymbol{v}, \tag{3.1}$$

where $\boldsymbol{H}_{j,i}$ is the channel convolutional matrix containing the channel impulse response from the ith transmit antenna to the jth receive antenna, $\tilde{\boldsymbol{x}}_u \in \mathbb{C}^{N \times 1}$ is the corresponding UW in the frequency domain, $\boldsymbol{v}$ is a zero-mean Gaussian noise vector and the subscript $(.)_{t,j}$ represents the time frames and the transmit antennas, respectively. After applying the FFT at the receiver and removing the UW, the received signal at the jth receive antenna in the frequency domain during the tth time frame is given by

$$\tilde{\boldsymbol{y}}_{t,j} = \sum_{i=1}^{M_T} \tilde{\boldsymbol{H}}_{j,i} \boldsymbol{G}\boldsymbol{s}_{t,i} + \tilde{\boldsymbol{v}} \in \mathbb{C}^{N_m \times 1}, \tag{3.2}$$

where the diagonal matrix $\tilde{\boldsymbol{H}}_{j,i} = \boldsymbol{B}^T \boldsymbol{F}_N \boldsymbol{H}_{j,i} \boldsymbol{F}_N^{-1} \boldsymbol{B} \in \mathbb{C}^{N_m \times N_m}$ contains the channel frequency response on its main diagonal and $\tilde{\boldsymbol{v}} = \boldsymbol{B}^T \boldsymbol{F}_N \boldsymbol{v}$ is the zero-mean Gaussian noise vector in the frequency domain. After taking the conjugate of the received signal in the second time frame, the combined signal for the two time frames in the frequency domain can be written as

$$
\begin{bmatrix}
\tilde{\boldsymbol{y}}_{1,1} \\
\vdots \\
\tilde{\boldsymbol{y}}_{1,M_R} \\
\tilde{\boldsymbol{y}}_{2,1}^* \\
\vdots \\
\tilde{\boldsymbol{y}}_{2,M_R}^*
\end{bmatrix}
= \boldsymbol{H}_{\text{eff}} \boldsymbol{G}_{\text{eff}}
\begin{bmatrix}
\boldsymbol{d}_1 \\
\boldsymbol{d}_2
\end{bmatrix}
+
\begin{bmatrix}
\tilde{\boldsymbol{v}}_{1,1} \\
\vdots \\
\tilde{\boldsymbol{v}}_{1,M_R} \\
\tilde{\boldsymbol{v}}_{2,1}^* \\
\vdots \\
\tilde{\boldsymbol{v}}_{2,M_R}^*
\end{bmatrix}
\in \mathbb{C}^{2 \cdot M_R \cdot N_m \times 1},
\tag{3.3}
$$

where $\boldsymbol{G}_{\text{eff}}$ is the concatenation of two block diagonal matrices and

$$
\boldsymbol{G}_{\text{eff}} =
\begin{bmatrix}
\boldsymbol{I}_{M_T} \otimes \boldsymbol{G} \\
\boldsymbol{I}_{M_T} \otimes \boldsymbol{G}^*
\end{bmatrix}
\in \mathbb{C}^{2 \cdot M_T \cdot N_m \times M_T \cdot N_m}
\tag{3.4}
$$

$$
\boldsymbol{H}_{\text{eff}} =
\begin{bmatrix}
\tilde{\boldsymbol{H}}_{1,1} & \tilde{\boldsymbol{H}}_{1,2} & \boldsymbol{0} & \boldsymbol{0} \\
\vdots & \vdots & \vdots & \vdots \\
\tilde{\boldsymbol{H}}_{M_R,1} & \tilde{\boldsymbol{H}}_{M_R,2} & \boldsymbol{0} & \boldsymbol{0} \\
\boldsymbol{0} & \boldsymbol{0} & \tilde{\boldsymbol{H}}_{1,2}^* & -\tilde{\boldsymbol{H}}_{1,1}^* \\
\vdots & \vdots & \vdots & \vdots \\
\boldsymbol{0} & \boldsymbol{0} & \tilde{\boldsymbol{H}}_{M_R,1}^* & -\tilde{\boldsymbol{H}}_{M_R,2}^*
\end{bmatrix}
\in \mathbb{C}^{2 \cdot M_R \cdot N_m \times 4 \cdot N_m}.
$$

The channel transfer functions (CTFs) $\tilde{\boldsymbol{H}}_{j,i} \in \mathbb{C}^{N_m \times N_m}$ are still the diagonal matrices with the channel from the ith transmit antenna to the jth receive antenna on the main diagonal. To facilitate a subcarrier-wise operation at the receiver, an equivalent representation of Eq. (3.3) can be written as

$$
\begin{bmatrix}
\boldsymbol{z}_1 \\
\boldsymbol{z}_2 \\
\vdots \\
\boldsymbol{z}_{N_m}
\end{bmatrix}
= \boldsymbol{H}_{\text{eff}}' \boldsymbol{G}_{\text{eff}}'
\begin{bmatrix}
\boldsymbol{d}_1 \\
\boldsymbol{d}_2
\end{bmatrix}
+
\begin{bmatrix}
\hat{\boldsymbol{v}}_1 \\
\hat{\boldsymbol{v}}_2 \\
\vdots \\
\hat{\boldsymbol{v}}_{N_m}
\end{bmatrix},
\tag{3.5}
$$

where $\boldsymbol{z}_l = [\tilde{y}_{1,1,l} \cdots \tilde{y}_{1,M_R,l} \ \tilde{y}_{2,1,l}^* \cdots \tilde{y}_{2,M_R,l}^*]^T$ and $\hat{\boldsymbol{v}}_l = [\tilde{v}_{1,1,l} \cdots \tilde{v}_{1,M_R,l} \ \tilde{v}_{2,1,l}^* \cdots \tilde{v}_{2,M_R,l}^*]^T$ are the combined received signal and noise vectors for the two time frames and for the lth subcarrier, respectively. Here $\tilde{y}_{t,j,l}$ and $\tilde{v}_{t,j,l}$ denote the lth component of the vectors defined in Eq. (3.2). Moreover, $\boldsymbol{H}_{\text{eff}}'$ and

$\boldsymbol{G}'_{\text{eff}}$ are given as

$$
\boldsymbol{H}'_{\text{eff}} = \begin{bmatrix} \boldsymbol{H}'_1 & \boldsymbol{0} & \cdots & \boldsymbol{0} \\ \boldsymbol{0} & \boldsymbol{H}'_2 & \cdots & \boldsymbol{0} \\ \vdots & \vdots & \ddots & \vdots \\ \boldsymbol{0} & \boldsymbol{0} & \cdots & \boldsymbol{H}'_{N_m} \end{bmatrix} \in \mathbb{C}^{2 \cdot M_R \cdot N_m \times 4 \cdot N_m}
$$

$$
\boldsymbol{G}'_{\text{eff}} = \begin{bmatrix} \boldsymbol{I}_{M_T} \otimes [\boldsymbol{G}^T]_1^T \\ \boldsymbol{I}_{M_T} \otimes [\boldsymbol{G}^T]_1^H \\ \vdots \\ \boldsymbol{I}_{M_T} \otimes [\boldsymbol{G}^T]_{N_m}^T \\ \boldsymbol{I}_{M_T} \otimes [\boldsymbol{G}^T]_{N_m}^H \end{bmatrix} \in \mathbb{C}^{2 \cdot M_T \cdot N_m \times M_T \cdot N_d},
$$

where $[\boldsymbol{G}^T]_l$ is the lth column of the matrix $\boldsymbol{G}^T$, and $\boldsymbol{H}'_{\text{eff}}$ is a block diagonal matrix containing the N_m subcarrier-wise effective CTFs. These effective CTFs for the lth subcarrier are given as

$$
\boldsymbol{H}'_l = \begin{bmatrix} \tilde{h}_{1,1,l} & \tilde{h}_{1,2,l} & 0 & 0 \\ \vdots & \vdots & \vdots & \vdots \\ \tilde{h}_{M_R,1,l} & \tilde{h}_{M_R,2,l} & 0 & 0 \\ 0 & 0 & \tilde{h}_{1,2,l}^* & -\tilde{h}_{1,1,l}^* \\ \vdots & \vdots & \vdots & \vdots \\ 0 & 0 & \tilde{h}_{M_R,2,l}^* & -\tilde{h}_{M_R,1,l}^* \end{bmatrix} \quad \forall \, l = 1, \ldots, N_m
$$

3.1.1.1. Detection Procedure

Clearly, $\boldsymbol{H}'_l$ is a non-orthogonal matrix, therefore the MRC scheme is not feasible. We can use a two step subcarrier-wise detection procedure or a joint detection scheme as discussed in the previous chapter.

Two Step Detection: Since $\boldsymbol{H}'_l$ is a non-orthogonal matrix so a subcarrier-wise ZF detection or MMSE detection scheme can be utilized in the first step. The equalized symbols on the lth subcarrier are

$$
\boldsymbol{b}_l = \boldsymbol{E}_l \boldsymbol{z}_l \in \mathbb{C}^{2 \cdot M_T \times 1}, \tag{3.6}
$$

where the equalizer weights can be derived using $\boldsymbol{E}_{\text{ZF}} \in \mathbb{C}^{2M_T \times 2M_R}$ in Eq. (2.19) or $\boldsymbol{E}_{\text{MMSE}} \in \mathbb{C}^{2M_T \times 2M_R}$ in Eq. (2.22) by replacing $\boldsymbol{H}_l$ with $\boldsymbol{H}'_l$. Note that we already have a higher dimension of equalizer weights than for conventional CP-OFDM, thus having a higher computational complexity. In the second step, an LMMSE based code generator demodulation is applied to estimate the data symbols

$$
\hat{\boldsymbol{d}} = \hat{\boldsymbol{W}}_{\text{MMSE}} \bar{\boldsymbol{b}} \in \mathbb{C}^{M_T \cdot N_d \times 1}, \tag{3.7}
$$

where $\hat{\boldsymbol{W}}_{\mathrm{MMSE}}$ is the MMSE based code generator demodulator matrix and

$$\bar{\boldsymbol{b}} = \begin{bmatrix} \boldsymbol{b}_1 \\ \boldsymbol{b}_2 \\ \vdots \\ \boldsymbol{b}_{N_m} \end{bmatrix} \in \mathbb{C}^{2 \cdot M_T \cdot N_m \times 1}.$$

The LMMSE based code generator demodulator $\hat{\boldsymbol{W}}_{\mathrm{MMSE}}$ is given by

$$\hat{\boldsymbol{W}}_{\mathrm{MMSE}} = \boldsymbol{G}_{\mathrm{eff}}^{\prime H} \left(\boldsymbol{G}_{\mathrm{eff}}^{\prime} \boldsymbol{G}_{\mathrm{eff}}^{\prime H} + \frac{\sigma_n^2}{\sigma_d^2} \boldsymbol{Z} \right)^{-1} \in \mathbb{C}^{M_T \cdot N_d \times 2 \cdot M_T \cdot N_m}. \tag{3.8}$$

Joint Detection: Note that the two step approach for the space-time encoder in the frequency domain requires a very high computational complexity at the receiver because of two reason. Firstly, the effective channel matrix on each subcarrier $\boldsymbol{H}_l'$ has a relatively large dimension. Secondly, the LMMSE based code generator demodulation requires a large dimension inversion in Eq. (3.8) that involve the effective code generator modulation matrix $\boldsymbol{G}_{\mathrm{eff}}'$ (the effective inversion of a matrix size $2 \cdot M_T \cdot N_m \times 2 \cdot M_T \cdot N_m$). Alternatively, joint detection can be applied where the equalizer weights are given as

$$\boldsymbol{E}_{\mathrm{BLUE}} = \left(\boldsymbol{G}_{\mathrm{eff}}^H \boldsymbol{H}_{\mathrm{eff}}^H \boldsymbol{H}_{\mathrm{eff}} \boldsymbol{G}_{\mathrm{eff}} \right)^{-1} \boldsymbol{G}_{\mathrm{eff}}^H \boldsymbol{H}_{\mathrm{eff}}^H \tag{3.9}$$

$$\boldsymbol{E}_{\mathrm{LMMSE}} = \left(\boldsymbol{G}_{\mathrm{eff}}^H \boldsymbol{H}_{\mathrm{eff}}^H \boldsymbol{H}_{\mathrm{eff}} \boldsymbol{G}_{\mathrm{eff}} + \frac{\sigma_n^2}{\sigma_d^2} \boldsymbol{I}_{(M_T \cdot N_m)} \right)^{-1} \boldsymbol{G}_{\mathrm{eff}}^H \boldsymbol{H}_{\mathrm{eff}}^H. \tag{3.10}$$

Note that the model represented in Eq. (3.5) is the equivalent representation of the model represented in Eq. (3.3). Therefore, a joint detection scheme can also be applied to the model in Eq. (3.5). In this case, $\boldsymbol{G}_{\mathrm{eff}}$ and $\boldsymbol{H}_{\mathrm{eff}}$ in Eq. (3.9) and Eq. (3.10) are replaced by $\boldsymbol{G}_{\mathrm{eff}}'$ and $\boldsymbol{H}_{\mathrm{eff}}'$. Clearly, for the space-time encoder in the frequency domain, joint detection is the best choice due to its lower computational complexity since it requires only one inversion (the effective inversion of a matrix size $M_T \cdot N_d \times M_T \cdot N_d$).

3.1.2. Space-time encoder in the time domain

The application of a conventional Alamouti based space-time encoder for UW-OFDM in the frequency domain results in a non-orthogonal equivalent channel matrix which is a disadvantage, because it increases the decoding complexity. An alternative strategy is the implementation of a space-time encoder in the time domain just after the IDFT operation. Such an encoding strategy is also referred to as time-reversal space-time coding (TR-STC). An Alamouti based TR-STC scheme was proposed for single-carrier block transmission with frequency domain equalization in [AD01]. This TR-STC scheme can also be implemented for UW-OFDM with a slight modification of the UW-OFDM frame structure.

In this approach, the time domain samples $\boldsymbol{x}_1$ and $\boldsymbol{x}_2$ at the output of the IDFT are first encoded by the space-time encoder according to Table 3.2 for $n = 0, 1, ..., N-1$, as shown in Fig. 3.2. Then a UW is added in the time domain signal. To correctly apply this TR-STC scheme, we propose to generate a zero UW at the start of the time domain signal instead of generating it at the end. This can be accomplished by designing a $\boldsymbol{G}$ matrix which fulfills the constraint $\boldsymbol{F}_N^{-1} \boldsymbol{B} \boldsymbol{G} = [\boldsymbol{0} \quad *]^T$ instead of the conventional
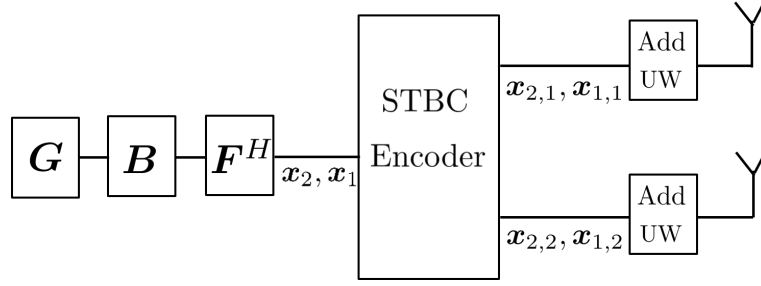
Figure 3.2.: Space-time encoder in the time domain

(a) Conventional UW-OFDM frame structure (also with STBC in the frequency domain)

(b) UW-OFDM frame structure with TR-STC
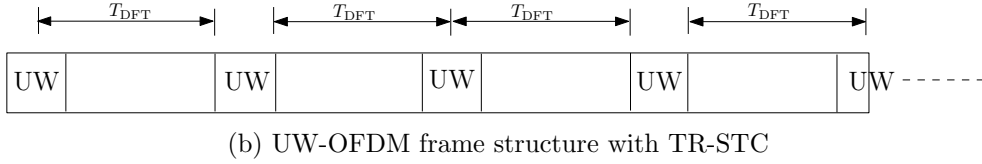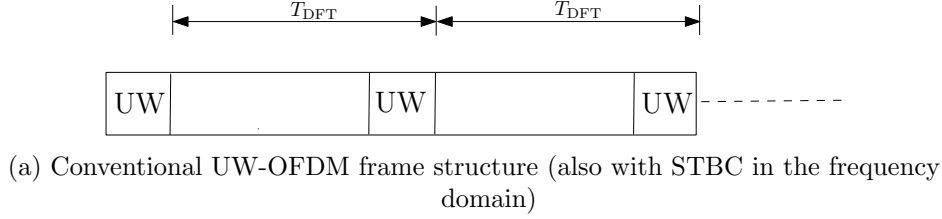
Figure 3.3.: Different frame structures for UW-OFDM

constraints $\boldsymbol{F}_N^{-1}\boldsymbol{B}\boldsymbol{G} = [* \quad \boldsymbol{0}]^T$. Moreover, we propose to generate $N_u/2 + 1$ zeros instead of N_u zeros,

	Antenna 1	Antenna 2
Time frame 1	$x_{1,1}[n] = x_1[n]$	$x_{1,2}[n] = x_2[n]$
Time frame 2	$x_{2,1}[n] = -x_2^*[(-n)_N]$	$x_{2,2}[n] = x_1^*[(-n)_N]$

Table 3.2.: TR-STC for UW-OFDM as illustrated in Fig. 3.4

thus requiring only $N_r/2 + 1$ redundant subcarriers instead of N_r. Additionally, a UW of length N_u needs to be inserted in between two encoded symbols to ensure cyclicity. The conventional and this modified frame structures are shown in Fig. 3.3a and Fig. 3.3b, respectively. To illustrate it further, we also show the block formats for two frames in Fig. 3.4. The extra addition of a UW in between two symbols is roughly compensated by the reduction of the redundancy in the frequency domain. Note that the length of the UW in this scheme is still the same as in the conventional UW-OFDM or when STBCs are applied in the frequency domain as shown in Fig. 3.3. The combined signal in the frequency domain after removing the UW can be written as

$$\begin{bmatrix} \hat{\boldsymbol{z}}_1 \\ \hat{\boldsymbol{z}}_2 \\ \vdots \\ \hat{\boldsymbol{z}}_{N_m} \end{bmatrix} = \boldsymbol{H}_{\text{eff}}''\boldsymbol{G}_{\text{eff}}'' \begin{bmatrix} \boldsymbol{d}_1 \\ \boldsymbol{d}_2 \end{bmatrix} + \begin{bmatrix} \hat{\boldsymbol{v}}_1 \\ \hat{\boldsymbol{v}}_2 \\ \vdots \\ \hat{\boldsymbol{v}}_{N_m} \end{bmatrix},$$ (3.11)
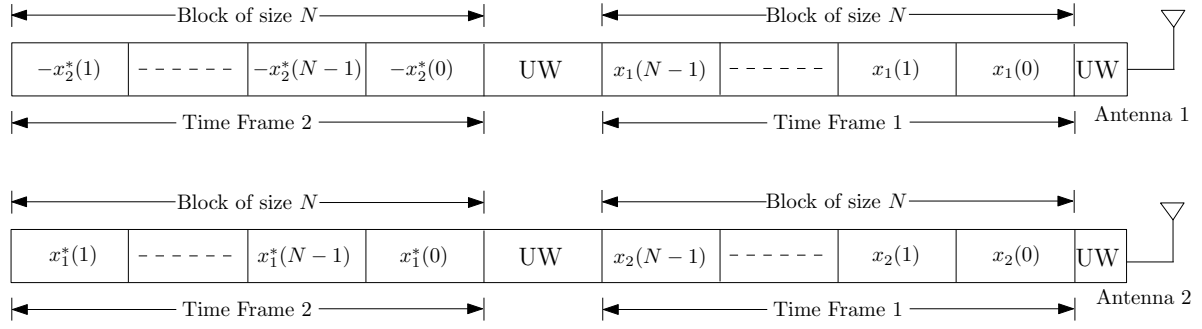
Figure 3.4.: Block formats of TR-STC for UW-OFDM in the time domain

where $\hat{\boldsymbol{z}}_l = [\tilde{y}_{1,1,l} \cdots \tilde{y}_{1,M_R,l} \quad \tilde{y}_{2,1,l}^* \cdots \tilde{y}_{2,M_R,l}^*]^T$ is the equivalent received signal for two time frames on the lth subcarrier, $\boldsymbol{G}_{\text{eff}}'' = \boldsymbol{I}_{M_T} \otimes \boldsymbol{G} \in \mathbb{C}^{M_T \cdot N_m \times M_T \cdot N_m}$, and $\boldsymbol{H}_{\text{eff}}'' \in \mathbb{C}^{2 \cdot M_R \cdot N_m \times M_T \cdot N_m}$ is a block diagonal matrix with the N_m subcarrier-wise combined CTFs ($\boldsymbol{H}_l''$) on its main block diagonal. The combined frequency response at the lth subcarrier is given as

$$\boldsymbol{H}_l'' = \begin{bmatrix} \tilde{h}_{1,1,l} & \tilde{h}_{1,2,l} \\ \vdots & \vdots \\ \tilde{h}_{M_R,1,l} & \tilde{h}_{M_R,2,l} \\ \tilde{h}_{1,2,l}^* & -\tilde{h}_{1,1,l}^* \\ \vdots & \vdots \\ \tilde{h}_{M_R,2,l}^* & -\tilde{h}_{M_R,1,l}^* \end{bmatrix} \in \mathbb{C}^{2 \cdot M_R \times M_T} \; \forall \; l = 1, \ldots, N_m \tag{3.12}$$

3.1.2.1. Receiver Design

A better estimate of the data symbols can be achieved if the redundancy introduced during the UW-OFDM symbol generation is well exploited at the receiver. Similar to the space-time encoder in the frequency domain, a two step detection procedure or a joint detection can be employed. But in this case, the two step approach has a smaller computational complexity since the effective channel matrix is orthogonal and also has a smaller dimension. Alternatively, we can apply a joint detection receiver by using $\boldsymbol{H}_{\text{eff}}''$ and $\boldsymbol{G}_{\text{eff}}''$ in Eq. (3.9) or Eq. (3.10). But this approach is computationally more expensive.

In the two step approach, we first remove the fading impact of the channel on the lth subcarrier by multiplying the combined received signal $\hat{\boldsymbol{z}}_l$, as defined in Eq. (3.11), containing two time frames on the lth subcarrier with an equalizer,

$$\hat{\boldsymbol{c}}_l = \boldsymbol{E}_l \hat{\boldsymbol{z}}_l \in \mathbb{C}^{M_T \times 1}, \tag{3.13}$$

where $\boldsymbol{E}_l \in \mathbb{C}^{M_T \times 2 \cdot M_R}$ are the equalizer weights. Since $\boldsymbol{H}_l''$ is an orthogonal matrix, the low-complexity MRC method can be used. Hence

$$\boldsymbol{E}_l = \frac{[\boldsymbol{H}_l'']^H}{\parallel \hat{\boldsymbol{H}}_l'' \parallel_{\text{F}}^2},$$

where

$$\hat{\boldsymbol{H}}_l'' = \begin{bmatrix} \tilde{h}_{1,1,l} & \tilde{h}_{1,2,l} \\ \vdots & \vdots \\ \tilde{h}_{M_R,1,l} & \tilde{h}_{l,M_R,2,l} \end{bmatrix}.$$

In the second step, all equalized symbols are jointly multiplied by a code generator demodulator matrix to get the estimated data symbols

$$\hat{\boldsymbol{D}} = \boldsymbol{W}\hat{\boldsymbol{C}}, \tag{3.14}$$

where $\hat{\boldsymbol{C}} = [\hat{\boldsymbol{c}}_1, ..., \hat{\boldsymbol{c}}_{N_m}]^T \in \mathbb{C}^{N_m \times M_T}$, and $\boldsymbol{W} \in \mathbb{C}^{N_d \times N_m}$ is the code generator demodulator matrix which can be a MF based demodulator or an MMSE based demodulator

$$\boldsymbol{W}_{\mathrm{MF}} = \boldsymbol{G}^H \tag{3.15}$$

$$\boldsymbol{W}_{\mathrm{MMSE}} = \boldsymbol{G}^H(\boldsymbol{G}\boldsymbol{G}^H + \sigma_n^2/\sigma_d^2\boldsymbol{Z})^{-1}, \tag{3.16}$$

where $\boldsymbol{Z} \in \mathbb{R}^{N_m \times N_m}$ is a diagonal matrix with $[\boldsymbol{Z}]_{l,l} = \mathrm{tr}(\boldsymbol{E}_l\boldsymbol{E}_l^H) \quad \forall \quad l = 1, \ldots, N_m$ on its main diagonal. Note that the matrices $\boldsymbol{E}_l \; \forall \quad l = 1, \ldots, N_m$ are already calculated in the first step.

	CP-OFDM	**UW-OFDM**
Modulation Scheme	QPSK	
Bandwidth	3 MHz	
Data Carriers (N_d)	180	162, 171
Redundant Carriers (N_r)		18, 9
FFT length (N)	256	
CP/UW duration	4.69 μs	
Channel	Extended Vehicular A (EVA)	
MIMO Configuration $M_R \times M_T$	2×2	

Table 3.3.: Simulation parameters

3.2. Simulation Results

In this section, we evaluate the performance of the proposed space-time block coded UW-OFDM system. To this end, we use the LTE parameters in Table 3.3. We assume that the whole bandwidth is allocated to a single user and no channel coding is applied. Moreover, the 3GPP channel model EVA is used for the simulations. All the simulation results are averaged over 10,000 channel realizations.

First we compare the performance of the proposed frequency domain STBC approach, denoted as "freq domain", and the time domain STBC approach, denoted as "TR-STC" with different detection schemes in Fig. 3.5a. The frequency domain STBC yields a slightly better performance as compared to TR-STC (approximately 0.2 dB at high E_b/N_0) when a joint detection based on the BLUE or MMSE criterion is applied. The two-step detection scheme also yields similar results as those of the joint detection for both schemes, when a subcarrier-wise equalization is performed in the first step
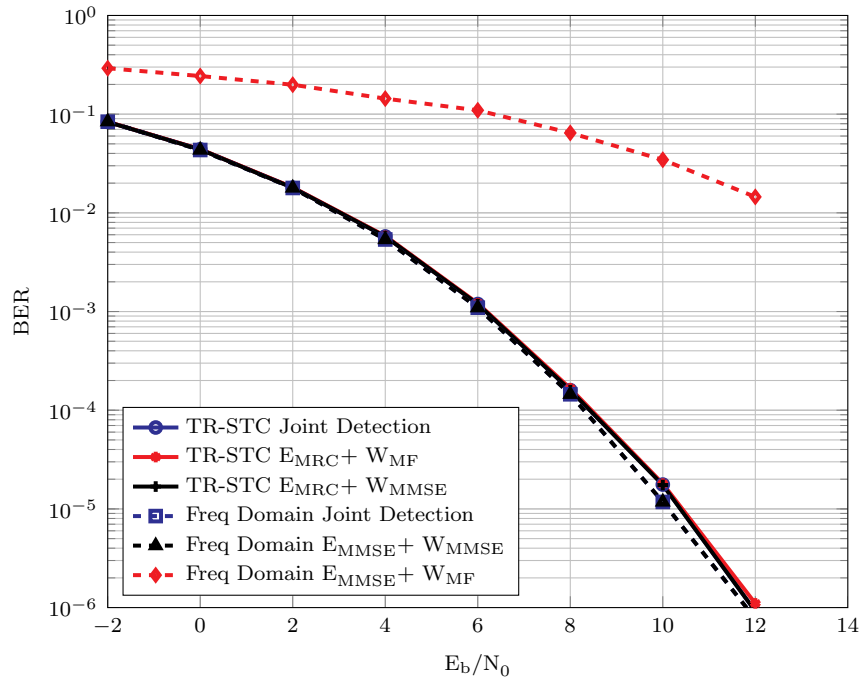
(a) Different detection schemes for both approaches using $\boldsymbol{G''}$
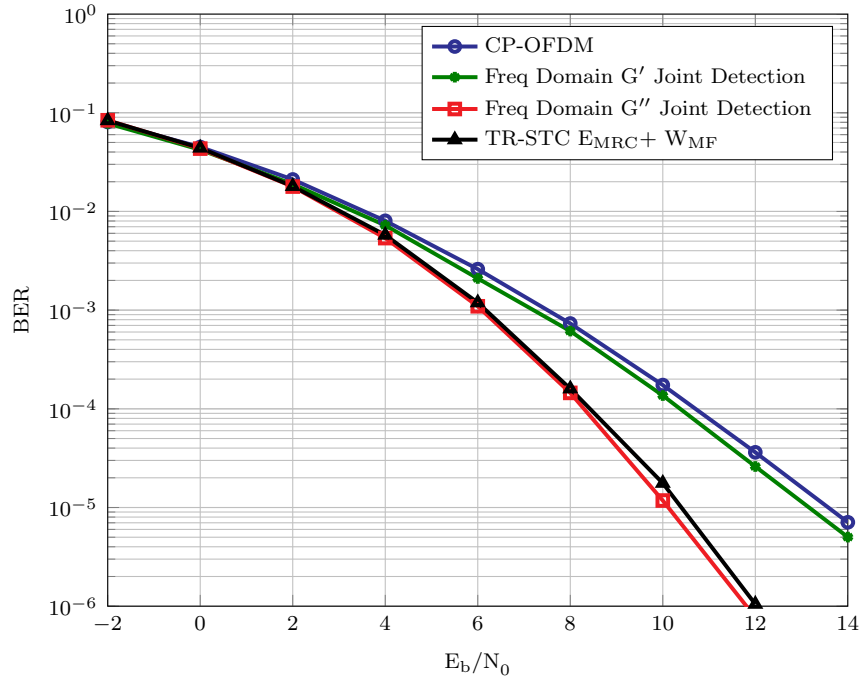
(b) Performance comparison of UW-OFDM with STBCs

Figure 3.5.: Performance comparison of 2×2 MIMO with Alamouti based STBCs

and an LMMSE based demodulator is used in the second step. Note that we have applied MRC based detection for UW-OFDM with TR-STC while MMSE based detection for UW-OFDM with STBCs in the frequency domain. However, the results are different when a MF demodulator is used in the second step. Furthermore, it is noteworthy that an MRC based detection combined with a MF based demodulation

shows the same performance as the joint detection for UW-OFDM with TR-STC. This is due to that fact that the received combined CTF on each subcarrier is orthogonal. This can be verified analytically from Eq. (3.9) which reduces to

$$
\begin{aligned}
\boldsymbol{E}_{\mathrm{BLUE}} &= \left(\boldsymbol{G}_{\mathrm{eff}}^{H}\boldsymbol{H}_{\mathrm{eff}}^{H}\boldsymbol{H}_{\mathrm{eff}}\boldsymbol{G}_{\mathrm{eff}}\right)^{-1}\boldsymbol{G}_{\mathrm{eff}}^{H}\boldsymbol{H}_{\mathrm{eff}}^{H} \\
&= \left(\boldsymbol{G}_{\mathrm{eff}}^{H}\boldsymbol{I}\boldsymbol{G}_{\mathrm{eff}}\right)^{-1}\boldsymbol{G}_{\mathrm{eff}}^{H}\boldsymbol{H}_{\mathrm{eff}}^{H} \\
&= \boldsymbol{G}_{\mathrm{eff}}^{H}\boldsymbol{H}_{\mathrm{eff}}^{H}
\end{aligned}
$$

This is true when $\boldsymbol{H}_{\mathrm{eff}}^{H}\boldsymbol{H}_{\mathrm{eff}} = \boldsymbol{I}$ (the effective channel is orthogonal) and $\boldsymbol{G}_{\mathrm{eff}}^{H}\boldsymbol{G}_{\mathrm{eff}} = \boldsymbol{I}$ (true for non-systematic code generator matrices). However, when the channel matrix is non-orthogonal e.g., when STBCs are applied in the frequency domain, a MF based demodulation is not feasible.

In Fig. 3.5b, we compare the performance of CP-OFDM with UW-OFDM using two code generator matrices $(\boldsymbol{G}', \boldsymbol{G}'')$. The simulation results show that the design of the code generator matrix plays an important role on the performance of UW-OFDM, where UW-OFDM with $\boldsymbol{G}''$ outperforms UW-OFDM with $\boldsymbol{G}'$. Note that $\boldsymbol{G}''$ is optimized using an MMSE criterion in an AWGN channel while $\boldsymbol{G}'$ is using the SVD of $\boldsymbol{U}$, as defined in Eq. (2.5). Moreover, UW-OFDM with both code generator matrices outperforms CP-OFDM. But the obtained gain is significant for UW-OFDM with $\boldsymbol{G}''$. Clearly UW-OFDM combined with TR-STC is a better and lower complexity choice for applying STBCs, since the effective channel matrix is orthogonal and therefore a subcarrier-wise detection based on MRC can be applied. Moreover, we can also use a MF based demodulation in this case.

3.3. Conclusion

In this chapter, we have proposed two approaches to apply OSTBCs to UW-OFDM. We have also proposed different detection procedures for these approaches. In the first approach, we exploit STBCs in the frequency domain which is an extension of space-frequency block codes for CP-OFDM. This results in a non-orthogonal effective channel matrix for UW-OFDM. Therefore, this approach has a much higher decoding complexity since detection based on MRC is not feasible. In the second approach, we use STBCs in the time domain. A slight modification of the conventional UW-OFDM frame structure is required to correctly use this approach. We have shown that just like CP-OFDM, a lower complexity MRC based detection can be used for UW-OFDM when time reversal based space-time coding is utilized. Moreover, we can also employ a MF based demodulation in the second step if the combined channel matrix is orthogonal. This combination has a slightly higher computational complexity as CP-OFDM where the additional complexity lies only in the multiplication by $\boldsymbol{G}^{H}$. But the performance of UW-OFDM with STBCs is far better than for CP-OFDM.

4. Performance Comparison of Space-Time Block Codes for Different 5G Air Interface Proposals

Several new multicarrier transmission techniques such as filter bank multicarrier (FBMC), universal filtered multicarrier (UFMC), and generalized frequency division multiplexing (GFDM) have been proposed as an alternative to CP-OFDM for future wireless communication systems. Since MIMO will be an integral part of the 5th Generation (5G) cellular systems, the performance of these new schemes needs to be investigated for MIMO systems. Space-time block codes are widely used in MIMO systems because of their ability to achieve full diversity and the simple linear processing at the receiver. In the previous chapter, we have proposed two approaches to apply OSTBCs to UW-OFDM. In this chapter, we evaluate the performance of UW-OFDM against these competing technologies for future systems. Specifically, we propose two methods for using STBCs in UFMC. We start by describing the system model of UFMC, GFDM, and FBMC in Section 4.2. Two methods to apply STBCs to UFMC are presented in Section 4.3. Moreover, we also give an overview of STBCs for GFDM and FBMC. Section 4.4 shows the simulation results and quantifies the system performance in terms of the bit error rate using LTE-A parameters. The chapter is summarized at the end in Section 4.5.

4.1. Introduction

5G cellular communication systems are expected to support many application scenarios such as the tactile Internet, machine-type communications (MTC), Internet of things (IoT), and many more, on top of providing data rates of a few Gigabits/s wireless connectivity. At present, CP-OFDM is the standard waveform for the 4th generation (4G) of cellular communication systems. CP-OFDM is a widely adopted solution mainly because of its robustness against multipath channels and its easy implementation. It is based on the FFT algorithm where the complete frequency band is digitally filtered as a whole. But CP-OFDM is not spectrum efficient due to its utilization of a guard band and a CP to avoid inter-carrier interference (ICI) and inter-symbol interference (ISI). Additionally, CP-OFDM suffers from high out-of-band (OOB) emissions which pose a challenge for opportunistic and dynamic spectrum access [Hos09].

A solution to these problems was provided by FBMC where the filtering functionality is applied on a per subcarrier basis instead of applying it on the complete frequency band [Bel10b]. Any filter design with low OOB emission can be chosen. The subcarrier filters are very narrow in frequency and thus require long filter lengths. This causes the overlapping of symbols in time and hence a CP is not required. However, the requirement of a long filter length for FBMC makes it unsuited for communication in short uplink bursts, as required in many potential 5G application scenarios. CP-OFDM and FBMC may be seen as the two extreme cases of a more general modulation paradigm where filtering is either applied on a complete band or on a per subcarrier basis. Therefore, in [SWC14], a new multicarrier waveform called universal filtered multicarrier (UFMC) was proposed which is a generalization of CP-OFDM and FBMC. Here, the filtering is applied on groups of subcarriers which allows for a significant reduction in

(a) UFMC modulator
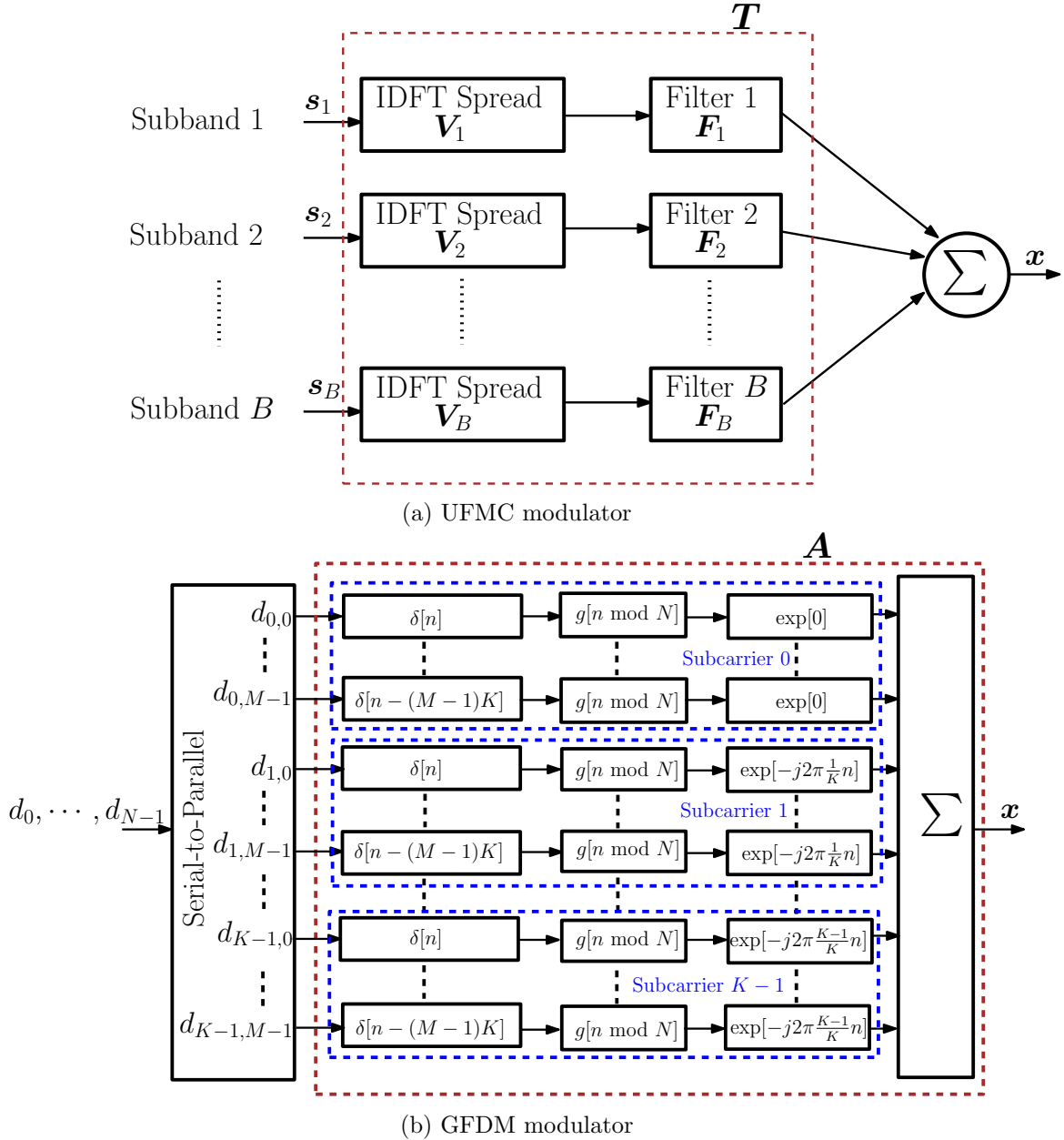
(b) GFDM modulator

Figure 4.1.: Generation of UFMC and GFDM modulation waveform

the filter length as compared to FBMC.

MIMO systems with multiple antenna elements at both link ends are an efficient solution for modern wireless communications systems to provide high data rates by exploiting the spatial domain under the constraints of limited bandwidth and transmit power. Space-time block coding is a MIMO transmit strategy which exploits transmit diversity to obtain a high reliability when no channel state information (CSI) is available at the transmitter. It uses both spatial and temporal diversity by transmitting multiple copies of the data that results in significant gains. Therefore, STBCs are an integral part of many modern wireless communication standards, i.e., WLAN, LTE. In this chapter, we investigate the performance of UFMC for MIMO systems while employing STBCs. Specifically we propose two techniques to apply

OSTBCs to the UFMC waveform. As an example, we have shown these techniques for Alamouti STBCs, but other STBCs can also be applied by employing the same technique. Moreover, the performance of these different 5G air interfaces is compared with each other. Specifically, in this chapter, we compare the performance of space-time block coded UW-OFDM systems with space-time block coded CP-OFDM, UFMC, GFDM, and FBMC systems.

4.2. System model

4.2.1. Universal Filtered Multicarrier

In UFMC, as shown in Fig. 4.1a, the overall K data subcarriers are grouped in B sub-bands where each sub-band comprises n_i subcarriers such that $K = \sum_{i=1}^{B} n_i$. Each sub-band operation may be referred to as a UFMC sub-module. The ith UFMC sub-module for $i = 1, ..., B$ takes the complex data symbols $\boldsymbol{s}_i \in \mathbb{C}^{n_i \times 1}$ as input. The vector $\boldsymbol{s}_i$ includes n_i complex-valued data symbols in baseband. Then an N point IDFT is applied on each sub-band to obtain the time domain signal. Afterwards, additional filtering is applied on each sub-band. For the choice of the filter characteristics many alternatives are available in the literature. For instance, a Dolph-Chebyshev filter maximizes the side lobe attenuation for a given main lobe width and is recommended for UFMC [SWC14]. Therefore, we have applied a Dolph-Chebyshev filter with N_f coefficients and side-lobe attenuation parameter α_SLA [Dol46]. The output for each UFMC module is then added together to form the transmit vector $\boldsymbol{x}$, given as,

$$\boldsymbol{x} = \sum_{i=1}^{B} \boldsymbol{x}_i = \sum_{i=1}^{B} \boldsymbol{F}_i \boldsymbol{V}_i \boldsymbol{s}_i \in \mathbb{C}^{N_\mathrm{ufmc} \times 1}, \tag{4.1}$$

where $N_\mathrm{ufmc} = N + N_\mathrm{f} - 1$, $\boldsymbol{V}_i \in \mathbb{C}^{N \times n_i}$ is the submatrix of IDFT matrix which includes the relevant columns of the inverse Fourier matrix according to the respective sub-band position within the overall available frequency range. The matrix $\boldsymbol{F}_i \in \mathbb{C}^{N_\mathrm{ufmc} \times N}$ is a Toeplitz matrix composed of the Dolph-Chebyshev filter impulse response which executes the linear convolution. The transmit signal $\boldsymbol{x} \in \mathbb{C}^{N_\mathrm{ufmc} \times 1}$ can be rewritten using the following definitions:

$$\boldsymbol{F} = [\boldsymbol{F}_1, \boldsymbol{F}_2, \cdots, \boldsymbol{F}_B] \in \mathbb{C}^{N_\mathrm{ufmc} \times (B \cdot N)}$$

$$\boldsymbol{V} = \mathrm{blkdiag}(\boldsymbol{V}_1, \boldsymbol{V}_2, \cdots, \boldsymbol{V}_B) \in \mathbb{C}^{(B \cdot N) \times K}$$

$$\boldsymbol{s} = [\boldsymbol{s}_1^T, \boldsymbol{s}_2^T, \cdots, \boldsymbol{s}_B^T]^T \in \mathbb{C}^{K \times 1},$$

resulting in

$$\boldsymbol{x} = \boldsymbol{T}\boldsymbol{s} \in \mathbb{C}^{N_\mathrm{ufmc} \times 1}, \tag{4.2}$$

where $\boldsymbol{T} = \boldsymbol{F}\boldsymbol{V} \in \mathbb{C}^{N_\mathrm{ufmc} \times K}$ is the UFMC modulation matrix. This enables column wise stacking of filter matrices, generating a block-diagonal IDFT matrix (indicated by the "blkdiag" operator) and stacking of all data symbols into one column, respectively.

UFMC does not essentially require a CP but it can still be used to further improve the robustness

against ISI. Assuming that the perfect time and frequency synchronization is accomplished and perfect channel state information is available at the receiver, the received signals $\boldsymbol{y}$ for the single-input single-output (SISO) system is

$$\boldsymbol{y} = \boldsymbol{H}\boldsymbol{x} + \boldsymbol{v} \in \mathbb{C}^{(N_{\mathrm{ufmc}}+N_{\mathrm{ch}}-1)\times 1}, \tag{4.3}$$

where $\boldsymbol{H}$ is the channel convolution matrix (as shown in Appendix B), N_{ch} is the length of the channel impulse response, and $\boldsymbol{v}$ is the zero-mean, circularly symmetric complex additive white Gaussian noise. The channel estimation and equalization for UFMC is as simple as for CP-OFDM. Both processes can be performed in the frequency domain [SWC14]. The equalized symbols in the frequency domain are given as

$$\tilde{\boldsymbol{y}}_{\mathrm{eq}} = \boldsymbol{E}\tilde{\boldsymbol{y}} \in \mathbb{C}^{N_{\mathrm{ufmc}}\times 1}, \tag{4.4}$$

where $\tilde{\boldsymbol{y}} = \boldsymbol{F}_{N_{\mathrm{ufmc}}}\boldsymbol{y}$ denotes the received symbols in the frequency domain after taking the DFT (denoted by $\boldsymbol{F}_{\mathrm{ufmc}}$) and $\boldsymbol{E} \in \mathbb{C}^{N_{\mathrm{ufmc}}\times N_{\mathrm{ufmc}}}$ denotes the equalizer coefficients which can be calculated using the ZF or the MMSE criterion, i.e.,

$$\boldsymbol{E}_{\mathrm{ZF}} = \left(\tilde{\boldsymbol{H}}^{H}\tilde{\boldsymbol{H}}\right)^{-1}\tilde{\boldsymbol{H}}^{H}, \tag{4.5}$$

$$\boldsymbol{E}_{\mathrm{MMSE}} = \left(\tilde{\boldsymbol{H}}^{H}\tilde{\boldsymbol{H}} + \frac{\sigma_n^2}{\sigma_s^2}\boldsymbol{I}_{N_{\mathrm{ufmc}}}\right)^{-1}\tilde{\boldsymbol{H}}^{H}, \tag{4.6}$$

where $\tilde{\boldsymbol{H}} \in \mathbb{C}^{N_{\mathrm{ufmc}}\times N_{\mathrm{ufmc}}}$ is the diagonal matrix containing the channel frequency response, σ_s^2 and σ_n^2 denote the signal and noise variance, respectively. After the equalization, the IDFT is applied and the UFMC demodulation process is carried out in the time domain which can be expressed as

$$\hat{\boldsymbol{s}} = \boldsymbol{U}\boldsymbol{y}_{\mathrm{eq}} \in \mathbb{C}^{K\times 1}, \tag{4.7}$$

where $\hat{\boldsymbol{s}}$ represents the estimated data symbols, $\boldsymbol{U} \in \mathbb{C}^{K\times N_{\mathrm{ufmc}}}$ is the UFMC demodulation matrix, and $\boldsymbol{y}_{\mathrm{eq}}$ are the equalized symbols in the time domain. Standard receiver options can be employed for the UFMC demodulator. It can be a matched filter (MF) receiver $\boldsymbol{U}_{\mathrm{MF}} = \boldsymbol{T}^{\mathrm{H}}$, or a zero forcing (ZF) receiver $\boldsymbol{U}_{\mathrm{ZF}} = \boldsymbol{T}^{+}$ which completely removes the self interference, or a minimum mean square error (MMSE) based receiver $\boldsymbol{U}_{\mathrm{MMSE}} = \left(\boldsymbol{T}^{H}\boldsymbol{T} + \sigma_n^2/\sigma_s^2\boldsymbol{I}_K\right)^{-1}\boldsymbol{T}^{H}$. We can also use an FFT based receiver for UFMC, which is a big advantage as the equalization and channel estimation can be performed in the frequency domain as in CP-OFDM. In such an FFT based receiver, a $2N$ point FFT is applied on the received signal $\boldsymbol{y}$ and then the frequency domain signal is down-sampled by a factor of 2. Later on, the channel estimation and equalization are performed on the down-sampled signal [SWC14].

4.2.2. Generalized Frequency Division Multiplexing

GFDM is a comparatively more flexible multicarrier scheme as it spreads the data symbols onto a time-frequency block and each subcarrier is filtered with a circular pulse shaping filter [MMG+14]. A block of N complex-valued data symbols is decomposed into K subcarriers with M subsymbols such that the total number of symbols is equal to $N = KM$. The serial-to-parallel conversion block converts the notation from $\boldsymbol{d} = [d_0, \cdots, d_{N-1}]^{\mathrm{T}} \in \mathbb{C}^{N\times 1}$ to $\boldsymbol{d}_{k,m}$ according to $\boldsymbol{d}_{k,m} = [d_{0,0}, ..., d_{0,M-1}, ..., d_{K-1,M-1}]^{\mathrm{T}} \in \mathbb{C}^{N\times 1}$
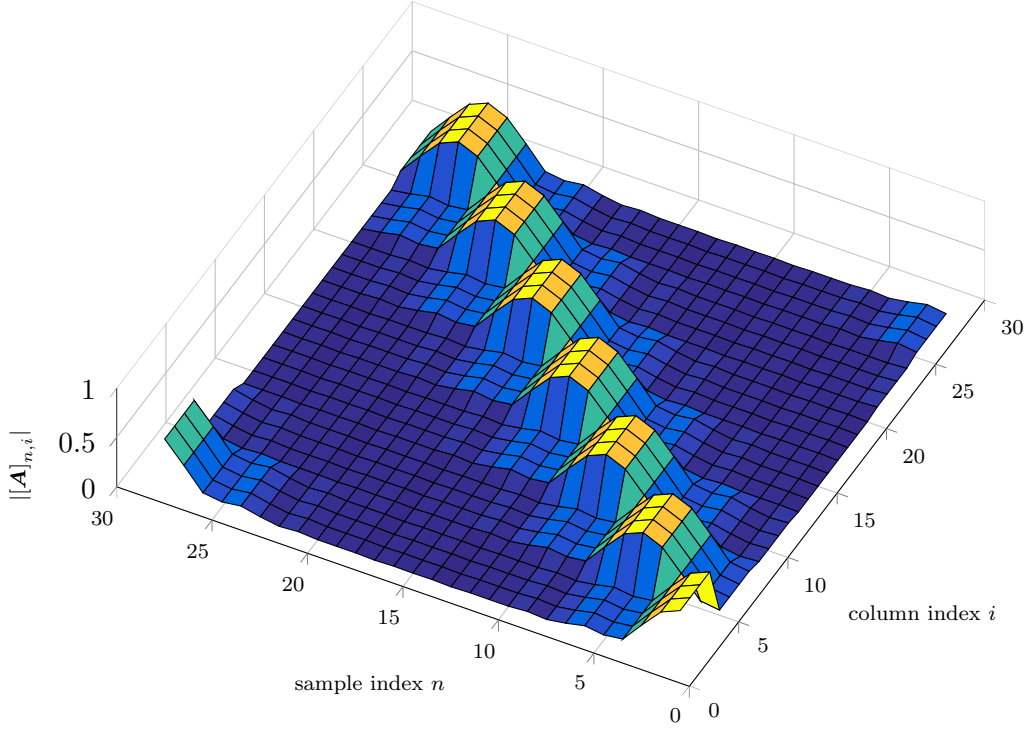
Figure 4.2.: GFDM transmitter matrix for $N = 28$, $K = 4$, $M = 7$, and a root raised cosine filter with a roll off factor $\alpha = 0.5$

as shown in Fig. 4.1b. Each element in $\boldsymbol{d}_{k,m}$ corresponds to the data that will be transmitted on the kth subcarrier and in the mth subsymbol of the GFDM signal. The indices n, k, and m are linked through $m = \lfloor \frac{n}{K} \rfloor$ and $k = n \bmod K$ in one direction and $n = mK + k$ in the other. Here the $\lfloor \cdot \rfloor$ operator indicates a floor function that takes as input a real number and gives as output the greatest integer that is less than or equal to that real number. After this operation, the signal path splits into N parallel substreams. In each stream, the respective data symbol $d_{k,m}$ is multiplied with a Dirac delta impulse $\delta[n - mK]$, which has two effects. First, the substream signal is added with $N - 1$ zeros, i.e., N times upsampling is performed. Second, a time shift of mK samples is introduced, which moves each data symbol to the correct subsymbol position in the GFDM block [MMG$^+$14]. Subsequently, the signal is modulated with a prototype pulse shape $g[n]$ and multiplied with a complex exponential $\exp[-j2\pi\frac{k}{K}n]$, which shifts the center frequency of the branch to address the K subcarriers in the system. Note that the prototype pulse is defined with circularity $g[n] = g[n \bmod N]$, as shown in Fig. 4.2. The overall prototype pulse shaping filter is given by

$$g_{k,m}[n] = g\left[(n - mK) \bmod N\right] \exp\left[-j2\pi\frac{k}{K}n\right], \qquad (4.8)$$

where $g_{k,m}[n]$ is the transmit filter circularly shifted to the mth subsymbol and modulated to the kth subcarrier as shown in Fig. 4.1b. The overall GFDM transmit signal samples $x[n]$ of one block are given

by

$$x[n] = \sum_{k=0}^{K-1} \sum_{m=0}^{M-1} g_{k,m}[n] d_{k,m} \quad n = 0, 1, ..., N-1 \tag{4.9}$$

We can rewrite Eq. (4.9) into a matrix according to

$$\boldsymbol{x} = \boldsymbol{A}\boldsymbol{d} \in \mathbb{C}^{KM \times 1}, \tag{4.10}$$

where $\boldsymbol{x}$ represents the transmit samples in the time domain and $\boldsymbol{A}$ is the GFDM modulator matrix of size $KM \times KM$ with a structure according to

$$\boldsymbol{A} = [\boldsymbol{g}_{0,0}, \cdots, \boldsymbol{g}_{K-1,0} \ \boldsymbol{g}_{0,1}, \cdots, \boldsymbol{g}_{K-1,M-1}] \in \mathbb{C}^{KM \times KM},$$

where filter coefficients in each column are achieved by varying $n = 0, 1, \cdots, N-1$ in Eq. (4.8). A CP is added to the modulated signal to provide easy frequency domain equalization at the receiver. After passing through the wireless channel, the received signal is given by Eq. (4.3). After removing the CP at the receiver, the frequency domain equalization can be performed as described for UFMC. The equalized time domain samples $\boldsymbol{y}_{\text{eq}}$ are then passed through the GFDM demodulator, given as

$$\hat{\boldsymbol{d}} = \boldsymbol{B}\boldsymbol{y}_{\text{eq}}, \tag{4.11}$$

where $\boldsymbol{B} \in \mathbb{C}^{KM \times KM}$ is the GFDM demodulator matrix. Just like the UFMC demodulator, a MF receiver $\boldsymbol{B}_{\text{MF}} = \boldsymbol{A}^{\text{H}}$, a ZF receiver $\boldsymbol{B}_{\text{ZF}} = \boldsymbol{A}^{+}$ or an MMSE receiver $\boldsymbol{B}_{\text{MMSE}} = \left(\boldsymbol{A}^{H}\boldsymbol{A} + \sigma_n^2/\sigma_s^2 \boldsymbol{I}_{KM}\right)^{-1} \boldsymbol{A}^{H}$ can be used as a GFDM demodulator. Moreover, it has been shown in [DMLF12] that even in the absence of noise and channel, $\boldsymbol{B}_{\text{MF}}$ does not completely eliminate the crosstalk between different symbols and channels. Therefore, a corresponding interference cancellation scheme is required for the MF.

4.2.3. Filter Bank Multicarrier

Another alternative to CP-OFDM is the filter bank multicarrier (FBMC) transmission technique. There are two main advantages for FBMC over CP-OFDM. First the subchannels can be designed in the frequency domain and secondly FBMC does not require a CP. Therefore FBMC is spectrally more efficient than CP-OFDM. However, these benefits come at the cost of higher system complexity [Bel10a].

In FBMC systems, a synthesis filter bank (SFB) and an analysis filter bank (AFB) are implemented in the modulator and demodulator, respectively. The SFB and AFB can be efficiently implemented using IDFT/DFT processing combined with polyphase filtering. The complex I/Q baseband signal, necessary for bandwidth efficient radio communications, at the output of the synthesis filter bank can be expressed as [RIS10]

$$s[m] = \sum_{k=0}^{M-1} \sum_{n=-\infty}^{+\infty} d_{k,n} \theta_{k,n} \beta_{k,n} p\left[m - n\frac{M}{2}\right] e^{j\frac{2\pi}{M}kn}, \tag{4.12}$$

where

$$\theta_{k,n} = e^{j\frac{\pi}{2}(k+n)} = j^{(k+n)} \tag{4.13}$$

and

$$\beta_{k,n} = (-1)^{kn} e^{-j\frac{2\pi k}{M}\left(\frac{L-1}{2}\right)} = j^{(k+n)}. \tag{4.14}$$

Moreover, k is the subcarrier index, n is the subchannel sample index, m is the sample index at high rate (at the SFB output), and M is the overall number of subchannels in the filter bank. Furthermore, $d_{k,n}$ is the real-valued symbol which modulates the k-th subcarrier during the n-th symbol interval and $\theta_{k,n}$ is the phase mapping between the real-valued symbol sequence and the complex-valued input samples to the SFB. This signal model can be interpreted as an offset-QAM (OQAM) modulation where $d_{k,n}$ and $d_{k,n+1}$ carry the in-phase and quadrature components of complex-valued symbols, respectively.

We define T as the basic subchannel signaling interval, then the complex QAM symbols are modulated at a rate of $1/T$, which is equal to the subcarrier spacing Δf. The sample rates at the SFB input and AFB output are $2/T$. The prototype filter defines the filter bank properties, and it is characterized by two parameters, the overlapping factor K and roll-off factor ρ. The overlapping factor determines the prototype filter impulse response length as $L = KM - 1$. The roll-off parameter determines the overlapping of the transition bands of adjacent subchannels. Often in FBMC, a roll-off factor of $\rho = 1$ is used, in which case the transmission bands of immediately adjacent subchannels are overlapping, but more distant subchannels are isolated very well from each other.

4.3. Space Time Block Codes

4.3.1. Space Time Block Coding for UFMC

In this section, we investigate the techniques to apply OSTBCs for the UFMC waveform. To this end, we consider Alamouti STBCs using $M_T = 2$ transmit antennas and M_R receive antennas. Initially Alamouti STBCs were designed for flat fading channels and the encoding rule was applied to two consecutive symbols instead of applying it to the blocks of data. Later on, in [BP00], Alamouti-based space-frequency coding for CP-OFDM was proposed. Moreover, in [AD01], work on combining the Alamouti scheme with single carrier block transmission and frequency domain equalization was presented. Since additional filtering is applied to lower the OOB emission for most of the newly proposed 5G transmission schemes, therefore the transceiver architecture for the STBCs differs to that of CP-OFDM. Especially for UFMC, the receiver design is strongly dependent on the type of receive filter employed. If an FFT based receiver is used, a direct implementation of STBCs is possible as it is performed for CP-OFDM. But in the case of other receive filters, the receiver architecture needs to be changed. Therefore, we propose two approaches, shown in Fig. 4.3, for the application of OSTBCs for UFMC using different receive filtering concepts.

(a) Space-time coding on UFMC data carriers

(b) TR-STC for UFMC
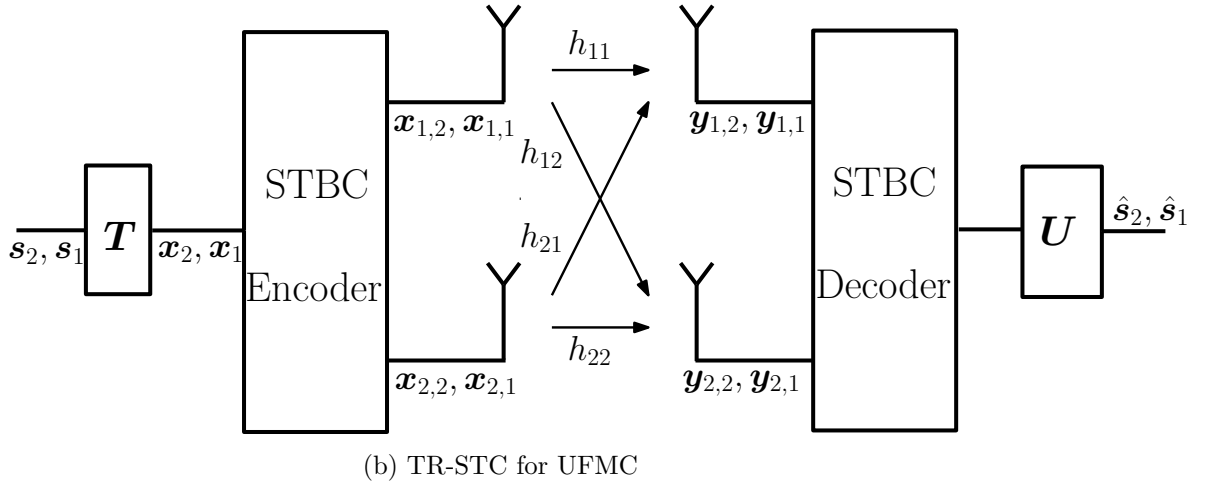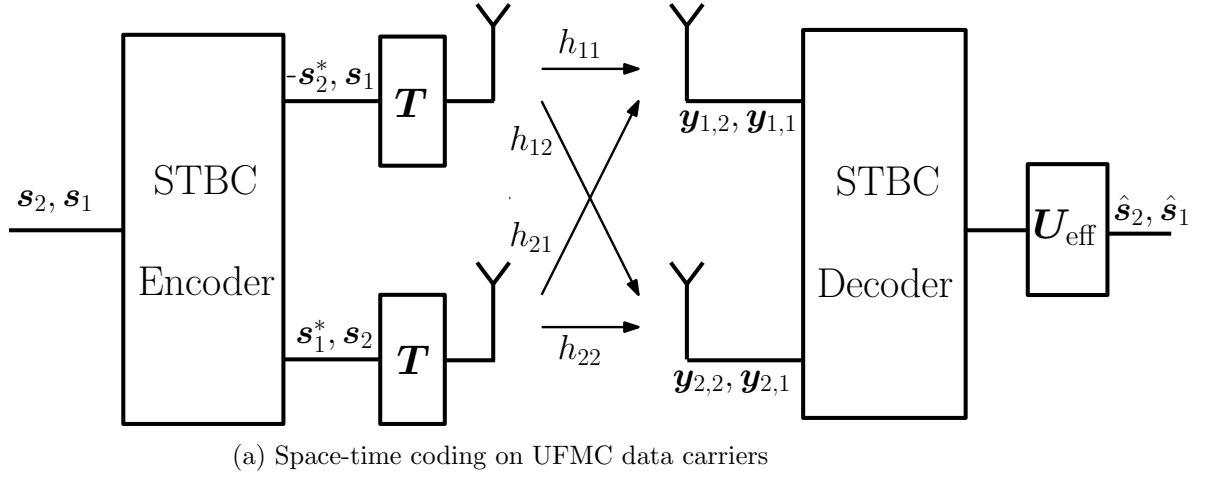
Figure 4.3.: Two approaches for Alamouti's STBCs for UFMC waveforms

4.3.1.1. Approach 1: Space-time encoder in the frequency domain

Here we investigate space-time block coding for UFMC where coding is applied in the frequency domain on data carriers. Fig. 4.3a shows the simplified block diagram for the Alamouti STBC for a UFMC system using this approach. The data signals $s_1 \in \mathbb{C}^{K \times 1}$ and $s_2 \in \mathbb{C}^{K \times 1}$ for two transmit antennas are processed by the space-time encoder to produce data symbols for two successive time frames as shown in Table 4.1. The two data vectors at the output of the space-time encoder are independently modulated

	Antenna 1	Antenna 2
Time frame 1	$\boldsymbol{d}_{1,1} = \boldsymbol{s}_1$	$\boldsymbol{d}_{1,2} = \boldsymbol{s}_2$
Time frame 2	$\boldsymbol{d}_{2,1} = -\boldsymbol{s}_2^*$	$\boldsymbol{d}_{2,2} = \boldsymbol{s}_1^*$

Table 4.1.: STBC in the frequency domain

by the UFMC modulator matrix $\boldsymbol{T}$ according to Eq. (4.2) and then transmitted by the two antennas.

The received signal at the jth receive antenna during the tth time frame is given by

$$\boldsymbol{y}_{t,j} = \sum_{i=1}^{M_T} \boldsymbol{H}_{j,i} \boldsymbol{T} \boldsymbol{d}_{t,i} + \tilde{\boldsymbol{v}} \in \mathbb{C}^{(N_{\text{ufmc}}+N_{\text{ch}}-1)\times 1}, \tag{4.15}$$

where $\boldsymbol{H}_{j,i} \in \mathbb{C}^{(N_{\text{ufmc}}+N_{\text{ch}}-1)\times N_{\text{ufmc}}}$ is the channel convolution matrix (as shown in Appendix B) between the jth receive antenna and the ith transmit antenna. The receiver architecture for this approach can be characterized by the type of receiver filter that are discussed in the following.

Receive filters other than FFT   First we discuss the STBC receiver architecture for the receive filters, as shown in Fig. 4.3a. Note that this architecture is not applicable to FFT based receivers that are discussed after this paragraph. After taking the conjugate of the received signal in the second time frame, the combined signal for the two time frames can be written as

$$\begin{bmatrix} \boldsymbol{y}_{1,1} \\ \vdots \\ \boldsymbol{y}_{1,M_R} \\ \boldsymbol{y}_{2,1}^* \\ \vdots \\ \boldsymbol{y}_{2,M_R}^* \end{bmatrix} = \boldsymbol{H}_{\text{eff}} \boldsymbol{T}_{\text{eff}} \begin{bmatrix} \boldsymbol{s}_1 \\ \boldsymbol{s}_2 \end{bmatrix} + \begin{bmatrix} \boldsymbol{v}_{1,1} \\ \vdots \\ \boldsymbol{v}_{1,M_R} \\ \boldsymbol{v}_{2,1}^* \\ \vdots \\ \boldsymbol{v}_{2,M_R}^* \end{bmatrix}, \tag{4.16}$$

where

$$\boldsymbol{H}_{\text{eff}} = \begin{bmatrix} \boldsymbol{H}_{1,1} & \boldsymbol{H}_{1,2} & \boldsymbol{0} & \boldsymbol{0} \\ \vdots & \vdots & \vdots & \vdots \\ \boldsymbol{H}_{M_R,1} & \boldsymbol{H}_{M_R,2} & \boldsymbol{0} & \boldsymbol{0} \\ \boldsymbol{0} & \boldsymbol{0} & \boldsymbol{H}_{1,2}^* & -\boldsymbol{H}_{1,1}^* \\ \vdots & \vdots & \vdots & \vdots \\ \boldsymbol{0} & \boldsymbol{0} & \boldsymbol{H}_{M_R,1}^* & -\boldsymbol{H}_{M_R,2}^* \end{bmatrix} \in \mathbb{C}^{2M_R(N_{\text{ufmc}}+N_{\text{ch}}-1)\times 4N_{\text{ufmc}}}$$

and

$$\boldsymbol{T}_{\text{eff}} = \begin{bmatrix} \boldsymbol{I}_{M_T} \otimes \boldsymbol{T} \\ \boldsymbol{I}_{M_T} \otimes \boldsymbol{T}^* \end{bmatrix} \in \mathbb{C}^{4N_{\text{ufmc}}\times 2K} \tag{4.17}$$

are the equivalent channel matrix and the modulation matrix, respectively, to be processed at the receiver for achieving diversity. This approach results in receivers with a very high computationally complexity. In the first step, the DFT and the IDFT have to be applied to perform frequency domain equalization at the receiver. Since the effective channel is non-orthogonal, linear equalization schemes such as ZF or MMSE may be applied. In the second step, the equalized symbols are multiplied by a demodulator matrix which utilizes the effcetive modulation matrix in Eq. (4.17) in the demodulation process.

FFT based receiver   Unlike the other multicarrier modulation schemes such as FBMC and GFDM, an FFT based receiver can be employed for UFMC as in the OFDM case, but with slightly higher

complexity. This offers a simple solution for frequency domain equalization and channel estimation. A $2N$ point FFT is applied on the received signal after zero padding and then it is downsampled by a factor 2, as shown in Fig. 4.4, where each second frequency value corresponds to a subcarrier main lobe. Similar to CP-OFDM, single-tap per-subcarrier frequency domain equalizers can be used which equalize the joint impact of the radio channel and the respective subband filter. This offers a straightforward implementation of the STBC decoder in the frequency domain. We can employ maximum ratio combining (MRC) based detection as in CP-OFDM that has a low complexity. The additional complexity of this approach lies only in applying the FFT that has twice the size as in CP-OFDM.
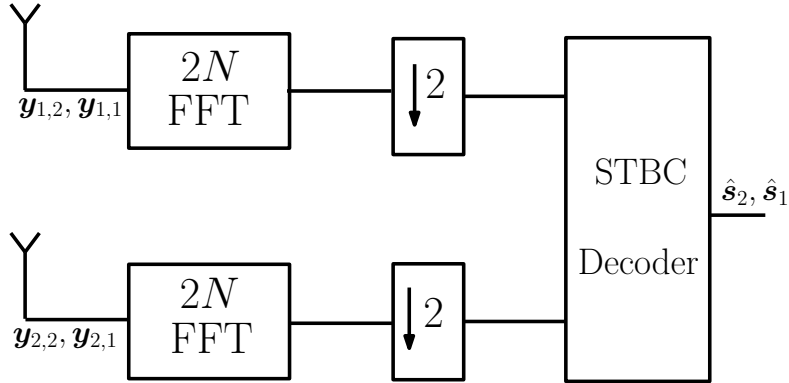
Figure 4.4.: An FFT based receiver for UFMC for $M_R = 2$

4.3.1.2. Approach 2: Space-time encoder in the time domain

Since approach 1 results in receivers with a very high computationally complexity for all filtering methods except for FFT based filtering, in approach 2, we propose to apply TR-STC on blocks of UFMC time domain samples as shown in Fig. 4.3b. The data symbols are first modulated using the UFMC modulator matrix $\boldsymbol{T}$ according to Eq. (4.2). Then the time domain output signals $\boldsymbol{x}_1$ and $\boldsymbol{x}_2$ are processed by the space-time encoder according to Table 4.2 for $n = 0, 1, ..., N_l - 1$, where N_l is the length of UFMC

	Antenna 1	Antenna 2
Time frame 1	$x_{1,1}[n] = x_1[n]$	$x_{2,1}[n] = x_2[n]$
Time frame 2	$x_{1,2}[n] = -x_2^*[(-n)_{N_l}]$	$x_{2,2}[n] = x_1^*[(-n)_{N_l}]$

Table 4.2.: TR-STC for UFMC

modulated signal vectors $\boldsymbol{x}_1$ or $\boldsymbol{x}_2$. At the receiver side, the signals at the jth receiving antenna for the two time frames are

$$\begin{aligned} \boldsymbol{y}_{1,j} &= \boldsymbol{H}_{j,1}\boldsymbol{x}_{1,1} + \boldsymbol{H}_{j,2}\boldsymbol{x}_{1,2} + \boldsymbol{v}_{j,1} \\ \boldsymbol{y}_{2,j} &= \boldsymbol{H}_{j,1}\boldsymbol{x}_{2,1} + \boldsymbol{H}_{j,2}\boldsymbol{x}_{2,2} + \boldsymbol{v}_{j,2}, \end{aligned}$$

(4.18)

where $\boldsymbol{H}_{j,i} \in \mathbb{C}^{(N_{\text{ufmc}}+N_{\text{ch}}-1) \times N_{\text{ufmc}}}$ is the channel convolution matrix (as shown in Appendix B) between the ith transmit antenna and the jth receive antenna and $\boldsymbol{v}_{j,1}$ and $\boldsymbol{v}_{j,2}$ are the noise vectors for the

two time frames. Both received signals are transformed into the frequency domain by applying the DFT. Assuming that the channel remains constant for two time slots, we can rewrite Eq. (4.18) in the frequency domain as

$$
\begin{bmatrix} \hat{\boldsymbol{z}}_1 \\ \hat{\boldsymbol{z}}_2 \\ \vdots \\ \hat{\boldsymbol{z}}_{N_{\mathrm{ufmc}}} \end{bmatrix} = \tilde{\boldsymbol{H}}_{\mathrm{eff}} \begin{bmatrix} \tilde{\boldsymbol{x}}_1 \\ \tilde{\boldsymbol{x}}_2 \end{bmatrix} + \begin{bmatrix} \hat{\boldsymbol{v}}_1 \\ \hat{\boldsymbol{v}}_2 \\ \vdots \\ \hat{\boldsymbol{v}}_{N_{\mathrm{ufmc}}} \end{bmatrix}, \tag{4.19}
$$

where $\hat{\boldsymbol{z}}_l = [\tilde{y}_{1,1,l} \cdots \tilde{y}_{1,M_R,l} \; \tilde{y}_{2,1,l}^* \cdots \hat{y}_{2,M_R,l}^*]^T$ is the equivalent received signal for two time frames, $\hat{\boldsymbol{v}}_l = [\tilde{v}_{1,1,l} \cdots \tilde{v}_{1,M_R,l} \; \tilde{v}_{2,1,l}^* \cdots \tilde{v}_{2,M_R,l}^*]^T$ is the equivalent noise vectors for the two time frames, and $\tilde{\boldsymbol{H}}_{\mathrm{eff}} = \mathrm{blkdiag}[\tilde{\boldsymbol{H}}_1, \cdots, \tilde{\boldsymbol{H}}_l] \in \mathbb{C}^{2 \cdot M_R \cdot N_{\mathrm{ufmc}} \times M_T \cdot N_{\mathrm{ufmc}}} \; \forall \, l = 1, \ldots, N_{\mathrm{ufmc}}$ is a block diagonal matrix with the N_{ufmc} subcarrier-wise combined channel transfer functions on its main diagonal. Here $\tilde{y}_{t,j,l}$ and $\tilde{v}_{t,j,l}$ denote the lth component in the frequency domain of the vectors defined in Eq. (4.18). The combined frequency response at the lth subcarrier is given as

$$
\tilde{\boldsymbol{H}}_l = \begin{bmatrix} h_{1,1,l} & h_{1,2,l} \\ \vdots & \vdots \\ h_{M_R,1,l} & h_{M_R,2,l} \\ h_{1,2,l}^* & -h_{1,1,l}^* \\ \vdots & \vdots \\ h_{M_R,2,l}^* & -h_{M_R,1,l}^* \end{bmatrix} \quad \forall \, l = 1, \ldots, N_{\mathrm{ufmc}} \tag{4.20}
$$

Since the effective channel on each subcarrier is orthogonal, we can employ maximum ratio combining. The equalized symbols are converted back to the time domain by applying the IDFT. Then in the second step an appropriate demodulation scheme is applied. Note that the demodulator matrix is based on the actual UFMC modulator matrix $\boldsymbol{T}$ in Eq. (4.2).

4.3.2. Space Time Block Coding for GFDM

We can also use space-time coding on data carriers or on time domain samples for GFDM. However, when STBCs are applied directly to the data symbols, the linear GFDM demodulator can not decouple the subcarriers and subsymbols because of the multipath propagation channel. Hence, it leads to a severe performance loss. Because of this reason, in [MMG$^+$15], TR-STC has been recommended for GFDM when space-time coding is utilized for blocks of GFDM samples. We have used the same approach in this work to evaluate the performance of GFDM.

4.3.3. Space Time Block Coding for FBMC

Space-time coding can also be applied in conjunction with FBMC for 2×2 MIMO systems using a block Alamouti scheme as presented in [RIS10]. Due to the fact that FBMC has an OQAM signal structure it is impossible to apply the Alamouti scheme for symbol-wise coding. Therefore the Alamouti scheme is

utilized for a whole block of symbols instead of just one. We have used the approach presented in [RIS10] in order to evaluate the performance of FBMC.

4.4. Simulation Results

For the simulations, a 2×2 LTE MIMO system with a bandwidth of 3 MHz is considered. The 3GPP channel models extended pedestrian-A (EPA) and extended vehicular A (EVA) are used. The simulation parameters for the three waveforms are defined in Table 4.3. It was assumed that all the resources are allocated to a single user. The performance of these schemes is compared in terms of the BER. Moreover, it is assumed that perfect synchronization and perfect channel state information are available at the receiver. Furthermore, the roll-off factors for the pulse-shaping filter used in these waveforms are indicated by α. Note that we have used the parameters in Table 3.3 for UW-OFDM using EPA and EVA channel models.

The BER performance of the two STBCs approaches for UFMC, described in Section 4.3, over the 3GPP EVA channel is shown in Fig. 4.5a. The results show that both approaches have a similar performance but the computational complexity of approach 1 is much higher than approach 2. Moreover, a modified UFMC demodulator is needed if the STBCs are used on the data subcarriers (approach 1). We also compare the performance of different UFMC receiver concepts for two modulation orders over the EVA channel in Fig. 4.5b. The results show that when we use a lower modulation order, i.e., QPSK, UFMC with a MF demodulator performs nearly the same as the ZF receiver or an FFT based receiver. However, the performance of the UFMC MF receiver decreases when the higher modulation order of 16 QAM is employed. Although, the FFT based receiver has a slightly worse performance than the ZF based receiver, an FFT based receiver is the simplest option to apply STBCs in the frequency domain due to its lower computational complexity. However, approach 2 is a better solution when we employ a MF, a ZF, or an MMSE based UFMC demodulator.

The performance comparison of the space-time block coded UFMC, GFDM, FBMC, UW-OFDM and CP-OFDM system is shown in Fig. 4.6, for MF and ZF based receivers. The results are presented for two different modulation orders, QPSK and 16 QAM, over the 3GPP EPA and EVA channel, as shown in Fig. 4.6a and Fig. 4.6b, respectively. We have shown the results for UFMC using a FFT based receiver using approach 1 and also for ZF receiver using approach 2. The UW-OFDM outperforms all of the schemes especially for a highly frequency selective channel (EVA). This is due to the fact that UW-OFDM achieves the maximum diversity even when no precoding is utilized at the transmitter [Ste13a]. To obtain this diversity, the $\boldsymbol{G}$ matrix needs to have full column rank. This condition is already fulfilled in our design.

Parameters	CP-OFDM	UFMC	GFDM	FBMC
Modulation Order	QPSK or 16 QAM			OQPSK or 16 OQAM
LTE Bandwidth	3 MHz			
No. of transmit antennas	2			
No.of receive antennas	2			
Channel model	EPA and EVA			
Sampling frequency	3.84 MHz			
Subcarrier spacing	15 kHz	15 kHz	240 kHz	15 kHz
No. of subcarriers	180	180	16	64
No. of subsymbols (M)			15	
No. of subcarriers in a sub-band		12		
IFFT length N	256	256		
CP duration	18 samples	18 samples (filter length -1)	16 samples	
Pulse shaping	Rectangular	Dolph-Chebyshev $\alpha_{SLB} = 60$	Root raised cosine $\alpha = 0.5$	Root raised cosine $\alpha = 1$

Table 4.3.: Simulation parameters.

Surprisingly, the GFDM waveform performs the worst. This is in contrast to our previous results in [CNA$^+$16] where we have shown that it performs better than UFMC and CP-OFDM. The symbols in GFDM are efficiently spread over time and frequency and the CP is utilized in a better way (over a data block, instead of just one symbol). Therefore, it is expected that this should results in a better BER performance as shown in various publications [MMG$^+$14, MMF14, MMG$^+$15]. But, we have noticed in our simulations that the time-frequency spread of GFDM symbols (number of subcarriers and number of subsymbols) should be carefully chosen for this improved performance. When the difference between the number of subcarriers and the number of subsymbols is not that much (as in our case, where $K = 16$ and $M = 15$), the performance of GFDM is significantly reduced. However, to have a fair comparison with other schemes, we have chosen the simulation parameters based on the LTE standard for a 3 MHz bandwidth. Specifically, for GFDM, we have used the parameters that fit in the LTE grid as discussed in [GMM$^+$14]. Moreover, for GFDM, an increase in the value of the pulse shaping filter's roll-off factor (α) results in a worse performance. We have, however, shown the results for the case of a $\alpha = 0.5$, because in a practical system setup α should be chosen small to neglect the noise enhancement factor [MMG$^+$14]. The results show that the GFDM with a MF receiver results in the worst performance because it cannot resolve the ISI. Therefore, a ZF or MMSE receiver or some interference cancellation scheme has to be employed.

The BER performance of UFMC using a FFT based receiver is approximately same as of CP-OFDM. However, when a ZF based receiver is employed, it performs slightly better than CP-OFDM. For FBMC, we have applied the block Alamouti scheme as described in [RIS10], where the performance of FBMC was shown for different channel models using only OQPSK modulation. However, in this work we have compared this performance with other schemes also for 16 OQAM. The results show that the proposed block wise Alamouti works for OQPSK, but its performance severely degrades for higher modulation orders. Moreover, even for OQPSK its performance is worst than all other schemes due to the presence of self inter-symbol interference. Therefore, some interference cancellation technique has to be employed additionally, for instance, [ZL13].
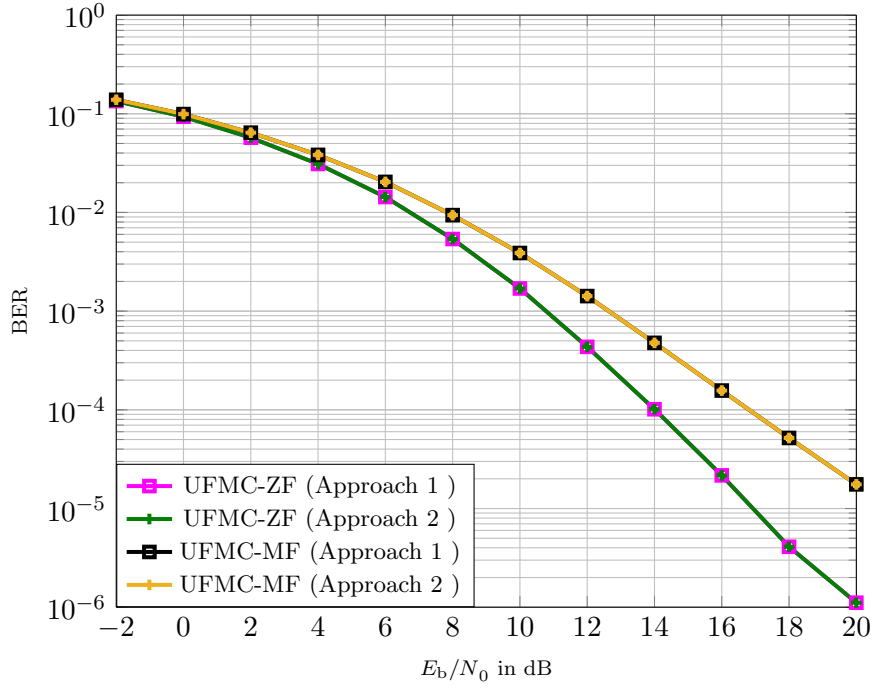
(a) BER performance for different approaches using 16-QAM and EVA channel model. Both approaches yield a similar performance.
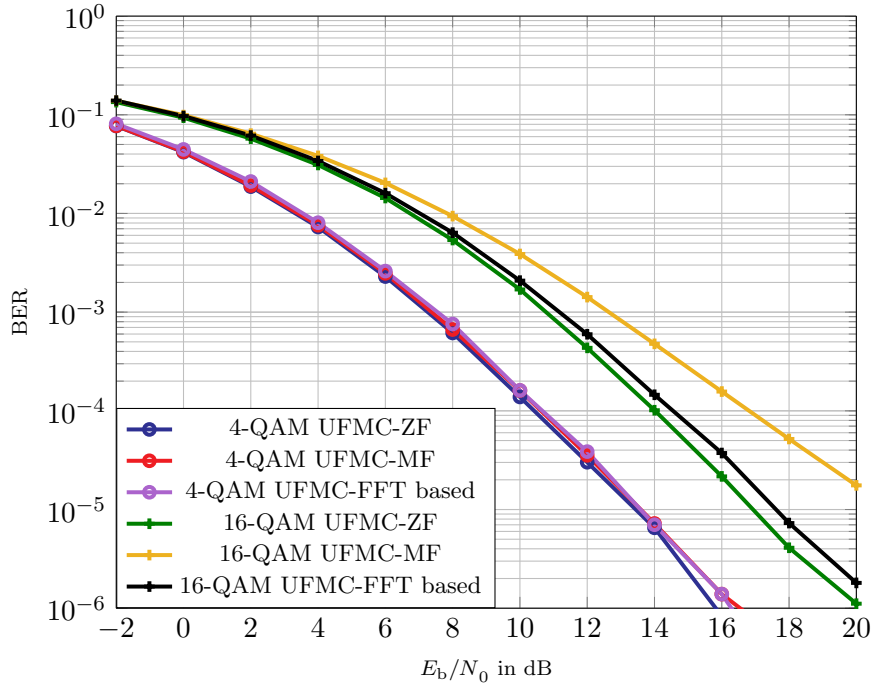
(b) BER performance for different receiver concepts over EVA channel model. The performance of UFMC with MF at the receiver degrades with higher modulation orders.

Figure 4.5.: BER performance of UFMC for different receive filtering techniques.
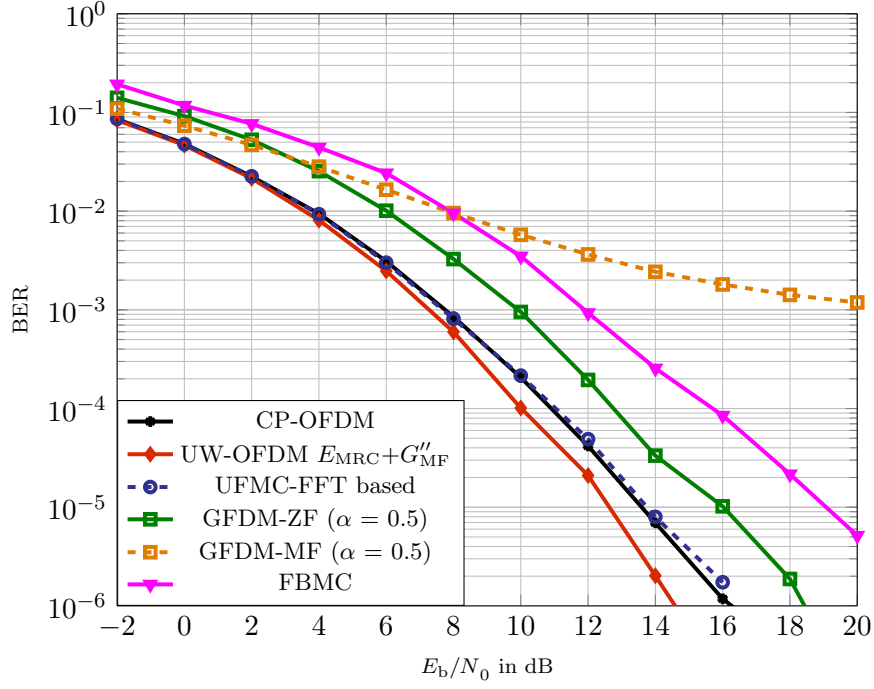
(a) BER performance for QPSK over EPA channel model
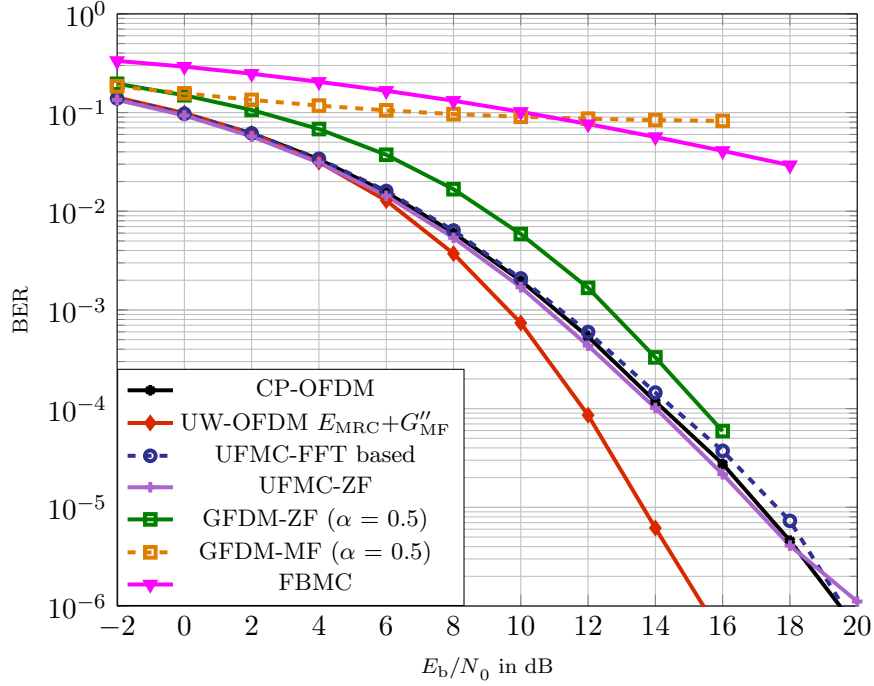
(b) BER performance for 16 QAM over EVA channel model

Figure 4.6.: BER performance for different 5G proposed transmission schemes. Space-time block coded UW-OFDM systems outperform all other schemes and also result in receivers with a lower computational complexity.

Waveforms	STBCs Approaches	References	Recommended Receivers	Complexity
CP-OFDM	SFBC	[BP00]	MRC detection	very low complexity
UW-OFDM	STBCs in the freq domain	Proposed (Chapter 3)	ZF/MMSE detection + MMSE demodulation	very high complexity
	TR-STC		MRC detection + MF demodulation	low complexity
GFDM	TR-STC	[MMG⁺15]	MRC detection + ZF/MMSE demodulation	moderate complexity
UFMC	STBCs in the freq domain	Proposed (Chapter 4)	FFT based receiver (2N FFT , MRC detection)	low/moderate complexity
	TR-STC		MRC detection + ZF/MMSE demodulation	moderate complexity
FBMC	Block Alamouti code	[RIS10], [ZL13]	Iterative interference cancellation techniques	very high complexity

Table 4.4.: Summary of space-time block coded 5G waveforms. The performance comparison of these waveforms is shown in Fig. 4.6.

4.5. Conclusion

In this chapter, we have developed different space-time coding concepts for UFMC waveforms. We can either use the STBCs on the data carriers in the frequency domain or on the time domain samples (TR-STC). The results show that both approaches yield similar results, but approach 1 has a much higher complexity for MF and ZF based receivers. If STBCs are used on the data carriers, an FFT based receiver is a feasible solution. But we have also shown that if a MF or ZF based receiver is utilized, TR-STC is recommended for UFMC, since it has a lower complexity. We have also compared the performance of different air interface techniques with STBCs. The results show that UW-OFDM has the best performance especially over highly frequency selective channels. This is due to the fact that UW-OFDM achieves the maximum diversity when the code generator matrix has full column rank, which is true for our case. Note that this better performance for space-time block coded UW-OFDM systems is achieved with a much lower computation complexity as compared to other 5G air interface proposals, since an MRC based detection along with a MF based receiver is employed. Moreover, UFMC has the same performance as CP-OFDM while MF based receivers for GFDM and FBMC exhibit a very bad performance. The performance of FBMC can be improved by using interference cancellation techniques as suggested in [ZL13]. STBCs approaches for these waveforms are summarized in Table 4.4 with the recommended receiver architectures.

Part II.

Transmission Strategies for Optical Systems with Intensity Modulation and Direct Detection

Part II of this thesis is devoted to the investigation of the transmission strategies for optical systems that employ intensity modulation and direct detection (IM/DD). The most popular examples for such optical systems are plastic optical fibers (POFs), multimode fibers and wireless optical transmission such as visible light communication (VLC) that employ a LED as a source. Both POFs and VLC suffer from electrical bandwidth limitation which occurs due to the source or due to the multipath propagation channel. This bandwidth limitation leads to severe inter-symbol interference (ISI) especially at higher data rates or transmission distances. Therefore, efficient transmission schemes along with robust equalization techniques are needed to achieve high data rates in these systems.

CP-OFDM and its real-valued version discrete multitone transmission (DMT) are popular schemes to compensate dispersion in direct detection optical systems. Since optical systems with IM/DD demand for real-valued and positive signals, a Hermitian symmetry is applied, thus reducing the bandwidth efficiency of the DMT schemes. Moreover, DMT schemes have a much higher peak-to-average power ratio (PAPR). An alternative approach for these optical systems is PAM block transmission with frequency domain equalization (PAM-FDE). The results indicate that PAM-FDE has not only a better performance but also lower PAPR. We start this part of the thesis by first discussing these transmission schemes in Chapter 5. We compared the performance of these transmission schemes for VLC and POF systems. Major parts of this chapter have been published in one book chapter [WCH16a] and in one conference paper [WCKL15]. In Chapter 6, the investigations are extended by considering non-linear precoding and equalization techniques for PAM transmission. These non-linear schemes achieve a much better performance for these optical systems but increase the overall complexity of the system. Therefore, an alternate hybrid scheme is proposed which has a relatively low complexity, but achieves the same performance as decision feedback equalization and Tomlinson-Harashima precoding. Parts of this chapter have already been published in a conference paper [CWTH15].

Chapter 7 presents three novel DMT schemes for optical systems with IM/DD. These schemes are derived from the UW-OFDM signaling concepts. In UW-OFDM, first redundancy is added to the data symbols with the help of a code generator matrix. Then the IDFT is applied to the coded symbols. This operation effectively maps the data symbols to different frequency bands of the resulting time domain signal. However, this procedure produces complex-valued bipolar time domain samples, while intensity modulation requires real non-negative signals. Therefore, the UW-OFDM signal has to be modified before it becomes suitable for an IM/DD system. A real signal can be obtained by imposing Hermitian symmetry in the information block on which an IDFT operation is applied during the signal generation procedure. This requires a new design of code generator matrices. Therefore, we derive new code generator matrices such that we obtain real-valued signals at the output of the IDFT. We also compare the performance of the proposed schemes with the conventional CP-DMT schemes. Major parts of this chapter have been published in one journal paper [CBWH17] and the remaining results are submitted in the form of a letter [CWHH17].

5. PAM Block Transmission with Frequency Domain Equalization

CP-OFDM and its real-valued version DMT are popular schemes to compensate dispersion in direct detection optical systems. In practice, a CP-OFDM signal is realized in a digital signal processor by taking an IDFT of a block of data symbols. This enables simple cost-effective equalization with single-tap equalizers in the frequency domain at the receiver. PAM or single subcarrier (SSC) modulation combined with block transmission and frequency domain equalization has been recognized as a possible alternative to the DMT schemes. Here, the IDFT is moved from the transmitter to the receiver, since the modulation takes place directly in the time domain. In this chapter, we investigate the suitability of PAM or SSC modulation combined with FDE for optical systems employing IM/DD. After the introduction, we present the system model in Section 5.2 where we also describe channel models for POF and VLC systems. We discuss the transmission schemes in Section 5.3. We compare the performance of these schemes for both VLC and POF systems in Section 5.4. The chapter is summarized in Section 5.5.

5.1. Introduction

Plastic optical fiber (POF) and visible light communication (VLC) employ light emitting diodes (LEDs) as a source. These optical systems get a lot of attention due to their applicability in a vast range of application scenarios. For example, large core step-index plastic optical fibers (SI-POFs) with a typical diameter of 1 mm are a low-cost solution for short-distance transmission in digital car networks, industrial networks, and home networks. Recently VLC has also received a lot of attention due to its advantages and its applicability in a vast range of scenarios such as indoor wireless communication, underwater communication, and car-to-car communication. Specifically, high data rates can be achieved for indoor wireless communications without any spectrum congestion problem. In such systems we have a limited temporal and spatial coherence of the source (LED) and of the received signal, making a field modulation impossible. This means that a quadrature modulation cannot take place at the optical level but only at the electrical level by modulating one or multiple electrical subcarriers. The only solution is to employ intensity modulation (IM) with direct detection (DD). Therefore, we need a real-valued positive signal.

In this work, we investigate the suitable transmission schemes for these optical systems. For radio frequency (RF) transmission, CP-OFDM is a widespread solution. The success of CP-OFDM is closely related to the fact that the signal processing is based on the FFT (fast Fourier transform) operation, where this advantage is achieved due to the periodic insertion of a cyclic prefix (CP). However, due to the problems associated with CP-OFDM such as a high peak-to-average power ratio, the concept of single carrier block transmission with frequency domain equalization (FDE) [FA$^+$02] has been recognized as a powerful alternative in RF communications. It basically uses the same "trick" as CP-OFDM. In this scheme, the linear convolution of the signal with the channel impulse response appears as a cyclic convolution within the correlation interval of the receiver, since a CP is inserted periodically between

blocks of data symbols. This opens the door for very efficient signal processing based on the FFT. The relation between the input signal and the output signal is determined by a pointwise multiplication of the DFT (discrete Fourier transform) input spectrum with the DFT of the channel impulse response. In contrast to CP-OFDM, where the data information is expressed and analyzed in the frequency domain, the modulation and demodulation for single carrier block transmission takes place in the time domain. Thus, single carrier block transmission systems do not require an inverse FFT (IFFT) at the transmitter, but an additional IFFT at the receiver, before the equalization step. The equalization step itself is basically the same as in CP-OFDM, where the FFT/IFFT usage ensures that fewer multiplications are required as compared to linear/non-linear time domain equalizers. Moreover, the major advantage of the single carrier approach is the reduced peak-to-average power ratio, which significantly decreases the power consumption of the amplifier at the transmitter. It also relaxes the resolution of the analog to digital converter (ADC) at the receiver.

Optical systems with IM/DD demand for real-valued (i.e., one dimensional) and non-negative signals. Therefore, the conventional CP-OFDM cannot be directly applied to these systems and a Hermitian symmetry is imposed to obtain a real-valued IDFT output signal [AS08, GL10, CCC14]. This real-valued version of the CP-OFDM is also referred as discrete multitone transmission (DMT) which clearly distinguishes such multiple subcarrier schemes from coherent OFDM approaches with a complex-valued IDFT output signal that is used for a two-dimensional field modulation of an optical carrier. Clearly, the necessity of a real-valued IDFT output reduces the bandwidth efficiency compared to CP-OFDM approaches with field modulation by a factor of two. Moreover, while a DMT signal suffers from a large peak-to-average power ratio, which demands for a correspondingly large dynamic range of the LED driver, PAM transmission based on rectangular pulses exhibits only a certain number of discrete amplitude levels equal to the modulation order, and the optical peak-to-average power ratio is as low as 3 dB, if the non-return-to-zero (NRZ) format is used. This provides another reason to compare FDE and DMT under the IM/DD constraint.

Due to the limited coherence of the optical carrier, QAM can either be applied on multiple electrical subcarriers (DMT) or on single subcarrier (SSC) [CK96, ABNW11]. We also investigate various SSC schemes for these optical systems. Specifically, we investigate whether block transmission with FDE may also benefit from single subcarrier (SSC) modulation. As we focus on optical transmission with IM, we avoid the term single carrier transmission in the following, since single carrier inherently suggests the availability of a sinusoidal optical carrier and it also suggests that we observe the optical spectrum but instead we focus on the spectrum of the modulating signal, where this signal is real-valued and positive. Regarding the FDE, we refer to the transmission schemes simply as PAM block transmission or, if a single electrical subcarrier is QAM-modulated, then as SSC-QAM with FDE.

In the following we summarize the main contributions of this chapter. So far, there have been minimal investigations in the literature regarding PAM block transmission with FDE as a suitable waveform for optical systems with IM/DD. We contribute in this regard by evaluating the performance of PAM block transmission for POFs and VLC systems from various aspects. Specifically, we use return-to-zero (RZ) and non-return-to-zero (NRZ) filtering methods and employ symbol-spaced and fractionally-spaced receivers. Moreover, we propose line coding methods that can be used with PAM block transmission. In addition, we present novel SSC transmission schemes, i.e., orthogonal PAM (OPAM) schemes. We

also show that SSC schemes can be combined with block transmission and FDE. We contribute to DMT schemes by proposing bit-loading methods. A comprehensive performance comparison of these schemes is also not available in the literature especially for VLC systems. Therefore, in the last section, we compare the performance of these schemes with and without the knowledge of channel state information at the transmitter.

5.2. System Model

We assume a linear time invariant systems where the optical channel for wired or wireless systems is modeled at the level of the instantaneous optical power as shown in Fig. 5.1. We denote the instantaneous optical powers at the LED output and the photodiode input by $p(t)$ and $p_{rx}(t)$, where $p_{rx}(t)$ is given as

$$p_{rx}(t) = p(t) * h_{ch}(t). \tag{5.1}$$

The term $h_{ch}(t)$ denotes the channel impulse response and $*$ is the convolution operator. The corresponding average optical powers at the transmitter and receiver for symbol interval T_i are given as

$$P = \lim_{T_i \to \infty} \frac{1}{T_i} \int_{T_i} p(t) \mathrm{d}t \quad \text{and} \quad P_{rx} = \lim_{T_i \to \infty} \frac{1}{T_i} \int_{T_i} p_{rx}(t) \mathrm{d}t, \tag{5.2}$$

where P_{rx} can be also expressed as

$$P_{rx} = P \cdot H_{ch}(0) \quad \text{where} \quad H_{ch}(f) = \int_{-\infty}^{\infty} h_{ch}(t) \exp[-j2\pi ft] \mathrm{d}t. \tag{5.3}$$

The term $H_{ch}(f)$ corresponds to channel transfer function. The photodiode converts the received optical
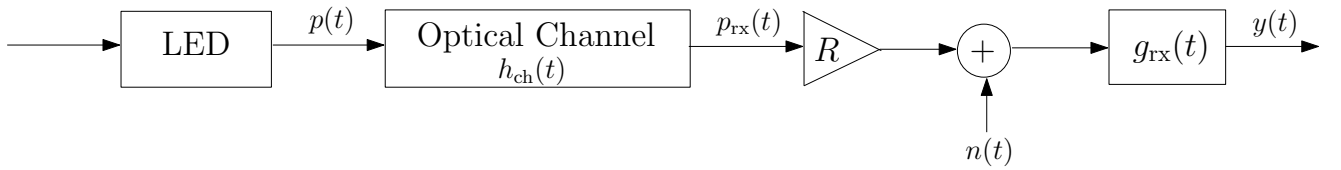
Figure 5.1.: Block diagram of the system model.

power $p_{rx}(t)$ linearly into a current $R \cdot p_{rx}(t)$, where R denotes the photodiode responsivity. Moreover, it is assumed that the current $R \cdot p_{rx}(t)$ at the diode output is superimposed by a signal independent additive white Gaussian noise (AWGN) current $n(t)$ with the two-sided power spectral density $N_0/2$.

5.2.1. Performance Criteria

The performance of the proposed schemes is evaluated in terms of an optical power penalty which is defined as

$$\kappa_{loss} = 10 \cdot \log_{10}(P/P_{ref}) \text{ dB}, \tag{5.4}$$

where P defines the required average optical power of the investigated transmission scheme and P_{ref} is the required reference power of NRZ-OOK (non-return-to-zero on-off keying). This reference power is measured in a flat additive white Gaussian noise (AWGN) channel and is given as

$$P_{\text{ref}} = P_{\text{OOK}} = \frac{\sqrt{N_0 R_{\text{b}}}}{R} \text{erfc}^{-1}(2p_{\text{b}}), \tag{5.5}$$

where $\text{erfc}(\cdot)$ denotes the complementary error function [Hay01], N_0 is the power spectral density (single-sided) of the signal independent additive white noise current (in A^2/Hz) at the photodiode output, R is the photodiode responsivity (in A/W), R_{b} is the bit rate, and p_{b} is the bit error ratio. The bit error ratio of any binary transmission scheme in a flat AWGN channel can be expressed as [Hay01]

$$p_{\text{b}} = \frac{1}{2} \cdot \text{erfc}\left(\frac{d_{\text{E}}/2}{\sqrt{N_0}}\right), \tag{5.6}$$

where d_{E} is the Euclidean distance [Hay01] between the OOK signal vectors measured at the photodiode output. For a unit energy rectangular basis function of duration T_{b}, d_{E} is

$$d_{\text{E}} = d_{\text{E,ref}} = 2RP/\sqrt{R_{\text{b}}}. \tag{5.7}$$

Clearly, the ratio P/P_{OOK} is measured at the same values of N_0, R, R_{b}, and p_{b}.

This approach has been adopted by various authors in the literature [KB97, CK94, PB95]. We prefer this approach against a comparison of the electrical $E_{\text{b,elec}}/N_0$ because of two reasons. Firstly, there is no fixed relationship between $E_{\text{b,elec}}$ and the mean optical power that is valid for all modulation schemes. For instance, even if a NRZ- and a 50 % RZ-rectangular pulse have the same electrical E_{b} value, their average optical powers differ by a factor $\sqrt{2}$, since the instantaneous electrical power depends on the square of the instantaneous optical power. Thus, for IM/DD and a flat AWGN channel, 50 % RZ-OOK exhibits a 1.5 dB power advantage over the reference scheme, since $P_{\text{OOK}}/P = \sqrt{2}$, as shown in Fig. 5.2. Note that the optical power P_0 is related to the mean optical power P according to

$$P = P_0 \cdot \mathbb{E}\{d_k\}, \tag{5.8}$$

where d_k denotes the data symbols to be transmitted i.e., for uniploar equiprobable PAM symbols $d_k \in \{0, 1, \cdots, M-1\}$ of modulation order of M we have $\mathbb{E}\{d_k\} = (M-1)/2$.

5.2.2. Channel Models

The most important examples for optical systems employing intensity modulation and direct detection are plastic optical fiber (POF) and visible light communication (VLC) systems. We evaluate the performance of transmission schemes for both systems. In the following, we present channel models which are used for our simulations.
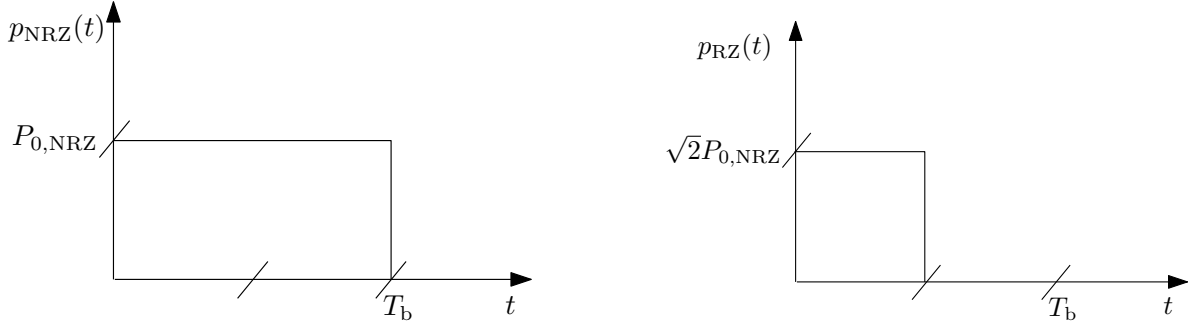
Figure 5.2.: Instantaneous power for transmitted "on" pulses for NRZ- and RZ-OOK. Both optical pulses lead to the same electrical energies, but their average optical powers differ by a factor $\sqrt{2}$.

5.2.2.1. Channel 1: POF

The presence of serious modal dispersion in the POF channel causes a low-pass frequency response. This low-pass channel frequency response is modeled as a Gaussian low-pass filter with the transfer function

$$H_{\text{POF}}(f) = e^{-\ln(\sqrt{2})\left(\frac{f}{f_{\text{3dB}}}\right)^2},$$
(5.9)

where f_{3dB} is the corresponding electrical 3 dB cut-off frequency compared to 1.5 dB in the optical domain. Eq. (5.9) is a valid model for the multipath dispersion in POFs [PHH13, WMS13]. Theoretically, the Gaussian function extends from $-\infty$ to $+\infty$, but the output pulse in the time domain cannot begin before the input pulse has started. Therefore, Eq. (5.9) is multiplied with an exponential function to make it casual and also restricted to some interval. However, for simplicity, we do not consider these facts in this work. Clearly, the 3 dB cut-off frequency differs for various lengths of POFs [PHH13]. Since the multipath dispersion increases with the fiber length, f_{3dB} decreases accordingly; for example, f_{3dB} of 130 MHz, 90 MHz, and 55 MHz are achieved for POF lengths of 15 m, 50 m, and 100 m, respectively [PHH13].

5.2.2.2. Channel 2: VLC

For VLC systems, we consider the effect of multipath propagation for indoor wireless environments. For such systems, the received optical signal experiences time dispersion due to the reflections from walls and other objects. Possibly there may be also several, spatially separated LED-lamps that transmit one and the same signal, which even leads to multiple LoS arrivals at the receiver (LoS: line-of-sight). In practice, most of the reflections are diffuse in nature and modeled as Lambertian [GB79]. Therefore, for such systems, the total channel impulse response (CIR) includes the contribution of both LoS and diffuse components. In the literature, several methods have been proposed for calculating the CIR of the diffuse part. These methods are generally based on ray-tracing models and the computational complexity of these approaches depends on the number of reflections considered. In this work, we use a recursive algorithm proposed by Barry in [BK+93]. In this method, the room surface for each reflection is decomposed into a number of reflectors and the reflected lights are summed at the receiver [LKW+14].
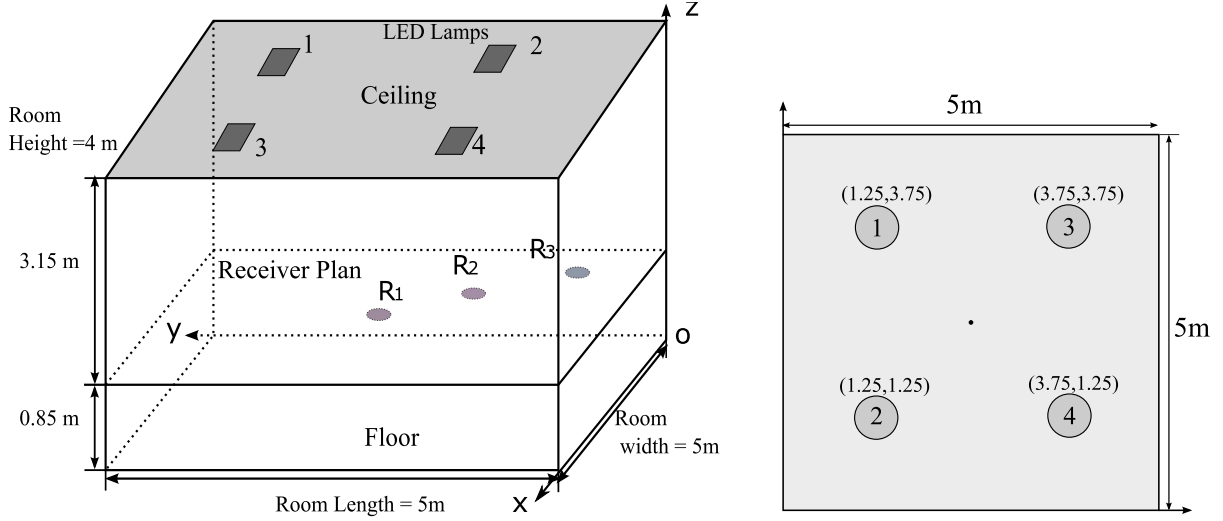
Figure 5.3.: Considered room configuration: room layout (left) and LED coordinates (right)

We consider a medium sized room of dimension $(5 \times 5 \times 4)$ m^3 as shown in Fig. 5.3. An array of (2×2) LED lamps is installed on the ceiling in a symmetrical arrangement to insure room illuminations. It is assumed that all lamps synchronously transmit the same signal, causing that several LoS components impinge at the receiver. Clearly, these LoS components could be resolved by means of an imaging receiver [KY$^+$98], and the delays could be compensated accordingly, but we do not consider this case here. We rather assume that the receiver has no angle-diversity capabilities. The receiver is positioned at the height of 0.85 m above the floor pointing vertically towards the ceiling. The receiver field of view (half angle) is set to 70° and we do not consider any receiver lens. Moreover, we show results for three alternative receiver positions R_1, R_2, and R_3: R_1 being at the center of the room with coordinates (2.5 m, 2.5 m), R_2 is nearly beneath LED 2 with coordinates (1.3 m, 1.2 m), and R_3 is at the room corner with coordinates (0.5 m, 0.5 m). The reflection coefficients of the Lambertian reflectors such as walls, floor, and the ceiling are considered to be 0.74, 0.61, and 0.38, respectively [LPB11]. We calculate the CIR with a time resolution of 0.2 ns and consider up to 8 diffuse reflections.

The transfer functions arising for three receiver positions discussed above are shown in Fig. 5.4. If

$$h_{\mathrm{MP}}(t) = h_{\mathrm{LoS}}(t) + h_{\mathrm{Diff}}(t) \tag{5.10}$$

denotes the multipath CIR decomposed into a pure LoS part and a pure diffuse part, the transfer function is given as

$$H_{\mathrm{MP}}(f) = H_{\mathrm{LoS}}(f) + H_{\mathrm{Diff}}(f). \tag{5.11}$$

The transfer functions $H_{\mathrm{MP}}(f)$ arising from both the LoS and the diffuse components are shown in Fig. 5.4a. To display the impact of $H_{\mathrm{Diff}}(f)$, Fig. 5.4b shows the functions $H_{\mathrm{LoS}}(f)$ and $H_{\mathrm{Diff}}(f)$ separately, too. It should be noted that all functions shown in Fig. 5.4 are normalized with respect to the channel gain

$$H_{\mathrm{L0}} = H_{\mathrm{LoS}}(0) = \int_0^\infty h_{\mathrm{LoS}}(t) \, \mathrm{d}t \tag{5.12}$$

of the LoS part.

(a) Transfer functions $|H_{\mathrm{MP}}(f)|$ at three Rx positions;
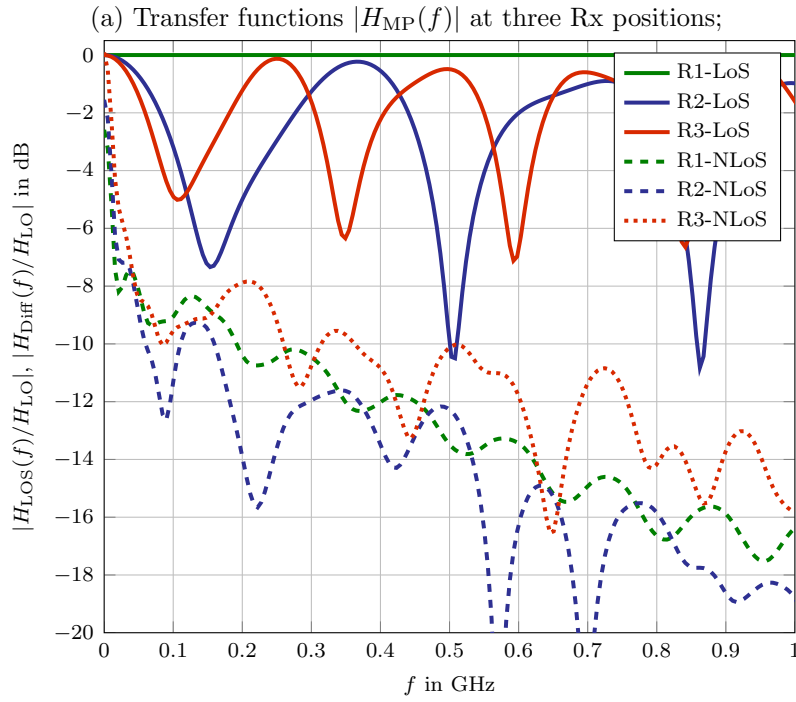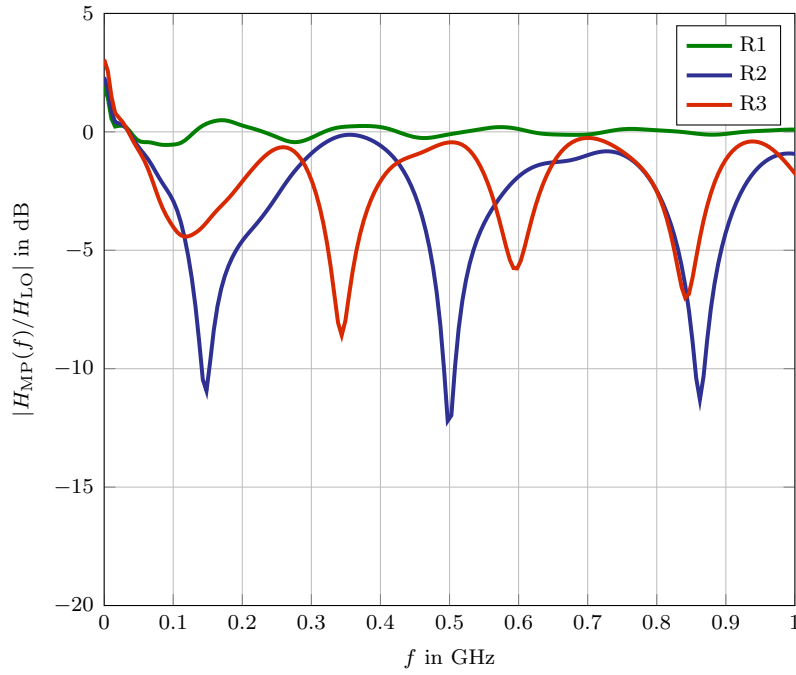
(b) Decomposed transfer functions for the LoS and diffuse parts. All transfer functions are normalized with respect to $H_{\mathrm{LoS}}(0)$

Figure 5.4.: Multipath channel transfer function

In VLC, fading with respect to the optical carrier cannot occur, since the light source is non-coherent. The CIR correspond to the small-scale averaged power delay profile known from RF. However, if an arrangement with multiple LoS arrivals is considered, fading can even take place on a subcarrier level. This makes a big difference since the frequencies, which lie within the transmission range of the LED, are

much smaller than the RF-carrier frequencies used in Wi-Fi networks. Thus, much larger path length differences are required for a destructive $\lambda/2$ interference.

As shown in Fig. 5.4a, the transmitted signal will undergo much deeper fades at receiver position R2 as compared to the other positions. The deep fade at approximately 150 MHz for the R2 position is not only caused due to a destructive interference of the 4 LoS multipath components. Fig. 5.4b shows that even the diffuse part interferes destructively at this frequency. However, since $H_{\mathrm{Diff}}(f)$ has a lowpass characteristic, its contribution to $H_{\mathrm{MP}}(f)$ disappears always in the high frequency range. In the lower frequency range, it leads to the distortions, but it also adds additional power to the received signal.
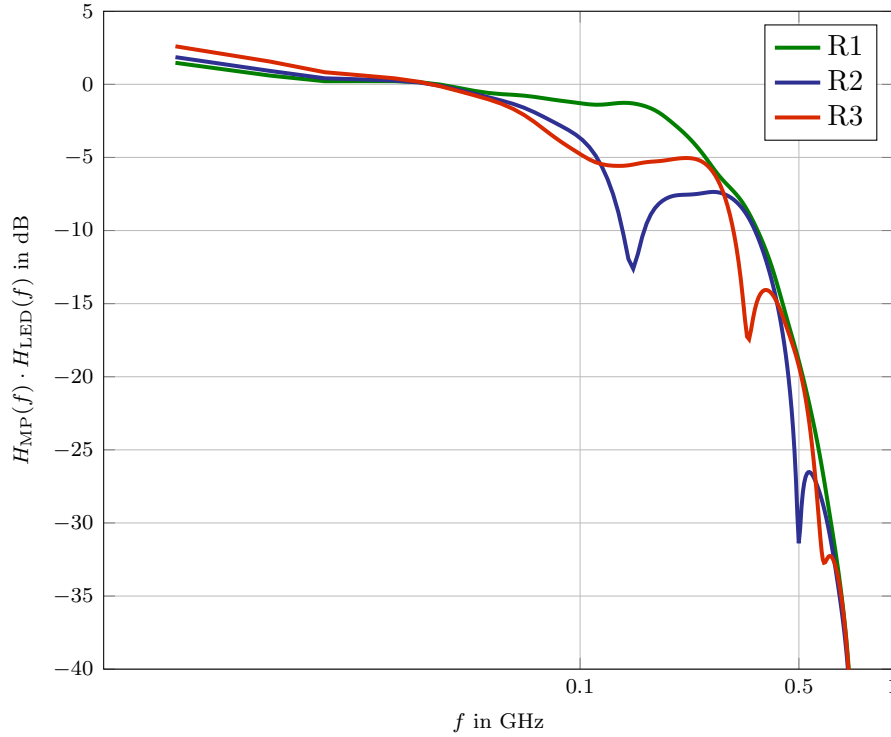
Figure 5.5.: Total transfer function of the VLC channel for three positions, as depicted in Fig. 5.3

VLC systems also suffer from the bandwidth limitation of the LED/LED driver combination which plays a decisive role in the VLC system performance. The measurement results in [GL13] show that this bandwidth limitation leads to a low pass characteristic which can approximately be modeled as a Gaussian low-pass filter or a first order low-pass filter. Therefore, the total channel frequency response of the VLC system can be defined as

$$H_{\mathrm{VLC}}(f) = H_{\mathrm{MP}}(f) \cdot H_{\mathrm{LED}}(f), \tag{5.13}$$

where $H_{\mathrm{LED}}(f)$ is the channel transfer function which models the bandwidth limitation of the LED/LED driver combination. In this work, we assume that this has the characteristic of a Gaussian lowpass filter with an optical 3 dB cut off frequency f_{3dB}. Thus, if we assume for simplicity that $p(t)$ denotes the modulated optical signal in the ideal case, the received signal $p_{\mathrm{rx}}(t)$ appears to be a filtered version of $p(t)$, i.e. , $P_{\mathrm{rx}}(f) = P(f) \cdot H_{\mathrm{LED}}(f)$ — even if an ideal free space channel exists between the LED and

the photodiode. The filter is modeled as a Gaussian lowpass with the transfer function

$$H_{\text{LED}}(f) = e^{-\ln(2)\left(\frac{f}{f_{3\text{dB}}}\right)^2}. \tag{5.14}$$

Note that the average optical power at the filter output is equal to the power at the input.

In Fig. 5.5, the total channel frequency response is shown for three positions where a Gaussian lowpass filter with $f_{3\text{dB}} = 200$ MHz is considered in order to take into account that the LED is bandwidth limited. It is interesting to note that the lowpass characteristics of the LED/LED driver combination dominates the overall channel transfer function. However, we also observe the multipath effects for the R2 receiver position.

5.3. Transmission Schemes for IM/DD systems

5.3.1. PAM Block Transmission with Frequency Domain Equalization

In PAM block transmission, the original source symbols d_k, unipolar and real-valued alphabets, are first grouped into a series of blocks, each of size N, at the transmitter. Then, a CP of length L is inserted at the beginning of each block, which decreases the net data rate to $R_{\text{b}}N/(N+L)$. The ratio $N/(N+L)$ can be interpreted as a bandwidth efficiency factor. For symbol spaced sampling, one such block excluding the CP is represented as a column vector

$$\boldsymbol{x} = RP_0 \begin{bmatrix} d_0 & d_1 & \ldots & d_{N-1} \end{bmatrix}^{\text{T}}. \tag{5.15}$$

After adding the CP, the symbols are convolved with the transmit filter as shown in Fig. 5.6. The transmit filter can produce a NRZ-OOK signal or a 50 % RZ, as shown in Fig. 5.2.
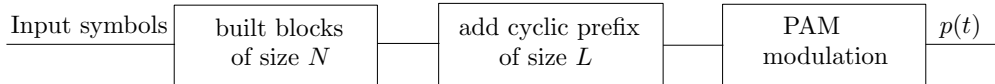
Figure 5.6.: PAM block transmission transmitter block diagram.

At the receiver side, first the CP is removed. The CP serves two purposes; first the neighboring blocks do not interfere, secondly the linear convolution of the transmitted symbols with the channel appears as cyclic convolution. This offers a way to perform simple frequency domain equalization, since a cyclic convolution in the time corresponds to a pointwise multiplication of the corresponding DFT vectors in the frequency domain. The received signal in the frequency domain is given as

$$\bar{\boldsymbol{y}} = \bar{\boldsymbol{H}}\bar{\boldsymbol{x}} + \boldsymbol{n}_F, \tag{5.16}$$

where

$$\bar{\boldsymbol{x}} = \boldsymbol{F}_N \cdot \boldsymbol{x} = \begin{bmatrix} X_0 & X_1 & \cdots & X_{N-1} \end{bmatrix}^{\text{T}},$$
$$\bar{\boldsymbol{y}} = \boldsymbol{F}_N \cdot \boldsymbol{y} = \begin{bmatrix} Y_0 & Y_1 & \cdots & Y_{N-1} \end{bmatrix}^{\text{T}},$$

and $\bar{\boldsymbol{H}} = \mathrm{diag}\begin{bmatrix} H_0 & H_1 & \cdots & H_{N-1} \end{bmatrix}$ is the diagonal matrix containing the channel frequency response on its diagonal. Each element of $\bar{\boldsymbol{y}}$ is given as

$$Y_\mu = H_\mu X_\mu + N_{\mathrm{F},\mu}, \qquad \mu = 0, \ldots, N-1. \tag{5.17}$$

Here, $\boldsymbol{F}_N$ denotes the DFT-matrix of size $N \times N$ with the elements $\frac{1}{\sqrt{N}} \mathrm{e}^{-j2\pi\frac{\mu n}{N}}$, where $\mu, n = 0, 1, \ldots, N-1$. Eq. (5.17) contains also the elements of the noise vector $\boldsymbol{n}_{\mathrm{F}} = \boldsymbol{F}_N \boldsymbol{n}$ in the frequency domain where $N_{\mathrm{F},\mu}$ denotes the component of $\boldsymbol{n}_{\mathrm{F}}$.

For fractional sampling, everything is basically the same, except that all vectors have the size $2N \times 1$ and all matrices have a size $2N \times 2N$. Thus the DFT/IDFT lengths are $2N$, where N is the block size in bits. The transmit vector $\check{\boldsymbol{x}}$ is now

$$\check{\boldsymbol{x}} = RP_0 \cdot \begin{bmatrix} d_0 & 0 & d_1 & 0 & \cdots & d_{N-1} & 0 \end{bmatrix}^{\mathrm{T}}. \tag{5.18}$$

5.3.1.1. Linear Detection Schemes

In this section, we discuss the frequency domain equalization process which is nothing else than the pointwise multiplication of $\bar{\boldsymbol{y}}$ ($\check{\boldsymbol{y}}$) with the equalizer coefficients $\boldsymbol{E}$ ($\check{\boldsymbol{E}}$) in the frequency domain, where the terms in the parentheses correspond to fractional sampling. However, since the data information is not directly contained in the frequency domain as in CP-OFDM (CP-DMT for optical system with IM/DD), a further IFFT is applied to the equalized symbols so that symbols are demodulated in the time domain, see Fig. 5.7.

5.3.1.1.1. Symbol Spaced Zero Forcing Equalization For zero forcing (ZF) equalization, where the noise is not considered with respect to the equalizer coefficients E_μ, the received signal is equalized such that each signal component $V_\mu = H_\mu X_\mu \cdot E_\mu$ of the equalizer output vector $\bar{\boldsymbol{u}}$ meets the condition $V_\mu \overset{!}{=} X_\mu$, which simply gives $E_\mu = 1/H_\mu$, as shown in Fig. 5.7. Note that the equalizer output $\bar{\boldsymbol{u}}$ consists of a desired signal component $\bar{\boldsymbol{v}} = [V_0, V_1, \cdots, V_{N-1}]^T$ and a noise component $\bar{\boldsymbol{w}}$, where each component of noise vector $\bar{\boldsymbol{w}}$ follows $W_\mu = E_\mu \cdot N_{\mathrm{F},\mu}$.
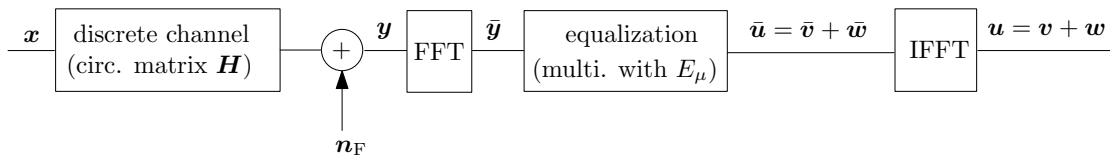
Figure 5.7.: High level block diagram for symbol spaced sampling. The vector at the equalizer output is denoted as $\bar{\boldsymbol{u}}$ and consists of a desired signal component $\bar{\boldsymbol{v}}$ and a noise component $\bar{\boldsymbol{w}}$. The time domain vector vector $\boldsymbol{u}$ is used for PAM de-mapping.

5.3.1.1.2. Fractionally Spaced Zero Forcing Equalization For fractionally spaced sampling, each receive vector $\boldsymbol{u}$ in the time domain consists of $2N$ samples. However, the final demodulation process is based on only N decisions. Thus, if $\bar{\check{\boldsymbol{v}}}$ and $\check{\boldsymbol{v}} = \check{\boldsymbol{F}}_{2N}^{-1} \bar{\check{\boldsymbol{v}}}$ denote the desired signal at the equalizer output in the frequency and time domain, the ZF condition is $\boldsymbol{v}_{\mathrm{dec}} = \begin{bmatrix} \check{v}_0 & \check{v}_2 & \check{v}_4 & \ldots & \check{v}_{2N-2} \end{bmatrix}^{\mathrm{T}} \overset{!}{=} \boldsymbol{x}$, where

$\boldsymbol{v}_{\text{dec}}$ is the factor 2 decimated version of $\check{\boldsymbol{v}}$. The frequency domain equivalence of this expression is

$$\bar{\boldsymbol{v}}_{\text{dec}} = \boldsymbol{F}_N \cdot \boldsymbol{v}_{\text{dec}} = \begin{bmatrix} \check{V}_0 + \check{V}_N & \check{V}_1 + \check{V}_{N+1} & \dots & \check{V}_{N-1} + \check{V}_{2N-1} \end{bmatrix}^{\text{T}} /2 \overset{!}{=} \bar{\boldsymbol{x}}. \tag{5.19}$$

Since $\check{X}_\mu = \check{X}_{\mu+N} = X_\mu$, the required relation between $\check{\boldsymbol{E}}$ and $\check{\boldsymbol{H}}$ is therefore

$$\check{H}_\mu \check{E}_\mu + \check{H}_{\mu+N} \check{E}_{\mu+N} = 2, \qquad \mu = 0, 1, \dots, N-1. \tag{5.20}$$

This intermediate solution shows nicely the first Nyquist criterion in the frequency domain and it indicates a degree of freedom in the selection of the coefficients, which can be used to minimize the noise. If white noise with $\Phi_{n_{\text{F}} n_{\text{F}}}(\mu) = N_0/2$ is assumed, the SNR on each frequency pair will be maximized[1] for $\check{E}_\mu = c_\mu \cdot \check{H}_\mu^*$ and $\check{E}_{\mu+N} = c_\mu \cdot \check{H}_{\mu+N}^*$, where c_μ is a constant in order to guarantee condition (5.20). Thus, the optimal coefficients are

$$\check{E}_\mu = \frac{2\check{H}_\mu^*}{|\check{H}_\mu|^2 + |\check{H}_{\mu+N}|^2}, \quad \check{E}_{\mu+N} = \frac{2\check{H}_{\mu+N}^*}{|\check{H}_\mu|^2 + |\check{H}_{\mu+N}|^2}. \tag{5.21}$$

It should be noted that an IFFT of size N can be used to obtain the equalized time domain vector $\boldsymbol{u}_{\text{dec}}$, if the IFFT is performed on

$$\bar{\boldsymbol{u}}_{\text{dec}} = \begin{bmatrix} \check{U}_0 + \check{U}_N & \check{U}_1 + \check{U}_{N+1} & \dots & \check{U}_{N-1} + \check{U}_{2N-1} \end{bmatrix}^{\text{T}} /2. \tag{5.22}$$

The frequency domain components $\check{U}_\mu$ and $\check{U}_{\mu+N}$ at the equalizer output are obtained by computing

$$\check{U}_\mu = \check{E}_\mu \cdot \check{Y}_\mu, \quad \check{U}_{\mu+N} = \check{E}_{\mu+N} \cdot \check{Y}_{\mu+N}, \tag{5.23}$$

where the equalizer coefficients are obtained using Eq. (5.21). Finally time domain symbols $\boldsymbol{u}_{\text{dec}}$ are demodulated using PAM de-mapping.

5.3.1.1.3. Symbol Spaced MMSE Equalization For MMSE (minimum mean square error) equalization, the coefficients E_μ shall satisfy the condition $\text{E}\{|\boldsymbol{u} - \boldsymbol{x}|^2\} \overset{!}{=} \min$. The solution can be directly obtained from the Wiener filter theory. In order to determine E_μ, it is advantageous to consider the channel as a part of a Wiener filter at a first step. The corresponding coefficients would be [KI89]

$$E_\mu^{\text{WNR}} = 1 \Big/ \left(1 + \frac{\Phi_{n_{\text{F}} n_{\text{F}}}(\mu)}{|H_\mu|^2 \cdot \Phi_{xx}(\mu)} \right), \tag{5.24}$$

where $\Phi_{xx}(\mu)$ denotes the power spectral density of the desired signal $\boldsymbol{x}$ and $\Phi_{n_{\text{F}} n_{\text{F}}}(\mu)/|H_\mu|^2$ denotes the power spectral density of the the original noise after it has passed a filter with the transfer function $1/H_\mu$.

---

[1]Cauchy Schwarz inequality. The solution for colored noise is given in [WH11].
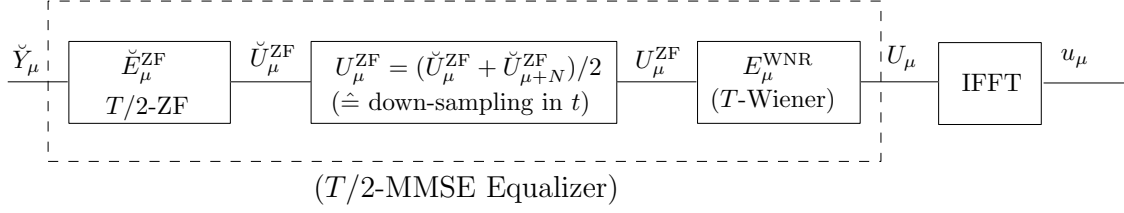
Figure 5.8.: Possible view on fractional MMSE equalization: A fractional ZF equalizer is cascaded with a symbol spaced Wiener filter.

Since $E_\mu^{\mathrm{WNR}} = H_\mu \cdot E_\mu$, the optimal solution for the actual equalizer coefficients E_μ is given as

$$E_\mu = \frac{1}{H_\mu} \cdot \frac{1}{1 + \frac{\Phi_{n_\mathrm{F} n_\mathrm{F}}(\mu)}{|H_\mu|^2 \cdot \Phi_{xx}(\mu)}} = E_\mu^{\mathrm{ZF}} \cdot E_\mu^{\mathrm{WNR}}, \qquad \mu = 0, 1, ..., N-1, \tag{5.25}$$

where we assume that the channel transfer function does not contain spectral zeros, i.e., $H_\mu \neq 0 \ (\forall \ \mu)$. Eq. (5.25) shows that the actual equalization process of the received signal $\bar{\boldsymbol{y}}$ can be split into a ZF equalization part — the coefficients are $E_\mu^{\mathrm{ZF}} = 1/H_\mu$ — and a Wiener filter part with the filter coefficients E_μ^{WNR}. This very intuitive result was also formulated by Yamazaki [YA10]. It should be noted that Eq. (5.25) can be rewritten as

$$E_\mu = \frac{H_\mu^*}{|H_\mu|^2 + 1/\eta_\mu}, \tag{5.26}$$

where η_μ is the signal-to-noise power ratio $\Phi_{xx}(\mu)/\Phi_{n_\mathrm{F} n_\mathrm{F}}(\mu)$.

5.3.1.1.4. Fractionally Spaced MMSE equalization In [WH11] it has been shown that the same approach can be used for fractional MMSE equalization. The main difference is that the present ZF equalizer operates on a fractional basis, whereas the subsequent Wiener filter remains symbol spaced, see Eq. (5.25) and Fig. 5.8. For white noise with $\Phi_{n_\mathrm{F} n_\mathrm{F}}(\mu) = N_0/2$, the coefficients of the ZF filter part can be obtained from Eq. (5.21).

The Wiener filter shown in Fig. 5.8 receives the desired signal superimposed by noise whose power spectral density is colored by the ZF equalizer. Since a factor 2 decimation in the time domain corresponds to a periodic repetition of the original spectrum (period $2N$) with a period N in the DFT frequency domain, the noise power spectral density at the Wiener filter input is given as [WGR+10]

$$\Phi_{nn}(\mu) = \left(\breve{\Phi}_{n_\mathrm{F} n_\mathrm{F}}(\mu) \left| \breve{E}_\mu^{\mathrm{ZF}} \right|^2 + \breve{\Phi}_{n_\mathrm{F} n_\mathrm{F}}(\mu + N) \left| \breve{E}_{\mu+N}^{\mathrm{ZF}} \right|^2 \right) / 2, \quad \mu = 0, 1, ..., N-1. \tag{5.27}$$

Thus the coefficients of the equalizer are given as

$$\breve{E}_\mu = \frac{2 \breve{H}_\mu^*}{|\breve{H}_\mu|^2 + |\breve{H}_{\mu+N}|^2 + 2/\eta_\mu}, \quad \breve{E}_{\mu+N} = \frac{2 \breve{H}_{\mu+N}^*}{|\breve{H}_\mu|^2 + |\breve{H}_{\mu+N}|^2 + 2/\eta_\mu}, \tag{5.28}$$

where η_μ is the signal-to-noise power ratio $\Phi_{xx}(\mu)/\Phi_{nn}(\mu)$.

5.3.1.2. DC-Balanced PAM-FDE - A solution for VLC

Since LED-light sources are additionally used for communications in VLC systems, it is aimed that the brightness should be data independent and there is no flickering of light. Thus, the transmit signals need to be DC-balanced for a constant brightness. Since PAM does not provide DC-balance for rectangular pulses (or baseband pulses in general), it needs to be combined with line coding.

5.3.1.2.1. Conventional Line Codes - 8B10B   A well known line code for binary transmission is the 8B10B IBM-code [WF83], which consists of a concatenation of a 5B6B and a 3B4B code. Since 8B10B line codes add more redundancy than 5B6B codes, we consider only the 5B6B line code for $M = 2$, where the symbol rate is increased by a factor $6/5$. For higher modulation orders ($M = 4$, $M = 8$), we assume the same $6/5$ increase of the symbol rate. The corresponding codes for these higher modulation orders, which rely on the same principle as the 5B6B code, have already been discussed in the literature [GCS$^+$05].

5.3.1.2.2. Partial Response Line Coding   DC-balance can also be achieved by partial-response line coding, where we only consider pseudo-ternary coding here. One well known example of such codes is alternate-mark inversion (AMI), where original 1-bits are alternately mapped to -1 and $+1$. This is achieved by means of a digital filter with the transfer function given as

$$G_z(z) = 0.5 \cdot (1 - z^{-1}).$$ (5.29)

For bipolar input bits, which are precoded in order to simplify the detection, the symbols at the filter output take the values -1, 0, $+1$. The DC is therefore removed and the data spectrum is additionally shaped with

$$|G(f)|^2 = |G_z(z)|^2_{z=e^{j2\pi fT}} = \sin^2(\pi fT),$$ (5.30)

where T is the symbol interval. As we need to ensure a non-negative signal, we assume that the 3-PAM modulator is fed by the unipolar 3-level symbols $d_k + 1$.
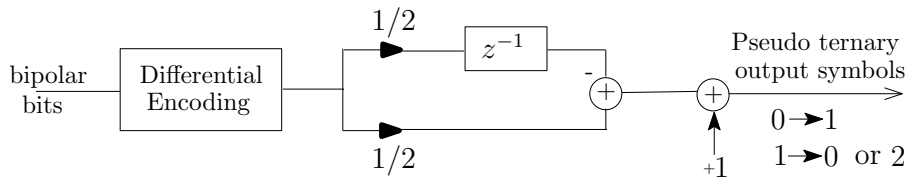
Figure 5.9.: Block diagram of pseudo-ternary coding.

A second type of pseudo ternary coding is also considered, denoted as PR-II, where the digital filter is given by [Kam08]

$$G_z(z) = 1 - z^{-2}.$$ (5.31)

This shapes the data spectrum additionally with $|G(f)|^2 = \sin^2(2\pi fT)$ and introduces a zero at $f = 1/(2T)$. In order to benefit from this spectral shaping, we have assumed MMSE equalization for these two schemes.

5.3.2. Discrete Multitone Transmission Schemes

Optical systems with IM/DD demands for real-valued and unipolar (positive) time domain signals. The real-valued base-band version of CP-OFDM is usually referred to as discrete multitone transmission (DMT). DMT schemes are widely recommended for optical systems with IM/DD. The main reason for their popularity comes from the success of CP-OFDM in RF transmission. However, due to IM/DD constraints, the bandwidth efficiency of the DMT schemes reduces. In the literature, many variants of CP-DMT schemes have been discussed [AS08, VFea10, DA13, LRBV09]. In the following, we summarize these DMT schemes. Specifically, we present these schemes in matrix/vector notation which is not found in the literature. Moreover, for the first time, we present bit-loading schemes that can be combined with these CP-DMT schemes.

First we present a general model that is used to obtain a real-valued signal. A classical discrete time DMT signal with bipolar amplitudes at the output of IDFT can be written as

$$x(n) = \sum_{\mu=1}^{N_m} \left(d_\mu e^{j2\pi\mu\frac{n}{N}} + d_\mu^* e^{-j2\pi\mu\frac{n}{N}} \right) \quad \forall n = 0, 1, 2, \cdots, N-1, \tag{5.32}$$

where d is the complex data symbol from QAM constellation, N is the FFT/IFFT length, and $N_m \leq \frac{N}{2}-1$ is number of effective data subcarriers. The Hermitian symmetry $d_\mu = d_\mu^*$ or $d_\mu = d_{N-\mu}^*$ of the data symbols ensures a real-valued time domain signal. In matrix/vector notation, we can write the real-valued signal at the IDFT output as

$$\boldsymbol{x} = \boldsymbol{F}_N^H \bar{\boldsymbol{B}} \begin{bmatrix} \boldsymbol{d} \\ \boldsymbol{d}^* \end{bmatrix} \in \mathbb{R}^{N\times 1}, \tag{5.33}$$

where $\boldsymbol{F}_N$ is the N-point DFT matrix with its elements $[\boldsymbol{F}_N]_{k,l} = \frac{1}{\sqrt{N}} e^{-j\frac{2\pi}{N}kl}$ for $k, l = 0, 1, 2, \ldots, N-1$ and $\bar{\boldsymbol{B}}$ maps the data symbols to the respective subcarrier positions. The $\bar{\boldsymbol{B}}$ matrix is given by

$$\bar{\boldsymbol{B}} = \begin{bmatrix} \mathbf{B} & \mathbf{0} \\ \mathbf{0} & \widehat{\mathbf{\Pi}}\mathbf{B} \end{bmatrix} \in \mathbb{R}^{N\times 2N_m}, \tag{5.34}$$

where $\widehat{\mathbf{\Pi}}$ is defined as

$$\widehat{\mathbf{\Pi}} = \begin{bmatrix} 0 & 0 & \ldots & 0 \\ 0 & 0 & \ldots & 1 \\ \vdots & \vdots & \vdots & \vdots \\ 0 & 1 & \ldots & 0 \end{bmatrix} = \left[\begin{array}{c|ccc} 0 & 0 & \ldots & 0 \\ \hline 0 & & & \\ \vdots & & \mathbf{\Pi} & \\ 0 & & & \end{array} \right],$$

and $\mathbf{\Pi} \in \{0,1\}^{(\frac{N}{2}-1)\times(\frac{N}{2}-1)}$ (therefore $\widehat{\mathbf{\Pi}} \in \{0,1\}^{\frac{N}{2}\times\frac{N}{2}}$) is an anti-diagonal matrix, which has ones in the anti-diagonal and zeros elsewhere. The real-valued matrix $\boldsymbol{B} \in \{0,1\}^{\frac{N}{2}\times N_m}$ maps these symbols to the respective subcarriers and $\widehat{\mathbf{\Pi}}\mathbf{B}$ ensures that a Hermitian symmetry is applied in the frequency domain to obtain a real-valued signal. Various variants of the DMT schemes have been discussed in the literature [AS08, DA13, WH12]. These schemes are discussed briefly in the following.

5.3.2.1. Asymmetrically Clipped DMT Scheme

In asymmetrically clipped DMT (AC-DMT), only the odd subcarriers are M-QAM modulated i.e., every second row of the $\boldsymbol{B}$ matrix in Eq. (5.34) is a zero row. One symbol of the discrete time optical signal $p(n)$ is given as

$$p(n) = \begin{cases} P_0 x(n) & x(n) \geq 0 \\ 0 & \text{else} \end{cases} \tag{5.35}$$

where P_0 is a given optical power which is related to the average optical power as Eq. (5.8) and $p(n)$ denotes the instantaneous optical power at the sampling time. Moreover, the symmetry $x(n) = -x(n + N/2), n = 0, 1, \cdots, N/2 - 1$ of $x(n)$ ensures that all negative parts of $x(n)$ can be clipped without an information loss on the odd subcarriers. This means that there is no clipping noise.

5.3.2.2. DC-biased DMT Scheme

The positive real-valued signal can also be obtained by adding a DC-bias to the time domain signal $x(n)$ (Eq. (5.32)). An arbitrarily high DC-bias value cannot be added since an increase in the bias value results in an increased value of the average optical power P. On the other hand, the increase in the bias value reduces the clipping noise. Since clipping may result in bit errors, the bias value needs to be carefully chosen. One symbol of the discrete time optical signal $p(n)$ for this scheme is written as

$$p(n) = \begin{cases} P_0 z(n) & z(n) \geq 0 \\ 0 & \text{else} \end{cases} \tag{5.36}$$

where

$$z(n) = x(n) + \underbrace{k_{\text{clip}} \sqrt{\mathbb{E}\{x^2(n)\}}}_{\text{DC-bias}}, \tag{5.37}$$

and k_{clip} is the clipping value. The DC-bias is expressed as a multiple $k_{\text{clip}} \geq 0$ of the standard deviation of $x(n)$ [AS08]. In this work, k_{clip} has been set in such a way that the clipping probability reduces to 5 %. Note that in the AC-DMT scheme, halfwave rectifying destroys the DC-balance for QAM modulation orders greater than 4. Thus it makes it less attractive for indoor VLC systems where a constant brightness is desired. Therefore, DC-biased DMT scheme is an ideal scheme for VLC systems since DC-biasing can also be used to ensure a DC-balance.

5.3.2.3. PAM DMT Scheme

In PAM-DMT, the real part of the data symbols is set to zero [LRBV09]. Let $\boldsymbol{s} = [s_1, s_2, \cdots, s_{N_m}]^T \in \mathbb{R}^{N_m \times 1}$ be the data symbol vector of length N_m which are taken from a bipolar M-PAM constellation. In order to ensure the odd symmetry in the time domain, these symbols are first converted to imaginary symbols by setting the real part to zero as

$$\boldsymbol{d} = j\boldsymbol{s} \in \mathbb{C}^{N_m \times 1}, \tag{5.38}$$

Then they are mapped to $\frac{N}{2}$ subcarriers in the frequency domain, with N being the DFT size. The real-valued signal is obtained by using Eq. (5.33). The negative part of the time domain samples $\boldsymbol{x}$ is then clipped without loss of any information. One symbols of the discrete time optical signal for PAM-DMT signal can be written as

$$p(n) = \begin{cases} P_0 x(n) & x(n) \geq 0 \\ 0 & \text{else} \end{cases} \tag{5.39}$$

where

$$x(n) = 2 \cdot \sum_{\mu=1}^{N_m} s_\mu \sin\left(2\pi\mu\frac{n}{N}\right) \tag{5.40}$$

The symmetry of $x(n)$ ensures that clipping noise occurs only in the $\cos(\cdot)$ components of the received signal. Therefore, the clipping of the negative part does not result in any loss of information.

5.3.2.4. Power loading and Bit loading

If channel state information is available at the transmitter, power-loading and bit-loading can be applied to DMT schemes to improve the performance. In power-loading, each d_μ, which is taken from a squared QAM constellation, is weighted with $1/|H(\mu f_0)|$ prior to the inverse DFT at the transmitter, where $f_0 = f_s/N$ is the frequency spacing between the subcarriers. This is due the fact that we have the same minimum Euclidean distance at the receiver for each d_μ. Weighting by $1/|H(\mu f_0)|$ increases the second moment of each subcarrier by a factor $1/|H(\mu f_0)|^2$, $\mu = 1, \cdots, N_m$. Moreover, to find the theoretical benchmark performance of DMT schemes, optimal bit-loading algorithms such as Hughes-Hartogs (HH) algorithm [HH89] can be applied. In this algorithm, the bits are incrementally assigned to the subcarriers, where the total number of bits depends on R_b and the subcarrier spacing (DMT-symbol interval). Starting with one single bit, the next bit is assigned to the subcarrier that needs the minimum incremental energy, where the incremental electrical energies depend on $1/|H(\mu f_0)|^2$ and the actual modulation orders M_μ at that iteration step. The complexity of the Hughes-Hartogs algorithm is high due to the iterative implementation. Therefore sub-optimal non-iterative bit-loading algorithms such as the Fischer-Huber (FH) algorithm [FH96] are an attractive choice. In the Fischer-Huber algorithm the bits are assigned according to the subchannel SNRs.

5.3.3. Single-Subcarrier (SSC) QAM Schemes

PAM is a modulation scheme with a one-dimensional signal space. In order to combine quadrature modulation (that is a two-dimensional scheme) with IM/DD, an electrical subcarrier needs to be modulated, where an additional bias or half wave rectifying is required to ensure a non-negative signal that modulates the LED. As explained earlier, VLC systems require DC-balanced schemes to ensure constant brightness. In the previous section, we have discussed DMT schemes where QAM is modulated on multiple subcarriers. In the following we discuss some of the state-of-the-art transmission schemes where QAM is modulated on a single subcarrier (SSC) and the DC-balance is achieved by adding a DC-bias. We also propose novel SSC schemes, i.e., orthogonal PAM (OPAM) schemes. Usually, in the literature, the performance of these state-of-the-art SSC schemes is evaluated by employing time domain

equalization techniques. However, we show for the first time that these schemes can also be combined with block transmission which offers a simple frequency domain equalization. Moreover, we also show that the carrier-less amplitude and phase modulation (CAP) scheme is nothing else but an extension of SSC schemes where root-raised cosine (RRC) filtering is used instead of the conventional rectangular filtering.
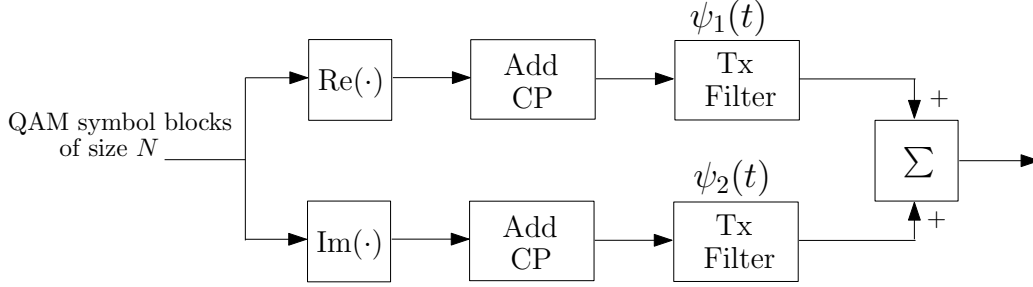
Figure 5.10.: Transmitter for SSC-QAM block transmission.

The block based transmission for the SSC schemes can be generalized by the transmitter architecture presented in Fig. 5.10. At the transmitter, the block of complex QAM data symbols is first separated in two two streams, i.e., the real and the imaginary symbols, as shown in Fig. 5.10. Then after adding the CP, these two data streams are transmitted by means of the two waveforms, i.e., $\psi_1(t)$ and $\psi_2(t)$, and the resulting modulated symbols are summed up. Based on the type of transmit filter basis functions, different SSC-QAM techniques can be designed. Note that these basis function $\psi_1(t)$ and $\psi_2(t)$ should be orthogonal in order to recover the original signal at the receiver. Block transmission with the addition of the CP offers a simple solution at the receiver. Since both equalization and filtering are point-wise multiplication in the frequency domain, both can be done at the same time. Moreover, both $\psi_1(t)$ and $\psi_2(t)$ exhibit the same half wave symmetry, the positive valued optical signal $p(t)$ can be demodulated by correlating the received and equalized signal with the matched filters $g_{\mathrm{rx1}}(t)$ and $g_{\mathrm{rx2}}(t)$ or with the complex equivalent

$$g_{\mathrm{rx}}(t) = g_{\mathrm{rx1}}(t) + jg_{\mathrm{rx2}}(t), \tag{5.41}$$

where equalization and receive filtering can be performed in the frequency domain, as shown in Fig. 5.11.
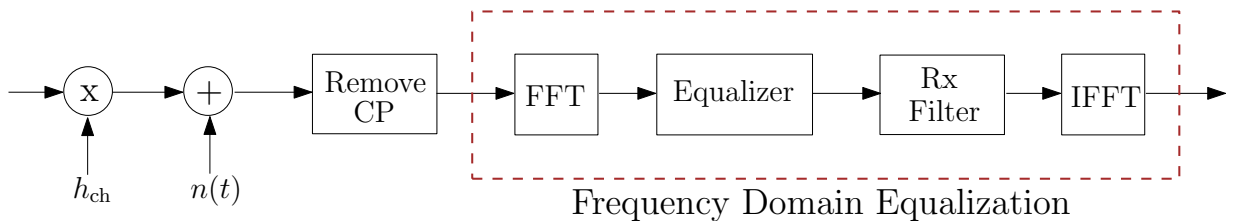
Figure 5.11.: Receiver for SSC-QAM block transmission.

5.3.3.1. SSC-QAM with a Rectangular Pulse-Shape

In optical systems, frequency reuse is not a big issue, therefore a rectangular pulse shape is an obvious first choice. If $a(t)$ is a unit energy rectangular pulse of duration T, then the two basis functions at subcarrier frequency $f_c = 1/T$ can be defined as

$$\psi_1(t) = a(t) \cdot \sqrt{2} \cos(2\pi f_c t), \quad \psi_2(t) = -a(t) \cdot \sqrt{2} \sin(2\pi f_c t). \tag{5.42}$$

These two basis functions are shown in Fig. 5.12. Note that orthogonality is achieved by a $90°$ phase
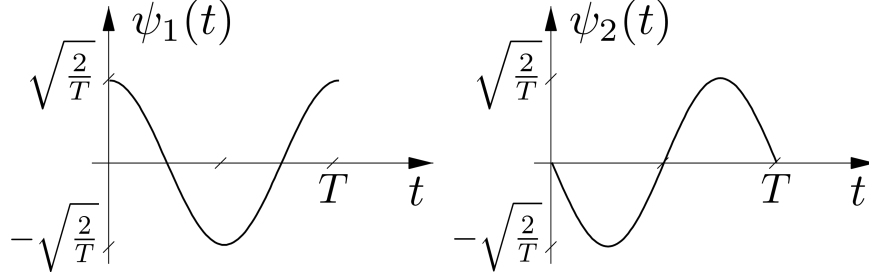
Figure 5.12.: Two basis functions for SSC-QAM with a rectangular pulse-shape.

shift. hence one block of the transmit signal (without CP) can be written as

$$p(t) = P_0 \sum_{n=0}^{N-1} \left(d'_n \cdot \sqrt{\frac{T}{2}} \cdot \psi_1(t - nT) + d''_n \cdot \sqrt{\frac{T}{2}} \cdot \psi_2(t - nT) \right), \tag{5.43}$$

where $d_n = d'_n + \mathrm{j}d''_n$, and d_n denotes the complex-valued M-QAM symbols. We may switch from asymmetrically clipped SSC transmission to DC-biased SSC transmission according to

$$p(t) = P + P_0 \sum_{n=0}^{N-1} \left(d'_n \cdot \sqrt{\frac{T}{2}} \cdot \psi_1(t - nT) + d''_n \cdot \sqrt{\frac{T}{2}} \cdot \psi_2(t - nT) \right), \tag{5.44}$$

For a modulation order $\sqrt{M}$ per orthogonal component, the required minimum DC-bias P to avoid clipping and to obtain a perfect DC-balance is $P = P_0 \cdot \max(|d_n|) = \sqrt{2}(\sqrt{M} - 1)P_0$.

5.3.3.2. Carrier-less Amplitude and Phase Modulation

For a rectangular pulse shaping and a QAM-symbol duration T, the subcarrier frequency f_c must be equal to $1/T$ (or an integer multiple of it) in order to ensure the orthogonality between the quadrature components. Assuming a channel with a low pass characteristic, this is a big disadvantage, since the spectral centroid is shifted from zero to $1/T$. In this case, M-PAM (based on rectangular pulses with modulation order M) would require exactly the same bandwidth (first zero crossing) as M^2-QAM, but QAM would suffer from the fact that the main signal energy is centered at higher frequencies. This disadvantage can be reduced, if a root-raised cosine (RRC) pulse shape is used for QAM. Assuming a roll-off factor r, $0 < r \le 1$, the center frequency can be reduced to $f_c = (1 + r)/(2T)$, and the total required physical bandwidth is only $(1+r)/T$. This approach is referred to as carrier-less amplitude and

phase modulation (CAP) [WL$^+$12], where the term 'carrier less' comes from the fact that the bandpass signal is not obtained by a quadrature up-conversion of two baseband signals. Instead, two bandpass FIR filters [WL$^+$12] are used to generate the QAM signal. The two filters with impulse responses $\psi_1(t)$ and $\psi_2(t)$ in Eq. (5.42) form a Hilbert transform pair, i.e., $\psi_2(t) = \mathcal{H}\{\psi_1(t)\}$ and $\Psi_2(f) = -j \cdot \Psi_1(f)$ for $f > 0$, and both transfer functions differ only in a 90° shift. Here $\psi_1(t)$ is chosen as root-raised cosine filter.

The biggest advantage of CAP is to implement the signal generation by means of two filters with the impulse responses $\psi_1(t)$ and $\psi_2(t)$, and not by a quadrature upconversion of a complex QAM-baseband signal to the subcarrier frequency f_c. However, these filters at the transmitter may be very large (multiple taps) which is not feasible in practical applications. Therefore, in practice, both $\psi_1(t)$ and $\psi_2(t)$ must be truncated which reduces its performance. Another disadvantage compared to the rectangular pulse-shape is the increased peak to average power ratio of the transmit signal, since several transmit pulses interfere with each other.

5.3.3.3. Orthogonal PAM (OPAM)

In order to simplify the signal generation and detection of an SSC-QAM like scheme, in [WCHG14], we have suggested to use the binary replacements of the quadrature pair shown in Fig. 5.12 and denoted this scheme as orthogonal PAM. The basic principle is identical to SSC-QAM, but the term QAM is simply avoided since the orthogonality of $\psi_1(t)$ and $\psi_2(t)$ is not achieved by a 90° phase shift as shown in Fig. 5.13. One block of the transmit signal (without CP) before clipping is given as
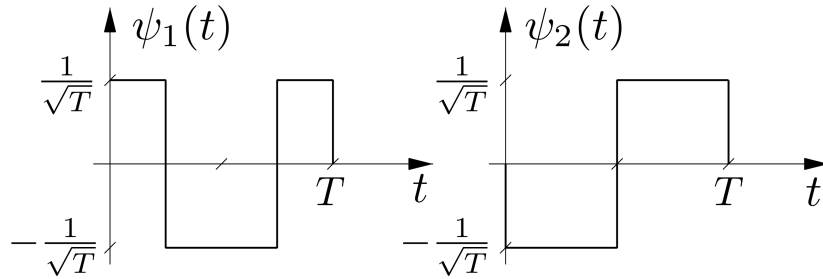
Figure 5.13.: Two basis functions for OPAM.

$$p(t) = P_0 \sum_{n=0}^{N-1} \left(d'_n \cdot \sqrt{T} \cdot \psi_1(t - nT) + d''_n \cdot \sqrt{T} \cdot \psi_2(t - nT) \right), \qquad (5.45)$$

To ensure a constant moving average, even for higher modulation orders, we may use line coding or we may switch from AC-OPAM to DC-biased OPAM according to

$$p(t) = P + P_0 \sum_{n=0}^{N-1} \left(d'_n \cdot \sqrt{T} \cdot \psi_1(t - nT) + d''_n \cdot \sqrt{T} \cdot \psi_2(t - nT) \right), \qquad (5.46)$$

Moreover, in [WCHG14] we have shown that OPAM has exactly the same AWGN power penalty as SSC-QAM with a rectangular baseband pulse shape $a(t)$.

5.4. Simulation Results

We evaluate the performance of these schemes for the two channels discussed in Section 5.2.2. For all schemes, perfect channel knowledge and block synchronization has been assumed. The required relative power P/P_{OOK} of a certain scheme, as indicated by Eq. (5.4), is shown for a fixed value of $p_{\mathrm{b}} = 10^{-3}$. First we show the performance of these schemes for the POF channel. In Section 5.4.2, we will discuss the performance of theses schemes for the VLC channel (channel 2).

5.4.1. Performance in Channel 1 (POF)

An FFT size of $N = 128$ with a CP length of $L = 16$ is used for all transmission schemes. For very low values of R_{b}, the results depict the power efficiency of the various transmission schemes in a flat AWGN channel, whereas the increase in the curves corresponds to the penalty caused by the Gaussian lowpass filter, that is the dispersive induced penalty.
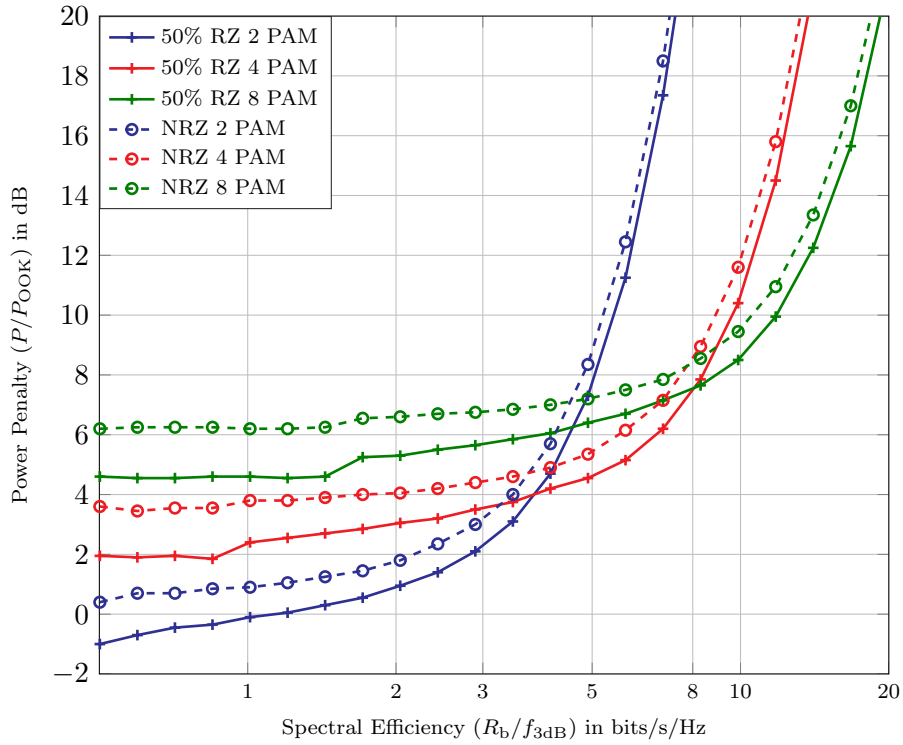
Figure 5.14.: Performance of PAM-FDE with different transmit filters. RZ-PAM results in a 1.5 dB gain over NRZ-PAM.

In Fig. 5.14, the results are shown for PAM block transmission with frequency domain equalization for two transmit filters, i.e., 50 % RZ and NRZ. Moreover, a $T/2$ fractionally spaced ZF receiver is employed. As expected, at lower bit rates, the RZ-format promises a gain of 1.5 dB compared to the NRZ-format, independent of the modulation order M. If the dispersion imposes a power penalty, this gain becomes slightly smaller. Note that, as explained in Section 5.2.1, power penalty refers to the additional power required by these schemes as compared to the reference scheme (OOK) in AWGN channel at $p_{\mathrm{b}} = 10^{-3}$.
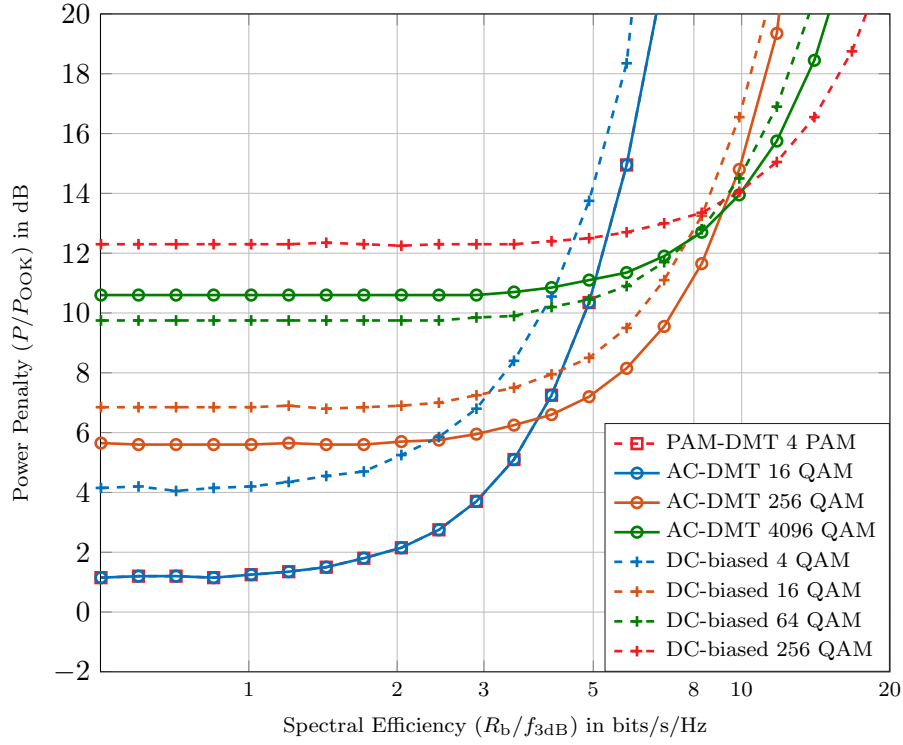
Figure 5.15.: Performance of different DMT schemes. PAM-DMT and AC-DMT have exactly the same performance.

In Fig. 5.15, the comparison between different DMT schemes is shown. To have a fair comparison, the results are shown for AC-DMT using an alphabet size of M^2, if DC-biased DMT and PAM-DMT use a modulation order of M. This is due to the fact that the AC-DMT scheme uses half of the subcarriers as compared to the DC-biased DMT and PAM-DMT schemes. In our simulations, we have used 26 subcarriers for AC-DMT while 52 subcarriers are used for PAM-DMT and DC-biased DMT schemes. The results show that AC-DMT and PAM-DMT schemes provide the same bandwidth efficiency and suffer in exactly the same way from the dispersive channel. Although PAM-DMT and AC-DMT systems seem to use very different approaches, the comparable performance is not as surprising [WH12], since an M^2-QAM constellation is a combination of two M-PAM modulated inphase and quadrature constellations. In DC-biased DMT, the positive signal is obtained by adding a DC-bias to the real-valued signal. However, due to the maximum power constraints, an addition of an infinite amount of the DC-bias is not appropriate. Therefore, a clipping of the negative signal is carried out after adding a feasible amount of bias. Since the clipping may result in bit errors, the bias needs to be chosen carefully. In this work, we have set the DC-bias to a value where the second moment of the clipping noise is equal to the power of the additive white Gaussian noise at the receiver after sampling. However, the clipping effect on the bit error rate also depends on the assignment of the modulation orders [WCHG14]. Note that both AC-DMT and PAM-DMT do not suffer from clipping noise. The results show that DC-biased DMT outperforms the AC-DMT or the PAM-DMT, if the modulation order M is greater or equal to 64. For lower modulation orders, the AC-DMT or PAM-DMT schemes outperforms the DC-biased scheme.
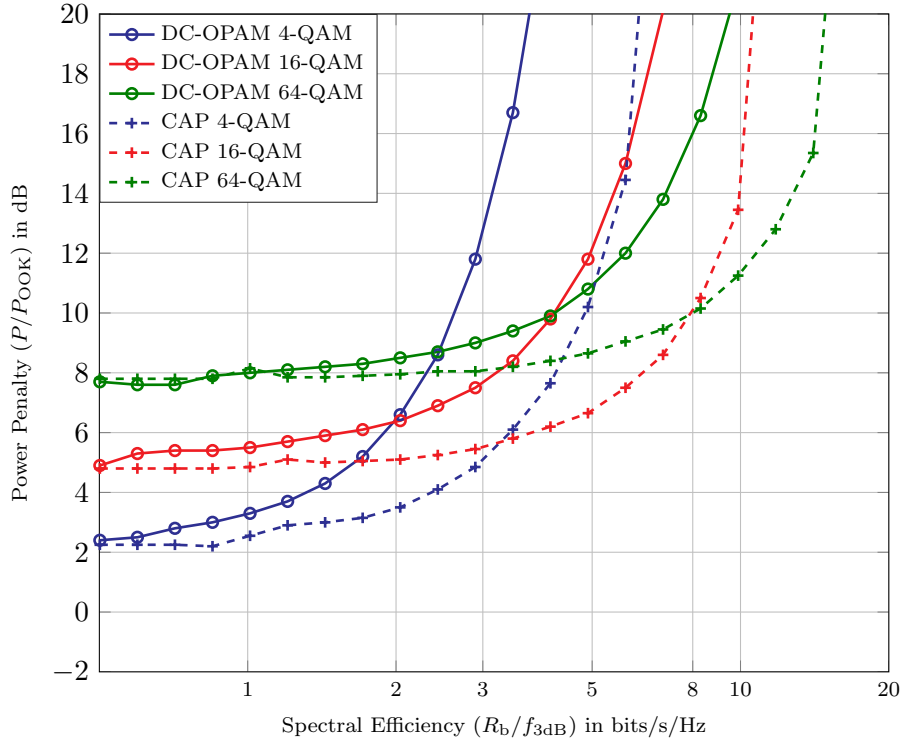
Figure 5.16.: Performance of different SSC schemes. CAP outperforms the OPAM significantly.

The comparison of the DC-biased SSC-QAM schemes is shown in Fig. 5.16. For CAP, i.e., SSC-QAM with a RRC pulse shape, a roll-off factor $r = 0.5$ and a baseband subcarrier frequency $f_c = (1+r)/(2T)$ has been assumed, where the transmit and receive pulses are truncated at $t = \pm 5T$. The DC bias was set in the same way as shown for the DC-biased DMT scheme, i.e., a small amount of clipping was allowed in order to minimize the required power for $p_b = 10^{-3}$. In this work, for $M = 4$, the clipping value k_{clip}, as defined in Eq. (5.37), has been set to 1.52 in order to limit the clipping probability to 5 %. For $M = 16$ and $M = 64$, k_{clip} has been set to 1.72 and 2.2 — the smallest values of the k_{clip} that achieve the cliping probability of 5 %. Clearly CAP outperforms the OPAM scheme significantly. Note that at very low values of R_b (equivalent to AWGN channel), OPAM has same performance of CAP but afterwards the performance degrades significantly. OPAM suffers from the fact that the spectral centroid of the spectrum is nearly at $1/T$, which is a big disadvantage if the signal is low pass filtered.

We compare the performance of these schemes in Fig. 5.17. Clearly, the RZ-PAM scheme outperforms all other schemes. The AC-DMT scheme with $M = 4096$ and the DC-biased DMT scheme with $M = 64$ do not even match the performance of the RZ-PAM with $M = 4$ for $R_b/f_{\text{3dB}} \leq 12$. Although the performance of CAP has been fine tuned by means of best DC-bias, still it cannot reach the performance of RZ-PAM. RZ-PAM with $M = 2$ outperforms the 4-CAP at all R_b/f_{3dB} values. As explained in Section 5.3.3.2, the performance of CAP suffers due to the truncation of the filters and the clipping noise. Note that the complexity of the CAP transmitter is also much larger, since it requires a long FIR filter and a larger amplifier back-off. Therefore, RZ-PAM is a better choice for POF systems.

Lastly, we compare the performance the DMT schemes with PAM-FDE when channel state information
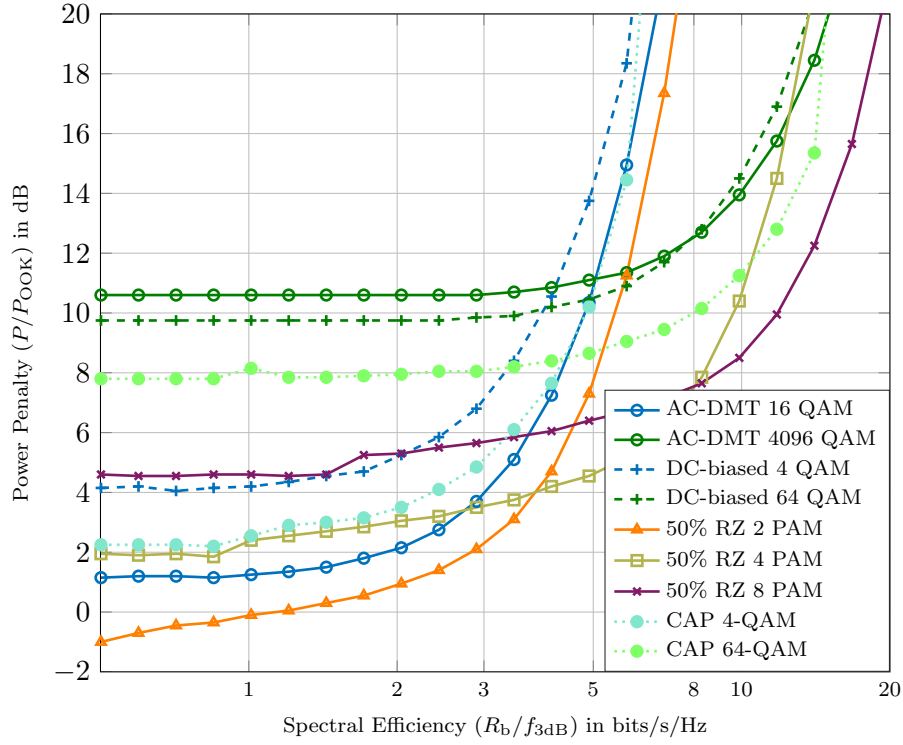
Figure 5.17.: Comparison of transmission schemes over a Gaussian low-pass channel. RZ-PAM outperforms all other schemes significantly.

is available at the transmitter. In this case, power-loading combined with bit-loading can be used for the DMT schemes. It can also be observed from Fig. 5.18 that the difference between the optimal bit-loading algorithm (Hughes-Hartogs) and the suboptimal Fischer-Huber algorithm is almost negligible for both AC-DMT and DC-biased DMT. For $R_{\mathrm{b}}/f_{3\mathrm{dB}}$ smaller than 12, AC-DMT performs better than DC-biased DMT. For DC-biased DMT, at $R_{\mathrm{b}}/f_{3\mathrm{dB}} \geq 5$, the suboptimal FH algorithm performs better than the optimal HH algorithm. This result is not caused by a simulation error, in fact it is due to the clipping noise [WCHG14]. We have also shown the result for RZ-PAM with the best modulation order selection at each $R_{\mathrm{b}}/f_{3\mathrm{dB}}$ value. The performance of RZ-PAM with the best selection of M is better than the AC-DMT and the DC-biased DMT schemes with optimal and suboptimal bit-loading algorithms. Note that the DMT schemes require the knowledge of full CSI at the transmitter while RZ-PAM requires only information about the modulation order and the symbol interval.

5.4.2. Performance in Channel 2 (VLC)

For VLC systems, the transmit signals need to be DC-balanced for a constant brightness. Therefore, we only consider DC-balanced schemes for the simulations. Since PAM does not provide DC-balance for rectangular pulses, we combine PAM with 5B6B line codes as discussed in Section 5.3.1.2. An FFT length of $N = 128$ with 25% overhead due to the CP has been assumed.

It can be seen from Fig. 5.5 that the $H_{\mathrm{Diff}}(f)$ contribution to $H_{\mathrm{MP}}(f)$ leads to distortions, but it also adds additional power to the received signal. The distortions can be removed by means of the discussed
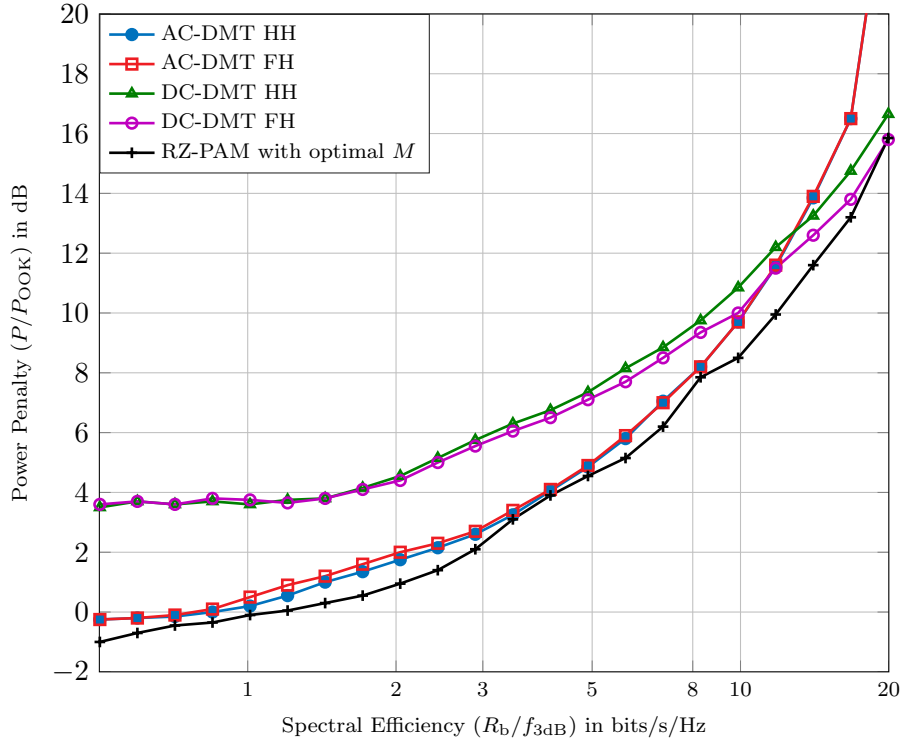
Figure 5.18.: Performance of DMT and PAM-FDE schemes with CSI at the transmitter. RZ-PAM with optimal modulation order outperforms the DMT schemes with optimal bit-loading that require full CSI at the transmitter.

transmission schemes, and all schemes benefit from the diffuse scattering, as shown in Fig. 5.19. Here, the power penalties compared to the reference scheme P_{OOK} are shown for the position R2, where we assume $h_{\mathrm{ch}}(t) = \delta(t)$ for P_{ref}. We show the results for this position since it suffers more from frequency selectivity. The results are shown not only for $H_{\mathrm{MP}}(f)$ but also for $H_{\mathrm{LoS}}(f)$ where both transfer functions are combined with $H_{\mathrm{LED}}(f)$.

The results in Fig. 5.19 show the same trends as for POF. The results show that the 4-PAM FDE scheme outperforms the DC-biased DMT scheme, and even the pseudo-ternary (pseudo-T) transmission works very well, if $R_{\mathrm{b}} \leq 500$ Mbps, and thus $R_{\mathrm{b}}/f_{\mathrm{3dB}} \leq 2.5$. As $H_{\mathrm{diff}}(f)$ adds additional power to the received signal, we observe a gain of roughly 2 dB for $H_{\mathrm{MP}}(f)$ as compared to the $H_{\mathrm{LoS}}(f)$ for lower data rates. Moreover, the results also indicate that there is negligible gain if we employ MMSE equalization for the PAM-FDE scheme.

We also consider a pure non-line-of-sight (NLoS) scenario, where we assume that all lines-of-sight are blocked. The results for such a scenario are shown in Fig. 5.20 for two receiver positions R2 and R3. In order to take into account that less power is received if all the LoS-paths are blocked, we still assume the normalization with respect to $H_{\mathrm{LoS}}(0)$ as discussed before. The multipath induced much higher penalties, but still all the FDE schemes are competitive or even better as the DC-biased DMT scheme. Furthermore, the multipaths have a different impact at different receiver positions. This is evident from the Fig. 5.20 where we achieve higher data rates at lower power penalties for the position R3 as compared
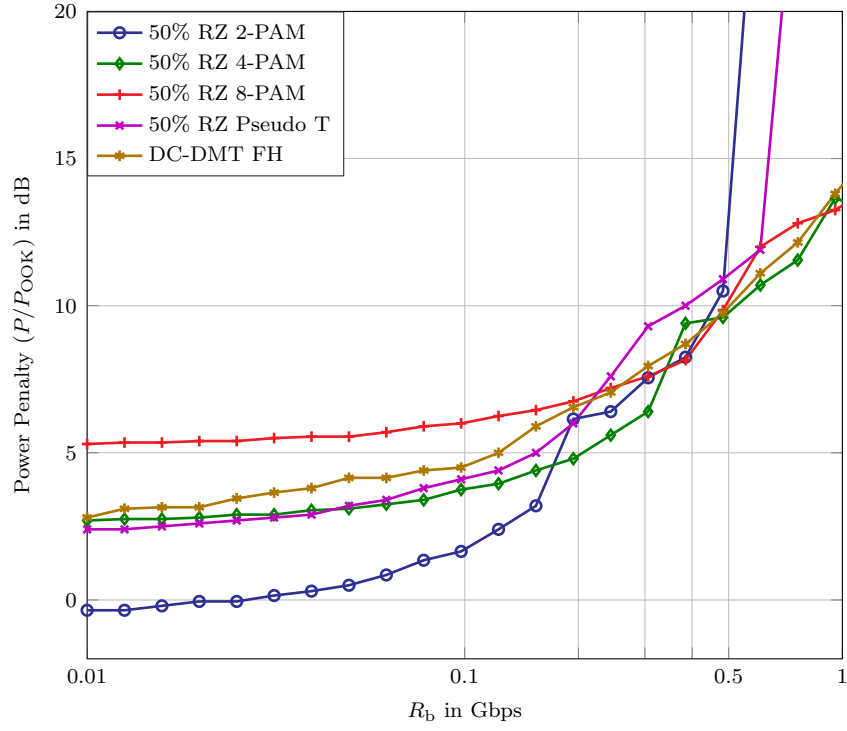
(a) Comparison of transmission schemes for R2 LoS scenario ($H_{\mathrm{LoS}}(f)$)
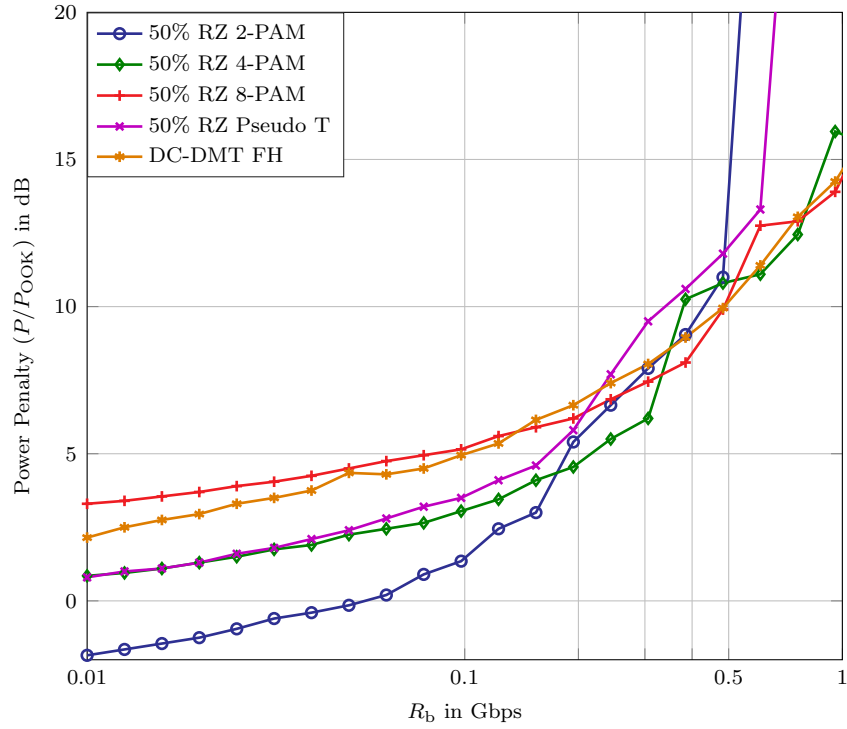
(b) Comparison of transmission schemes for R2 LoS and NLoS combined scenario $H_{\mathrm{MP}}(f)$)

Figure 5.19.: Performance comparison of transmission schemes for R2 position

to the position R2.
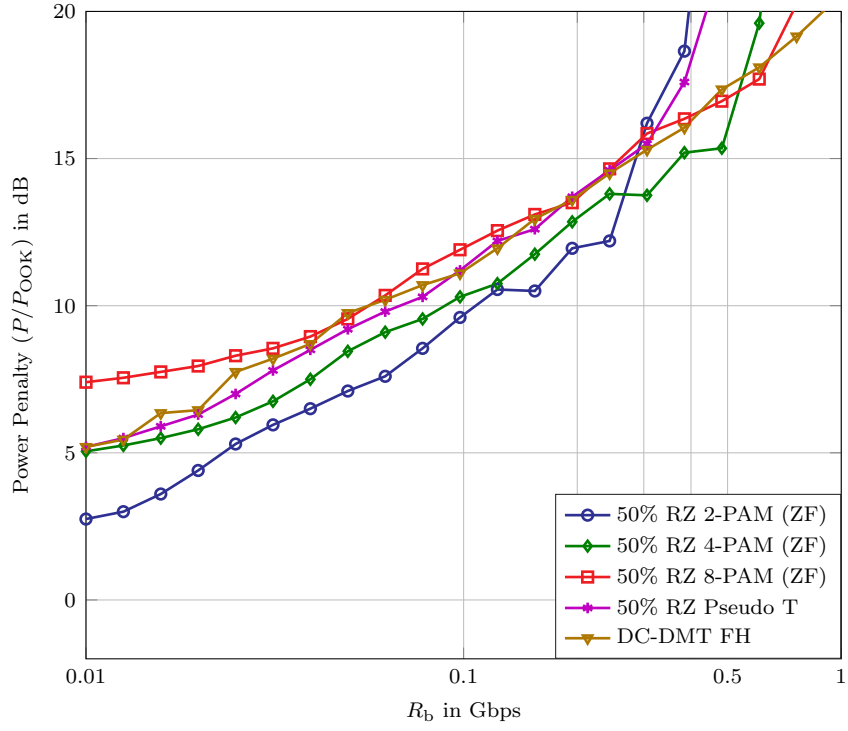
(a) Comparison of transmission schemes for the diffuse part of R2 position
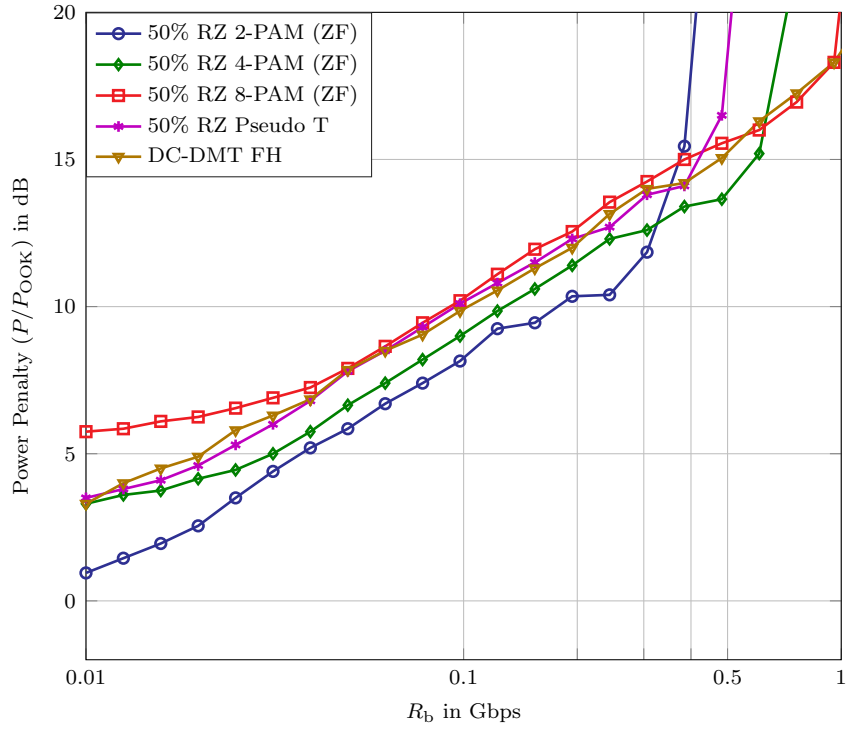
(b) Comparison of transmission schemes for the diffuse part of R3 position

Figure 5.20.: Comparison of transmission schemes for the diffuse part only (blocked LoS) for two receiver position. In both cases, a $H_{\text{LED}}(f)$ is additionally considered.

5.5. Conclusion

In this chapter, we have discussed various transmission schemes for optical systems with intensity modulation and direct detection. We have shown the performance of these schemes for two such optical systems, i.e., POFs and VLC. The results suggest that block transmission with FDE is a very good alternative to DMT schemes. Under the constraint of a low-pass channel with a Gaussian profile for POF systems, it has been shown that there is no performance gain for DMT schemes over PAM block transmission with FDE. Moreover, single subcarrier schemes such as OPAM or CAP also do not reach to the performance of PAM-FDE. Specifically, DC-biased OPAM shows a considerable loss compared to PAM-FDE, since the spectral centroid is not at zero. The optimal performance of these schemes can be obtained when CSI is available at the transmitter. Although DC-biased DMT loses against AC-DMT, but at a given average optical power, neither AC-DMT nor DC-biased DMT with optimal bit-loading offers a higher data rate as compared to PAM-FDE. Moreover, bit-loading enhanced DMT schemes require a more complex transmitter architecture since the whole magnitude frequency response needs to be known to the transmitter whereas in the case of PAM-FDE, only the information of the modulation order and the symbol interval is required at the transmitter.

For VLC systems, the performance of the proposed modulation schemes has been evaluated by considering two types of dispersion. The dispersion caused by the LED has been modeled by means of a Gaussian low-pass filter. The multipath propagation effect has been studied based on a scenario where four lamps are placed in a medium sized room at different locations. Here we decompose the total CIR into a LoS-part and a diffuse part. The results show that the impact of the diffuse part disappears at higher frequencies, whereas it provides additional power in the lower frequency range. Throughout the whole chapter, absolute powers have not been considered. Instead, the power penalty caused by the dispersion has been estimated. We have shown that PAM-FDE combined with line-coding or partial-response coding is a serious alternative to DC-biased DMT, even if bit-loading is used in the latter case. CAP transmission, i.e., DC-biased single subcarrier QAM with a RRC pulse-shaping (CAP), seems to be less attractive because the transmitter requires additional high order FIR filters and a LED driver with an increased dynamic range. Moreover, its performance cannot compete with PAM-FDE or DMT.

6. Non-linear Techniques for Dispersive Optical Systems

In the previous chapter, we have shown that PAM block transmission with linear FDE has not only a better performance than other state-of-the-art schemes but also has other advantages such as lower PAPR. Although linear FDE can fully compensate ISI, it suffers from noise enhancement. Therefore, non-linear techniques such as decision feedback equalization (DFE) and Tomlinson-Harashima precoding (THP) can enhance the system performance significantly in dispersive optical channels. But these techniques have a very high computational complexity, thus making them less appealing for practical applications. In the literature, the performance of PAM transmission with these schemes is often not evaluated for optical systems using IM/DD constraints. Therefore, in this chapter, we expand our investigations to non-linear equalization and precoding techniques for PAM transmission. Specifically, we present a new transceiver design for PAM block transmission that employs a hybrid equalization technique. This hybrid equalization technique has a lower computational complexity as compared to the conventional non-linear equalization techniques but achieves the same performance. This equalization technique still employs a linear frequency domain equalizer, but an additional time domain feedback filter with significantly fewer taps is added. Such a hybrid equalization technique still suffers from error propagation, therefore a solution to solve this problem is also discussed.

6.1. Introduction

Optical Systems such as POF and VLC suffer from bandwidth limitation. The bandwidth limitation occurs due to the source (LED) or due to the multipath propagation channel. In dispersive channels, the transmitted pulses are received with some inter symbol interference (ISI). More precisely, a received symbol depends not only on the symbol sent at that time, but, in general, on the previous and future transmitted symbols. ISI is mainly caused by the bandwidth limited and dispersive nature of the propagation channel. The ISI caused by the previous and future symbols are called pre-cursor and post-cursor ISI, respectively. Due to the dispersive nature of the optical channel, efficient and robust equalization techniques need to be employed that can mitigate both types of ISI (pre-cursor and post-cursor). The equalization can be performed either in the frequency domain or in the time domain. The choice is determined by which domain leads to a smaller computational complexity to achieve the same performance. Frequency domain equalization is computationally simpler than the corresponding time domain equalization for channels with a severe delay spread. The time and frequency domain equalizers can be further divided into two broad categories based on their structure: linear and non-linear. The non-linear equalizers outperform the linear equalizers in dispersive optical channels but at the cost of a higher computational complexity.

In this chapter, we discuss some of the equalization and precoding techniques that can be combined with the PAM transmission. In the previous chapter, we have already discussed the linear frequency domain equalization techniques. Therefore, we expand our investigations to the non-linear equalization and precoding techniques such as decision feedback equalization (DFE) and Tomlinson-Harashima pre-

coding (THP). In such techniques, a feedforward filter is used to remove pre-cursor ISI while a feedback filter is used for post-cursor ISI. But these techniques have a very high computational complexity. Specifically, DFE suffers from error propagation and THP requires full channel state information (CSI) at the transmitter. A low complexity non-linear equalization technique is also discussed in the last part of the chapter. This equalization technique still employs a linear frequency domain equalizer, but an additional time domain feedback filter with significantly fewer taps is added. Such a hybrid equalization technique also suffers from error propagation which is resolved by using a unique word (UW) instead of a cyclic prefix (CP). Moreover, as discussed in the previous chapter, spectrally efficient transmission schemes combined with robust equalization techniques at the receiver are required for such systems in order to cope with the bandwidth limitation of the LED/LED-driver combination and the multipath propagation environment. There are several papers on this topic which propose different solutions for these optical systems. For instance, a 3-Gbits/s transmission scheme for 10 m of POF used for an automotive physical layer is presented in [WMS13] and a combination of THP with an adaptive time domain equalizer at the receiver is recommended. In [WL+12], a CAP transmission with DFE is recommended for VLC. However, in this chapter, we show that the non-linear techniques such as THP and DFE outperform the linear time and frequency domain equalization, at the expense of a very high computational complexity. Therefore, we recommend a low-complex but efficient transceiver design for these dispersive optical systems. Moreover, we not only evaluate the performance of PAM transmission with different equalization and precoding techniques but also compare it with other schemes that are discussed in Chapter 5.

6.2. System Model
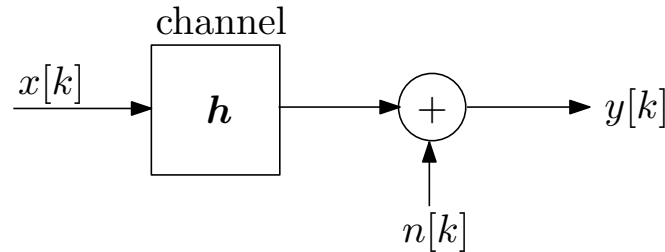
Figure 6.1.: Block diagram of the system model.

We assume a linear time invariant system as shown in Fig. 6.1. The received signal $y[k]$ in the symbol-spaced sampled discrete time form is given by

$$y[k] = \sum_{m=-L}^{L} h[m]x[k-m] + n[k], \tag{6.1}$$

where k is the discrete-time sample index, $x[k]$ is the transmitted signal and the noise $n[k]$ is assumed to be additive white Gaussian noise (AWGN).

Fig. 6.2 shows an example of a sampled POF channel (channel 1, as discussed in Section 5.2.2.1) with $L = 4$. The channel impulse response $h[m]$ is symmetrical where the total number of samples is equal to $2L + 1$. We use positive and negative index values for this 9 tap channel to indicate that

the main tap is not the first one. Thus, the taps other than the main tap with index 0 (left and right components around the main one) in Fig. 6.2 cause pre-cursor and post-cursor ISI. This type of channel is non-causal [RSR13], although it is just a channel with an even symmetry with respect to the main sample of the impulse response. Eq. (6.1) can be further elaborated as,
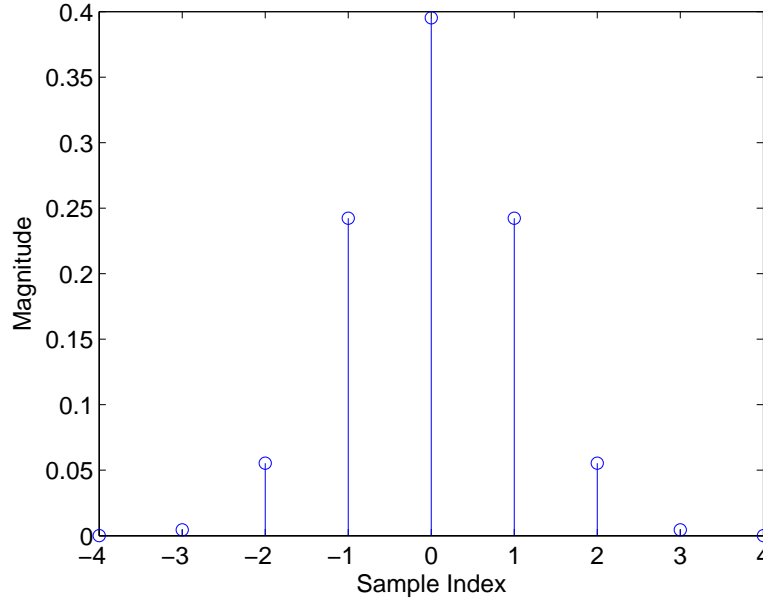
Figure 6.2.: Example of sampled Gaussian impulse response of POF channel.

$$
y[k] = \underbrace{\sum_{m=-L}^{-1} h[m]x[k-m]}_{\text{Pre-cursor ISI}} + \underbrace{h[0]x[k]}_{\substack{\text{Information} \\ \text{bearing cursor}}} + \underbrace{\sum_{m=1}^{L} h[m]x[k-m]}_{\text{Post-cursor ISI}} + n[k] \tag{6.2}
$$

The product of $h[0]x[k]$ is the desired signal component (main cursor), all other components in the Eq. (6.2) contribute towards the pre-cursor and post-cursor ISI. The positive and negative sample index values indicate the left and right samples of the main tap. The goal of an equalizer is to eliminate both of those ISI components effectively.

6.3. Decision Feedback Equalization

Non-linear equalization techniques such as DFE provide a better performance for optical systems since they completely remove the ISI. The DFE, in its basic implementation, involves only a single feedback loop as shown in Fig. 6.3. Here, $\boldsymbol{b}^H$ represents the vector containing the feedback filter coefficients. The feedback filter is used to reduce the ISI by utilizing the information of the previous symbols. Due to the decision device, the operation of the DFE is non-linear. But it can be analyzed using linear techniques if the outputs of the decision device are assumed to be correct.

In order to illustrate the mechanism of equalization by using the feedback filter, we assume a channel
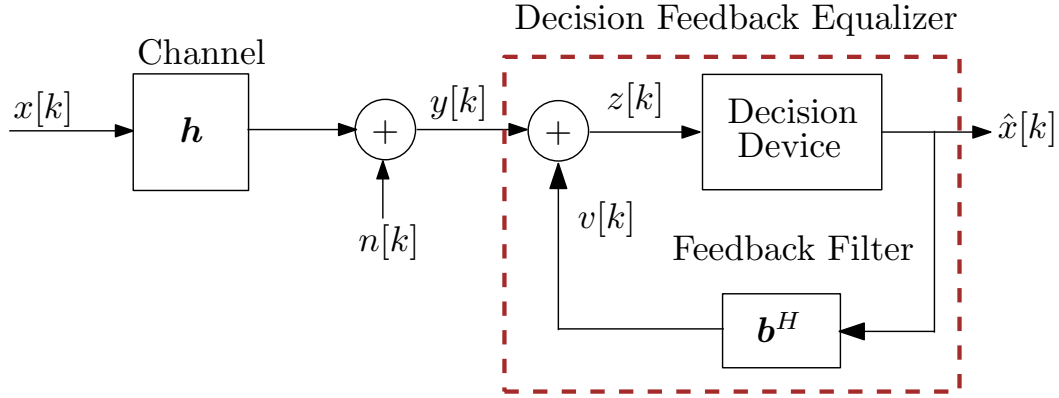
Figure 6.3.: Block diagram of the system including the basic implementation of the DFE

$\tilde{\boldsymbol{h}} \in \mathbb{R}^{2L+1}$ with its first tap as the main cursor $\tilde{h}[0]$ (which is the largest coefficient of the channel), i.e., the channel causes only post-cursor ISI (Eq. (6.2)). Although this is not true for the POF optical channel, this assumption is used to make the analytical explanation simple. Therefore, the received signal $y[k]$ over this channel can be expressed as

$$y[k] = \sum_{m=0}^{2L} \tilde{h}[m]x[k-m] + n[k] \tag{6.3}$$

$$= \tilde{h}[0]x[k] + \sum_{m=1}^{2L} h[m]x[k-m] + n[k], \tag{6.4}$$

where the channel impulse response $\tilde{\boldsymbol{h}}$ is

$$\tilde{\boldsymbol{h}} = \begin{bmatrix} \tilde{h}[0] & \tilde{h}[1] & \tilde{h}[2] & \cdots & \tilde{h}[2L] \end{bmatrix}^T. \tag{6.5}$$

Moreover, the feedback filter must be strictly causal so that it does not have a direct path from its output to its input, since previous decisions are being fed back through this filter. This requires that first coefficient of the feedback filter $\boldsymbol{b}^H$ is $b[0] = 0$. Therefore, we can express the feedback filter as

$$\boldsymbol{b}^H = \begin{bmatrix} 0 & -\tilde{h}[1] & -\tilde{h}[2] & \cdots & -\tilde{h}[2L] \end{bmatrix}. \tag{6.6}$$

Assuming that all previous decisions are correct, i.e., $\hat{x}[k-m] = x[k-m]$, the output of the feedback filter becomes,

$$v[k] = -\left(\sum_{m=1}^{2L} \tilde{h}[m]\hat{x}[k-m] \right) = -\left(\sum_{m=1}^{2L} \tilde{h}[m]x[k-m] \right), \tag{6.7}$$

Next, we can write the signal at the input of the decision device as

$$z[k] = y[k] + v[k] \tag{6.8}$$

$$= \tilde{h}[0]x[k] + \sum_{m=1}^{2L} \tilde{h}[m]x[k-m] - \sum_{m=1}^{2L} \tilde{h}[m]x[k-m] + n[k] \tag{6.9}$$

$$= \tilde{h}[0]x[k] + n[k]. \tag{6.10}$$

This simple implementation is efficient for eliminating only the post-cursor ISI. Since the optical channel has both pre-cursor and post-cursor ISI, as shown in Eq. (6.2), an additional feedforward filter is used to force the channel response to have only post-cursor ISI. This is the reason why decision feedback equalizers generally contain an additional feedforward filter as shown in Fig. 6.4. These two filters are required to efficiently eliminate both types of ISI. The filter coefficients can be derived using either of
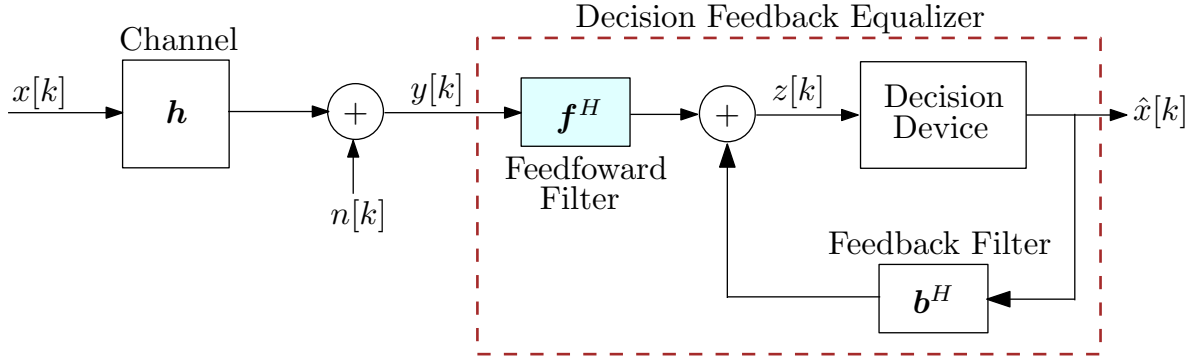
Figure 6.4.: Block diagram of the system including a DFE with a feedforward filter

the ZF or the MMSE criterion. In this work, we use the MMSE algorithm for our simulations since it is expected to perform better than the ZF algorithm. The MMSE algorithm is applied at the input of the decision device and the error variance before the decision is aimed to be minimized. The cost function is defined as

$$J(\boldsymbol{f}, \boldsymbol{b}) = \mathbb{E}\left\{|e[k]|^2\right\} \tag{6.11}$$

$$= \mathbb{E}\left\{|x[k] - z[k]|^2\right\} \tag{6.12}$$

$$= \mathbb{E}\left\{|x[k] - (\boldsymbol{f}^H\boldsymbol{y} + \boldsymbol{b}^H\hat{\boldsymbol{x}})|^2\right\}, \tag{6.13}$$

where $\boldsymbol{f}^H = \begin{bmatrix} f[0] & f[1] & \cdots & f[F-1] \end{bmatrix}$ is the feedforward filter with a length of F and $\boldsymbol{b}^H = \begin{bmatrix} 0 & b[1] & \cdots & b[B-1] \end{bmatrix}$ is the feedback filter with a length of B. Here $b[0] = 0$ since the feedback filter is strictly causal as mentioned before.

We assume that all decisions of the decision device are correct, i.e., $\hat{\boldsymbol{x}} = \boldsymbol{x}$. Therefore, we can rewrite the cost function in terms of the input data as

$$J(\boldsymbol{f}, \boldsymbol{b}) = \mathbb{E}\left\{|x[k] - (\boldsymbol{f}^H\boldsymbol{y} + \boldsymbol{b}^H\boldsymbol{x})|^2\right\}. \tag{6.14}$$

In Eq. (6.14), it can be seen that $(x[k] - \boldsymbol{b}^H\boldsymbol{x})$ component is equivalent to the product of a row vector $\bar{\boldsymbol{b}}^H = \begin{bmatrix} 1 & -b[1] & -b[2] & \cdots & -b[B-1] \end{bmatrix}$ with $\boldsymbol{x} = \begin{bmatrix} x[k] & x[k-1] & \cdots & x[k-B+1] \end{bmatrix}^T$. Therefore, the cost function can be rewritten as follows,

$$J(\boldsymbol{f}, \bar{\boldsymbol{b}}) = \mathbb{E}\left\{|\bar{\boldsymbol{b}}^H\boldsymbol{x} - \boldsymbol{f}^H\boldsymbol{y}|^2\right\} \tag{6.15}$$
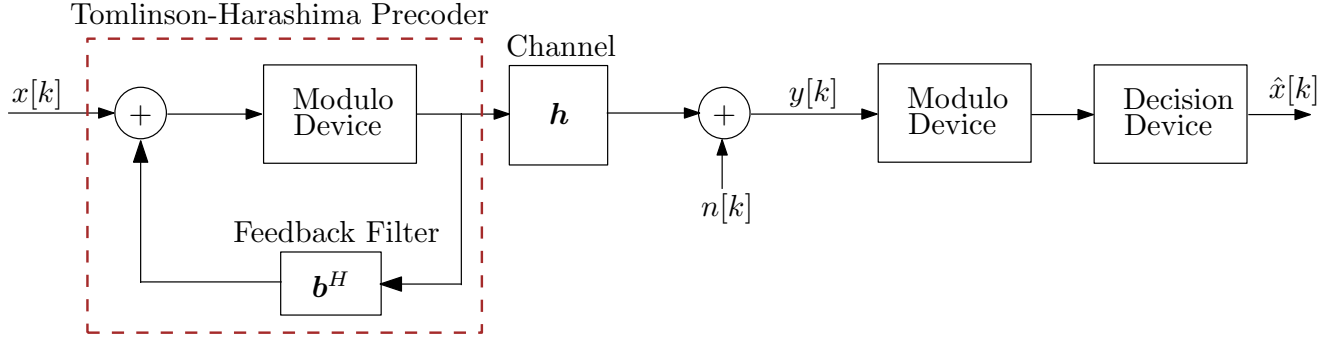
Figure 6.5.: Block diagram of the system including THP

The filter coefficients $\boldsymbol{f}^H$ and $\bar{\boldsymbol{b}}^H$ are determined by minimizing the cost function. This task is accomplished in [Say03] by firstly minimizing the cost function over one of the vectors, and then, determining the other one. As a result, the filter vectors containing the optimum coefficients are given in [Say03] as

$$\bar{\boldsymbol{b}}_{\mathrm{opt}}^H = \frac{\boldsymbol{e}_1^T \boldsymbol{R}_\delta^{-1}}{\boldsymbol{e}_1^T \boldsymbol{R}_\delta^{-1} \boldsymbol{e}_1}, \tag{6.16}$$

$$\boldsymbol{f}_{\mathrm{opt}}^H = \bar{\boldsymbol{b}}_{\mathrm{opt}}^H \boldsymbol{R}_{xy} \boldsymbol{R}_{yy}^{-1}, \tag{6.17}$$

where $\boldsymbol{e}_1 = \begin{bmatrix} 1 & 0 & 0 & \cdots & 0 \end{bmatrix}^T \in \mathbb{R}^{(B+1)\times 1}$ is the first basis vector and $\boldsymbol{R}_\delta = \boldsymbol{R}_{xx} - \boldsymbol{R}_{xy}\boldsymbol{R}_{yy}^{-1}\boldsymbol{R}_{yx}$ is introduced. Further details of the derivation of $\bar{\boldsymbol{b}}_{\mathrm{opt}}^H$ and $\boldsymbol{f}_{\mathrm{opt}}^H$ can be found in Appendix C.

6.4. Tomlinson-Harashima Precoding

Although the DFE is a better solution than linear equalization for channels having both pre-cursor and post-cursor ISI, it has two major drawbacks. Firstly, we assume that the decisions at the output of the decision device are absolutely correct and if this assumption does not hold true, the erroneous decisions cause a problem of error propagation, that is, the following decisions would include errors because of that triggering error. In practice, the probability of the occurrence of this phenomenon increases as the constellation distance between the symbols decreases. Secondly, the integration of channel coding schemes with the DFE is not straightforward. Employing a channel decoder simply at the output of the DFE would be inefficient, because the error propagation may destroy the coding gain. Therefore, it is feasible to have a channel decoder as a part of the decision device for reliable and accurate decisions. But, in such a case, the channel encoder will be a part of the feedback loop and it will increase the system complexity too much as symbol by symbol decisions are performed in the DFE.

These disadvantages of the DFE can be mitigated by employing a similar feedback equalization algorithm at the transmitter if the CSI is known. This type of pre-equalization can be implemented by using the Tomlinson-Harashima precoding (THP). The conventional THP uses a feedback filter at the transmitter and modulo devices at both the transmitter and the receiver. Implementing a feedback filter at the transmitter eliminates the error propagation problem, because the noise does not come into play at the transmitter yet. It also makes the integration of the channel coding schemes straightforward. The

feedback filter is again causal, that is, $b[0] = 0$ as in the case of the DFE. The modulo operation in the classical THP structure is required to keep the sum of the input data and the feedback value within the constellation interval. If the input to the modulo device is greater than the modulation order M, $2M$ is subtracted until the result is less than M and if the input is less than $-M$, $2M$ is added until the output of the modulo device is greater than $-M$. As an example, this function is also schematically represented in Fig. 6.6 for a biploar PAM with $M = 4$. As seen in the figure the output of the modulo device is kept in the interval of $[-4, +4]$ for 4-PAM modulation.
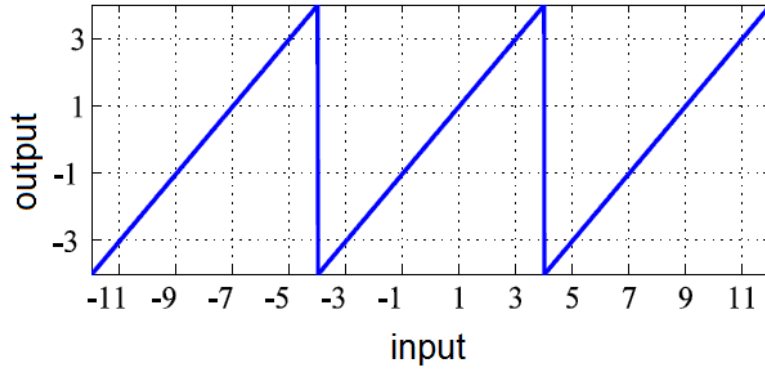
Figure 6.6.: Input-output relation of $2M$-modulo function for 4-PAM modulation

As optical systems with IM/DD require a unipolar PAM modulation constellation, a change is made to the classical THP modulo device. That is, the bipolar input symbols are shifted from an integer valued PAM constellation $[-M + 1, M - 1]$ to the soft valued range $[0, 2M]$ at the output of modulo device. The modulo operation is like adding a unique value to the input symbol at each time instant such that the channel input signal lies in the interval $[0, 2M]$. Even though the operation of the modulo device is non-linear, the mechanism of the THP can be described by using its equivalent linear model which is shown in Fig. 6.7. In this figure, the addition of $d[k]$ corresponds to the operation of the modulo device, $c[k]$ is the transmit signal, and $f[k]$ is the output of the feedback filter. Moreover, these signals can be expressed as,

$$v[k] = x[k] + d[k] \tag{6.18}$$

$$c[k] = v[k] + f[k]. \tag{6.19}$$

We again assume for the explanation purposes that the channel causes only post-cursor ISI, i.e., the first element of the channel vector $\tilde{\boldsymbol{h}}$ is again chosen as the main tap. The received signal is given by

$$y[k] = \sum_{m=0}^{2L} \tilde{h}[m]c[k - m] + n[k] \tag{6.20}$$

$$= \tilde{h}[0]c[k] + \sum_{m=1}^{2L} \tilde{h}[m]c[k - m] + n[k]. \tag{6.21}$$

The same feedback filter coefficients as in the case of DFE are chosen in the following form,

$$\boldsymbol{b}^H = \begin{bmatrix} 0 & -\tilde{h}[1] & -\tilde{h}[2] & \cdots & -\tilde{h}[2L] \end{bmatrix} \tag{6.22}$$

Therefore, the output of the feedback filter becomes,
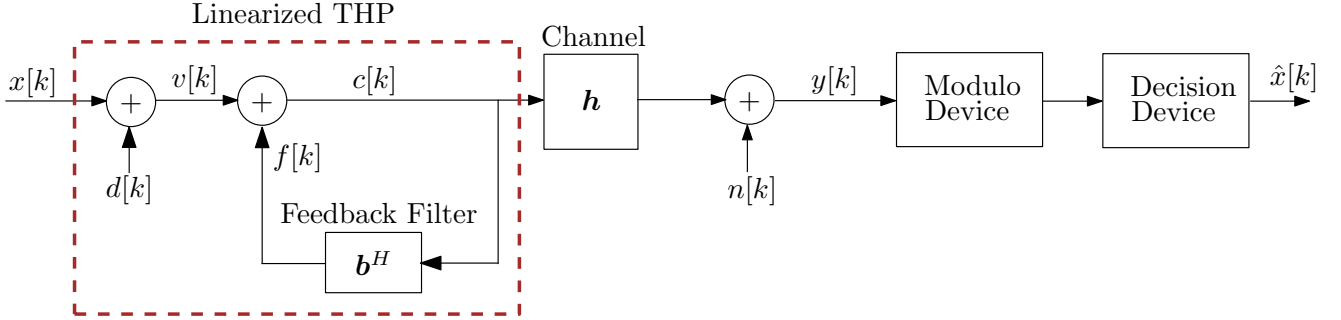
Figure 6.7.: Block diagram of the system including equivalent linear model of THP

$$f[k] = -\sum_{m=1}^{2L} \tilde{h}[m]c[k-m] \tag{6.23}$$

Using this results, we can rewrite Eq. (6.21) as,

$$
\begin{aligned}
y[k] &= \tilde{h}[0]c[k] + \sum_{m=1}^{2L} \tilde{h}[m]c[k-m] + n[k] \\
&= \tilde{h}[0]c[k] - f[k] + n[k] \\
&= \tilde{h}[0]\left(v[k] + f[k]\right) - f[k] + n[k].
\end{aligned} \tag{6.24}
$$

The channel is assumed to be *monic* which means that $h[0]$ is 1 in Eq. (6.24). This results in

$$
\begin{aligned}
y[k] &= v[k] + n[k] \\
&= x[k] + d[k] + n[k].
\end{aligned} \tag{6.25}
$$

At the receiver, the modulo operation is again performed to remove the addition of $d[k]$ from $y[k]$. As in the case of the DFE, this basic structure of THP can only be used to remove all post-cursor ISI efficiently. Hence, we need an additional feedforward equalizer at the receiver to mitigate the impact of the pre-cursor ISI, as shown in Fig. 6.8. This structure is almost similar to the DFE implementation but the feedback filter is moved to the transmitter. Therefore, the feedforward and the feedback filter coefficients defined by Eq. (6.16) and Eq. (6.17) can also be used in this precoding structure. As a result, it can be stated that, DFE and THP schemes in their basic form (without feedforward filters) have the ability to efficiently eliminate only post-cursor ISI. But since the optical channels cause pre-cursor and post-cursor ISI, an additional feedforward filter is required to efficiently remove these both types of ISI.
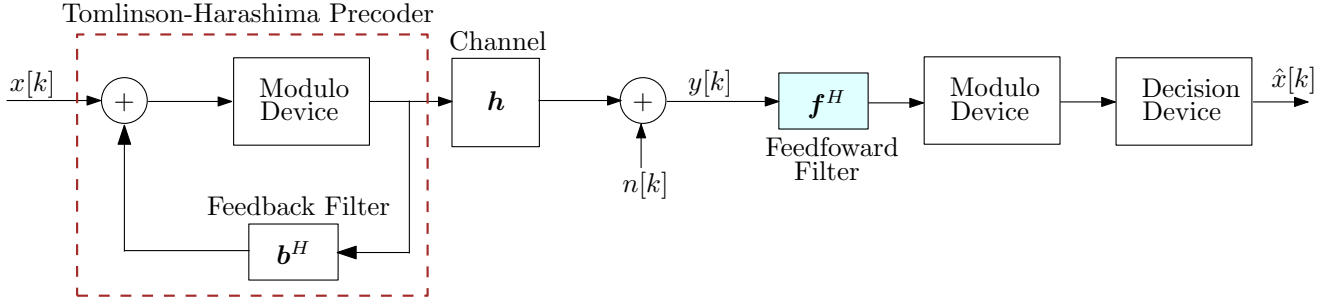
Figure 6.8.: Block diagram of the system including THP with a feedforward filter

6.5. Hybrid Detection Scheme

The introduction of a feedback filter in DFE improves the system performance since the ISI can be canceled in two subsequent steps but at the cost of a much higher complexity. The computational complexity of the DFE can be significantly reduced by employing a hybrid non-linear equalization technique, where the feedforward filter processes a block of data in the frequency domain, as in linear FDE, and the feedback filter operates on symbol by symbol basis in the time domain. This hybrid equalization technique was first proposed in [FABSE02] for single-carrier (SC) systems in RF communications. A joint design to calculate the frequency domain feed-forward filter and time domain feedback filter weights has also been presented in [FABSE02]. Block transmission with FDE offers a straightforward implementation for such a hybrid equalizer since only an additional time domain equalizer is added in the feedback loop after linear FDE, as shown in Fig. 6.9.
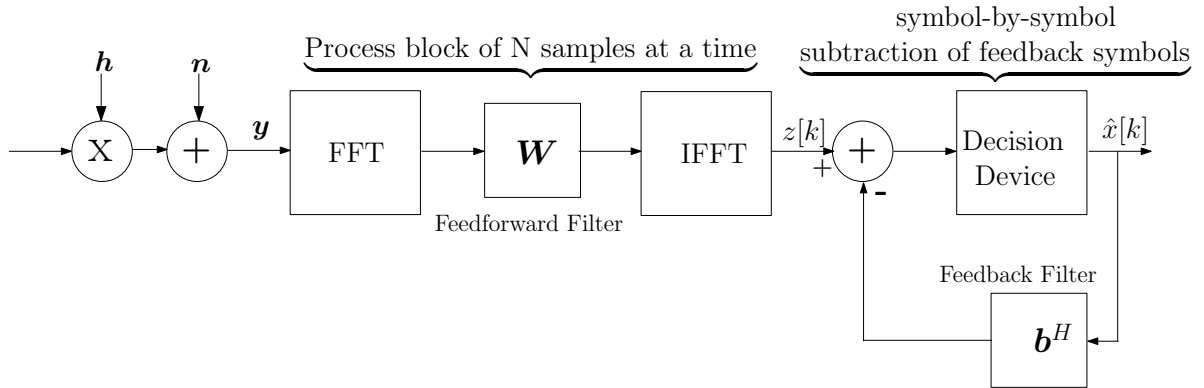
Figure 6.9.: Block diagram of Hybrid Equalizer

In the first step, the received symbols are multiplied by a forward filter in the frequency domain. This feedforward filter has N complex frequency domain coefficients $W_n \; \forall n = 1, \cdots, N$ which are given by

$$W_n = \frac{H_n^*[1 - \sum\limits_{i=1}^{B} b_i \exp(-j2\pi\frac{ni}{N})]}{\frac{\sigma_n^2}{\sigma_x^2} + |H_n|^2},$$

(6.26)

where σ_n^2 is the noise variance, σ_x^2 is the signal variance, b_i denotes the i-th feedback filter coefficient, and B is the length of feedback filter. After the frequency domain equalization, the equalized symbols

are converted to the time domain by applying the IFFT. In the second step, the time domain output is sampled once per symbol interval where the feedback filter coefficients $\boldsymbol{b}^H$ of length B are calculated as

$$\boldsymbol{b}^H = \boldsymbol{V}^{-1}\boldsymbol{v}. \tag{6.27}$$

Here the quantities $\boldsymbol{V}$ and $\boldsymbol{v}$ are calculated as

$$[\boldsymbol{V}]_{m,i} = \sum_{n=0}^{N-1} \frac{\exp(-j2\pi\frac{n(i-m)}{N})]}{\frac{\sigma_n^2}{\sigma_x^2} + |H_n|^2}$$

$$[\boldsymbol{v}]_m = \sum_{n=0}^{N-1} \frac{\exp(j2\pi\frac{nm}{N})]}{\frac{\sigma_n^2}{\sigma_x^2} + |H_n|^2},$$

where $1 \leq m, i \leq B$ and $[\boldsymbol{V}]_{m,i}$ denotes the m, i-th components of the matrix $\boldsymbol{V}$. Due to the block structure, the feedback filter is not able to cancel interference more than the length of the CP. Therefore, the number of the feedback filter coefficients should be less than or equal to the length of the CP. Moreover, to minimize complexity, the number of feedback coefficients B should be kept as low as possible. This can be accomplished if the indices $i \in B$ correspond to the relative estimated delays of the largest channel impulse response echoes.

A major challenge of the DFE is its error propagation problem. This problem can also be resolved in a hybrid equalizer via two ways. Firstly, the length of the time domain feedback filter is limited by only a few taps which not only limits the error propagation but also reduces the complexity of the equalizer. Secondly, a unique word (UW) can be used instead of a CP, as shown in Fig. 6.10. Note that adding a UW to the PAM block transmission scheme is different to the UW-OFDM signaling concept that has been discussed in Part 1. In UW-OFDM, we add redundancy in the frequency domain to get zeros at the tail of the IFFT output. Then in the time domain, a UW is added. However, in PAM block transmission, PAM data symbols are already in the time domain, so we can add a UW according to the Fig. 6.10. Moreover as described in Part 1, a UW refers to a deterministic sequence which is known at the transmitter and the receiver. Since a CP is only used to have cyclic convolution, this property can still be maintained by using a UW. Furthermore, a UW can advantageously be used for synchronization and channel estimation purposes. Since the UW is known at the receiver, the error propagation problem is also resolved for the hybrid equalizer . Therefore, we propose to use a UW instead of a CP for PAM block transmission.

6.6. Simulation Results

The performance comparison of different schemes is evaluated in terms of power penalties as discussed in Section 5.2. In this work, we have used a bit error ratio $p_{\rm b} = 10^{-3}$ in Eq. (5.5) for the calculation of power penalties. Moreover, we have assumed perfect channel knowledge and time synchronization. The CP/UW overhead is 12.5 % with an FFT size of $N = 128$ for all block-based transmission schemes. Note that we have used a UW instead of a CP for PAM block transmission schemes.

We first discuss the performance of PAM transmission combined with different equalization techniques.

(a) PAM block transmission with a CP

(b) PAM block transmission with a UW
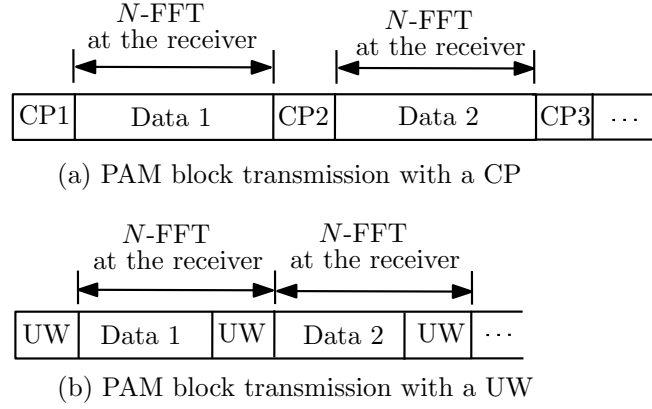
Figure 6.10.: PAM block transmission with a CP or a UW

In Fig. 6.11a, the performance of 4 NRZ-PAM with a hybrid equalizer is shown for different feedback filter taps. Here, we have used a UW instead of a CP. Moreover, we have employed an MMSE based criterion to calculate the frequency domain and the time domain filter weights as discussed in the previous sections. As expected, with an increasing number of feedback filter taps, the performance improves. There is a significant gain between a 1-tap feedback equalizer and a 3-tap equalizer, but thereafter the gain is negligible with an increasing number of taps. The performance of NRZ-PAM with different equalization techniques and THP is compared in Fig. 6.11b. We have used a 13-tap feedforward filter for all time domain equalization techniques. Moreover, a 11-tap feedback filter is used for DFE and THP. We have observed in our simulations that the gain is negligible even if we use more taps for the considered channel models. All filter weights are calculated using the MMSE criterion. As evident from the results, the performance of PAM with linear frequency domain equalization (FDE) is slightly worse than linear time domain equalization (TDE). This is due to the fact that a UW/CP is inserted periodically to perform FDE at the receiver. Therefore, some energy is utilized for this purpose. On the other hand, the computational complexity of FDE is much lower than TDE. The performance of NRZ-PAM with linear equalization techniques is similar to the non-linear equalization techniques for low data rates ($R_{\mathrm{b}}/f_{3\mathrm{dB}} \leq 5$). But the gain of non-linear techniques is significant at higher data rates. This is due the fact that the optical channel causes pre- and post-cursor ISI and the linear equalization techniques cannot fully mitigate the ISI. It can also be seen that the hybrid equalizer has a similar performance as the DFE, but with a significantly smaller computational complexity. Note that the hybrid equalizer uses only a 5-tap feedback filter while the DFE employs an 11-tap feedback filter. Moreover, we have used a UW instead of a CP to resolve the error propagation of the DFE. Furthermore, it can be observed that the DFE and the hybrid equalizer are slightly more power efficient than THP at low data rates. This is because of the modulo and precoding losses of THP. At higher data rates, the performance of THP is similar to the DFE and the hybrid equalization technique. Although the error propagation problem of the DFE can be resolved by THP, THP has a much higher computational complexity and also requires CSI at the transmitter. Clearly, PAM block transmission combined with a hybrid equalizer is a better choice due to its low complexity and better performance.

In Fig. 6.12, the performance of the transmission techniques discussed in Chapter 5 is compared using the POF channel (channel 1). For very low values of R_{b}, the penalty depicts the power efficiency of
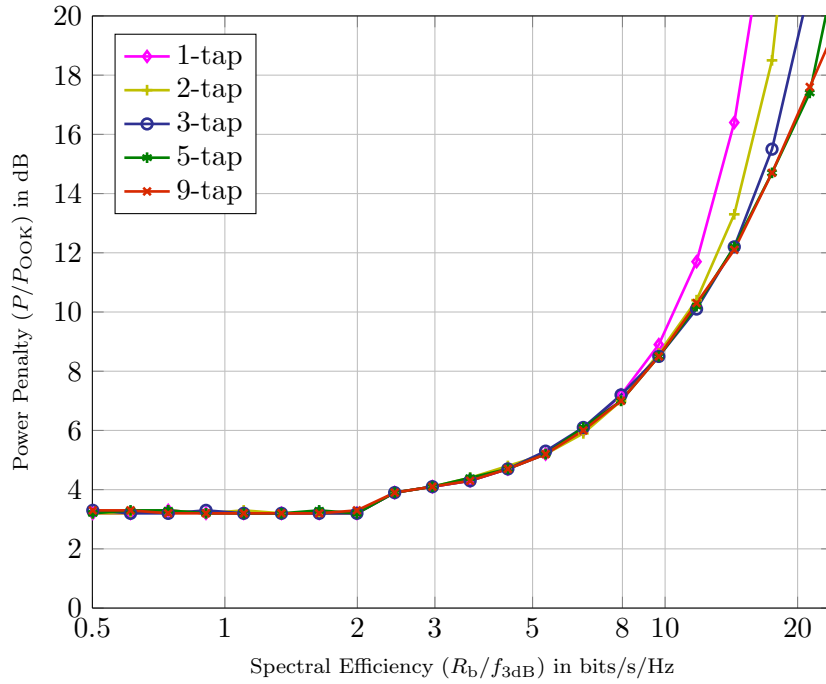
(a) Performance of NRZ-PAM with hybrid equalizer using different number of feedback filter taps. The gain is negligible after 5-tap feedback equalizer.
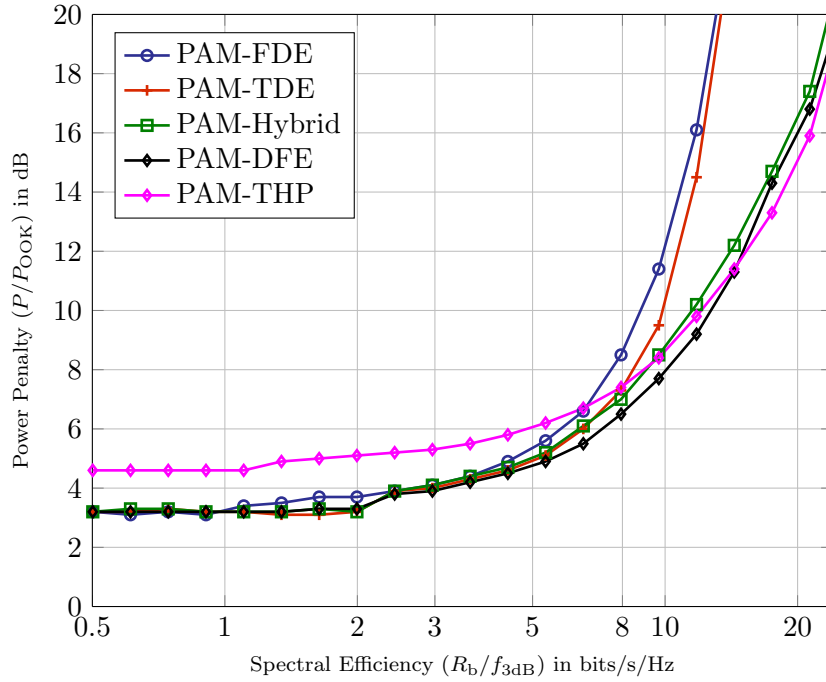
(b) Performance of PAM-NRZ with different equalizers

Figure 6.11.: Performance Comparison of 4 NRZ-PAM transmission with different equalization techniques. A 15-tap feedforward filter is used for TDE, DFE, and THP while a 13-tap feedback filter is used for DFE and THP. The hybrid equalizer employs only 5-tap feedback filter.

the various transmission schemes in a flat AWGN channel. For instance, OOK in such an ideal AWGN channel has a normalized power requirement of 0 dB. The increase in the curves corresponds to the
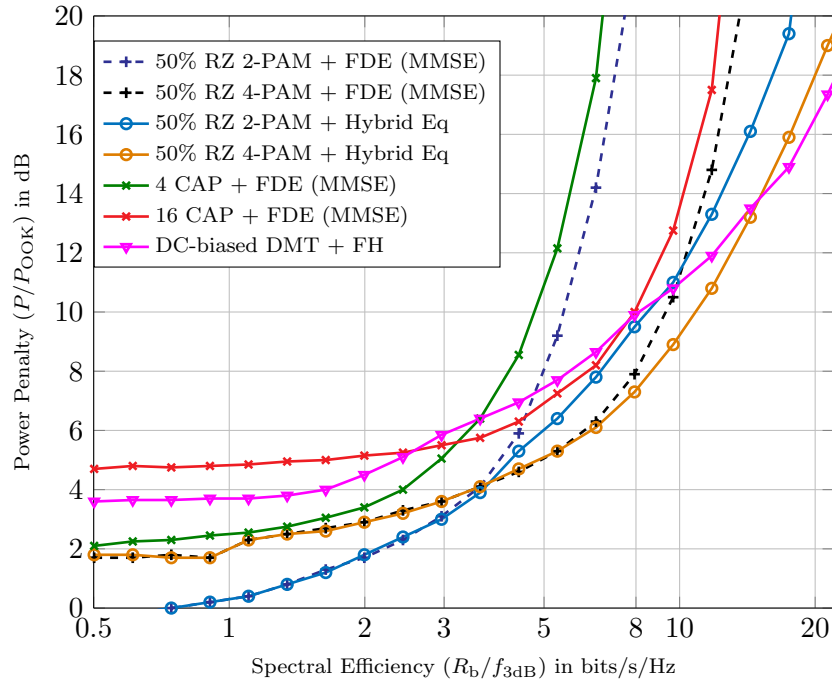
(a) Performance comparison of transmission schemes for POF. RZ-PAM with hybrid equalizer outperforms all other schemes significantly.
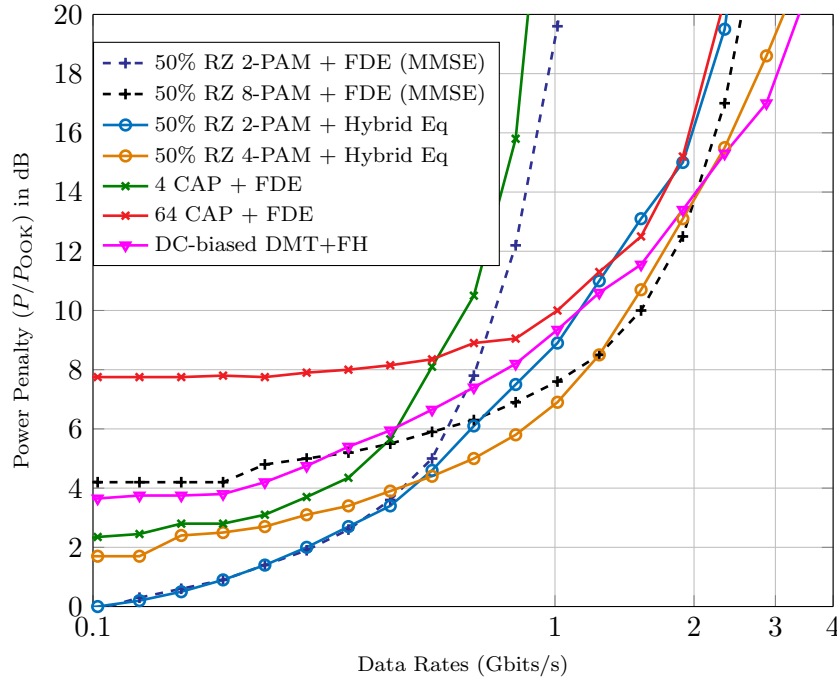
(b) Data rates for different transmission schemes for SI-POF of 10 m (MOST 150 standard). RZ-PAM schemes with linear and hybrid equalization achieve the best data rates at lower power penalties.

Figure 6.12.: Performance Comparison of transmission strategies.

penalty caused by the Gaussian lowpass filter. Here, we have shown results for PAM block transmission with a 50 % RZ pulse shaping filter since it exhibits a better performance compared to a NRZ filter.

First we discuss the performance of these schemes in terms of spectral efficiency ($R_{\mathrm{b}}/f_{\mathrm{3dB}}$), as shown in Fig. 6.12a. PAM block transmission with linear FDE shows a better performance than the CAP scheme with an approximate gain of 3 dB for all values. The gain becomes significant when we use a hybrid equalizer for PAM block transmission. Even 16 CAP has a worse performance than 2 RZ-PAM (OOK) with a hybrid equalizer. Note that we have fine tuned the CAP performance with its best clipping value but it still cannot reach the performance of RZ-PAM with linear FDE or hybrid equalization. Moreover, the CAP transmitter also has a much higher complexity, since it requires a long FIR filter and a large amplifier back-off. Therefore, we only show the results of CAP with FDE.

The performance of the DC-biased DMT schemes with Fisher Huber bit-loading is also shown in Fig. 6.12a. The result shows that even 2 PAM-RZ with a hybrid equalizer outperforms DC-biased DMT with bit-loading up to $R_{\mathrm{b}}/f_{\mathrm{3dB}} \leq 10$ and thereafter 4 RZ-PAM matches the DC-biased DMT. Note that DMT with bit-loading requires the full CSI at the transmitter and a careful selection of the clipping factor, whereas PAM block transmission does not require CSI or clipping. Moreover, an adaptive PAM block transmission combined with linear FDE or hybrid equalization can also be used to achieve the best performance. In contrast to the DMT with bit-loading, it requires only knowledge of the modulation order and the pulse duration.

As an example, in Fig. 6.12b we show the data rates achieved by these schemes for a step index POF of 10 m length used in an automotive environment according to the media oriented systems transport (MOST) 150 specifications [MOS10, Grz11]. Data rates up to 2 Gbits/s or slightly more can be achieved with a 2 RZ-PAM (OOK) modulation combined with a hybrid equalizer. Even the 64 CAP does not match the performance of 2 RZ-PAM (OOK) with a hybrid equalizer or 8 PAM with linear FDE. Therefore, the CAP scheme is not a good solution for achieving high data rates in these optical systems due to its higher complexity and lower performance. The performance of DC-biased DMT with FH bit-loading is also worse than 4 RZ-PAM with a hybrid equalizer or 8 PAM with linear FDE up to 2 Gbits/s and thereafter it matches the 4 RZ-PAM with a hybrid equalizer or is slightly better. Clearly UW based PAM block transmission combined with a hybrid equalizer or even with a linear FDE is a better choice because of its good performance and low complexity.

6.7. Conclusion

In this chapter, we have investigated the performance of PAM transmission with different equalization and precoding techniques. PAM block transmission combined with frequency domain equalization offers an attractive and low complexity solution for optical systems employing IM/DD. Other state-of-the-art transmission strategies such as CAP and DC-biased DMT with bit-loading do not match the performance of RZ-PAM even with linear FDE and also require a much higher computational complexity. Since optical channels cause pre- and post-cursor ISI, the non-linear techniques offer a better solution as they can mitigate both ISIs in an efficient manner. The statement is verified by the results where the non-linear techniques such as DFE and THP significantly outperform the linear equalizers but at the cost of much higher computational complexity. Alternatively, a hybrid equalization technique can be employed which not only has a lower complexity but also achieves the same performance. PAM block transmission with a hybrid equalizer not only significantly outperforms PAM block transmission with linear FDE but

also others schemes. In such a technique, an additional time domain feedback filter with fewer taps is employed along with a linear frequency domain equalizer. Moreover, the error propagation problem of DFE can be resolved by using a unique word instead of a cyclic prefix. The results show that PAM block transmission with a hybrid equalizer has the similar performance of DFE and THP but significantly reduce computational complexity. Moreover, THP requires CSI at the transmitter and DFE suffers from error propagation.

7. Unique Word DMT Schemes

Discrete multitone transmission schemes such as AC-DMT, DC-biased DMT, and PAM-DMT are popular multicarrier transmission schemes for dispersive optical channels employing intensity modulation and direct detection. These transmission schemes utilize a cyclic prefix (CP) to have a simple frequency domain equalization at the receiver. In this chapter, we propose three novel DMT signaling schemes for such optical systems, where the guard interval is built of a unique word, i.e., a deterministic data independent sequence. These schemes are derived from the UW-OFDM signaling concept which is discussed in Part I of the thesis. This approach becomes possible since redundancy is added in the frequency domain and the UW is a part of the DFT interval. The results show that the proposed UW-DMT schemes outperform the conventional CP-DMT schemes in dispersive optical channels. Furthermore, the UW can be additionally used for other purposes such as synchronization and channel estimation.

7.1. Introduction

Optical systems with non-coherent sources such as light emitting diodes rely on intensity modulation and direct detection. As a result of the limited coherence of the source (the electrical field appears as broadband noise), a field modulation of two high frequencies carriers with $90°$ phase shift (quadrature up conversion) as in RF is impossible. On the contrary, for IM/DD, all signals need to be real-valued and non-negative. The real-valued baseband version of OFDM is usually referred to as discrete multitone transmission. As compared to OFDM, the DMT scheme requires some extra signal manipulations before and after the IFFT to make the time domain signal real-valued and positive. Depending on the type of pre- and post-IFFT processing, many variants of DMT schemes such as AC-DMT, DC-biased DMT schemes, and PAM-DMT have been proposed in the literature [AS08, LRBV09, VFea10, WH12] and are also discussed in Section 5.3.2. These schemes take different approaches for complex-valued and real-valued modulation formats to obtain a real-valued signal at the output of the IFFT. Moreover, similar to OFDM, these DMT schemes utilize a CP for simple frequency domain equalization.

In this chapter, we propose new unique word DMT signaling schemes for optical systems employing IM/DD. These schemes are derived from the UW-OFDM signaling concept [HHH10b, OH10] which has been introduced for RF in [HHH10b, OH10] and discussed in the first part of the thesis. It has already been shown in [HHH10b, OH10, HHH10a, HHOH14] that UW-OFDM has superior BER performance over classical CP-OFDM in frequency selective environments for RF communication. However, due to IM/DD constraints, the original UW-OFDM design cannot be directly applied to the optical systems such as POFs and VLC. Therefore, our proposed UW-DMT concept is different to the original UW-OFDM design. In our concept, the redundancy introduced in the frequency domain not only ensures that the signals are real-valued at the output of the IFFT but also we get zeros at the start or at the end of the time domain signal so that a UW can be added in the time domain. This is achieved by designing a code generator matrix which is multiplied with the data symbols in the frequency domain. Specifically, the design of the code generator matrix is different for complex-valued and real-valued

modulation formats. This is in contrast to UW-OFDM where the code generator matrix is independent of the type of the modulation format. Moreover, the design of this code generator matrix is not unique and different matrices yield different performances. In this work, we propose different types of code generator matrices. We refer to these new schemes as UW-DMT schemes while the classical CP based DMT schemes are referred to as CP-DMT.

The remainder of this chapter is organized as follows. The UW-DMT schemes that use complex-valued modulation formats are presented in Section 7.2 whereas the UW-DMT schemes for real-valued modulation formats are discussed in Section 7.3. We also discuss different designs for code generator matrices and receiver concepts for these proposed schemes. We also show the performance of the proposed transmission schemes and compare these schemes with the conventional CP-DMT schemes. Finally, we summarize our results in Section 7.4.

7.2. UW-DMT Transmission Techniques for Complex-Valued Constellations

In this section, we present the proposed UW-DMT schemes for complex-valued constellations such as QAM. The conventional CP-DMT schemes in the literature, which use complex-valued constellations, are AC-DMT and DC-biased DMT schemes [AS08, VFea10, WH12]. These schemes have been discussed in Section 5.3.2. First we present the system model and in the subsequent part, we discuss the proposed DMT schemes.

Let N_m be the effective number of data symbols which are to be mapped on $\frac{N}{2}$ subcarriers in the frequency domain, with N being the DFT size. Since IM/DD requires for real-valued signals, a Hermitian symmetry has to be enforced in the frequency domain. The real-valued signal at the IFFT output for these CP-DMT schemes is given as

$$\boldsymbol{x} = \boldsymbol{F}_N^H \bar{\boldsymbol{B}} \hat{\boldsymbol{d}} \in \mathbb{R}^{N \times 1}, \tag{7.1}$$

where $\boldsymbol{F}_N$ is the N-point DFT matrix with its elements $[\boldsymbol{F}_N]_{k,l} = \frac{1}{\sqrt{N}} e^{-j\frac{2\pi}{N}kl}$ for $k, l = 0, 1, 2, \ldots, N-1$, $\hat{\boldsymbol{d}} = [\boldsymbol{d} \ \boldsymbol{d}^*]^T \in \mathbb{C}^{2N_m \times 1}$ contains the complex-valued data vector $\boldsymbol{d}$ and its conjugate, and $\bar{\boldsymbol{B}} \in \mathbb{R}^{N \times 2N_m}$ (as defined in Eq. (5.34)) maps these symbols to the respective subcarriers. Depending upon the variant of the DMT scheme, the post-IFFT processing (such as clipping for AC-DMT or adding an appropriate DC-bias along with clipping for DC-biased DMT) is carried out to ensure that the transmit signal is positive-valued.

In the UW-DMT symbol generation, we propose to generate a symbol $\boldsymbol{x} = \begin{bmatrix} \boldsymbol{0} & \boldsymbol{x}_d^T \end{bmatrix}^T$ with a zero UW in the first step. Note that $\boldsymbol{x}$ in Eq. (7.1) does not contain the cyclic prefix. In the second step, the desired UW is added in the time domain. Let $\boldsymbol{x}_u \in \mathbb{R}^{N_u \times 1}$ be a unique word of length N_u which is added at the start of the time domain UW-DMT symbol such that

$$\boldsymbol{x}' = \begin{bmatrix} \boldsymbol{0} \\ \boldsymbol{x}_d \end{bmatrix} + \begin{bmatrix} \boldsymbol{x}_u \\ \boldsymbol{0} \end{bmatrix} \tag{7.2}$$

$$= \boldsymbol{x} + \begin{bmatrix} \boldsymbol{x}_u \\ \boldsymbol{0} \end{bmatrix} = \begin{bmatrix} \boldsymbol{x}_u \\ \boldsymbol{x}_d \end{bmatrix} \in \mathbb{R}^{N \times 1} \tag{7.3}$$

The symbol $\boldsymbol{x}$ with a zero UW is obtained by adding redundancy in the frequency domain. Let $\boldsymbol{G} \in \mathbb{C}^{N_m \times N_d}$ be a code generator matrix which adds redundancy in the frequency domain, then the time domain vector at the output of the IDFT is given as,

$$\boldsymbol{x} = \begin{bmatrix} \boldsymbol{0} \\ \boldsymbol{x}_d \end{bmatrix} = \boldsymbol{F}_N^H \begin{bmatrix} \boldsymbol{B} & \boldsymbol{0} \\ \boldsymbol{0} & \widehat{\boldsymbol{\Pi}} \boldsymbol{B} \end{bmatrix} \begin{bmatrix} \boldsymbol{G} & \boldsymbol{0} \\ \boldsymbol{0} & \boldsymbol{G}^* \end{bmatrix} \begin{bmatrix} \boldsymbol{d} \\ \boldsymbol{d}^* \end{bmatrix}$$
$$= \boldsymbol{F}_N^H \bar{\boldsymbol{B}} \boldsymbol{c}, \tag{7.4}$$

where $\boldsymbol{d} \in \mathbb{C}^{N_d \times 1}$ contains the data symbols in the frequency domain, $\boldsymbol{c} \in \mathbb{C}^{2N_m \times 1}$ contains the coded symbols using the code generator matrix, and $N_m = N_d + N_r$ with N_r being the redundancy added in the frequency domain. It has been shown for UW-OFDM in [HHH10a, HHOH14] that the design of the $\boldsymbol{G}$ matrix is not unique and different types of code generator matrices can be obtained. Using a similar idea as for UW-OFDM, we derive different code generator matrices for UW-DMT schemes that satisfy Eq. (7.4). Since we have a different problem (Eq. (7.4)) for UW-DMT schemes as compared to UW-OFDM, we will also get different solutions. Depending on how the redundancy is added, the design of the $\boldsymbol{G}$ matrix can be divided into two categories that are discussed in the following.

7.2.1. Systematic Code Generator Matrix

In the systematic approach, UW-DMT symbols are generated by appropriately loading so-called redundant subcarriers $\boldsymbol{r} \in \mathbb{C}^{N_r \times 1}$ with the help of a permutation matrix $\boldsymbol{P} \in \mathbb{R}^{N_m \times N_m}$. In this approach, the data and the redundant symbols are distinguishable at the output of the code generator matrix. We redefine Eq. (7.4) for this approach as

$$\boldsymbol{x} = \begin{bmatrix} \boldsymbol{0} \\ \boldsymbol{x}_d \end{bmatrix} = \underbrace{\boldsymbol{F}_N^H \begin{bmatrix} \boldsymbol{B} & \boldsymbol{0} \\ \boldsymbol{0} & \widehat{\boldsymbol{\Pi}} \boldsymbol{B} \end{bmatrix} \begin{bmatrix} \boldsymbol{P} & \boldsymbol{0} \\ \boldsymbol{0} & \boldsymbol{P} \end{bmatrix}}_{\begin{bmatrix} \boldsymbol{M}_{11} & \boldsymbol{M}_{12} & \boldsymbol{M}_{13} & \boldsymbol{M}_{14} \\ \boldsymbol{M}_{21} & \boldsymbol{M}_{22} & \boldsymbol{M}_{23} & \boldsymbol{M}_{24} \end{bmatrix}} \begin{bmatrix} \boldsymbol{d} \\ \boldsymbol{r} \\ \boldsymbol{d}^* \\ \boldsymbol{r}^* \end{bmatrix}. \tag{7.5}$$

From the first block, we see that

$$\boldsymbol{M}_{11} \boldsymbol{d} + \boldsymbol{M}_{12} \boldsymbol{r} + \boldsymbol{M}_{13} \boldsymbol{d}^* + \boldsymbol{M}_{14} \boldsymbol{r}^* = \boldsymbol{0}.$$

Note that $(\boldsymbol{M}_{13} \boldsymbol{d}^* + \boldsymbol{M}_{14} \boldsymbol{r}^*)$ corresponds to the IDFT of the negative part of the spectrum. This means that

$$\boldsymbol{M}_{13} \boldsymbol{d}^* + \boldsymbol{M}_{14} \boldsymbol{r}^* = (\boldsymbol{M}_{11} \boldsymbol{d} + \boldsymbol{M}_{12} \boldsymbol{r})^*,$$

therefore,

$$0 = \boldsymbol{M}_{11}\boldsymbol{d} + \boldsymbol{M}_{12}\boldsymbol{r} + \boldsymbol{M}_{13}\boldsymbol{d}^* + \boldsymbol{M}_{14}\boldsymbol{r}^*$$

$$0 = 2 \cdot \mathrm{Re}\left\{\boldsymbol{M}_{11}\boldsymbol{d} + \boldsymbol{M}_{12}\boldsymbol{r}\right\}.$$

Our aim is to express $\boldsymbol{r}$ as a function of $\boldsymbol{d}$ which is achieved by solving

$$0 = \mathrm{Re}\left\{\boldsymbol{M}_{11}\boldsymbol{d} + \boldsymbol{M}_{12}\boldsymbol{r}\right\}. \tag{7.6}$$

Note that this equation has more than one solution, since the $\mathrm{Re}\{\cdot\}$ operator offers an extra degree of freedom. In the following we present two approaches to solve the Eq. (7.6).

7.2.1.1. Solution 1

The simplest solution for Eq. (7.6) is

$$0 = \boldsymbol{M}_{11}\boldsymbol{d} + \boldsymbol{M}_{12}\boldsymbol{r}$$

$$\boldsymbol{r} = (\boldsymbol{M}_{12})^{-1}\boldsymbol{M}_{11}\boldsymbol{d}$$

$$\boldsymbol{r} = \boldsymbol{T}'\boldsymbol{d}, \tag{7.7}$$

where $\boldsymbol{T}' = (\boldsymbol{M}_{22})^{-1}\boldsymbol{M}_{21}$ is an invertible matrix. We simplify Eq. (7.5) by inserting $\boldsymbol{r}$ from Eq. (7.7) which results in

$$
\begin{aligned}
\boldsymbol{x} &= \boldsymbol{F}_N^H \begin{bmatrix} \boldsymbol{B} & \boldsymbol{0} \\ \boldsymbol{0} & \widehat{\boldsymbol{\Pi}}\boldsymbol{B} \end{bmatrix} \begin{bmatrix} \boldsymbol{P} & \boldsymbol{0} \\ \boldsymbol{0} & \boldsymbol{P} \end{bmatrix} \begin{bmatrix} \boldsymbol{d} \\ \boldsymbol{T}'\boldsymbol{d} \\ \boldsymbol{d}^* \\ (\boldsymbol{T}'\boldsymbol{d})^* \end{bmatrix} \\
&= \boldsymbol{F}_N^H \bar{\boldsymbol{B}} \begin{bmatrix} \boldsymbol{P} & \boldsymbol{0} \\ \boldsymbol{0} & \boldsymbol{P} \end{bmatrix} \begin{bmatrix} \boldsymbol{I}_{N_d} & \boldsymbol{0} \\ \boldsymbol{T}' & \boldsymbol{0} \\ \boldsymbol{0} & \boldsymbol{I}_{N_d} \\ \boldsymbol{0} & (\boldsymbol{T}')^* \end{bmatrix} \begin{bmatrix} \boldsymbol{d} \\ \boldsymbol{d}^* \end{bmatrix} \\
&= \boldsymbol{F}_N^H \bar{\boldsymbol{B}} \begin{bmatrix} \boldsymbol{G}_{\mathrm{Sys1}} & \boldsymbol{0} \\ \boldsymbol{0} & \boldsymbol{G}_{\mathrm{Sys1}}^* \end{bmatrix} \begin{bmatrix} \boldsymbol{d} \\ \boldsymbol{d}^* \end{bmatrix}
\end{aligned}
\tag{7.8}
$$

where

$$\boldsymbol{G}_{\mathrm{Sys1}} = \boldsymbol{P} \begin{bmatrix} \boldsymbol{I}_{N_d} \\ \boldsymbol{T}' \end{bmatrix} \in \mathbb{C}^{N_m \times N_d} \tag{7.9}$$

is the code generator matrix for this solution.

7.2.1.2. Solution 2

The design of the $\boldsymbol{G}_{\text{Sys1}}$ matrix in Eq. (7.9) does not exploit the extra degrees of freedom that are provided by the Re{.} operation in Eq. (7.6). In this section, we exploit the property, Re$\{\boldsymbol{V} \cdot \boldsymbol{Q}\} = $ Re$\{\boldsymbol{V}\}$Re$\{\boldsymbol{Q}\} - Im\{\boldsymbol{V}\}Im\{\boldsymbol{Q}\}$ for two complex matrices $\boldsymbol{V}$ and $\boldsymbol{Q}$. Using this property, we rewrite our original problem in Eq. (7.6) as

$$\begin{aligned}
\boldsymbol{0} &= \text{Re}\left\{\boldsymbol{M}_{11}\boldsymbol{d} + \boldsymbol{M}_{12}\boldsymbol{r}\right\} \\
&= \text{Re}\{\boldsymbol{M}_{11}\}\text{Re}\{\boldsymbol{d}\} - \text{Im}\{\boldsymbol{M}_{11}\}\text{Im}\{\boldsymbol{d}\} \\
&\quad + \text{Re}\{\boldsymbol{M}_{12}\}\text{Re}\{\boldsymbol{r}\} - \text{Im}\{\boldsymbol{M}_{12}\}\text{Im}\{\boldsymbol{r}\}.
\end{aligned}$$

The solution is given by

$$\begin{cases}
\text{Re}\left\{\boldsymbol{r}\right\} &= -\text{Re}\left\{\boldsymbol{M}_{12}\right\}^{-1} \cdot \text{Re}\left\{\boldsymbol{M}_{11}\right\} \cdot \text{Re}\left\{\boldsymbol{d}\right\} \\
\text{Im}\left\{\boldsymbol{r}\right\} &= -\text{Im}\left\{\boldsymbol{M}_{12}\right\}^{-1} \cdot \text{Im}\left\{\boldsymbol{M}_{11}\right\} \cdot \text{Im}\left\{\boldsymbol{d}\right\}
\end{cases}.$$

Next, let us define two real-valued matrices $\boldsymbol{T}_r$ and $\boldsymbol{T}_i$ as

$$\begin{cases}
\boldsymbol{T}_r &= -\text{Re}\left\{\boldsymbol{M}_{12}\right\}^{-1} \cdot \text{Re}\left\{\boldsymbol{M}_{11}\right\} \\
\boldsymbol{T}_i &= -\text{Im}\left\{\boldsymbol{M}_{12}\right\}^{-1} \cdot \text{Im}\left\{\boldsymbol{M}_{11}\right\}
\end{cases}.$$

Therefore, vector $\boldsymbol{r}$ for this solution can be expressed as

$$\boldsymbol{r} = \boldsymbol{T}_r \cdot \text{Re}\left\{\boldsymbol{d}\right\} + j\boldsymbol{T}_i \cdot \text{Im}\left\{\boldsymbol{d}\right\}. \tag{7.10}$$

Inserting $\boldsymbol{r}$ in Eq. (7.5) results in

$$\boldsymbol{x} = \boldsymbol{F}_N^H \bar{\boldsymbol{B}} \begin{bmatrix} \boldsymbol{P} & \boldsymbol{0} \\ \boldsymbol{0} & \boldsymbol{P} \end{bmatrix} \left(\begin{bmatrix} \boldsymbol{I}_{N_d} \\ \boldsymbol{T}_r \\ \boldsymbol{I}_{N_d} \\ \boldsymbol{T}_r \end{bmatrix} \text{Re}\{\boldsymbol{d}\} + j \begin{bmatrix} \boldsymbol{I}_{N_d} \\ \boldsymbol{T}_i \\ -\boldsymbol{I}_{N_d} \\ -\boldsymbol{T}_i \end{bmatrix} \text{Im}\{\boldsymbol{d}\} \right). \tag{7.11}$$

Defining two real-valued code generator matrices as

$$\boldsymbol{G}_{r,\text{Sys}} = \boldsymbol{P} \begin{bmatrix} \boldsymbol{I}_{N_d} \\ \boldsymbol{T}_r \end{bmatrix} \in \mathbb{R}^{N_m \times N_d} \qquad\qquad \boldsymbol{G}_{i,\text{Sys}} = \boldsymbol{P} \begin{bmatrix} \boldsymbol{I}_{N_d} \\ \boldsymbol{T}_i \end{bmatrix} \in \mathbb{R}^{N_m \times N_d}$$

Eq. (7.11) simplifies to

$$\boldsymbol{x} = \boldsymbol{F}_N^H \bar{\boldsymbol{B}} \left(\hat{\boldsymbol{G}}_{r,\text{Sys}}\text{Re}\{\boldsymbol{d}\} + j\hat{\boldsymbol{G}}_{i,\text{Sys}}\text{Im}\{\boldsymbol{d}\} \right),$$

where

$$\hat{\boldsymbol{G}}_{r,\text{Sys}} = \begin{bmatrix} \boldsymbol{G}_{r,\text{Sys}} \\ \boldsymbol{G}_{r,\text{Sys}} \end{bmatrix} \qquad\qquad \hat{\boldsymbol{G}}_{i,\text{Sys}} = \begin{bmatrix} \boldsymbol{G}_{i,\text{Sys}} \\ -\boldsymbol{G}_{i,\text{Sys}} \end{bmatrix} \tag{7.12}$$

(a) Solution 1 for AC-UW-DMT

(b) Solution 2 for AC-UW-DMT

(c) Solution 1 for DC-biased UW-DMT

(d) Solution 2 for DC-biased UW-DMT
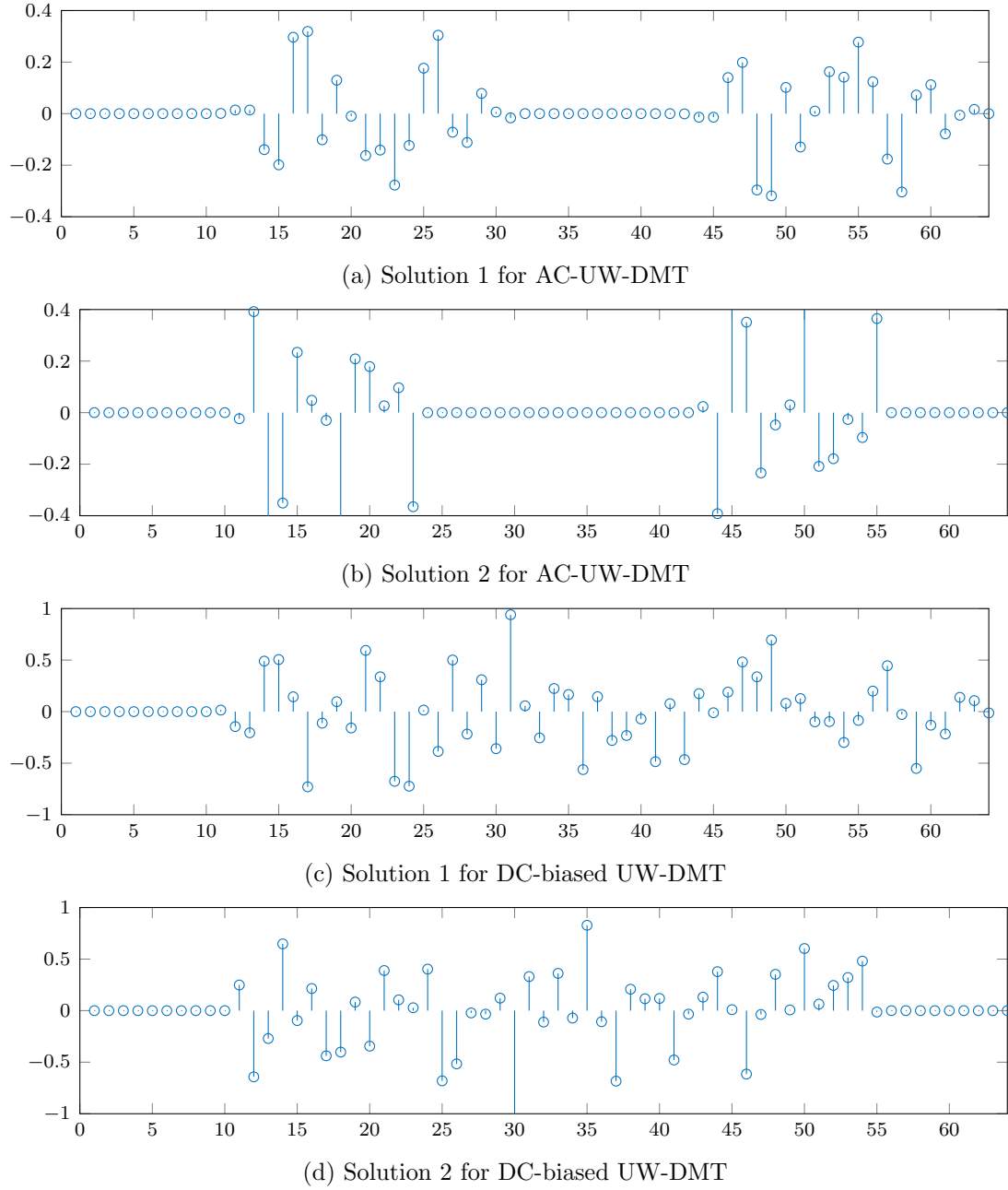
Figure 7.1.: Time domain comparison of both solutions for AC-UW-DMT and DC-biased UW-DMT for $N = 64$, $N_r = 10$

7.2.1.3. Design of the Permutation Matrix

The position of redundant subcarriers in the systematic UW-DMT schemes plays an important role regarding its performance. Therefore, the design of the $\boldsymbol{P}$ matrix is crucial for the performance of systematic UW-DMT. We use a similar procedure as proposed for UW-OFDM in [HHH10b] to find the optimal permutation matrix $\boldsymbol{P}$. The goal is to find a matrix $\boldsymbol{P}$ that minimizes the redundant energy.

We use the heuristic method proposed in [HHOH14] to calculate almost optimal positions. The expected redundant energy for the DMT schemes is given as

$$E_r = \frac{2}{N} \mathbb{E} \left\{ \boldsymbol{r}^H \boldsymbol{r} \right\}, \tag{7.13}$$

where the factor 2 is due to the conjugate symmetry of DMT schemes. In the following, we calculate the redundant energy for both solutions. Then we apply the heuristic algorithm in [HHOH14] to calculate the $\boldsymbol{P}$ matrix.

7.2.1.3.1. Redundant Energy for Solution 1 By using the properties of the trace operator (i.e. $\mathrm{tr}(\cdot)$), we get

$$\begin{aligned} E_{r,1} &= \frac{2}{N} \mathbb{E} \left\{ \boldsymbol{r}^H \boldsymbol{r} \right\} \\ &= \frac{2}{N} \mathbb{E} \left\{ \mathrm{tr}(\boldsymbol{r}\boldsymbol{r}^H) \right\} \\ &= \frac{2}{N} \mathbb{E} \left\{ \mathrm{tr}(\boldsymbol{T}'\boldsymbol{d}\boldsymbol{d}^H\boldsymbol{T}'^H) \right\} \\ &= 2\frac{\sigma_d^2}{N} \mathrm{tr} \left(\boldsymbol{T}'\boldsymbol{T}'^H \right) \end{aligned}$$

where σ_d^2 is the variance of the data symbols.

7.2.1.3.2. Redundant Energy for Solution 2 Let $\boldsymbol{r}'$ be the real part of $\boldsymbol{r}$ and $\boldsymbol{r}''$ be the imaginary part. Similarly, let $\boldsymbol{d}'$ be the real part of $\boldsymbol{d}$ and $\boldsymbol{d}''$ be the imaginary part. Then

$$\begin{aligned} E_{r,2} &= \frac{2}{N} \mathbb{E} \left\{ \boldsymbol{r}^H \boldsymbol{r} \right\} = \frac{2}{N} \mathbb{E} \left\{ (\boldsymbol{r}' - j\boldsymbol{r}'')^T (\boldsymbol{r}' + j\boldsymbol{r}'') \right\} \\ &= \frac{2}{N} \mathbb{E} \left\{ (\boldsymbol{r}')^T \boldsymbol{r}' + (\boldsymbol{r}'')^T \boldsymbol{r}'' \right\} \\ &= \frac{2}{N} \mathbb{E} \left\{ \mathrm{tr}(\boldsymbol{r}'(\boldsymbol{r}')^T) + \mathrm{tr}(\boldsymbol{r}''(\boldsymbol{r}'')^T) \right\} \\ &= \frac{2\sigma_{d'}^2}{N} \mathrm{tr} \left(\boldsymbol{T}_r \boldsymbol{T}_r^T \right) + \frac{2\sigma_{d''}^2}{N} \mathrm{tr} \left(\boldsymbol{T}_i \boldsymbol{T}_i^T \right) \\ &= \frac{2\frac{\sigma_d^2}{2}}{N} \mathrm{tr} \left(\boldsymbol{T}_r \boldsymbol{T}_r^T \right) + \frac{2\frac{\sigma_d^2}{2}}{N} \mathrm{tr} \left(\boldsymbol{T}_i \boldsymbol{T}_i^T \right) \\ &= \frac{\sigma_d^2}{N} \left(\mathrm{tr} \left(\boldsymbol{T}_r \boldsymbol{T}_r^T \right) + \mathrm{tr} \left(\boldsymbol{T}_i \boldsymbol{T}_i^T \right) \right), \end{aligned}$$

where we have used $\sigma_{d'}^2 = \sigma_{d''}^2 = \frac{\sigma_d^2}{2}$ which is true for uncorrelated QAM symbols.

7.2.2. Non-Systematic Code Generator Matrix

In the non-systematic design, we abandon the idea of dedicated redundant subcarriers and design a code generator matrix that distributes the energy over all subcarriers. Therefore, at the output of the code

generator matrix, the data and redundant symbols are not anymore distinguishable. Let us define

$$\begin{bmatrix} \boldsymbol{M}_{11} & \boldsymbol{M}_{12} \\ \boldsymbol{M}_{21} & \boldsymbol{M}_{22} \end{bmatrix} = \boldsymbol{F}_N^H \begin{bmatrix} \boldsymbol{B} & \boldsymbol{0} \\ \boldsymbol{0} & \widehat{\boldsymbol{\Pi}}\boldsymbol{B} \end{bmatrix} \tag{7.14}$$

Inserting this definition in Eq. (7.4), we get

$$\begin{bmatrix} \boldsymbol{M}_{11} & \boldsymbol{M}_{12} \\ \boldsymbol{M}_{21} & \boldsymbol{M}_{22} \end{bmatrix} \begin{bmatrix} \boldsymbol{G} & \boldsymbol{0} \\ \boldsymbol{0} & \boldsymbol{G}^* \end{bmatrix} \begin{bmatrix} \boldsymbol{d} \\ \boldsymbol{d}^* \end{bmatrix} = \begin{bmatrix} \boldsymbol{0} \\ \boldsymbol{x}_d \end{bmatrix} \tag{7.15}$$

Hence, we can extract the following relation from the above equation,

$$\boldsymbol{0} = \boldsymbol{M}_{11}\boldsymbol{G}\boldsymbol{d} + \boldsymbol{M}_{12}\boldsymbol{G}^*\boldsymbol{d}^*,$$

where $\boldsymbol{M}_{12}\boldsymbol{G}^*\boldsymbol{d}^*$ corresponds to the IDFT of the negative part of the spectrum. Therefore,

$$\begin{aligned} \boldsymbol{0} &= \boldsymbol{M}_{11}\boldsymbol{G}\boldsymbol{d} + \boldsymbol{M}_{12}\boldsymbol{G}^*\boldsymbol{d}^* \\ \boldsymbol{0} &= 2 \cdot \operatorname{Re}\left\{ \boldsymbol{M}_{11}\boldsymbol{G}\boldsymbol{d} \right\}. \end{aligned} \tag{7.16}$$

Note that this problem is similar to the systematic code generator design and a unique solution does not exist. In the following, we will present two solutions as presented for the systematic code generator matrix.

7.2.2.1. Solution 1

Since the relation in Eq. (7.29) must hold for any $\boldsymbol{d}$ vector, the simplest solution is

$$\boldsymbol{0} = \boldsymbol{M}_{11}\boldsymbol{G}. \tag{7.17}$$

Note that Eq. (7.17) implies that the columns of $\boldsymbol{G}$ should belong to the null-space of $\boldsymbol{M}_{11}$. There exist multiple solutions to this problem but all should fulfill the constraints in Eq. (7.17). One solution can be a matrix that contains an orthonormal basis of the null space. This can be achieved by computing the singular value decomposition (SVD) of $\boldsymbol{M}_{11}$. We denote the code matrix as $\boldsymbol{G}_{\text{Nsys1}}$ which is computed in this way.

7.2.2.2. Solution 2

In the second approach, we design two real-valued generator matrices for the real and the imaginary parts of the data symbols, respectively. Let $\boldsymbol{G}_r \in \mathbb{R}^{N_m \times N_d}$ and $\boldsymbol{G}_i \in \mathbb{R}^{N_m \times N_d}$ denote two real-valued generator matrices. We can rewrite Eq. (7.4) as

$$\begin{bmatrix} \boldsymbol{0} \\ \boldsymbol{x}_d \end{bmatrix} = \boldsymbol{F}_N^H \begin{bmatrix} \boldsymbol{B} & \boldsymbol{0} \\ \boldsymbol{0} & \widehat{\boldsymbol{\Pi}}\boldsymbol{B} \end{bmatrix} \left(\begin{bmatrix} \boldsymbol{G}_r \\ \boldsymbol{G}_r \end{bmatrix} \operatorname{Re}\{\boldsymbol{d}\} + j \begin{bmatrix} \boldsymbol{G}_i \\ -\boldsymbol{G}_i \end{bmatrix} \operatorname{Im}\{\boldsymbol{d}\} \right)$$

Using the Eq. (7.14), we obtain

$$\begin{bmatrix} \mathbf{0} \\ \boldsymbol{x}_d \end{bmatrix} = \begin{bmatrix} \boldsymbol{M}_{11} & \boldsymbol{M}_{12} \\ \boldsymbol{M}_{21} & \boldsymbol{M}_{22} \end{bmatrix} \left(\begin{bmatrix} \boldsymbol{G}_r \\ \boldsymbol{G}_r \end{bmatrix} \mathrm{Re}\{\boldsymbol{d}\} + j \begin{bmatrix} \boldsymbol{G}_i \\ -\boldsymbol{G}_i \end{bmatrix} \mathrm{Im}\{\boldsymbol{d}\} \right), \qquad (7.18)$$

where

$$\boldsymbol{M}_{12}\boldsymbol{G}_r\mathrm{Re}\{\boldsymbol{d}\} = (\boldsymbol{M}_{11}\boldsymbol{G}_r\mathrm{Re}\{\boldsymbol{d}\})^*$$
$$-\boldsymbol{M}_{12}\boldsymbol{G}_i\mathrm{Im}\{\boldsymbol{d}\} = (\boldsymbol{M}_{11}\boldsymbol{G}_i\mathrm{Im}\{\boldsymbol{d}\})^*.$$

Using the above properties, we can simplify the first block of Eq. (7.18) as

$$\mathbf{0} = \mathrm{Re}\left\{\boldsymbol{M}_{11}\boldsymbol{G}_r\mathrm{Re}\{\boldsymbol{d}\} + j\boldsymbol{M}_{11}\boldsymbol{G}_i\mathrm{Im}\{\boldsymbol{d}\}\right\}$$
$$= \mathrm{Re}\{\boldsymbol{M}_{11}\}\boldsymbol{G}_r\mathrm{Re}\{\boldsymbol{d}\} - \mathrm{Im}\{\boldsymbol{M}_{11}\}\boldsymbol{G}_i\mathrm{Im}\{\boldsymbol{d}\}.$$

Therefore, following constraints have to be fulfilled for the design of these two code generator matrices.

$$\begin{cases} \mathbf{0} &= \mathrm{Re}\{\boldsymbol{M}_{11}\}\boldsymbol{G}_r \\ \mathbf{0} &= \mathrm{Im}\{\boldsymbol{M}_{11}\}\boldsymbol{G}_i \end{cases}.$$

Note that, this implies that the columns of $\boldsymbol{G}_r$ and $\boldsymbol{G}_i$ matrices belong to the null space of $\mathrm{Re}\{\boldsymbol{M}_{11}\}$ and $\mathrm{Im}\{\boldsymbol{M}_{11}\}$, respectively. Similar to solution 1, we can compute the SVD of $\mathrm{Re}\{\boldsymbol{M}_{11}\}$ and $\mathrm{Im}\{\boldsymbol{M}_{11}\}$ to obtain $\boldsymbol{G}_r$ and $\boldsymbol{G}_i$, respectively. In this work, we refer to the matrices obtained through this method as $\boldsymbol{G}_{r,\mathrm{Nsys}}$ and $\boldsymbol{G}_{i,\mathrm{Nsys}}$. Therefore, the signal at the output of the IDFT is

$$\boldsymbol{x} = \boldsymbol{F}_N^H \bar{\boldsymbol{B}} \left(\hat{\boldsymbol{G}}_{r,\mathrm{Nsys}}\mathrm{Re}\{\boldsymbol{d}\} + j\hat{\boldsymbol{G}}_{i,\mathrm{Nsys}}\mathrm{Im}\{\boldsymbol{d}\} \right),$$

where

$$\hat{\boldsymbol{G}}_{r,\mathrm{Nsys}} = \begin{bmatrix} \boldsymbol{G}_{r,\mathrm{Nsys}} \\ \boldsymbol{G}_{r,\mathrm{Nsys}} \end{bmatrix} \qquad\qquad \hat{\boldsymbol{G}}_{i,\mathrm{Nsys}} = \begin{bmatrix} \boldsymbol{G}_{i,\mathrm{Nsys}} \\ -\boldsymbol{G}_{i,\mathrm{Nsys}} \end{bmatrix} \qquad (7.19)$$

7.2.3. Comparison of Both Solutions

A realization of the real-valued time domain samples at the output of the IDFT is shown in Fig. 7.1 for both solutions and for both unique word DMT schemes. Different numbers of zeros at different positions are obtained for both solutions and also for both DMT schemes. Since solution 1 does not take full advantage of the real operator in Eq. (7.6) and Eq. (7.29), we only get N_u zeros at the start of the symbols for both UW-DMT schemes. Additionally, we also get N_u zeros in the middle for AC-DMT due to the Hermitian symmetry property. Since in solution 2, we use two real-valued generator matrices for the positive and the negative spectrum, we get N_u zeros at the start and $N_u - 1$ zeros at the end of the time domain samples. Since the first row of $\mathrm{Im}\{\boldsymbol{M}_{11}\}$ contains only zeros, we get only $N_u - 1$ zeros at the end instead of N_u zeros. Moreover, we get an additional $2N_u - 1$ zeros in the middle for AC-UW-DMT.
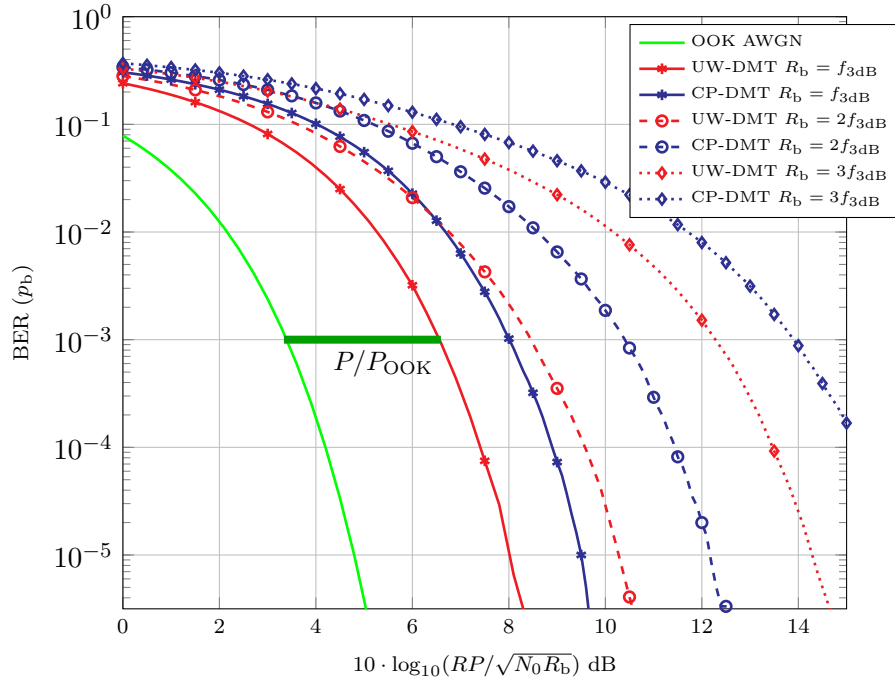
Figure 7.2.: Comparison of 4-QAM DC-biased UW-DMT scheme for different $R_{\mathrm{b}}/f_{\mathrm{3dB}}$ values using $\boldsymbol{G}_{\mathrm{Nsys}}$ and solution 2

Clearly, solution 2 is a better option since we need only half of the redundancy $(N_r/2)$ as compared to solution 1 to add a unique word of length N_u. This is accomplished by adding a UW in between two symbols since we get zeros not only at the start but also at the end of time domain symbols.

7.2.4. Receiver Design

The data received in the frequency domain after subtracting the UW and removing the zero subcarriers is given by

$$
\begin{aligned}
\boldsymbol{y} &= \bar{\boldsymbol{B}}^T \boldsymbol{F}_N \hat{\boldsymbol{H}} \boldsymbol{F}_N^H \bar{\boldsymbol{B}} \boldsymbol{c} + \bar{\boldsymbol{B}}^T \boldsymbol{F}_N \hat{\boldsymbol{n}} \\
&= \boldsymbol{H} \boldsymbol{c} + \boldsymbol{n},
\end{aligned}
\tag{7.20}
$$

where $\hat{\boldsymbol{H}} \in \mathbb{R}^{N \times N}$ is the circulant convolutional matrix containing the channel impulse response, $\boldsymbol{H} = \bar{\boldsymbol{B}}^T \boldsymbol{F}_N \hat{\boldsymbol{H}} \boldsymbol{F}_N^H \bar{\boldsymbol{B}} \in \mathbb{C}^{2N_m \times 2N_m}$ is a diagonal matrix with the channel transfer function on its diagonal, and $\boldsymbol{n} = \bar{\boldsymbol{B}}^T \boldsymbol{F}_N \hat{\boldsymbol{n}}$ denotes the noise in the frequency domain. The impact of the channel is removed by utilizing an appropriate detector. In this work, we present only linear detectors for UW-DMT schemes. The linear detection schemes differ for both solutions.

7.2.4.1. Linear Detectors for Solution 1

Irrespective of the type of code generator matrix (systematic or non-systematic) used, the symbols at the output of the code generator matrix for solution 1 are given as

$$c = \begin{bmatrix} G & 0 \\ 0 & G^* \end{bmatrix} \begin{bmatrix} d \\ d^* \end{bmatrix}$$

where G can be chosen as G_{Sys1} or G_{Nsys1}. The symbols can be estimated as

$$\hat{d} = E\hat{y} \in \mathbb{C}^{N_d \times 1},$$

where $\hat{y}$ corresponds to the received spectrum of the positive frequencies and $E \in \mathbb{C}^{N_d \times N_m}$ contains the equalizer filter weights. In [HOH11, CZHH16], it has been shown that the optimum linear estimators such as the best linear unbiased estimator (BLUE) or the linear minimum mean square error (LMMSE) estimator can be used to estimate the data symbols for UW-OFDM. We use the same estimators for UW-DMT schemes. The estimators for the solution 1 are given as

$$E_{\text{BLUE}} = \left(G^H \tilde{H}^H \tilde{H} G \right)^{-1} G^H \tilde{H}^H, \tag{7.21}$$

$$E_{\text{MMSE}} = \left(G^H \tilde{H}^H \tilde{H} G + N \frac{\sigma_n^2}{\sigma_d^2} I_{N_d} \right)^{-1} G^H \tilde{H}^H, \tag{7.22}$$

where $\tilde{H} \in \mathbb{C}^{N_m \times N_m}$ denotes a diagonal matrix with the channel transfer function of the spectrum of the positive frequencies on its diagonal, G can be either G_{Sys1} or G_{Nsys1}, σ_n^2 is the variance of the noise samples, and σ_d^2 is the variance of the data symbols.

7.2.4.2. Linear Detectors for Solution 2

If the G matrices based on the solution 2 are used, then the received signal will be,

$$y = H \left(\hat{G}_r \text{Re}\{d\} + j\hat{G}_i \text{Im}\{d\} \right) + n$$
$$= H\hat{G}_r \text{Re}\{d\} + jH\hat{G}_i \text{Im}\{d\} + n,$$

where $\hat{G}_r$ and $\hat{G}_i$ can be the generator matrices for the systematic or non-systematic approach. The symbols are then estimated as

$$\hat{d} = \text{Re}\{E_r\hat{y}\} + j\text{Im}\{E_i\hat{y}\} \in \mathbb{C}^{N_d \times 1},$$

where E_r and E_i are the equalizer filter weights for the real and the imaginary part of the data symbols. The equalizer weights can be calculated by replacing G in Eq. (7.21) and Eq. (7.22) with $G'_{r,\text{Sys}}$ or $G'_{r,\text{Nsys}}$ for E_r and $G'_{r,\text{sSys}}$ or $G'_{r,\text{Nsys}}$ for E_i.
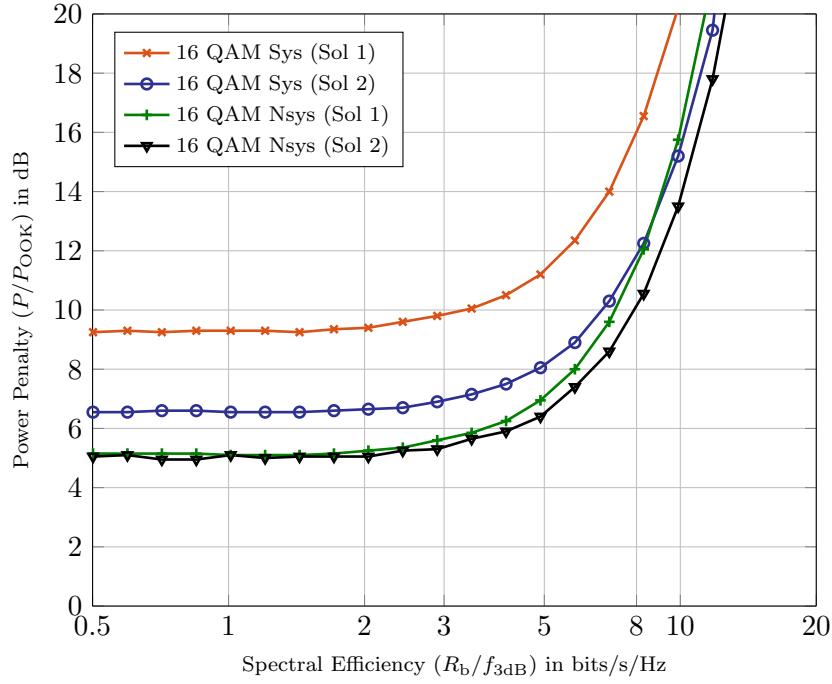
Figure 7.3.: Comparison of DC-biased UW-DMT schemes with different $\boldsymbol{G}$ matrices

	UW-DMT	**CP-DMT**
FFT size (N)	128	
p_b	10^{-3}	
Data Carriers (N_d)	AC-DMT: 16, 21 DC-biased: 42, 47	AC-DMT: 26 DC-biased: 52
Redundant Carriers (N_r)	Solution 1: 10 Solution 2: 5	-
CP/UW duration	10 Samples	
Oversampling,factor	2	
Channel	Gaussian Low Pass	

Table 7.1.: Simulation Parameters

7.2.5. Simulation Results

We evaluate the performance of these schemes over POF channel which has been discussed in Section 5.2.2. The performance of the proposed schemes is evaluated in terms of an optical power penalty as discussed in Section 5.2.1. We also show results for the BER vs. the required average optical power for the DC-biased UW-DMT scheme in Fig. 7.2. Note that the ratio $RP/\sqrt{N_0 R_\mathrm{b}}$ in this figure corresponds to the ratio $E_\mathrm{b,elec}/N_0$ which is usually used for performance analysis in RF communication. Moreover, the horizontal green line at $p_\mathrm{b} = 10^{-3}$ represents an example of the power penalty. Since we would need a separate curve for each $R_\mathrm{b}/f_\mathrm{3dB}$ value, we do not show the BER plots in the following figures. Instead, we show the power penalty mentioned above over $R_\mathrm{b}/f_\mathrm{3dB}$ at $p_\mathrm{b} = 10^{-3}$. Moreover, we have used a zero UW in our simulations but other sequences such as m-sequence can also be used. The rest of the simulation parameters are described in Table 7.1.
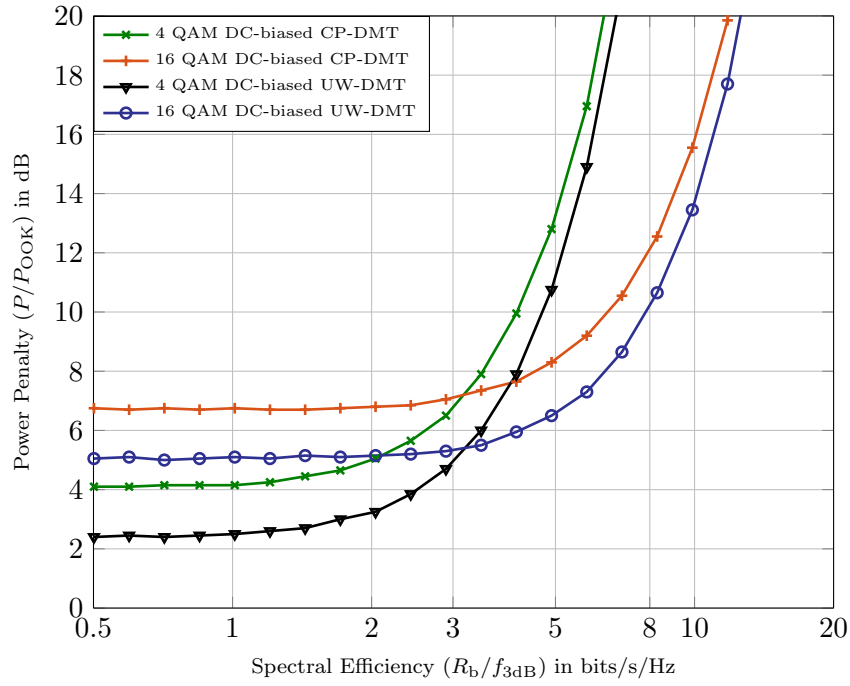
(a) Comparison of DC-biased UW-DMT with DC-biased CP-DMT using $\boldsymbol{G}_{\mathrm{Nsys}}$ and solution 2
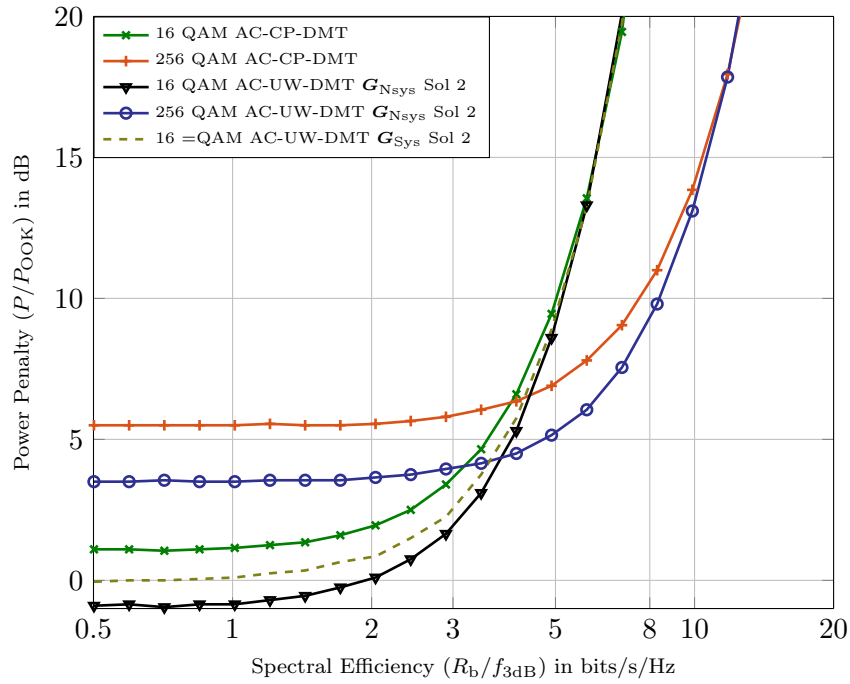
(b) Comparison of AC-UW-DMT with AC-CP-DMT

Figure 7.4.: Comparison of UW-DMT schemes with CP-DMT schemes

First we discuss the performance of the UW-DMT schemes with different code generator matrices designed for both solutions. As an example, we show the performance of 16 QAM DC-biased UW-DMT in Fig. 7.3 but the results are similar for AC-UW-DMT as shown in Fig. 7.4b. It is evident from the

results that all $\boldsymbol{G}$ matrices result in different performance where the systematic and the non systematic code generator matrices using solution 2 outperform the solution 1. One of the reasons is the use of less number of redundant carriers for solution 2. Moreover, the UW-DMT schemes with $\boldsymbol{G}_{\mathrm{Nsys}}$ matrices outperforms the $\boldsymbol{G}_{\mathrm{Sys}}$. This is due to the fact that the redundancy is distributed over all subcarriers for the non-systematic approach. It is also analogous to the UW-OFDM system where the UW-OFDM with non-systematic code generator matrices outperforms the UW-OFDM with systematic matrices. Clearly, the $\boldsymbol{G}_{\mathrm{Nsys}}$ matrix designed using the solution 2 is a better choice for UW-DMT schemes. Note that the code generator matrices are designed only once for the given system parameters.

We compare the performance of the DC-biased UW-DMT scheme with the DC-biased CP-DMT scheme in Fig. 7.2 and Fig. 7.4a. Here, we have only shown the results for the UW-DMT scheme with non-systematic generator matrices using solution 2 since this combination outperforms the other solutions. However, we also show the performance of the AC-UW-DMT scheme with systematic generator matrices using solution 2 in Fig. 7.4b. The results show that DC-biased UW-DMT scheme outperforms the DC-biased CP-DMT scheme at all $R_{\mathrm{b}}/f_{\mathrm{3dB}}$ values for a fixed $p_{\mathrm{b}} = 10^{-3}$, as shown in Fig. 7.4a. The same is true in Fig. 7.2 where we show results for the BER vs. the normalized power for a fixed R_{b} value. The results are slightly different for the AC-DMT scheme as shown in Fig. 7.4b, where we observe approximately the same power penalties at very high $R_{\mathrm{b}}/f_{\mathrm{3dB}}$ values, but still a high gain for AC-UW-DMT is observed at lower $R_{\mathrm{b}}/f_{\mathrm{3dB}}$ values. Note that the design of the code generator matrix is not unique and different code generator matrices yield different performances. In this work, we have only used the non-systematic $\boldsymbol{G}_{\mathrm{Nsys}}$ matrix based on the singular value decomposition but other matrices can also be designed. These code generator matrices can be designed using the channel statistics and may further improve the performance of the UW-DMT schemes.

7.3. UW-DMT Transmission Techniques for Real-Valued Constellations

In this section, we propose a novel UW-DMT scheme that uses real-valued modulation formats such as PAM (a counterpart of the PAM CP-DMT scheme as proposed in [LRBV09]). PAM CP-DMT scheme has already been introduced in Section 5.3.2. In this scheme, the data symbols are first converted to imaginary symbols as $\boldsymbol{d} = j\boldsymbol{s} \in \mathbb{C}^{N_m \times 1}$ to ensure the odd symmetry in the time domain, where $\boldsymbol{s} \in \mathbb{R}^{N_m \times 1}$ is the data symbol vector of length N_m in the frequency domain.

We use a similar procedure to generate the PAM UW-DMT symbols as proposed for other UW-DMT schemes in the previous section. In the first step, we generate a symbol $\boldsymbol{x} = \begin{bmatrix} \boldsymbol{0} & \boldsymbol{x}_d^T \end{bmatrix}^T$ with a zero UW, as shown in Fig. 7.5. In the second step, the desired UW is added in the time domain. The symbols at the output of the IDFT are given as,

$$
\begin{aligned}
\boldsymbol{x} = \begin{bmatrix} \boldsymbol{0} \\ \boldsymbol{x}_d \end{bmatrix} &= \boldsymbol{F}_N^H \bar{\boldsymbol{B}} \begin{bmatrix} \boldsymbol{G} & \boldsymbol{0} \\ \boldsymbol{0} & \boldsymbol{G}^* \end{bmatrix} \begin{bmatrix} \boldsymbol{d} \\ \boldsymbol{d}^* \end{bmatrix} \\
&= \boldsymbol{F}_N^H \bar{\boldsymbol{B}} \boldsymbol{c},
\end{aligned}
\tag{7.23}
$$

where $\boldsymbol{c} \in \mathbb{C}^{N_m \times 1}$ contains the N_m coded symbols at the output of the code generator matrix with

$N_m = N_d + N_r$. As shown in the previous section, the design of the $\boldsymbol{G}$ matrix plays an important role regarding the performance of UW-DMT where different $\boldsymbol{G}$ matrices are proposed for UW-DMT schemes using complex-valued constellations. In this section, we first derive the $\boldsymbol{G}$ matrices for PAM UW-DMT. In the following we discuss the design of two types of code generator matrices where we only consider solution 2 since it is a better choice for UW-DMT schemes.
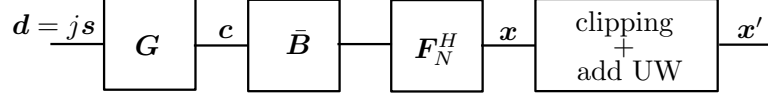
Figure 7.5.: Transmit structure for PAM UW-DMT

7.3.1. Systematic Code Generator Matrix

Similar to UW-DMT schemes for complex-valued formats, we start by redefining Eq. (7.4) as

$$
\boldsymbol{x} = \begin{bmatrix} \mathbf{0} \\ \boldsymbol{x}_d \end{bmatrix} = \underbrace{\boldsymbol{F}_N^H \begin{bmatrix} \boldsymbol{B} & \mathbf{0} \\ \mathbf{0} & \widehat{\boldsymbol{\Pi}} \boldsymbol{B} \end{bmatrix} \begin{bmatrix} \boldsymbol{P} & \mathbf{0} \\ \mathbf{0} & \boldsymbol{P} \end{bmatrix}}_{\begin{bmatrix} \boldsymbol{M}_{11} & \boldsymbol{M}_{12} & \boldsymbol{M}_{13} & \boldsymbol{M}_{14} \\ \boldsymbol{M}_{21} & \boldsymbol{M}_{22} & \boldsymbol{M}_{23} & \boldsymbol{M}_{24} \end{bmatrix}} \begin{bmatrix} \boldsymbol{d} \\ \boldsymbol{r} \\ \boldsymbol{d}^* \\ \boldsymbol{r}^* \end{bmatrix} , \tag{7.24}
$$

that yields

$$
\begin{aligned}
\mathbf{0} &= \boldsymbol{M}_{11}\boldsymbol{d} + \boldsymbol{M}_{12}\boldsymbol{r} + \boldsymbol{M}_{13}\boldsymbol{d}^* + \boldsymbol{M}_{14}\boldsymbol{r}^* \\
\mathbf{0} &= 2 \cdot \operatorname{Re}\left\{ \boldsymbol{M}_{11}\boldsymbol{d} + \boldsymbol{M}_{12}\boldsymbol{r} \right\} \\
\mathbf{0} &= \operatorname{Re}\left\{ \boldsymbol{M}_{11}\boldsymbol{d} + \boldsymbol{M}_{12}\boldsymbol{r} \right\} .
\end{aligned} \tag{7.25}
$$

Next, we use the property, $\operatorname{Re}\{\boldsymbol{V} \cdot \boldsymbol{Q}\} = \operatorname{Re}\{\boldsymbol{V}\}\operatorname{Re}\{\boldsymbol{Q}\} - \operatorname{Im}\{\boldsymbol{V}\}\operatorname{Im}\{\boldsymbol{Q}\}$ for two complex matrices $\boldsymbol{V}$ and $\boldsymbol{Q}$, to get

$$
\begin{aligned}
\mathbf{0} &= \operatorname{Re}\left\{ \boldsymbol{M}_{11}\boldsymbol{d} + \boldsymbol{M}_{12}\boldsymbol{r} \right\} \\
&= \operatorname{Re}\{\boldsymbol{M}_{11}\}\operatorname{Re}\{\boldsymbol{d}\} - \operatorname{Im}\{\boldsymbol{M}_{11}\}\operatorname{Im}\{\boldsymbol{d}\} + \operatorname{Re}\{\boldsymbol{M}_{12}\}\operatorname{Re}\{\boldsymbol{r}\} - \operatorname{Im}\{\boldsymbol{M}_{12}\}\operatorname{Im}\{\boldsymbol{r}\}.
\end{aligned}
$$

Note that $\operatorname{Re}\{\boldsymbol{d}\} = \mathbf{0}$, such that with the choice $\operatorname{Re}\{\boldsymbol{r}\} = \mathbf{0}$, (or $\boldsymbol{r} = j \cdot \operatorname{Im}\{\boldsymbol{r}\}$) we obtain the solution

$$
\begin{aligned}
\operatorname{Im}\{\boldsymbol{r}\} &= -\operatorname{Im}\{\boldsymbol{M}_{12}\}^{-1} \cdot \operatorname{Im}\{\boldsymbol{M}_{11}\} \cdot \operatorname{Im}\{\boldsymbol{d}\} \\
&= \boldsymbol{T} \cdot \operatorname{Im}\{\boldsymbol{d}\} = \boldsymbol{T}\boldsymbol{s},
\end{aligned}
$$

where $\boldsymbol{T} = -\text{Im}\left\{\boldsymbol{M}_{12}\right\}^{-1} \cdot \text{Im}\left\{\boldsymbol{M}_{11}\right\} \in \mathbb{R}^{N_r \times N_d}$. Inserting the $\boldsymbol{r}$ in Eq. (7.24) results in

$$
\begin{aligned}
\boldsymbol{x} &= \boldsymbol{F}_N^H \bar{\boldsymbol{B}} \begin{bmatrix} \boldsymbol{P} & \boldsymbol{0} \\ \boldsymbol{0} & \boldsymbol{P} \end{bmatrix} \begin{bmatrix} \boldsymbol{I}_{N_d} \\ \boldsymbol{T} \\ -\boldsymbol{I}_{N_d} \\ -\boldsymbol{T} \end{bmatrix} \boldsymbol{d} \\
&= \boldsymbol{F}_N^H \bar{\boldsymbol{B}} \begin{bmatrix} \boldsymbol{G}_{\text{Sys}} \\ -\boldsymbol{G}_{\text{Sys}} \end{bmatrix} \boldsymbol{d},
\end{aligned}
\tag{7.26}
$$

where $\boldsymbol{G}_{\text{Sys}} = \boldsymbol{P} \begin{bmatrix} \boldsymbol{I}_{N_d} \\ \boldsymbol{T} \end{bmatrix} \in \mathbb{R}^{N_m \times N_d}$ is the code generator matrix for the systematic approach. To calculate the best $\boldsymbol{P}$ matrix for the PAM UW-DMT scheme,we define the expected redundant energy as

$$
E_r = \frac{2}{N} \mathbb{E}\left\{\boldsymbol{r}^H \boldsymbol{r}\right\} = \frac{\sigma_d^2}{N} \text{tr}\left(\boldsymbol{T}\boldsymbol{T}^H\right).
\tag{7.27}
$$

Then we use the heuristic method proposed in [HHOH14] to calculate the best position of the redundant subcarriers ($\boldsymbol{P}$ matrix).

7.3.2. Non-Systematic Code Generator Matrix

We have shown in the previous section that even with the optimal positions of the redundant subcarriers, the systematic approach still results in a high energy contribution of the redundant subcarriers. Therefore, we present a non-systematic code generator matrix design for PAM UW-DMT where the data and the redundant symbols are not distinguishable at the output of the code generator matrix. We rewrite Eq. (7.23) as

$$
\underbrace{\boldsymbol{F}_N^H \begin{bmatrix} \boldsymbol{B} & \boldsymbol{0} \\ \boldsymbol{0} & \widehat{\boldsymbol{\Pi}}\boldsymbol{B} \end{bmatrix}}_{\begin{bmatrix} \boldsymbol{M}_{11} & \boldsymbol{M}_{12} \\ \boldsymbol{M}_{21} & \boldsymbol{M}_{22} \end{bmatrix}} \begin{bmatrix} \boldsymbol{G} & \boldsymbol{0} \\ \boldsymbol{0} & \boldsymbol{G}^* \end{bmatrix} \begin{bmatrix} \boldsymbol{d} \\ \boldsymbol{d}^* \end{bmatrix} = \begin{bmatrix} \boldsymbol{0} \\ \boldsymbol{x}_d \end{bmatrix}.
\tag{7.28}
$$

Using a similar procedure as for the systematic approach, we get

$$
\begin{aligned}
\boldsymbol{0} &= \boldsymbol{M}_{11}\boldsymbol{G}\boldsymbol{d} + \boldsymbol{M}_{12}\boldsymbol{G}^*\boldsymbol{d}^* \\
\boldsymbol{0} &= 2 \cdot \text{Re}\left\{\boldsymbol{M}_{11}\boldsymbol{G}\boldsymbol{d}\right\}.
\end{aligned}
\tag{7.29}
$$

By choosing a real-valued generator matrix ($\text{Im}\{\boldsymbol{G}\} = 0$), this results in

$$
\boldsymbol{0} = \text{Re}\{\boldsymbol{M}_{11}\}\text{Re}\{\boldsymbol{G}\}\text{Re}\{\boldsymbol{d}\} - \text{Im}\{\boldsymbol{M}_{11}\}\text{Re}\{\boldsymbol{G}\}\text{Im}\{\boldsymbol{d}\}.
$$

Since $\text{Re}\{\boldsymbol{d}\} = \boldsymbol{0}$, and with $\boldsymbol{G}_{\text{Nsys}} = \text{Re}\{\boldsymbol{G}\}$, we finally end up at the constraint

$$\boldsymbol{0} = \text{Im}\{\boldsymbol{M}_{11}\}\boldsymbol{G}_{\text{Nsys}},$$

i.e., the columns of $\boldsymbol{G}_{\text{Nsys}}$ matrix are in the null space of $\text{Im}\{\boldsymbol{M}_{11}\}$. Note that there exist multiple solutions of this problem and the code generator matrix is not unique. Hence, we compute the singular value decomposition (SVD) of $\text{Im}\{\boldsymbol{M}_{11}\}$ and select the orthonormal columns corresponding to the null space of the $\text{Im}\{\boldsymbol{M}_{11}\}$ matrix. We refer to this code generator matrix as $\boldsymbol{G}_{\text{Nsys}} \in \mathbb{R}^{N_m \times N_d}$ which simplifies Eq. (7.4) as

$$\boldsymbol{x} = \boldsymbol{F}_N^H \bar{\boldsymbol{B}} \begin{bmatrix} \boldsymbol{G}_{\text{Nsys}} \\ -\boldsymbol{G}_{\text{Nsys}} \end{bmatrix} \boldsymbol{d}. \tag{7.30}$$

7.3.3. Receiver Design

The data received in the frequency domain after subtracting the UW and removing the zero subcarriers is given by

$$\boldsymbol{y} = \bar{\boldsymbol{B}}^T \boldsymbol{F}_N \hat{\boldsymbol{H}} \boldsymbol{F}_N^H \bar{\boldsymbol{B}} \begin{bmatrix} \boldsymbol{G} \\ -\boldsymbol{G} \end{bmatrix} \boldsymbol{d} + \bar{\boldsymbol{B}}^T \boldsymbol{F}_N \hat{\boldsymbol{n}}$$

$$= \boldsymbol{H}\boldsymbol{G}_{\text{eff}}\boldsymbol{d} + \boldsymbol{n}, \tag{7.31}$$

where $\boldsymbol{G}_{\text{eff}}$ is the combined code generator matrix that consist of either of a systematic or a non-systematic code generator matrix, $\hat{\boldsymbol{H}} \in \mathbb{R}^{N \times N}$ is the circulant convolutional matrix containing the channel impulse response, $\boldsymbol{H} = \bar{\boldsymbol{B}}^T \boldsymbol{F}_N \hat{\boldsymbol{H}} \boldsymbol{F}_N^H \bar{\boldsymbol{B}} \in \mathbb{C}^{2N_m \times 2N_m}$ is a diagonal matrix with the channel transfer function on its diagonal, and $\boldsymbol{n} = \bar{\boldsymbol{B}}^T \boldsymbol{F}_N \hat{\boldsymbol{n}}$ is the noise in the frequency domain. We use the BLUE and LMMSE estimators for the PAM UW-DMT scheme which are given as

$$\boldsymbol{E}_{\text{BLUE}} = \left(\boldsymbol{G}_{\text{eff}}^H \boldsymbol{H}^H \boldsymbol{H} \boldsymbol{G}_{\text{eff}}\right)^{-1} \boldsymbol{G}_{\text{eff}}^H \boldsymbol{H}^H, \tag{7.32}$$

$$\boldsymbol{E}_{\text{MMSE}} = \left(\boldsymbol{G}_{\text{eff}}^H \boldsymbol{H}^H \boldsymbol{H} \boldsymbol{G}_{\text{eff}} + \frac{\sigma_n^2}{\sigma_d^2} \boldsymbol{I}_{N_d}\right)^{-1} \boldsymbol{G}_{\text{eff}}^H \boldsymbol{H}^H, \tag{7.33}$$

where σ_n^2 is the variance of the noise samples and σ_d^2 is the variance of the data symbols. The estimated symbols $\hat{\boldsymbol{s}}$ are given as

$$\hat{\boldsymbol{s}} = \text{Im}\{\boldsymbol{E}\boldsymbol{y}\} \in \mathbb{C}^{N_d \times 1}.$$

7.3.4. Simulation Results

In this work, we evaluate the performance of the proposed scheme over a Gaussian low pass channel (Channel 1). Moreover, we also include the impact of the transmit and the receive filtering in our
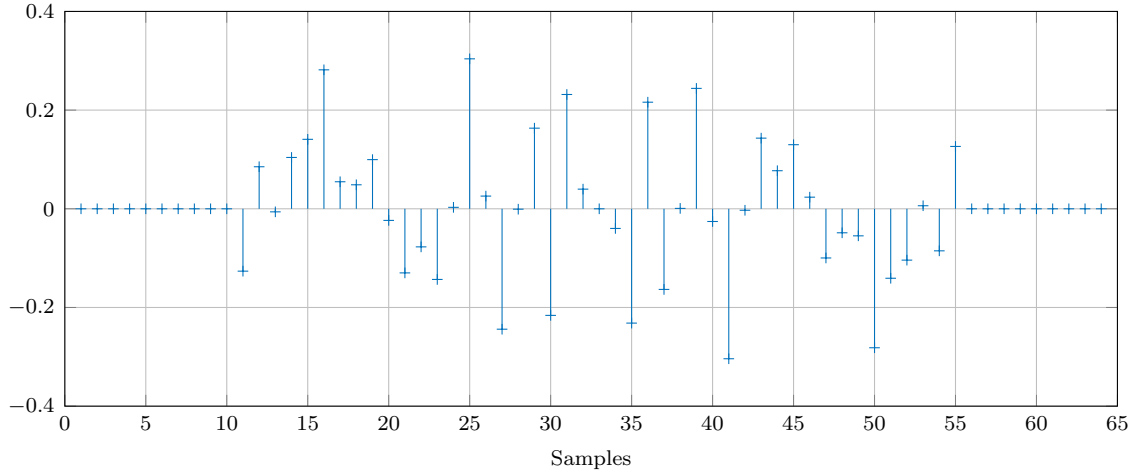
Figure 7.6.: Time domain samples at the output of IDFT (before clipping) for $N = 64$ and $N_r = 10$

simulation. The overall impulse response is given as

$$h(t) = g_{\text{tx}}(t) * g_{\text{ch}}(t) * g_{\text{rx}}(t), \tag{7.34}$$

where $*$ is the convolution operator, $g_{\text{tx}}(t)$ is the impulse response of the transmit filter, $g_{\text{ch}}(t)$ is the channel impulse response of the Gaussian low pass filter, and $g_{\text{rx}}(t)$ is the impulse response of the receive filter. In this work, we use a rectangular filter as the transmit filter whereas a 5th order Bessel filter is used as the receive filter. Moreover, we evaluate the performance in terms of the BER versus the normalized optical power which is given as $RP/\sqrt{N_0 R_{\text{b}}}$. Here P defines the required average optical power of the investigated transmission scheme, R is the photodiode responsivity which is chosen as one in this work, R_{b} is the bit rate, and N_0 is the noise power spectral density of the signal independent noise current. Note that the ratio $RP/\sqrt{N_0 R_{\text{b}}}$ corresponds to the ratio $E_{\text{b,elec}}/N_0$ which is usually used for performance analysis in RF communication. The remaining parameters are shown in Table 7.2. We used half of the redundant carriers for the length of the UW. This is due to the fact that our proposed code generator matrices produce $N_r = N_u$ zeros at the start of the time domain samples and N_u zeros at the end of the time domain samples, as shown in Fig. 7.6. Therefore, a UW of length N_u can be added in between two symbols by generating $N_u/2$ zeros in the first step.

	UW-DMT	CP-DMT
FFT size (N)	128	
Data Carriers (N_d)	55	60
Redundant Carriers (N_r)	5	-
CP/UW duration	10 Samples	
Oversampling factor	2	
Channel	Gaussian Low Pass	

Table 7.2.: Simulation Parameters

We compare the performance of the proposed scheme with the conventional PAM CP-DMT scheme for two modulation orders, 4-PAM and 16-PAM, and for different cut-off frequencies of the Gaussian
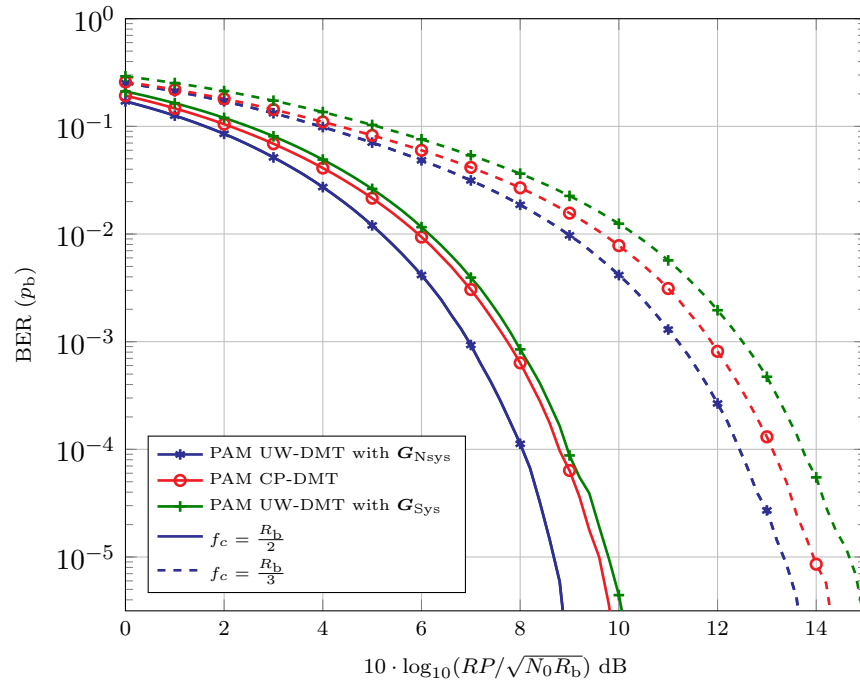
(a) Performance of 4-PAM with different 3-dB cut-off frequencies
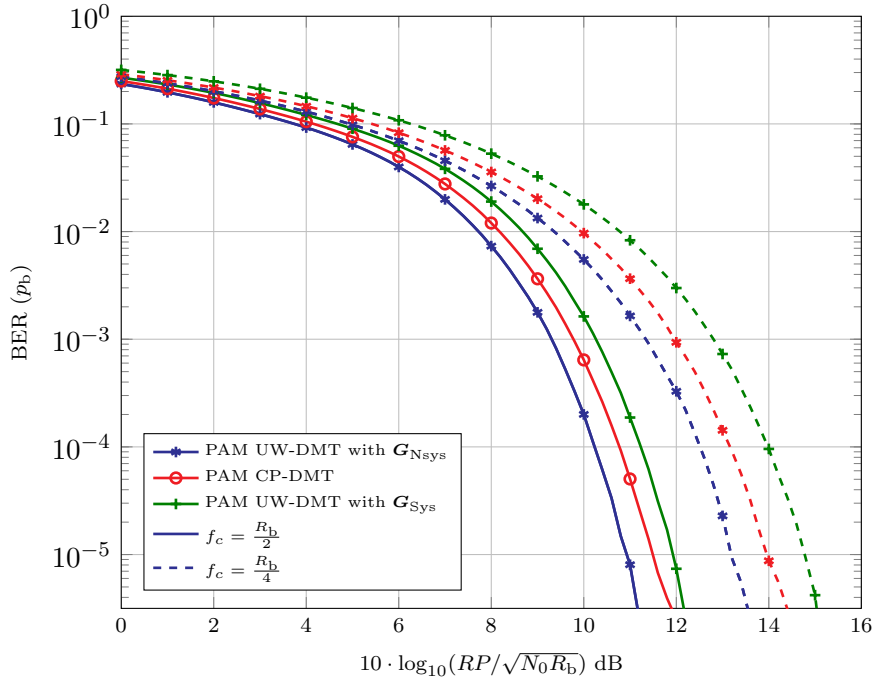
(b) Performance of 16-PAM with different 3-dB cut-off frequencies

Figure 7.7.: Performance comparison of PAM UW-DMT scheme

channel, as shown in Fig. 7.7. Note that $R_\mathrm{b}/f_\mathrm{3dB}$ characterizes the spectral efficiency in bits/s/Hz. Therefore, the results can be interpreted as showing plots for the BER versus the required normalized optical power to achieve a particular spectral efficiency. Moreover, we show results for the two proposed generator matrix designs where both generator matrices result in a different UW-DMT performance.

Even when using the optimum positions of the redundant subcarriers, the systematic design suffers from the high redundant energy contribution, i.e., the mean power of the redundant subcarrier symbols is still considerably higher than that of the data symbols. However, in the non-systematic case, the redundant energy is distributed over all symbols, resulting in a lower contribution of the redundant energy. Therefore, the PAM UW-DMT performance with $\boldsymbol{G}_{\mathrm{Sys}}$ is worse than UW-DMT with $\boldsymbol{G}_{\mathrm{Nsys}}$, especially at higher cut-off frequencies. Moreover, the results show that our proposed scheme with $\boldsymbol{G}_{\mathrm{Nsys}}$ outperforms CP-DMT by 0.9 dB to 1.2 dB, depending on the modulation order and the cut-off frequency. Thus, the proposed PAM UW-DMT scheme requires lower optical power to achieve the same spectral efficiency. Note that the $\boldsymbol{G}$ matrix is only designed once for the system specific parameters and does not need to be changed in run-time. Therefore, the additional complexity at the transmitter side compared to the CP-DMT scheme lies in the multiplication with the $\boldsymbol{G}$ matrix. At the receiver, the complexity depends on the type of detector employed.

7.4. Conclusion

In this work, we have proposed three novel unique word DMT schemes for complex- and real-valued formats, namely AC UW-DMT, DC-biased UW-DMT, and PAM UW-DMT for optical systems with IM/DD. We have proposed different types of code generator matrices for these schemes. In the DMT schemes, a Hermitian symmetry has to be enforced to obtain real-valued signals. This constraint offers an extra degree of freedom in designing the code generator matrices where we have proposed two solutions for complex-valued UW-DMT scheme. The solution 2 is a better choice as compared to solution 1, since it generates zeros not only at the tail, but also at the start of the time domain samples, thus reducing the amount of redundancy required to employ a UW of length N_u. The results show that the non-systematic code generator matrix that uses solution 2 is the best design choice for all UW-DMT schemes. The UW-DMT schemes with this design not only outperform the other designs in terms of power penalties but also the conventional CP-DMT schemes significantly. In addition to the improved performance, the UW in the UW-DMT schemes can be used for other purposes such as synchronization or parameter estimation.

Part III.

Analytical Performance Analysis of Multi-linear (tensor) Algebraic Concepts

In the last part of the thesis, we discuss the first-order analytical performance of some of the fundamental multi-linear algebraic concepts such as the truncated higher order singular value decomposition (HOSVD) and the SEmi-algebraic canonical polyadic decomposition via SImultaneous Matrix Diagonalization (SECSI) framework. These algorithms have been used in a vast range of applications. For instance, the HOSVD is most commonly applied to the extraction of relevant information from multi-way arrays, e.g., for real-time event detection from complex data streams in disease surveillance [FG14]. Similarly, the SECSI framework has already been successfully applied for source localization and source extraction from EEG recordings [BCA+10] and also for space-time-frequency component analysis of event-related EEGs [WRH+09]. The performance of these multi-linear algorithms is often evaluated using the Monte-Carlo simulations in the literature. However, a perturbation analysis of these algorithms is of major importance for analyzing the performance of these algorithms without using the computational expensive Monte-Carlo trials. It also helps in acquiring better insights on the behavior of the reconstruction error beforehand.

We start this part of the thesis by first discussing the first-order perturbation analysis of the truncated HOSVD in Chapter 8. We evaluate the performance of the obtained analytical expressions not only by using computer generated data but also by using some low rank images. Parts of this chapter have been published in one conference paper [BCS+16]. In Chapter 9, we provide an analytical performance analysis of the SECSI framework for the computation of the approximate canonical polyadic decomposition (CPD) of noise corrupted low-rank 3-dimensional (3D) tensors. Since the truncated HOSVD is the first step performed in the SECSI framework, we also utilize the results obtained in Chapter 8. We derive closed-form expressions of the relative mean square error for each of the estimated factor matrices. Parts of the results of this chapter have been published in one conference paper [CBW+17] and the remaining results are submitted in a journal paper [CBC+17].

8. First-order Performance Analysis of Truncated HOSVD

The truncated version of the higher-order singular value decomposition (HOSVD) has a great significance in multi-dimensional tensor-based signal processing. It allows to extract the principal components from noisy observations in order to find a low-rank approximation of the multi-dimensional data. In this chapter, we address the question of how good the approximation is by analytically quantifying the tensor reconstruction error introduced by the truncated HOSVD. After introducing the state-of-the-art, we discuss the system model in Section 8.2. We present a first-order perturbation analysis of the truncated HOSVD in Section 8.3 to obtain analytical expressions for the signal subspace error in each dimension as well as the tensor reconstruction error induced by the low-rank approximation of the noise corrupted tensor. We further simplify the obtained expressions for the special case of uncorrelated noise with equal variance. We show the simulation results using computer generated data and also using images in Section 8.4. The chapter is concluded in Section 8.5.

8.1. Introduction

The problem of extracting information and parameters of multi-dimensional signals from noisy observations plays an important role in a broad variety of applications in signal processing. In order to exploit the multi-dimensional structure of the signals, tensor-based algorithms are often used. Many of these algorithms require a low-rank approximation of the measurement tensor as a preprocessing step. Such an approximation is usually obtained by the higher-order singular value decomposition (HOSVD) [dLdMV00b], which preserves the multi-dimensional nature inherent in the data. Its truncated version enables the retrieval of the principal components to form a low-rank approximation of the measurement tensor. In contrast to the matrix case, the truncated HOSVD is not necessarily the best low-rank approximation of a tensor in the Frobenius norm. Thus, [dLdMV00a] proposes an iterative algorithm based on higher-order orthogonal iterations (HOOI) to compute the best rank-$(r_1, r_2, \ldots, r_N)$ approximation. However, as shown in [Roe12], the improvement in terms of the reconstruction error from the HOOI algorithm over the truncated HOSVD is only marginal in the low signal-to-noise ratio (SNR) regime and negligible for high SNRs. Hence, the truncated HOSVD is usually preferred. Applications where the truncated HOSVD is commonly used are, for instance, image processing [LZH09a, DLS+15, AG13], object/pattern recognition [JSI+07, FKC+12, MNM11, AHF+14, CS14], parameter estimation [CB10, HRdG08, BGPF12], control engineering [ORV11, HX14], data analysis [LYD+15, RSV13, MPG09, RSSV13, RD13, LZY+05], and others. Therefore, a performance analysis to assess the reconstruction error introduced by the low-rank approximation based on the truncated HOSVD is of major importance when analyzing the performance of several algorithms that are based on such a low-rank approximation.

A first-order perturbation analysis for the n-mode singular vectors and singular values obtained from the HOSVD was first presented in [dLdMV00b]. Therein, however, only the full HOSVD without the truncation was investigated. In [dL04], a first-order performance analysis for the best low-rank approximation of a tensor [dLdMV00a] in the least squares sense was presented. However, both perturba-

tion analyses do not provide explicit analytical expressions for the reconstruction error in terms of the noise statistics. In the case of the multidimensional harmonic retrieval problem, a first-order expansion of the HOSVD-based subspace estimation error of the noisy measurement tensor has been proposed in [RHDG14], which generalizes the first-order performance analysis framework for the subspace estimation error from the SVD of the measurement matrix [LLV93] to the tensor case. This framework is applicable whenever the signal component is superimposed by a small noise contribution. In [RHDG14], the derived analytical mean square error (MSE) expressions merely depend on the second-order moments of the noise and hence, only require the noise to be zero-mean. However, to the best of our knowledge, we are the first ones to perform such a perturbation analysis for the truncated HOSVD.

In this chapter, we further extend [RHDG14] and propose a first-order perturbation analysis of the truncated HOSVD. Specifically, we provide analytical closed-form MSE expressions for the tensor reconstruction error in terms of the second-order moments of the noise. Thus, apart from a zero-mean and finite second-order moments, no assumptions on the statistics of the noise are required, i.e., the derived expressions are even valid for non-Gaussian or colored noise. Moreover, the expressions are asymptotic in the signal-to-noise ratio (SNR). In order to provide further insights into the truncated HOSVD, we also provide analytical MSE expressions for the subspace estimation error in the n-th mode, which may be of interest in some of the aforementioned applications. Additionally, we derive simplified versions of the analytical MSE expressions for the reconstruction error and the subspace estimation error for the special case of uncorrelated noise with equal variance. Simulations show that the analytical results provide an excellent match to the empirical ones.

8.2. Data Model

A generalization of the singular value decomposition to R-way arrays or order R tensors is referred as higher order singular value decomposition. It is special case of the Tucker3 decomposition for the 3-D case [Tuc66]. In the general R-D case, the HOSVD of a R order $\boldsymbol{\mathcal{X}} \in \mathbb{C}^{M_1 \times M_2 \times \cdots \times M_R}$ is given by

$$\boldsymbol{\mathcal{X}} = \boldsymbol{\mathcal{S}} \times_1 \boldsymbol{U}_1 \cdots \times_R \boldsymbol{U}_R = \boldsymbol{\mathcal{S}} \bigtimes_{r=1}^{R} \boldsymbol{U}_r, \tag{8.1}$$

where $\boldsymbol{\mathcal{S}} \in \mathbb{C}^{p_1 \times p_2 \times \cdots \times p_R}$ is the core tensor and $\boldsymbol{U}_r \in \mathbb{C}^{M_r \times p_r}$ are the unitary basis for the r-th space of $\boldsymbol{\mathcal{X}}$. Here p_r refers to the r-rank of $\boldsymbol{\mathcal{X}}$ which are defined as $p_r = \text{rank}\left([\boldsymbol{\mathcal{X}}]_{(r)}\right)$ for $r = 1, 2, \ldots, R$. The unitary basis are obtained from the matrix SVDs of the r-mode unfoldings of $\boldsymbol{\mathcal{X}}$. Moreover, the full core tensor is obtained by

$$\boldsymbol{\mathcal{S}} = \boldsymbol{\mathcal{X}} \times_1 \boldsymbol{U}_1^H \cdots \times_R \boldsymbol{U}_R^H. \tag{8.2}$$

An example of HOSVD of a 3-way tensor is shown in Fig. 8.1.

In reality, the tensor $\boldsymbol{\mathcal{X}}$ is corrupted by the noise which can be modeled as a low rank tensor plus a full-rank noise tensor. Therefore we have

$$\boldsymbol{\mathcal{X}} = \boldsymbol{\mathcal{X}}_0 + \boldsymbol{\mathcal{N}}, \tag{8.3}$$
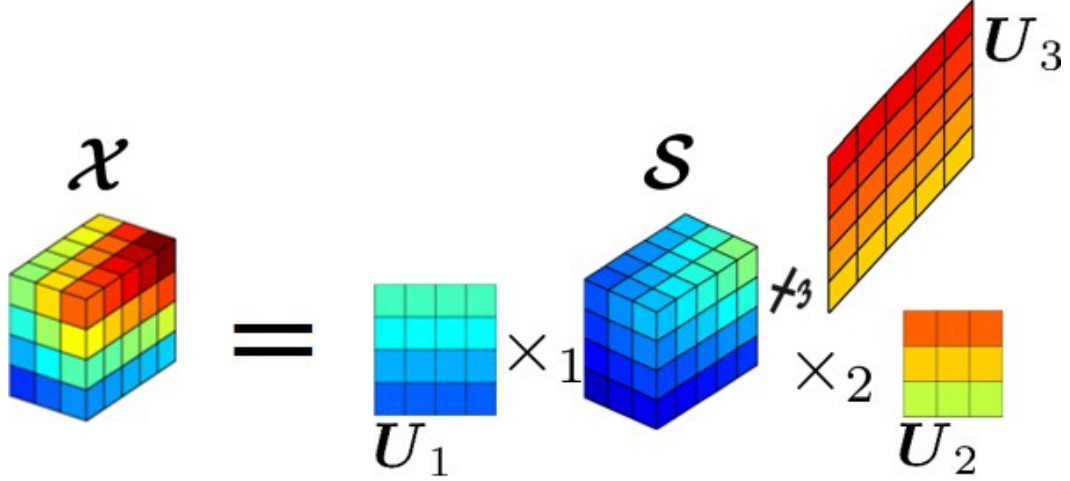
Figure 8.1.: Graphical representation of HOSVD of 3-way tensor.

where $\boldsymbol{\mathcal{X}}_0 \in \mathbb{C}^{M_1 \times M_2 \times \cdots \times M_R}$ is the noiseless low-rank tensor and $\boldsymbol{\mathcal{N}} \in \mathbb{C}^{M_1 \times M_2 \times \cdots \times M_R}$ is a random additive noise full-rank tensor. Moreover, we define the r-mode correlation matrices $\boldsymbol{R}_r$ of $\boldsymbol{\mathcal{N}}$ as[1]

$$\boldsymbol{R}_r \triangleq \mathbb{E}\left\{ \text{vec}\left\{ [\boldsymbol{\mathcal{N}}]_{(r)} \right\} \cdot \text{vec}\left\{ [\boldsymbol{\mathcal{N}}]_{(r)} \right\}^{\mathrm{H}} \right\} \in \mathbb{C}^{M \times M}.$$

Note that the signal to be represented by $\boldsymbol{\mathcal{X}}$ and $\boldsymbol{\mathcal{X}}_0$ depends on the application. To illustrate this point, some examples are shown in Table 8.1. Therefore, a low-rank approximation is of great important in

Application	$\boldsymbol{\mathcal{X}}_0$	$\boldsymbol{\mathcal{X}}$
De-noising	True data	Noisy data
Compression	Compressed data	Uncompressed data
Parameter Estimation	Ideal measurements	Noisy measurements

Table 8.1.: Different interpretations for the low-rank tensor $\boldsymbol{\mathcal{X}}_0$, and the noisy tensor $\boldsymbol{\mathcal{X}}$ according to Eq. (8.3)

such application. For a low-rank tensor, the SVD of the r-mode unfolding is given by

$$
\begin{aligned}
[\boldsymbol{\mathcal{X}}_0]_{(r)} &= \boldsymbol{U}_r \cdot \boldsymbol{\Sigma}_r \cdot \boldsymbol{V}_r^{\mathrm{H}} \\
&= \begin{bmatrix} \boldsymbol{U}_r^{[\mathrm{s}]} & \boldsymbol{U}_r^{[\mathrm{n}]} \end{bmatrix} \begin{bmatrix} \boldsymbol{\Sigma}_r^{[\mathrm{s}]} & \boldsymbol{0}_{p_r \times M/M_r} \\ \boldsymbol{0}_{(M_r - p_r) \times p_r} & \boldsymbol{0}_{(M_r - p_r) \times M/M_r} \end{bmatrix} \begin{bmatrix} \boldsymbol{V}_r^{[\mathrm{s}]} & \boldsymbol{V}_r^{[\mathrm{n}]} \end{bmatrix}^{\mathrm{H}},
\end{aligned}
$$

where $\boldsymbol{\Sigma}_r^{[\mathrm{s}]} = \text{diag}\left\{ \sigma_r^{(i)} \right\}_{i=1}^{p_r}$ is the diagonal matrix that contains the singular values of $[\boldsymbol{\mathcal{X}}_0]_{(r)}$, and $\boldsymbol{U}_r^{[\mathrm{s}]} \in \mathbb{C}^{M_r \times p_r}$, $\boldsymbol{U}_r^{[\mathrm{n}]} \in \mathbb{C}^{M_r \times (M_r - p_r)}$, $\boldsymbol{V}_r^{[\mathrm{s}]} \in \mathbb{C}^{\frac{M_r}{M} \times p_r}$, and $\boldsymbol{V}_r^{[\mathrm{n}]} \in \mathbb{C}^{\frac{M_r}{M} \times (\frac{M_r}{M} - p_r)}$ have unitary columns $\forall r = 1, 2, \ldots, R$. Hence the noiseless tensor $\boldsymbol{\mathcal{X}}_0$ can be represented by the economy size HOSVD, which

---

[1]Note that $\boldsymbol{R}_1, \boldsymbol{R}_2, \ldots, \boldsymbol{R}_R$ are permuted versions of each other.

is given by

$$\boldsymbol{\mathcal{X}}_0 = \boldsymbol{\mathcal{S}}^{[\mathrm{s}]} \times_1 \boldsymbol{U}_1^{[\mathrm{s}]} \cdots \times_R \boldsymbol{U}_R^{[\mathrm{s}]} = \boldsymbol{\mathcal{S}}^{[\mathrm{s}]} \bigtimes_{r=1}^{R} \boldsymbol{U}_r^{[\mathrm{s}]}. \tag{8.4}$$

Similarly, for the noisy full-rank tensor, the SVD of the r-mode unfolding is given by

$$[\boldsymbol{\mathcal{X}}]_{(r)} = \hat{\boldsymbol{U}}_r \cdot \hat{\boldsymbol{\Sigma}}_r \cdot \hat{\boldsymbol{V}}_r^{\mathrm{H}}$$

$$= \begin{bmatrix} \hat{\boldsymbol{U}}_r^{[\mathrm{s}]} & \hat{\boldsymbol{U}}_r^{[\mathrm{n}]} \end{bmatrix} \begin{bmatrix} \hat{\boldsymbol{\Sigma}}_r^{[\mathrm{s}]} & \boldsymbol{0}_{p_r \times M/M_r} \\ \boldsymbol{0}_{(M_r - p_r) \times p_r} & \hat{\boldsymbol{\Sigma}}_r^{[\mathrm{n}]} \end{bmatrix} \begin{bmatrix} \hat{\boldsymbol{V}}_r^{[\mathrm{s}]} & \hat{\boldsymbol{V}}_r^{[\mathrm{n}]} \end{bmatrix}^{\mathrm{H}}.$$

In this case, $\hat{\boldsymbol{U}}_r^{[\mathrm{s}]} \in \mathbb{C}^{M_r \times p_r}$ is an estimate of $\boldsymbol{U}_r^{[\mathrm{s}]}$.

The low-rank approximation in the tensor case can be provided by the truncated HOSVD. In this case, the low-rank approximation of the original tensor ($\boldsymbol{\mathcal{X}}_0 \approx \hat{\boldsymbol{\mathcal{X}}}$) is achieved by truncating the core tensor and the signal subspace matrices. Assuming that the r-ranks of the noiseless tensor $\boldsymbol{\mathcal{X}}_0$ are either known, fixed, or estimated before performing the truncated HOSVD, the noiseless tensor $\boldsymbol{\mathcal{X}}_0$ can be estimated from $\boldsymbol{\mathcal{X}}$ as

$$\hat{\boldsymbol{\mathcal{X}}} = \hat{\boldsymbol{\mathcal{S}}}^{[\mathrm{s}]} \times_1 \hat{\boldsymbol{U}}_1^{[\mathrm{s}]} \cdots \times_R \hat{\boldsymbol{U}}_R^{[\mathrm{s}]} = \hat{\boldsymbol{\mathcal{S}}}^{[\mathrm{s}]} \bigtimes_{r=1}^{R} \hat{\boldsymbol{U}}_r^{[\mathrm{s}]}, \tag{8.5}$$

where the truncated core tensor $\hat{\boldsymbol{\mathcal{S}}}^{[\mathrm{s}]}$ can be computed using the definition in Eq. (8.2) as

$$\hat{\boldsymbol{\mathcal{S}}}^{[\mathrm{s}]} = \boldsymbol{\mathcal{X}} \bigtimes_{r=1}^{R} \hat{\boldsymbol{U}}_r^{[\mathrm{s}]\mathrm{H}} \in \mathbb{C}^{p_1 \times p_2 \times \cdots p_R}. \tag{8.6}$$

8.3. First-order Perturbation Analysis of Truncated HOSVD

The estimated tensor, truncated core tensor, and subspace estimates in Eq. (8.5) are related to the true tensor, core tensor, and subspace for the noiseless tensor in Eq. (8.4) as

$$\hat{\boldsymbol{\mathcal{X}}} = \boldsymbol{\mathcal{X}}_0 + \Delta\boldsymbol{\mathcal{X}} \tag{8.7}$$

$$\hat{\boldsymbol{\mathcal{S}}}^{[\mathrm{s}]} = \boldsymbol{\mathcal{S}}^{[\mathrm{s}]} + \Delta\boldsymbol{\mathcal{S}}^{[\mathrm{s}]} \tag{8.8}$$

$$\hat{\boldsymbol{U}}_r^{[\mathrm{s}]} = \boldsymbol{U}_r^{[\mathrm{s}]} + \Delta\boldsymbol{U}_r^{[\mathrm{s}]}, \tag{8.9}$$

where $\Delta\boldsymbol{\mathcal{X}}$, $\Delta\boldsymbol{\mathcal{S}}^{[\mathrm{s}]}$, and $\Delta\boldsymbol{U}_r^{[\mathrm{s}]}$ are the perturbations present in $\boldsymbol{\mathcal{X}}_0$, $\hat{\boldsymbol{\mathcal{S}}}^{[\mathrm{s}]}$, and $\hat{\boldsymbol{U}}_r^{[\mathrm{s}]}$, respectively. Eq. (8.5) can be further simplified by using Eq. (8.6) to obtain

$$\hat{\boldsymbol{\mathcal{X}}} = \hat{\boldsymbol{\mathcal{S}}}^{[\mathrm{s}]} \bigtimes_{r=1}^{R} \hat{\boldsymbol{U}}_r^{[\mathrm{s}]} = \boldsymbol{\mathcal{X}} \bigtimes_{r=1}^{R} \hat{\boldsymbol{\Gamma}}_r, \tag{8.10}$$

where the $\hat{\mathbf{\Gamma}}_r$ matrices are the estimated signal subspace projection matrices which are defined as

$$\hat{\mathbf{\Gamma}}_r = \hat{\boldsymbol{U}}_r^{[\mathrm{s}]} \cdot \hat{\boldsymbol{U}}_r^{[\mathrm{s}]^{\mathrm{H}}}. \tag{8.11}$$

We can express the perturbation in $\hat{\mathbf{\Gamma}}_r$ as

$$\hat{\mathbf{\Gamma}}_r = \mathbf{\Gamma}_r + \Delta\mathbf{\Gamma}_r, \tag{8.12}$$

where $\mathbf{\Gamma}_r = \boldsymbol{U}_r^{[\mathrm{s}]} \cdot \boldsymbol{U}_r^{[\mathrm{s}]^{\mathrm{H}}}$ be the projection matrix onto the column space spanned by $\boldsymbol{U}_r^{[\mathrm{s}]}$ for the noiseless tensor. By inserting the above definition and the relation $\boldsymbol{\mathcal{X}} = \boldsymbol{\mathcal{X}}_0 + \boldsymbol{\mathcal{N}}$, Eq. (8.10) can be further simplified as

$$
\begin{aligned}
\hat{\boldsymbol{\mathcal{X}}} &= (\boldsymbol{\mathcal{X}}_0 + \boldsymbol{\mathcal{N}}) \overset{R}{\underset{r=1}{\times_r}} \hat{\mathbf{\Gamma}}_r \\
&= \boldsymbol{\mathcal{X}}_0 \overset{R}{\underset{r=1}{\times_r}} \hat{\mathbf{\Gamma}}_r + \boldsymbol{\mathcal{N}} \overset{R}{\underset{r=1}{\times_r}} \hat{\mathbf{\Gamma}}_r \\
&= \boldsymbol{\mathcal{X}}_0 \overset{R}{\underset{r=1}{\times_r}} (\mathbf{\Gamma}_r + \Delta\mathbf{\Gamma}_r) + \boldsymbol{\mathcal{N}} \overset{R}{\underset{r=1}{\times_r}} (\mathbf{\Gamma}_r + \Delta\mathbf{\Gamma}_r) \\
&= \boldsymbol{\mathcal{X}}_0 \overset{R}{\underset{r=1}{\times_r}} \mathbf{\Gamma}_r + \boldsymbol{\mathcal{N}} \overset{R}{\underset{r=1}{\times_r}} \mathbf{\Gamma}_r + \sum_{r=1}^{R} \left(\boldsymbol{\mathcal{X}}_0 \times_r \Delta\mathbf{\Gamma}_r \overset{R}{\underset{\substack{i=1 \\ i \neq r}}{\times_i}} \mathbf{\Gamma}_i \right) + \mathcal{O}(\Delta^2) \tag{8.13}
\end{aligned}
$$

Note that, all the terms with more than one error variable (such as $\boldsymbol{\mathcal{N}}, \Delta\mathbf{\Gamma}_1, \Delta\mathbf{\Gamma}_2, \ldots, \Delta\mathbf{\Gamma}_R$) are included inside $\mathcal{O}(\Delta^2)$. For the sake of simplicity, let us define the noise tensor projected on the signal subspaces $\boldsymbol{\mathcal{N}}^{[\mathrm{s}]}$ as $\boldsymbol{\mathcal{N}}^{[\mathrm{s}]} \triangleq \boldsymbol{\mathcal{N}} \overset{R}{\underset{r=1}{\times_r}} \mathbf{\Gamma}_r$. Since the term $\boldsymbol{\mathcal{X}}_0 \times_r \mathbf{\Gamma}_r = \boldsymbol{\mathcal{X}}_0$ for all $r = 1, 2, \ldots, R$, we can further simplify Eq. (8.13) by using the relation $\hat{\boldsymbol{\mathcal{X}}} = \boldsymbol{\mathcal{X}}_0 + \Delta\boldsymbol{\mathcal{X}}$ to get

$$
\boldsymbol{\mathcal{X}}_0 + \Delta\boldsymbol{\mathcal{X}} = \boldsymbol{\mathcal{X}}_0 + \sum_{r=1}^{R} (\boldsymbol{\mathcal{X}}_0 \times_r \Delta\mathbf{\Gamma}_r) + \boldsymbol{\mathcal{N}}^{[\mathrm{s}]} + \mathcal{O}(\Delta^2)
$$

$$
\Delta\boldsymbol{\mathcal{X}} = \sum_{r=1}^{R} (\boldsymbol{\mathcal{X}}_0 \times_r \Delta\mathbf{\Gamma}_r) + \boldsymbol{\mathcal{N}}^{[\mathrm{s}]} + \mathcal{O}(\Delta^2). \tag{8.14}
$$

Our goal is to find an analytical expression for $\mathbb{E}\left\{\|\Delta\boldsymbol{\mathcal{X}}\|_{\mathrm{H}}^2\right\}$. Since $\Delta\boldsymbol{\mathcal{X}}$ in Eq. (8.14) is a function of the perturbation in signal subspace projection matrices, we first analyze the signal subspace perturbation.

8.3.1. Signal Subspace Perturbation

For the truncated HOSVD tensor estimation, we are only interested in the perturbation on the column space spanned by $\hat{\boldsymbol{U}}_r^{[\mathrm{s}]}$. Note that the choice of $\boldsymbol{U}_r^{[\mathrm{s}]}$ is not unique when the HOSVD of $\boldsymbol{\mathcal{X}}_0$ is calculated, but the projection matrix into the subspace spanned by the columns of $\boldsymbol{U}_r^{[\mathrm{s}]}$ is always unique, i.e., $\mathbf{\Gamma}_r$. Therefore we first analyze the perturbation of the r-mode signal subspaces, which are defined as the column spaces spanned by $\boldsymbol{U}_r^{[\mathrm{s}]}$ for $r = 1, 2, \ldots, R$.

8.3.1.1. General Expression

The perturbation $\Delta\boldsymbol{\Gamma}_r$ can be computed by using the definitions in Eq. (8.9) and Eq. (8.11) in Eq. (8.12) to get

$$\Delta\boldsymbol{\Gamma}_r + \boldsymbol{U}_r^{[\mathrm{s}]} \cdot \boldsymbol{U}_r^{[\mathrm{s}]\mathrm{H}} = \hat{\boldsymbol{U}}_r^{[\mathrm{s}]} \cdot \hat{\boldsymbol{U}}_r^{[\mathrm{s}]\mathrm{H}}$$
$$\Delta\boldsymbol{\Gamma}_r + \boldsymbol{U}_r^{[\mathrm{s}]} \cdot \boldsymbol{U}_r^{[\mathrm{s}]\mathrm{H}} = (\boldsymbol{U}_r^{[\mathrm{s}]} + \Delta\boldsymbol{U}_r^{[\mathrm{s}]}) \cdot (\boldsymbol{U}_r^{[\mathrm{s}]} + \Delta\boldsymbol{U}_r^{[\mathrm{s}]})^{\mathrm{H}}$$
$$\Delta\boldsymbol{\Gamma}_r = \boldsymbol{U}_r^{[\mathrm{s}]} \cdot \Delta\boldsymbol{U}_r^{[\mathrm{s}]\mathrm{H}} + \Delta\boldsymbol{U}_r^{[\mathrm{s}]} \cdot \boldsymbol{U}_r^{[\mathrm{s}]\mathrm{H}} + \mathcal{O}(\Delta^2). \tag{8.15}$$

Note that $\Delta\boldsymbol{U}_r^{[\mathrm{s}]} \cdot \Delta\boldsymbol{U}_r^{[\mathrm{s}]\mathrm{H}}$ is a second order term and, therefore, it is considered inside $\mathcal{O}(\Delta^2)$. Moreover, we can use the result for $\Delta\boldsymbol{U}_r^{[\mathrm{s}]}$, obtained in [RHDG14, LLV93], which is

$$\Delta\boldsymbol{U}_r^{[\mathrm{s}]} = \boldsymbol{U}_r^{[\mathrm{n}]} \cdot \boldsymbol{U}_r^{[\mathrm{n}]\mathrm{H}} \cdot [\boldsymbol{\mathcal{N}}]_{(r)} \cdot \boldsymbol{V}_r^{[\mathrm{s}]} \cdot \boldsymbol{\Sigma}_r^{[\mathrm{s}]^{-1}} + \mathcal{O}(\Delta^2). \tag{8.16}$$

Note that $\Delta\boldsymbol{U}_r^{[\mathrm{s}]\mathrm{H}} \cdot \boldsymbol{U}_r^{[\mathrm{s}]} = \boldsymbol{0}$, which means that the perturbation is orthogonal to the column space of $\boldsymbol{U}_r^{[\mathrm{s}]}$. To simplify this expression, let $\widetilde{\boldsymbol{N}}_r \in \mathbb{C}^{(M_r - p_r) \times p_r}$ be the transformed version of r-mode unfolding of the noise, defined as

$$\widetilde{\boldsymbol{N}}_r \triangleq \boldsymbol{U}_r^{[\mathrm{n}]\mathrm{H}} \cdot [\boldsymbol{\mathcal{N}}]_{(r)} \cdot \boldsymbol{V}_r^{[\mathrm{s}]}, \tag{8.17}$$

with its corresponding correlation matrix denoted as $\widetilde{\boldsymbol{R}}_r \triangleq \mathbb{E}\{\mathrm{vec}\{\widetilde{\boldsymbol{N}}_r\} \cdot \mathrm{vec}\{\widetilde{\boldsymbol{N}}_r\}^{\mathrm{H}}\}$. Note that we can express $\widetilde{\boldsymbol{R}}_r$ in terms of the r-mode correlation matrix of the noise $\boldsymbol{R}_r$ as

$$\begin{aligned}
\widetilde{\boldsymbol{R}}_r &= \mathbb{E}\left\{ \mathrm{vec}\left\{\widetilde{\boldsymbol{N}}_r\right\} \cdot \mathrm{vec}\left\{\widetilde{\boldsymbol{N}}_r\right\}^{\mathrm{H}} \right\} \\
&= \mathbb{E}\left\{ \mathrm{vec}\left\{\boldsymbol{U}_r^{[\mathrm{n}]\mathrm{H}} \cdot [\boldsymbol{\mathcal{N}}]_{(r)} \cdot \boldsymbol{V}_r^{[\mathrm{s}]}\right\} \cdot \mathrm{vec}\left\{\boldsymbol{U}_r^{[\mathrm{n}]\mathrm{H}} \cdot [\boldsymbol{\mathcal{N}}]_{(r)} \cdot \boldsymbol{V}_r^{[\mathrm{s}]}\right\}^{\mathrm{H}} \right\} \\
&= \mathbb{E}\left\{ \left(\boldsymbol{V}_r^{[\mathrm{s}]\mathrm{T}} \otimes \boldsymbol{U}_r^{[\mathrm{n}]\mathrm{H}}\right) \cdot \mathrm{vec}\left\{[\boldsymbol{\mathcal{N}}]_{(r)}\right\} \cdot \mathrm{vec}\left\{[\boldsymbol{\mathcal{N}}]_{(r)}\right\}^{\mathrm{H}} \cdot \left(\boldsymbol{V}_r^{[\mathrm{s}]^*} \otimes \boldsymbol{U}_r^{[\mathrm{n}]}\right) \right\} \\
&= \left(\boldsymbol{V}_r^{[\mathrm{s}]\mathrm{T}} \otimes \boldsymbol{U}_r^{[\mathrm{n}]\mathrm{H}}\right) \cdot \boldsymbol{R}_r \cdot \left(\boldsymbol{V}_r^{[\mathrm{s}]^*} \otimes \boldsymbol{U}_r^{[\mathrm{n}]}\right). \tag{8.18}
\end{aligned}$$

Therefore, by applying the notation proposed in Eq. (8.17), we rewrite Eq. (8.16) as

$$\Delta\boldsymbol{U}_r^{[\mathrm{s}]} = \boldsymbol{U}_r^{[\mathrm{n}]} \cdot \widetilde{\boldsymbol{N}}_r \cdot \boldsymbol{\Sigma}_r^{[\mathrm{s}]^{-1}} + \mathcal{O}(\Delta^2). \tag{8.19}$$

The goal is to obtain an analytical expression for the expected value of the Frobenius norm of the r-mode subspace estimation error, i.e., $\mathbb{E}\left\{\|\Delta\boldsymbol{\Gamma}_r\|_{\mathrm{F}}^2\right\}$. To that end, we first analyze the following expression

$$\|\Delta\boldsymbol{\Gamma}_r\|_{\mathrm{F}}^2 = \mathrm{tr}\left[\Delta\boldsymbol{\Gamma}_r \cdot \Delta\boldsymbol{\Gamma}_r^{\mathrm{H}}\right] \tag{8.20}$$

Substituting Eq. (8.15) into Eq. (8.20) and neglecting the terms that contain $\mathcal{O}(\Delta^2)$, we obtain

$$\begin{aligned}
\|\Delta\boldsymbol{\Gamma}_r\|_{\mathrm{F}}^2 &\approx \mathrm{tr}\left[\boldsymbol{U}_r^{[\mathrm{s}]} \cdot \Delta\boldsymbol{U}_r^{[\mathrm{s}]\mathrm{H}} \cdot \boldsymbol{U}_r^{[\mathrm{s}]} \cdot \Delta\boldsymbol{U}_r^{[\mathrm{s}]\mathrm{H}}\right] + \mathrm{tr}\left[\boldsymbol{U}_r^{[\mathrm{s}]} \cdot \Delta\boldsymbol{U}_r^{[\mathrm{s}]\mathrm{H}} \cdot \Delta\boldsymbol{U}_r^{[\mathrm{s}]} \cdot \boldsymbol{U}_r^{[\mathrm{s}]\mathrm{H}}\right] \\
&\quad + \mathrm{tr}\left[\Delta\boldsymbol{U}_r^{[\mathrm{s}]} \cdot \boldsymbol{U}_r^{[\mathrm{s}]\mathrm{H}} \cdot \boldsymbol{U}_r^{[\mathrm{s}]} \cdot \Delta\boldsymbol{U}_r^{[\mathrm{s}]\mathrm{H}}\right] + \mathrm{tr}\left[\Delta\boldsymbol{U}_r^{[\mathrm{s}]} \cdot \boldsymbol{U}_r^{[\mathrm{s}]\mathrm{H}} \cdot \Delta\boldsymbol{U}_r^{[\mathrm{s}]} \cdot \boldsymbol{U}_r^{[\mathrm{s}]\mathrm{H}}\right].
\end{aligned}$$

Since $\Delta \boldsymbol{U}_r^{[\text{s}]\text{H}} \cdot \boldsymbol{U}_r^{[\text{s}]} = \left(\boldsymbol{U}_r^{[\text{s}]\text{H}} \cdot \Delta \boldsymbol{U}_r^{[\text{s}]} \right)^{\text{H}} = \boldsymbol{0}_{p_r \times p_r}$ and $\boldsymbol{U}_r^{[\text{s}]\text{H}} \cdot \boldsymbol{U}_r^{[\text{s}]} = \boldsymbol{I}_{p_r}$, we can use the properties of the trace operator to simply this further to

$$\|\Delta \boldsymbol{\Gamma}_r\|_{\text{F}}^2 \approx 2 \cdot \text{tr}\left[\Delta \boldsymbol{U}_r^{[\text{s}]\text{H}} \cdot \Delta \boldsymbol{U}_r^{[\text{s}]} \right] \tag{8.21}$$

Now, by using Eq. (8.19) and neglecting the second order term, we get

$$\begin{aligned}
\text{tr}\left[\Delta \boldsymbol{U}_r^{[\text{s}]\text{H}} \cdot \Delta \boldsymbol{U}_r^{[\text{s}]} \right] &\approx \text{tr}\left[\boldsymbol{\Sigma}_r^{[\text{s}]^{-1}} \cdot \widetilde{\boldsymbol{N}}_r^{\text{H}} \cdot \boldsymbol{U}_r^{[\text{n}]\text{H}} \cdot \boldsymbol{U}_r^{[\text{n}]} \cdot \widetilde{\boldsymbol{N}}_r \cdot \boldsymbol{\Sigma}_r^{[\text{s}]^{-1}} \right] \\
&= \text{tr}\left[\boldsymbol{\Sigma}_r^{[\text{s}]^{-1}} \cdot \widetilde{\boldsymbol{N}}_r^{\text{H}} \cdot \widetilde{\boldsymbol{N}}_r \cdot \boldsymbol{\Sigma}_r^{[\text{s}]^{-1}} \right] \\
&= \text{tr}\left[\left(\widetilde{\boldsymbol{N}}_r \cdot \boldsymbol{\Sigma}_r^{[\text{s}]^{-1}} \right)^{\text{H}} \cdot \left(\widetilde{\boldsymbol{N}}_r \cdot \boldsymbol{\Sigma}_r^{[\text{s}]^{-1}} \right) \right] = \|\widetilde{\boldsymbol{N}}_r \cdot \boldsymbol{\Sigma}_r^{[\text{s}]^{-1}}\|_{\text{F}}^2 \\
&= \text{tr}\left[\text{vec}\left\{ \widetilde{\boldsymbol{N}}_r \cdot \boldsymbol{\Sigma}_r^{[\text{s}]^{-1}} \right\} \cdot \text{vec}\left\{ \widetilde{\boldsymbol{N}}_r \cdot \boldsymbol{\Sigma}_r^{[\text{s}]^{-1}} \right\}^{\text{H}} \right] \\
&= \text{tr}\left[\left(\boldsymbol{\Sigma}_r^{[\text{s}]^{-1}} \otimes \boldsymbol{I}_{(M_r - p_r)} \right) \cdot \text{vec}\{\widetilde{\boldsymbol{N}}_r\} \cdot \text{vec}\{\widetilde{\boldsymbol{N}}_r\}^{\text{H}} \cdot \left(\boldsymbol{\Sigma}_r^{[\text{s}]^{-1}} \otimes \boldsymbol{I}_{(M_r - p_r)} \right) \right] \\
&= \text{tr}\left[\left(\boldsymbol{\Sigma}_r^{[\text{s}]^{-2}} \otimes \boldsymbol{I}_{(M_r - p_r)} \right) \cdot \text{vec}\{\widetilde{\boldsymbol{N}}_r\} \cdot \text{vec}\{\widetilde{\boldsymbol{N}}_r\}^{\text{H}} \right].
\end{aligned} \tag{8.22}$$

Next, we take the expected value of Eq. (8.22) and obtain

$$\begin{aligned}
\mathbb{E}\left\{ \text{tr}\left[\Delta \boldsymbol{U}_r^{[\text{s}]\text{H}} \cdot \Delta \boldsymbol{U}_r^{[\text{s}]} \right] \right\} &\approx \mathbb{E}\left\{ \text{tr}\left[\left(\boldsymbol{\Sigma}_r^{[\text{s}]^{-2}} \otimes \boldsymbol{I}_{(M_r - p_r)} \right) \cdot \text{vec}\{\widetilde{\boldsymbol{N}}_r\} \cdot \text{vec}\{\widetilde{\boldsymbol{N}}_r\}^{\text{H}} \right] \right\} \\
&= \text{tr}\left[\left(\boldsymbol{\Sigma}_r^{[\text{s}]^{-2}} \otimes \boldsymbol{I}_{(M_r - p_r)} \right) \cdot \mathbb{E}\left\{ \text{vec}\{\widetilde{\boldsymbol{N}}_r\} \cdot \text{vec}\{\widetilde{\boldsymbol{N}}_r\}^{\text{H}} \right\} \right] \\
&= \text{tr}\left[\left(\boldsymbol{\Sigma}_r^{[\text{s}]^{-2}} \otimes \boldsymbol{I}_{(M_r - p_r)} \right) \cdot \widetilde{\boldsymbol{R}}_r \right].
\end{aligned}$$

We can now take the expected value of $\|\Delta \boldsymbol{\Gamma}_r\|_{\text{F}}^2$ (from Eq. (8.21)) and use this relation to obtain the desired closed-form expression

$$\begin{aligned}
\mathbb{E}\left\{ \|\Delta \boldsymbol{\Gamma}_r\|_{\text{F}}^2 \right\} &\approx \mathbb{E}\left\{ 2 \cdot \text{tr}\left[\Delta \boldsymbol{U}_r^{[\text{s}]\text{H}} \cdot \Delta \boldsymbol{U}_r^{[\text{s}]} \right] \right\} \\
&= 2 \cdot \text{tr}\left[\left(\boldsymbol{\Sigma}_r^{[\text{s}]^{-2}} \otimes \boldsymbol{I}_{(M_r - p_r)} \right) \cdot \widetilde{\boldsymbol{R}}_r \right].
\end{aligned} \tag{8.23}$$

8.3.1.2. Special Case of Uncorrelated Noise

Eq. (8.23) can be simplified even further if we assume that the noise is zero-mean and uncorrelated with variance σ_N^2, i.e., $\boldsymbol{R}_r = \sigma_N^2 \cdot \boldsymbol{I}_M$. Therefore, $\widetilde{\boldsymbol{R}}_r$ in Eq. (8.18) is simplified to

$$\begin{aligned}
\widetilde{\boldsymbol{R}}_r &= \left(\boldsymbol{V}_r^{[\text{s}]\text{T}} \otimes \boldsymbol{U}_r^{[\text{n}]\text{H}} \right) \cdot \sigma_N^2 \cdot \boldsymbol{I}_M \cdot \left(\boldsymbol{V}_r^{[\text{s}]^*} \otimes \boldsymbol{U}_r^{[\text{n}]} \right) \\
&= \sigma_N^2 \cdot \left((\boldsymbol{V}_r^{[\text{s}]\text{T}} \cdot \boldsymbol{V}_r^{[\text{s}]^*}) \otimes (\boldsymbol{U}_r^{[\text{n}]\text{H}} \cdot \boldsymbol{U}_r^{[\text{n}]}) \right) \\
&= \sigma_N^2 \cdot (\boldsymbol{I}_{p_r} \otimes \boldsymbol{I}_{M_r - p_r}) = \sigma_N^2 \cdot \boldsymbol{I}_{p_r \cdot (M_r - p_r)}.
\end{aligned} \tag{8.24}$$

Thus, the desired expression in Eq. (8.23) becomes

$$\mathbb{E}\left\{ \|\Delta \boldsymbol{\Gamma}_r\|_{\text{F}}^2 \right\} = 2 \cdot \text{tr}\left[\left(\boldsymbol{\Sigma}_r^{[\text{s}]^{-2}} \otimes (\sigma_N^2 \cdot \boldsymbol{I}_{(M_r - p_r)}) \right) \right]$$

$$= 2 \cdot (M_r - p_r) \cdot \sigma_N^2 \cdot \sum_{i=1}^{p_r} \frac{1}{\left(\sigma_r^{(i)}\right)^2}. \tag{8.25}$$

8.3.2. Perturbation in the Truncated HOSVD estimate

8.3.2.1. General Expression

In the previous section, we obtained the closed-form expressions for the perturbation in the signal subspace matrices. In this section, we derive an analytical expression for the expected value of the Frobenius norm of the error term of interest (i.e., $\mathbb{E}\left\{\|\Delta\boldsymbol{\mathcal{X}}\|_{\mathrm{H}}^2\right\}$) by utilizing the obtained results. Let us assume that $\Delta\boldsymbol{\Gamma}_1, \Delta\boldsymbol{\Gamma}_2, \ldots, \Delta\boldsymbol{\Gamma}_R$ and $\boldsymbol{\mathcal{N}}^{[\mathrm{s}]}$ are independent from each other. Therefore, we approximate $\mathbb{E}\left\{\|\Delta\boldsymbol{\mathcal{X}}\|_{\mathrm{H}}^2\right\}$ in Eq. (8.14) as

$$\mathbb{E}\left\{\|\Delta\boldsymbol{\mathcal{X}}\|_{\mathrm{H}}^2\right\} \approx \mathbb{E}\left\{\sum_{r=1}^{R} \|\boldsymbol{\mathcal{X}}_0 \times_r \Delta\boldsymbol{\Gamma}_r\|_{\mathrm{H}}^2 + \|\boldsymbol{\mathcal{N}}^{[\mathrm{s}]}\|_{\mathrm{H}}^2\right\}. \tag{8.26}$$

The term $\|\boldsymbol{\mathcal{X}}_0 \times_r \Delta\boldsymbol{\Gamma}_r\|_{\mathrm{H}}^2$ contained in Eq. (8.26) can be written as

$$\|\boldsymbol{\mathcal{X}}_0 \times_r \Delta\boldsymbol{\Gamma}_r\|_{\mathrm{H}}^2 = \mathrm{tr}\left[[\boldsymbol{\mathcal{X}}_0]_{(r)}^{\mathrm{H}} \cdot \Delta\boldsymbol{\Gamma}_r^{\mathrm{H}} \cdot \Delta\boldsymbol{\Gamma}_r \cdot [\boldsymbol{\mathcal{X}}_0]_{(r)}\right]$$

By applying the result obtained in Eq. (8.15), we can approximate the term $\Delta\boldsymbol{\Gamma}_r^{\mathrm{H}} \cdot \Delta\boldsymbol{\Gamma}_r$ (by neglecting the terms that contain $\mathcal{O}(\Delta^2)$ in Eq. (8.15)) to

$$\Delta\boldsymbol{\Gamma}_r^{\mathrm{H}} \cdot \Delta\boldsymbol{\Gamma}_r \approx \boldsymbol{U}_r^{[\mathrm{s}]} \cdot \Delta\boldsymbol{U}_r^{[\mathrm{s}]^{\mathrm{H}}} \cdot \Delta\boldsymbol{U}_r^{[\mathrm{s}]} \cdot \boldsymbol{U}_r^{[\mathrm{s}]^{\mathrm{H}}} + \Delta\boldsymbol{U}_r^{[\mathrm{s}]} \cdot \Delta\boldsymbol{U}_r^{[\mathrm{s}]^{\mathrm{H}}}.$$

We can now use this relation to further expand Eq. (8.26) as

$$\begin{aligned}
\|\boldsymbol{\mathcal{X}}_0 \times_r \Delta\boldsymbol{\Gamma}_r\|_{\mathrm{H}}^2 &= \mathrm{tr}\left[[\boldsymbol{\mathcal{X}}_0]_{(r)}^{\mathrm{H}} \cdot \Delta\boldsymbol{\Gamma}_r^{\mathrm{H}} \cdot \Delta\boldsymbol{\Gamma}_r \cdot [\boldsymbol{\mathcal{X}}_0]_{(r)}\right] \\
&\approx \mathrm{tr}\left[(\boldsymbol{U}_r^{[\mathrm{s}]} \cdot \Delta\boldsymbol{U}_r^{[\mathrm{s}]^{\mathrm{H}}} \cdot \Delta\boldsymbol{U}_r^{[\mathrm{s}]} \cdot \boldsymbol{U}_r^{[\mathrm{s}]^{\mathrm{H}}} + \Delta\boldsymbol{U}_r^{[\mathrm{s}]} \cdot \Delta\boldsymbol{U}_r^{[\mathrm{s}]^{\mathrm{H}}}) \cdot [\boldsymbol{\mathcal{X}}_0]_{(r)} \cdot [\boldsymbol{\mathcal{X}}_0]_{(r)}^{\mathrm{H}}\right] \\
&= \mathrm{tr}\left[\boldsymbol{U}_r^{[\mathrm{s}]} \cdot \Delta\boldsymbol{U}_r^{[\mathrm{s}]^{\mathrm{H}}} \cdot \Delta\boldsymbol{U}_r^{[\mathrm{s}]} \cdot \boldsymbol{U}_r^{[\mathrm{s}]^{\mathrm{H}}} \cdot [\boldsymbol{\mathcal{X}}_0]_{(r)} \cdot [\boldsymbol{\mathcal{X}}_0]_{(r)}^{\mathrm{H}}\right].
\end{aligned}$$

Now, we use Eq. (8.19) and again neglect the terms that contain $\mathcal{O}(\Delta^2)$ to simplify this further to

$$\begin{aligned}
\|\boldsymbol{\mathcal{X}}_0 \times_r \Delta\boldsymbol{\Gamma}_r\|_{\mathrm{H}}^2 &\approx \mathrm{tr}\left[\boldsymbol{U}_r^{[\mathrm{s}]} \cdot \boldsymbol{\Sigma}_r^{[\mathrm{s}]^{-1}} \cdot \widetilde{\boldsymbol{N}}_r^{\mathrm{H}} \cdot \boldsymbol{U}_r^{[\mathrm{n}]^{\mathrm{H}}} \cdot \boldsymbol{U}_r^{[\mathrm{n}]} \cdot \widetilde{\boldsymbol{N}}_r \cdot \boldsymbol{\Sigma}_r^{[\mathrm{s}]^{-1}} \cdot \boldsymbol{U}_r^{[\mathrm{s}]^{\mathrm{H}}} \cdot [\boldsymbol{\mathcal{X}}_0]_{(r)} \cdot [\boldsymbol{\mathcal{X}}_0]_{(r)}^{\mathrm{H}}\right] \\
&= \mathrm{tr}\left[\boldsymbol{U}_r^{[\mathrm{s}]} \cdot \boldsymbol{\Sigma}_r^{[\mathrm{s}]^{-1}} \cdot \widetilde{\boldsymbol{N}}_r^{\mathrm{H}} \cdot \widetilde{\boldsymbol{N}}_r \cdot \boldsymbol{\Sigma}_r^{[\mathrm{s}]^{-1}} \cdot \boldsymbol{U}_r^{[\mathrm{s}]^{\mathrm{H}}} \cdot \boldsymbol{U}_r^{[\mathrm{s}]} \cdot \boldsymbol{\Sigma}_r^{[\mathrm{s}]} \cdot \boldsymbol{V}_r^{[\mathrm{s}]^{\mathrm{H}}} \cdot \boldsymbol{V}_r^{[\mathrm{s}]} \cdot \boldsymbol{\Sigma}_r^{[\mathrm{s}]} \cdot \boldsymbol{U}_r^{[\mathrm{s}]^{\mathrm{H}}}\right] \\
&= \mathrm{tr}\left[\boldsymbol{U}_r^{[\mathrm{s}]} \cdot \boldsymbol{\Sigma}_r^{[\mathrm{s}]^{-1}} \cdot \widetilde{\boldsymbol{N}}_r^{\mathrm{H}} \cdot \widetilde{\boldsymbol{N}}_r \cdot \boldsymbol{\Sigma}_r^{[\mathrm{s}]^{-1}} \cdot \boldsymbol{\Sigma}_r^{[\mathrm{s}]} \cdot \boldsymbol{\Sigma}_r^{[\mathrm{s}]} \cdot \boldsymbol{U}_r^{[\mathrm{s}]^{\mathrm{H}}}\right] \\
&= \mathrm{tr}\left[\widetilde{\boldsymbol{N}}_r^{\mathrm{H}} \cdot \widetilde{\boldsymbol{N}}_r \cdot \boldsymbol{\Sigma}_r^{[\mathrm{s}]} \cdot \boldsymbol{U}_r^{[\mathrm{s}]^{\mathrm{H}}} \cdot \boldsymbol{U}_r^{[\mathrm{s}]} \cdot \boldsymbol{\Sigma}_r^{[\mathrm{s}]^{-1}}\right] \\
&= \mathrm{tr}\left[\widetilde{\boldsymbol{N}}_r^{\mathrm{H}} \cdot \widetilde{\boldsymbol{N}}_r\right] \\
&= \mathrm{tr}\left[\mathrm{vec}\{\widetilde{\boldsymbol{N}}_r\} \cdot \mathrm{vec}\{\widetilde{\boldsymbol{N}}_r\}^{\mathrm{H}}\right].
\end{aligned}$$

Therefore, $\mathbb{E}\{\|\boldsymbol{\mathcal{X}}_0 \times_r \Delta\boldsymbol{\Gamma}_r\|_{\mathrm{H}}^2\}$ is reduced to

$$\mathbb{E}\{\|\boldsymbol{\mathcal{X}}_0 \times_r \Delta\boldsymbol{\Gamma}_r\|_{\mathrm{F}}^2\} \approx \mathrm{tr}[\widetilde{\boldsymbol{R}}_r]. \tag{8.27}$$

Next, we need to obtain an expression for $\mathbb{E}\left\{\|\boldsymbol{\mathcal{N}}^{[\mathrm{s}]}\|_{\mathrm{H}}^2\right\}$. To that end, let us express $\boldsymbol{\mathcal{N}}^{[\mathrm{s}]}$ and $\boldsymbol{\mathcal{N}}$ as $(R+1)$-order tensors $\boldsymbol{\mathcal{N}}^{[\mathrm{s}]} = \boldsymbol{\mathcal{N}} \times_{r=1}^{R} \boldsymbol{\Gamma}_r \times_{R+1} 1$ and $\boldsymbol{\mathcal{N}} = \boldsymbol{\mathcal{N}} \times_{R+1} 1$. Using this formulation we can take the $(R+1)$-mode unfolding of $\boldsymbol{\mathcal{N}}^{[\mathrm{s}]}$ (i.e., $[\boldsymbol{\mathcal{N}}^{[\mathrm{s}]}]_{(R+1)} \in \mathbb{C}^{1 \times M}$) to obtain $[\boldsymbol{\mathcal{N}}^{[\mathrm{s}]}]_{(R+1)} = 1 \cdot [\boldsymbol{\mathcal{N}}]_{(R+1)} \cdot \left(\bigotimes_{r=1}^{R} \boldsymbol{\Gamma}_r\right)^{\mathrm{T}} =$ $\mathrm{vec}\left\{[\boldsymbol{\mathcal{N}}]_{(R)}\right\}^{\mathrm{T}} \cdot \left(\bigotimes_{r=1}^{R} \boldsymbol{\Gamma}_r\right)^{*}$. Using this expression we get

$$\begin{aligned}
\mathbb{E}\left\{\|\boldsymbol{\mathcal{N}}^{[\mathrm{s}]}\|_{\mathrm{H}}^2\right\} &= \mathbb{E}\left\{\|[\boldsymbol{\mathcal{N}}^{[\mathrm{s}]}]_{(R+1)}^{\mathrm{T}}\|_2^2\right\} \\
&= \mathbb{E}\left\{\mathrm{tr}\left[[\boldsymbol{\mathcal{N}}^{[\mathrm{s}]}]_{(R+1)}^{\mathrm{T}} \cdot [\boldsymbol{\mathcal{N}}^{[\mathrm{s}]}]_{(R+1)}^{*}\right]\right\} \\
&= \mathrm{tr}\left[\left(\bigotimes_{r=1}^{R} \boldsymbol{T}_r\right) \cdot \boldsymbol{R}_R\right].
\end{aligned} \tag{8.28}$$

Finally, using Eq. (8.27) and Eq. (8.28), $\mathbb{E}\left\{\|\Delta\boldsymbol{\mathcal{X}}\|_{\mathrm{F}}^2\right\}$ from Eq. (8.26) is approximated to

$$\begin{aligned}
\mathbb{E}\left\{\|\Delta\boldsymbol{\mathcal{X}}\|_{\mathrm{H}}^2\right\} &\approx \sum_{r=1}^{R} \mathrm{tr}[\widetilde{\boldsymbol{R}}_r] + \mathrm{tr}\left[\left(\bigotimes_{r=1}^{R} \boldsymbol{\Gamma}_r\right) \cdot \boldsymbol{R}_R\right] \\
&= \sum_{r=1}^{R} \mathrm{tr}\left[\left(\boldsymbol{V}_r^{[\mathrm{s}]\mathrm{T}} \otimes \boldsymbol{U}_r^{[\mathrm{n}]\mathrm{H}}\right) \cdot \boldsymbol{R}_r \cdot \left(\boldsymbol{V}_r^{[\mathrm{s}]*} \otimes \boldsymbol{U}_r^{[\mathrm{n}]}\right)\right] + \mathrm{tr}\left[\left(\bigotimes_{r=1}^{R} \boldsymbol{\Gamma}_r\right) \cdot \boldsymbol{R}_R\right].
\end{aligned} \tag{8.29}$$

8.3.2.2. Special Case of Uncorrelated Noise

As in Section 8.3.1, we simplify this expression for the special case of uncorrelated noise with variance σ_N^2. It can be easily shown that, in this case, $\mathbb{E}\left\{\|\boldsymbol{\mathcal{N}}^{[\mathrm{s}]}\|_{\mathrm{H}}^2\right\} = \sigma_N^2 \cdot \prod_{r=1}^{R} p_r$. Using this property and Eq. (8.24), we simplify Eq. (8.29) further to $\mathbb{E}\left\{\|\Delta\boldsymbol{\mathcal{X}}\|_{\mathrm{H}}^2\right\} \approx \sum_{r=1}^{R} \mathrm{tr}\left[\sigma_N^2 \cdot \boldsymbol{I}_{p_r(M_r - p_r)}\right] + \sigma_N^2 \cdot \prod_{r=1}^{R} p_r$. Finally, we reach the desired $\mathbb{E}\left\{\|\Delta\boldsymbol{\mathcal{X}}\|_{\mathrm{H}}^2\right\}$ in terms of the noise variance for the uncorrelated noise case, i.e.,

$$\mathbb{E}\left\{\|\Delta\boldsymbol{\mathcal{X}}\|_{\mathrm{H}}^2\right\} \approx \sigma_N^2 \cdot \left(\sum_{r=1}^{R} (M_r - p_r) \cdot p_r + \prod_{r=1}^{R} p_r\right). \tag{8.30}$$

8.4. Simulation Results

To validate the analytical results obtained in the previous sections, we perform empirical simulations not only on computer generated data but also on low-rank compressed images.

8.4.1. Simulation Results using Computer Generated Data

First we define the noiseless tensor(s) and the noise characteristics for the computer generated data. For all such simulations, the noiseless low-rank tensor $\boldsymbol{\mathcal{X}}_0$ is $\boldsymbol{\mathcal{X}}_0 \in \mathbb{R}^{20 \times 20 \times 20}$ and norm $\|\boldsymbol{\mathcal{X}}_0\|_{\mathrm{H}}^2 = 1$. Note
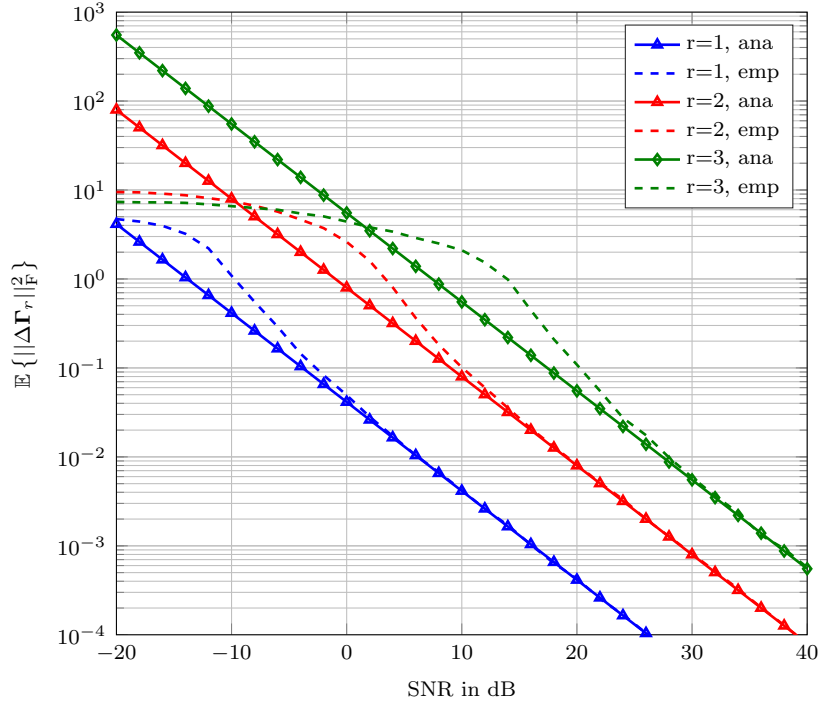
(a) Subspace estimation error $\mathbb{E}\left\{||\Delta\mathbf{\Gamma}_r||_{\mathrm{F}}^2\right\}$.
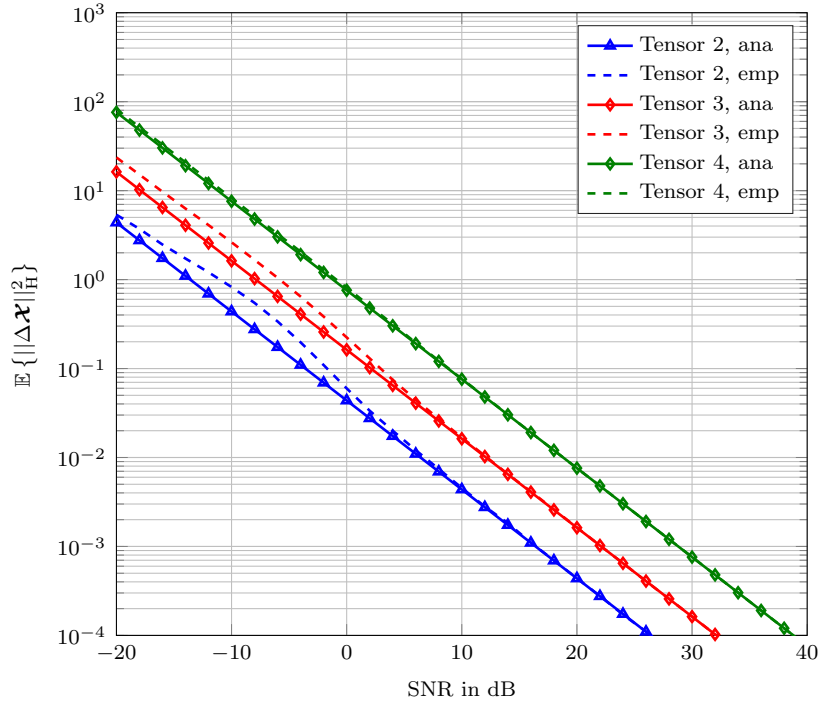
(b) Tensor estimation error $\mathbb{E}\left\{||\Delta\boldsymbol{\mathcal{X}}||_{\mathrm{H}}^2\right\}$.

Figure 8.2.: (a): Subspace estimation errors corresponding to each of the subspaces of tensor 1, described in Table 8.2. (b): Tensor estimation error for tensors 2, 3 and 4, described in Table 8.3.

	p_r	Tr $\left[\mathbf{\Sigma}_r^{[s]^{-2}}\right]$
$r = 1$	3	9.7420
$r = 2$	9	290.0909
$r = 3$	15	4418.2000

Table 8.2.: Parameters of tensor 1, used in Figure 8.2(a)

$\mathcal{X}_0$	p_1	p_2	p_3
Tensor 2	5	5	5
Tensor 3	10	10	10
Tensor 4	15	20	20

Table 8.3.: r-ranks of tensors 2, 3, and 4, used in Figure 8.2(b)

that, a tensor $\mathcal{B} \in \mathbb{R}^{20 \times 20 \times 20}$ with r-ranks (p_1, p_2, p_3) can be generated as $\mathcal{B} = \mathcal{A} \times_1 \mathbf{W} \times_2 \mathbf{Y} \times_3 \mathbf{Z}$, where $\mathcal{A} \in \mathbb{R}^{p_1 \times p_2 \times p_3}$, $\mathbf{W} \in \mathbb{R}^{20 \times p_1}$, $\mathbf{Y} \in \mathbb{R}^{20 \times p_2}$ and $\mathbf{Z} \in \mathbb{R}^{20 \times p_3}$ are randomly generated using independent zero-mean Gaussian distributions with equal variance. Furthermore, we use uncorrelated zero-mean Gaussian distributed noise with variance σ_N^2 for the realizations of the noise tensor $\mathcal{N} \in \mathbb{R}^{20 \times 20 \times 20}$, where σ_N^2 is calculated as

$$\sigma_N^2 = \frac{\|\mathcal{X}_0\|_{\mathrm{H}}^2}{\mathrm{SNR} \cdot M}$$

for the different signal-to-noise ratio (SNR) values [2].

In Figure 8.2(a), we validate the results obtained in Section 8.3.1. Here, the noiseless tensor $\mathcal{X}_0$ (referred to as tensor 1 in Figure 8.2(a)), has the characteristics shown in Table 8.2. Then, after 1000 trials of uncorrelated noise realizations for each SNR point, the empirical error curve for $\mathbb{E}\left\{\|\Delta\mathbf{\Gamma}_r\|_{\mathrm{F}}^2\right\}$ is computed for $r = 1, 2, 3$. Furthermore, we can observe how the analytical expressions obtained using equation (8.25) asymptotically match the empirical error curve for each of the subspace estimates of the noiseless tensor.

Likewise, in Figure 8.2(b) we validate the results obtained in Section 8.3.2. Here, the simulations are conducted for 3 different noiseless tensors (i.e., tensors 2, 3 and 4) of the same sizes, but with different r-ranks. Furthermore, the r-ranks (p_1, p_2, p_3) of this tensors are shown in Table 8.3. As before, 1000 trials of uncorrelated noise realizations for each SNR point are simulated to obtain the empirical error curve for $\mathbb{E}\left\{\|\Delta\mathcal{X}\|_{\mathrm{H}}^2\right\}$. Furthermore, we can see how the analytical expressions obtained using equation (8.30) match the empirical curves as expected.

8.4.2. Simulation Results using Images

The truncated HOSVD is a widely recommended technique for image compression and image denoising. Especially when the compression ratio is high or image is very noisy, reconstructed images based on the truncated HOSVD show a better performance. We take examples of color images that can be interpreted as third-order tensors. The first and second dimension correspond to the image pixels while third dimension corresponds to RGB channels. We have taken two images as an example, i.e., Lenna image of size $512 \times 512 \times 3$ with truncated $1-\mathrm{rank} = 70$, truncated $2-\mathrm{rank} = 70$, and $3-\mathrm{rank} = 3$ and a fruit image of size $400 \times 800 \times 3$ with truncated $1-\mathrm{rank} = 70$, truncated $2-\mathrm{rank} = 100$, and $3-\mathrm{rank} = 3$, as shown in Fig. 8.3a and Fig. 8.3b, respectively. We first evaluate the performance of the truncated HOSVD for these images at two SNR values of 4 dB and 12 dB. The results suggest that the truncated HOSVD shows a good denoising performance as suggested in various publications [RRB13, LZH09a, DLS$^+$15, AG13]. We

---

[2]The SNR here is defined on a linear scale (not in dB).

(a) Low-rank Lenna image of size $512 \times 512 \times 3$ with $1-\mathrm{rank} = 70$,
$2-\mathrm{rank} = 70$, and $3-\mathrm{rank} = 3$
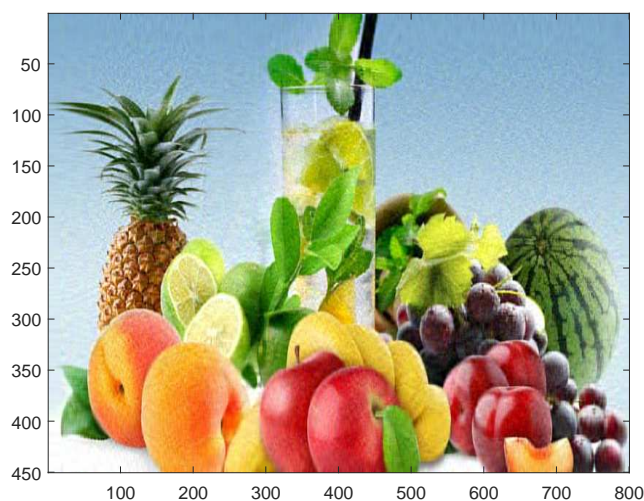
(b) Low-rank fruit image of size $400 \times 800 \times 3$ with $1-\mathrm{rank} = 70$,
$2-\mathrm{rank} = 100$, and $3-\mathrm{rank} = 3$

Figure 8.3.: Two low-rank images.

evaluate the performance of the derived analytical expressions against the Monte-carlo simulations for the reconstruction error of these images for different SNRs, as shown in Fig. 8.6. The performance analysis achieves a very good match to the empirical results for both images.

8.5. Conclusion

In this chapter, a first-order perturbation analysis of the truncated HOSVD is presented, where we provide closed-form expressions for the tensor reconstruction error. The derived expressions are formulated in terms of the second-order moments of the noise, such that apart from a zero-mean, no assumptions

(a) The images corrupted by Gaussian noise for
SNR =4 dB
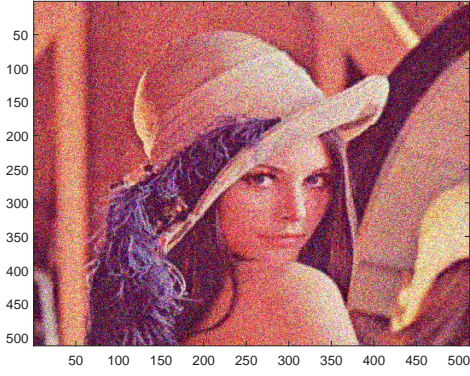
(b) Recovered image

(c) The images corrupted by Gaussian noise for
SNR =12 dB

(d) Recovered image

Figure 8.4.: Noisy and recovered Lenna images of size $512 \times 512 \times 3$ and $1-\mathrm{rank} = 70$, $2-\mathrm{rank} = 70$, and $3-\mathrm{rank} = 3$ for different SNRs.

on the noise statistics are required. In addition, the obtained general expressions have been simplified for the special case of uncorrelated noise with equal variance. This simplification provides better insights into the truncated HOSVD performance. The simulation results show that the proposed solution achieves an excellent match to the empirical results.

(a) The images corrupted by Gaussian noise for SNR =4 dB
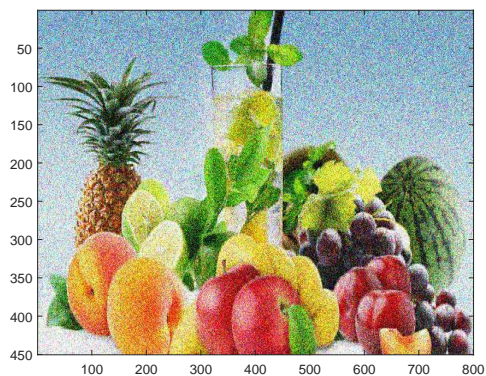
(b) Recovered image

(c) The images corrupted by Gaussian noise for SNR =12 dB
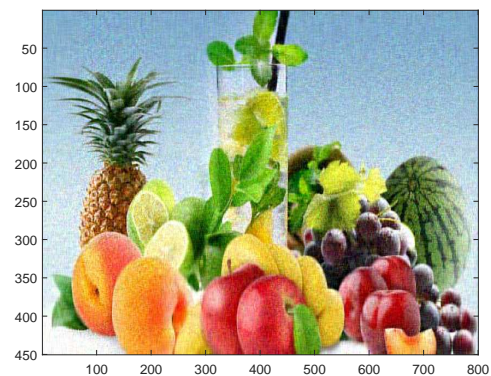
(d) Recovered image

Figure 8.5.: Noisy and recovered fruit images of size $400 \times 800 \times 3$ with $1-\text{rank} = 70$, $2-\text{rank} = 100$, and $3-\text{rank} = 3$ for different SNRs.
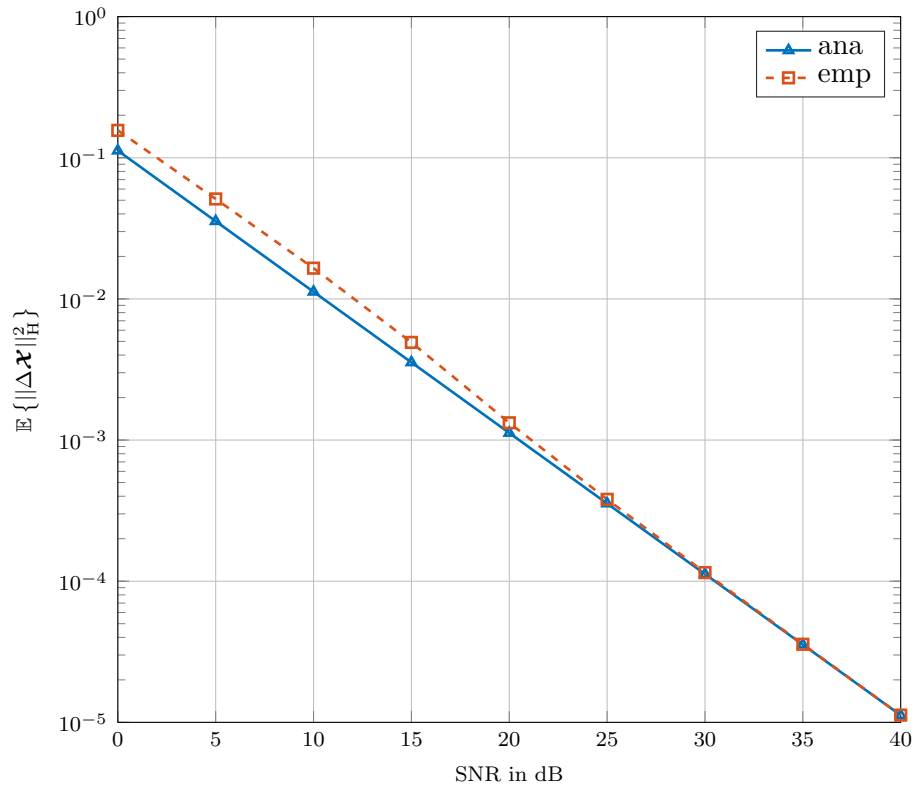
(a) Reconstruction error for Lenna image
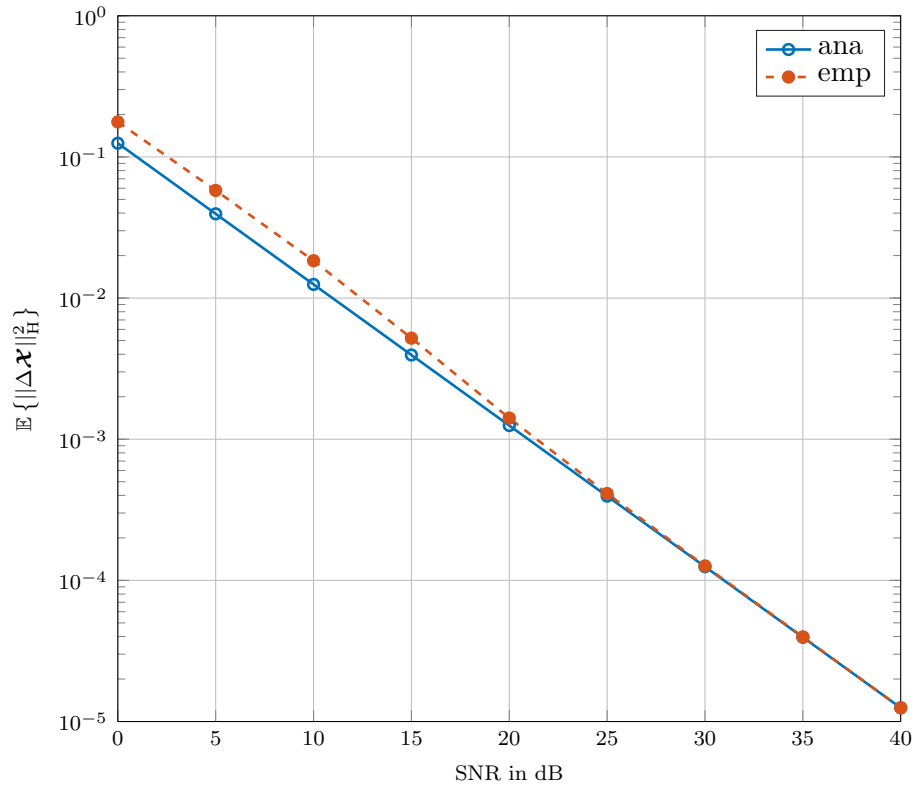
(b) Reconstruction error for fruit image

Figure 8.6.: Reconstruction error for both images for different SNRs.

9. First-Order Perturbation Analysis of the SECSI Framework for the Approximate CPD

The Semi-Algebraic framework for the approximate canonical polyadic decomposition (CPD) via simultaneaous matrix diagonalization (SECSI) is an efficient tool for the computation of the CPD. The SECSI framework reformulates the CPD into a set of joint eigenvalue decomposition (JEVD) problems. Solving all JEVDs, we obtain multiple estimates of the factor matrices and the best estimate is chosen in a subsequent step by using an exhaustive search or some heuristic strategy that reduces the computational complexity. Moreover, the SECSI framework retains the option of choosing the number of JEVDs to be solved, thus providing an adjustable complexity-accuracy trade-off. In this chapter, we provide an analytical performance analysis of the SECSI framework for the computation of the approximate CPD of a noise corrupted low-rank tensor, where we derive closed-form expressions of the relative mean square error for each of the estimated factor matrices. These expressions are obtained using a first-order perturbation analysis and are formulated in terms of the second-order moments of the noise, such that apart from a zero-mean, no assumptions on the noise statistics are required. We also propose a new performance analysis based selection (PAS) scheme to choose the final factor matrix estimate. The results show that the proposed PAS scheme outperforms the existing heuristics, especially in the high SNR regime. After the introduction, we start by performing the first-order perturbation analysis of the SECSI framework in terms of a known noisy tensor in Section 9.3. The closed-form relative Mean Square Factor Error (rMSFE) expressions for each of the factor matrices for the first JEVD are presented in Section 9.4. The results are extended for each of the factor matrices resulting from the second JEVD in Section 9.5.1. The results of the remaining JEVDs are obtained via a permutation of the previous results that are discussed in Section 9.4. In Section 9.6, we propose a new estimate selection scheme that is based on the performance analysis results. The simulation results are discussed in Section 9.7 and the conclusions are provided in Section 9.8.

9.1. Introduction

The canonical polyadic decomposition (CPD) of R-way arrays is a powerful tool in multi-linear algebra. It allows to decompose a tensor into a sum of rank-one components. There exist many applications where the underlying signal of interest can be represented by a trilinear or multilinear canonical polyadic model. These range from psychometrics and chemometrics over array signal processing and communications to biomedical signal processing, image compression or numerical mathematics [KB09, dL05, SGB00]. In practice, the signal of interest in these applications is contaminated by the noise. Therefore, we only compute an approximate CPD of the noisy signal.

Algorithms for the computation of an approximate CPD from noisy observations are often based on Alternating Least Squares (ALS). These algorithms compute the CPD in an iterative manner procedure [CC70, Har70]. The main drawbacks of ALS-based algorithms is that the number of required iter-

ations may be very large, and convergence is not guaranteed. Moreover, ALS based algorithms are less accurate in ill-conditioned scenarios, especially if the columns of the factor matrices are highly correlated. Alternatively, semi-algebraic solutions, where the CPD is rephrased into a generic problem such as the Joint Eigenvalue Decomposition (JEVD) (also called Simultaneous Matrix Diagonalization (SMD)), have been proposed in the literature [dL05]. The link between the CPD and the JEVD is discussed in [dL06] where it has been shown that the canonical components can be obtained from a simultaneous matrix diagonalization by congruence. A SEmi-algebraic framework for CPD via SImultaneous matrix diagonalization (SECSI) was presented in [RH08a,RH08b,RH13] for $R = 3$ dimensional tensors and was extended for tensors with $R > 3$ dimensions using the concept of generalized unfoldings (SECSI-GU) in [RSH12]. The SECSI concept facilitates a distributed implementation on a parallel JEVDs to be solved depending upon the accuracy and the computational complexity requirements of the system. By solving all JEVDs, multiple estimates of the factor matrices are obtained. The selection of the best factor matrices from the resulting estimates can be obtained either by using an exhaustive search based best matching scheme or by using heuristic selection schemes with a reduced computational complexity. Several schemes with different accuracy-complexity trade-off points are presented in [RH13]. Thus, the SECSI framework results in more reliable estimates and also offers a flexible accuracy-complexity trade-off.

An analytical performance assessment of the semi-algebraic algorithms to compute an approximate CPD is of considerable research interest. In the literature, the performance of the CPD is often evaluated using Monte-Carlo simulations. To the best of our knowledge, there exists no analytical performance analysis of an approximate CPD of noise-corrupted low-rank tensors in the literature. In this chapter, a first-order perturbation analysis of the SECSI framework is carried out, where apart from zero-mean and finite second order moments, no assumptions about the noise are required. The SECSI framework performs three distinct steps to compute the approximate CPD of a noisy tensor, as summarized in Fig. 9.1. First, the truncated higher order singular value decomposition (HOSVD) is used to suppress the noise. In the second step, several JEVDs are constructed from the core tensor. This results in several estimates of the factor matrices. Lastly, the best factor matrices are selected from these estimates by applying the best matching scheme or an appropriate heuristic scheme that has a lower computational complexity [RH13]. Hence, a perturbation analysis for each of the steps is required for the overall performance analysis of the SECSI framework. In the previous chapter, we have already presented a first-order perturbation analysis of low-rank tensor approximations based on the truncated HOSVD. We have also performed the perturbation analysis of JEVD algorithms which are based on the indirect least squares (LS) cost function in [BCW+17]. In this chapter, we extend our work to the overall performance analysis of the SECSI framework for 3-D tensors. Finally, we present closed-form expressions for the rMSFE for each of the estimates of the three factor matrices. These expressions are asymptotic in the SNR and are expressed in terms of the covariance matrix of the noise. Furthermore, we devise a new heuristic approach based on the performance analysis results to select the best estimates that we call Performance Analysis based Selection (PAS) scheme.

Compute HOSVD

$$\hat{\mathcal{X}} = \hat{\mathcal{S}}^{[s]} \times_1 \hat{U}_1^{[s]} \times_2 \hat{U}_2^{[s]} \times_3 \hat{U}_3^{[s]}$$

Compute

$$\hat{S}_1^{[s]} = \hat{\mathcal{S}}^{[s]} \times_1 \hat{U}_1^{[s]}$$
$$\hat{S}_2^{[s]} = \hat{\mathcal{S}}^{[s]} \times_2 \hat{U}_2^{[s]}$$
$$\hat{S}_3^{[s]} = \hat{\mathcal{S}}^{[s]} \times_3 \hat{U}_3^{[s]}$$

Eliminate one of the transform matrices, $\hat{p} = \arg\min_{k=1,2,\ldots,M_3} \mathrm{cond}\left(\hat{S}_{i,k}\right),\, i = 1,2,3$

$$\hat{S}_{3,k}^{\mathrm{rhs}} = \hat{S}_{3,k} \cdot \hat{S}_{3,p}^{-1} \approx \hat{T}_1 \cdot \hat{D}_{3,k} \cdot \hat{T}_1^{-1} \quad k = 1,2,\cdots,M_3$$

$$\hat{S}_{3,k}^{\mathrm{lhs}} = \left(\hat{S}_{3,p}^{-1} \cdot \hat{S}_{3,k}\right)^{\mathrm{T}} \approx \hat{T}_2 \cdot \hat{D}_{3,k} \cdot \hat{T}_2^{-1} \quad k = 1,2,\cdots,M_3$$

$$\hat{S}_{2,k}^{\mathrm{rhs}} = \hat{S}_{2,k} \cdot \hat{S}_{2,p}^{-1} \approx \hat{T}_1 \cdot \hat{D}_{2,k} \cdot \hat{T}_1^{-1} \quad k = 1,2,\cdots,M_2$$

$$\hat{S}_{2,k}^{\mathrm{lhs}} = \left(\hat{S}_{2,p}^{-1} \cdot \hat{S}_{2,k}\right)^{\mathrm{T}} \approx \hat{T}_3 \cdot \hat{D}_{2,k} \cdot \hat{T}_3^{-1} \quad k = 1,2,\cdots,M_2$$

$$\hat{S}_{1,k}^{\mathrm{rhs}} = \hat{S}_{1,k} \cdot \hat{S}_{1,p}^{-1} \approx \hat{T}_2 \cdot \hat{D}_{1,k} \cdot \hat{T}_2^{-1} \quad k = 1,2,\cdots,M_1$$

$$\hat{S}_{1,k}^{\mathrm{lhs}} = \left(\hat{S}_{1,p}^{-1} \cdot \hat{S}_{1,k}\right)^{\mathrm{T}} \approx \hat{T}_3 \cdot \hat{D}_{1,k} \cdot \hat{T}_3^{-1} \quad k = 1,2,\cdots,M_1$$

Estimate the transform matrices via JEVD

$\hat{T}_1$ $\hat{T}_2$ $\hat{T}_1$ $\hat{T}_3$ $\hat{T}_2$ $\hat{T}_3$

Estimate the factor matrices

$$\hat{F}_{\mathrm{IV}}^{(1)} = \hat{U}_1^{[s]} \cdot \hat{T}_1$$
$$\hat{F}_{\mathrm{I}}^{(3)} \text{ (from diagonal)}$$
$$\hat{F}_{\mathrm{V}}^{(2)} \text{ (LS)}$$

$$\hat{F}_{\mathrm{IV}}^{(2)} = \hat{U}_2^{[s]} \cdot \hat{T}_2$$
$$\hat{F}_{\mathrm{II}}^{(3)} \text{ (from diagonal)}$$
$$\hat{F}_{\mathrm{V}}^{(1)} \text{ (LS)}$$

$$\hat{F}_{\mathrm{III}}^{(1)} = \hat{U}_1^{[s]} \cdot \hat{T}_1$$
$$\hat{F}_{\mathrm{I}}^{(2)} \text{ (from diagonal)}$$
$$\hat{F}_{\mathrm{V}}^{(3)} \text{ (LS)}$$

$$\hat{F}_{\mathrm{IV}}^{(3)} = \hat{U}_3^{[s]} \cdot \hat{T}_3$$
$$\hat{F}_{\mathrm{II}}^{(2)} \text{ (from diagonal)}$$
$$\hat{F}_{\mathrm{VI}}^{(1)} \text{ (LS)}$$

$$\hat{F}_{\mathrm{III}}^{(2)} = \hat{U}_2^{[s]} \cdot \hat{T}_2$$
$$\hat{F}_{\mathrm{I}}^{(1)} \text{ (from diagonal)}$$
$$\hat{F}_{\mathrm{VI}}^{(3)} \text{ (LS)}$$

$$\hat{F}_{\mathrm{III}}^{(3)} = \hat{U}_3^{[s]} \cdot \hat{T}_3$$
$$\hat{F}_{\mathrm{II}}^{(1)} \text{ (from diagonal)}$$
$$\hat{F}_{\mathrm{VI}}^{(2)} \text{ (LS)}$$

Selection of the final factor matrix estimate

Figure 9.1.: Overview of the SECSI framework to compute an approximate CPD of a noise-corrupted low-rank tensor.

9.2. Data Model

One of the major challenges in data-driven applications is that only a noise-corrupted version of the noiseless tensor $\boldsymbol{\mathcal{X}}_0 \in \mathbb{C}^{M_1 \times M_2 \times M_3}$ of tensor rank d is observed. Let us consider the non-degenerate case first where $d \leq \min\{M_1, M_2, M_3\}$. However, as discussed in Section 9.5.2, the SECSI framework can also be applied in the degenerate case where the tensor rank of the noiseless tensor may be greater than any one of the dimensions (i.e., $M_1 < d \leq \min\{M_2, M_3\}$). The CPD of such a low-rank noiseless tensor is given by

$$\boldsymbol{\mathcal{X}}_0 = \boldsymbol{\mathcal{I}}_{3,d} \times_1 \boldsymbol{F}^{(1)} \times_2 \boldsymbol{F}^{(2)} \times_3 \boldsymbol{F}^{(3)}, \tag{9.1}$$

where $\boldsymbol{F}^{(r)} \in \mathbb{C}^{M_r \times d}, \forall r = 1, 2, 3$ is the factor matrix in the r-th mode and $\boldsymbol{\mathcal{I}}_{3,d}$ is the 3-way identity tensor of size $d \times d \times d$. In this work, we assume that the factor matrices are known, and the goal of the SECSI framework is to estimate them. For future reference, the SVD of the r-mode unfolding of the noiseless low-rank tensor $\boldsymbol{\mathcal{X}}_0 \in \mathbb{C}^{M_1 \times M_2 \times M_3}$ is given as

$$\begin{aligned}
[\boldsymbol{\mathcal{X}}_0]_{(r)} &= \boldsymbol{U}_r \cdot \boldsymbol{\Sigma}_r \cdot \boldsymbol{V}_r^{\mathrm{H}} \\
&= \begin{bmatrix} \boldsymbol{U}_r^{[\mathrm{s}]} & \boldsymbol{U}_r^{[\mathrm{n}]} \end{bmatrix} \begin{bmatrix} \boldsymbol{\Sigma}_r^{[\mathrm{s}]} & \boldsymbol{0}_{d \times M_r} \\ \boldsymbol{0}_{(M_r - d) \times d} & \boldsymbol{0}_{(M_r - d) \times M_r} \end{bmatrix} \begin{bmatrix} \boldsymbol{V}_r^{[\mathrm{s}]} & \boldsymbol{V}_r^{[\mathrm{n}]} \end{bmatrix}^{\mathrm{H}} \\
&= \boldsymbol{U}_r^{[\mathrm{s}]} \cdot \boldsymbol{\Sigma}_r^{[\mathrm{s}]} \cdot \boldsymbol{V}_r^{[\mathrm{s}]^{\mathrm{H}}}, \forall r = 1, 2, 3
\end{aligned} \tag{9.2}$$

where the superscripts [s] and [n] represent the signal and the noise subspaces, respectively. Let

$$\boldsymbol{\mathcal{X}} = \boldsymbol{\mathcal{X}}_0 + \boldsymbol{\mathcal{N}} \in \mathbb{C}^{M_1 \times M_2 \times M_3} \tag{9.3}$$

be the observed noisy tensor where the desired signal component $\boldsymbol{\mathcal{X}}_0$ is superimposed by a zero-mean additive noise tensor $\boldsymbol{\mathcal{N}} \in \mathbb{C}^{M_1 \times M_2 \times M_3}$. The SVD of the r-mode unfolding of the observed noisy tensor $\boldsymbol{\mathcal{X}}$ is given as

$$\begin{aligned}
[\boldsymbol{\mathcal{X}}]_{(r)} &= \hat{\boldsymbol{U}}_r \cdot \hat{\boldsymbol{\Sigma}}_r \cdot \hat{\boldsymbol{V}}_r^{\mathrm{H}} \\
&= \begin{bmatrix} \hat{\boldsymbol{U}}_r^{[\mathrm{s}]} & \hat{\boldsymbol{U}}_r^{[\mathrm{n}]} \end{bmatrix} \begin{bmatrix} \hat{\boldsymbol{\Sigma}}_r^{[\mathrm{s}]} & \boldsymbol{0}_{d \times M_r} \\ \boldsymbol{0}_{(M_r - d) \times d} & \hat{\boldsymbol{\Sigma}}_r^{[\mathrm{n}]} \end{bmatrix} \begin{bmatrix} \hat{\boldsymbol{V}}_r^{[\mathrm{s}]} & \hat{\boldsymbol{V}}_r^{[\mathrm{n}]} \end{bmatrix}^{\mathrm{H}}.
\end{aligned} \tag{9.4}$$

9.3. First-Order Perturbation Analysis

The SECSI framework performs three distinct steps to compute the approximate CPD of noise corrupted low-rank tensor, as shown in Fig. 9.1. In the first step, the truncated HOSVD is used to suppress the noise. Then using the truncated core tensor, the whole set of JEVDs is constructed, Finally, the factor matrices are estimated by solving these JEVDs. In the following, we calculate the perturbation in each of the involved step.

9.3.1. Perturbation of the Truncated HOSVD

As discussed in Chapter 8, a low-rank approximation of $\boldsymbol{\mathcal{X}}$ can be computed by truncating the HOSVD of the noisy tensor

$$\boldsymbol{\mathcal{X}} = \hat{\boldsymbol{\mathcal{S}}} \times_1 \hat{\boldsymbol{U}}_1 \times_2 \hat{\boldsymbol{U}}_2 \times_3 \hat{\boldsymbol{U}}_3$$

as [dLdMV00b]

$$\hat{\boldsymbol{\mathcal{X}}} = \hat{\boldsymbol{\mathcal{S}}}^{[\mathrm{s}]} \times_1 \hat{\boldsymbol{U}}_1^{[\mathrm{s}]} \times_2 \hat{\boldsymbol{U}}_2^{[\mathrm{s}]} \times_3 \hat{\boldsymbol{U}}_3^{[\mathrm{s}]}, \tag{9.5}$$

where $\hat{\boldsymbol{\mathcal{S}}}^{[\mathrm{s}]} \in \mathbb{C}^{d \times d \times d}$ is the truncated core tensor and $\hat{\boldsymbol{U}}_r^{[\mathrm{s}]} \in \mathbb{C}^{M_r \times d}, \forall r = 1, 2, 3$ is obtained from Eq. (9.4). In Chapter 8, we have presented a first order perturbation analysis of the truncated HOSVD where we have obtained analytical expressions for the signal subspace error in each dimension of the tensor. Additionally, we have also obtained the analytical expressions for the tensor reconstruction error induced by the low-rank approximation of the noise corrupted tensor. Let us express the noisy estimates in Eq. (9.5) as

$$\hat{\boldsymbol{U}}_r^{[\mathrm{s}]} \triangleq \boldsymbol{U}_r^{[\mathrm{s}]} + \Delta \boldsymbol{U}_r^{[\mathrm{s}]}, \quad \forall r = 1, 2, 3 \tag{9.6}$$

$$\hat{\boldsymbol{\mathcal{S}}}^{[\mathrm{s}]} \triangleq \boldsymbol{\mathcal{S}}^{[\mathrm{s}]} + \Delta \boldsymbol{\mathcal{S}}^{[\mathrm{s}]}. \tag{9.7}$$

The perturbation present in the r-mode signal subspace estimate $\hat{\boldsymbol{U}}_r^{[\mathrm{s}]}$ is given by [LLV93]

$$\begin{aligned} \Delta \boldsymbol{U}_r^{[\mathrm{s}]} &= \boldsymbol{U}_r^{[\mathrm{n}]} \cdot \boldsymbol{U}_r^{[\mathrm{n}]\mathrm{H}} \cdot [\boldsymbol{\mathcal{N}}]_{(r)} \cdot \boldsymbol{V}_r^{[\mathrm{s}]} \cdot \boldsymbol{\Sigma}_r^{[\mathrm{s}]-1} + \mathcal{O}(\Delta^2) \\ &= \boldsymbol{\Gamma}_r^{[\mathrm{n}]} \cdot [\boldsymbol{\mathcal{N}}]_{(r)} \cdot \boldsymbol{V}_r^{[\mathrm{s}]} \cdot \boldsymbol{\Sigma}_r^{[\mathrm{s}]-1} + \mathcal{O}(\Delta^2), \end{aligned} \tag{9.8}$$

where $\boldsymbol{\Gamma}_r^{[\mathrm{n}]} \triangleq \boldsymbol{U}_r^{[\mathrm{n}]} \cdot \boldsymbol{U}_r^{[\mathrm{n}]\mathrm{H}}$ and all higher order terms are contained in $\mathcal{O}(\Delta^2)$. Furthermore, we use this result to expand the expression for the truncated core tensor $\hat{\boldsymbol{\mathcal{S}}}^{[\mathrm{s}]} = \boldsymbol{\mathcal{X}} \overset{3}{\underset{r=1}{\times_r}} \hat{\boldsymbol{U}}_r^{[\mathrm{s}]\mathrm{H}}$ as

$$\begin{aligned} \boldsymbol{\mathcal{S}}^{[\mathrm{s}]} + \Delta \boldsymbol{\mathcal{S}}^{[\mathrm{s}]} &= (\boldsymbol{\mathcal{X}}_0 + \boldsymbol{\mathcal{N}}) \overset{3}{\underset{r=1}{\times_r}} \left(\boldsymbol{U}_r^{[\mathrm{s}]\mathrm{H}} + \Delta \boldsymbol{U}_r^{[\mathrm{s}]\mathrm{H}} \right) + \mathcal{O}(\Delta^2) \\ &= \boldsymbol{\mathcal{X}}_0 \overset{3}{\underset{r=1}{\times_r}} \boldsymbol{U}_r^{[\mathrm{s}]\mathrm{H}} + \boldsymbol{\mathcal{N}} \overset{3}{\underset{r=1}{\times_r}} \boldsymbol{U}_r^{[\mathrm{s}]\mathrm{H}} + \boldsymbol{\mathcal{X}}_0 \times_1 \Delta \boldsymbol{U}_1^{[\mathrm{s}]\mathrm{H}} \times_2 \boldsymbol{U}_2^{[\mathrm{s}]\mathrm{H}} \times_3 \boldsymbol{U}_3^{[\mathrm{s}]\mathrm{H}} \\ &\quad + \boldsymbol{\mathcal{X}}_0 \times_1 \boldsymbol{U}_1^{[\mathrm{s}]\mathrm{H}} \times_2 \Delta \boldsymbol{U}_2^{[\mathrm{s}]\mathrm{H}} \times_3 \boldsymbol{U}_3^{[\mathrm{s}]\mathrm{H}} + \boldsymbol{\mathcal{X}}_0 \times_1 \boldsymbol{U}_1^{[\mathrm{s}]\mathrm{H}} \times_2 \boldsymbol{U}_2^{[\mathrm{s}]\mathrm{H}} \times_3 \Delta \boldsymbol{U}_3^{[\mathrm{s}]\mathrm{H}} + \mathcal{O}(\Delta^2). \end{aligned}$$

Note that all terms that include products of more than one "Δ term" are included in $\mathcal{O}(\Delta^2)$. Moreover, $\boldsymbol{\mathcal{N}}$ is also considered as a Δ term. In the noiseless case, the truncated core tensor $\boldsymbol{\mathcal{S}}^{[\mathrm{s}]}$ is equal to $\boldsymbol{\mathcal{S}}^{[\mathrm{s}]} \triangleq \boldsymbol{\mathcal{X}}_0 \overset{3}{\underset{r=1}{\times_r}} \boldsymbol{U}_r^{[\mathrm{s}]\mathrm{H}}$. Using the definitions in Eq. (9.2) and Eq. (9.8), the above expression simplifies to

$$\Delta \boldsymbol{\mathcal{S}}^{[\mathrm{s}]} = \boldsymbol{\mathcal{N}} \overset{3}{\underset{r=1}{\times_r}} \boldsymbol{U}_r^{[\mathrm{s}]\mathrm{H}} + \mathcal{O}(\Delta^2). \tag{9.9}$$

1: Compute $\hat{\boldsymbol{U}}_r^{[\mathrm{s}]}$ for $r = 1, 2, 3$ via the HOSVD of $\boldsymbol{\mathcal{X}}$
2: $\hat{\boldsymbol{\mathcal{S}}}^{[\mathrm{s}]} = \boldsymbol{\mathcal{X}} \overset{R}{\underset{r=1}{\times_r}} \hat{\boldsymbol{U}}_r^{[\mathrm{s}]\mathrm{H}}$
3: $\hat{\boldsymbol{\mathcal{S}}}_3^{[\mathrm{s}]} = \hat{\boldsymbol{\mathcal{S}}}^{[\mathrm{s}]} \times_3 \hat{\boldsymbol{U}}_3^{[\mathrm{s}]}$
4: $\hat{\boldsymbol{S}}_{3,k} = \hat{\boldsymbol{\mathcal{S}}}_3^{[\mathrm{s}]} \times_3 \boldsymbol{e}_{M_3,k}^{\mathrm{T}}$ for $k = 1, 2, \ldots, M_3$
5: $\hat{p} = \mathrm{argmin}_{k=1,2,\ldots,M_3} \mathrm{cond}\left(\hat{\boldsymbol{S}}_{3,k}\right)$

6: $\hat{\boldsymbol{S}}_{3,k}^{\mathrm{rhs}} = \hat{\boldsymbol{S}}_{3,k} \cdot \hat{\boldsymbol{S}}_{3,p}^{-1}$ for $k = 1, 2, \ldots, M_3$	6: $\hat{\boldsymbol{S}}_{3,k}^{\mathrm{lhs}} \triangleq \left(\hat{\boldsymbol{S}}_{3,p}^{-1} \cdot \hat{\boldsymbol{S}}_{3,k}\right)^{\mathrm{T}}$ for $k = 1, 2, \ldots, M_3$
7: Compute $\hat{\boldsymbol{T}}_1$ and $\hat{\boldsymbol{D}}_{3,k}$ via JEVD of $\left\{\hat{\boldsymbol{S}}_{3,k}^{\mathrm{rhs}}\right\}_{k=1}^{M_3}$	7: Compute $\hat{\boldsymbol{T}}_2$ and $\hat{\boldsymbol{D}}_{3,k}$ via JEVD of $\left\{\hat{\boldsymbol{S}}_{3,k}^{\mathrm{lhs}}\right\}_{k=1}^{M_3}$
8: $\hat{\boldsymbol{F}}^{(1)} = \hat{\boldsymbol{U}}_1^{[\mathrm{s}]} \cdot \hat{\boldsymbol{T}}_1$	8: $\hat{\boldsymbol{F}}^{(1)} = [\boldsymbol{\mathcal{X}}]_{(1)} \cdot \left[\hat{\boldsymbol{F}}^{(2)} \diamond \hat{\boldsymbol{F}}^{(3)}\right]^{+\mathrm{T}}$
9: $\hat{\bar{\boldsymbol{F}}}^{(3)}(k,:) = \mathrm{diag}\left(\hat{\boldsymbol{D}}_{3,k}\right)^{\mathrm{T}}$	9: $\hat{\boldsymbol{F}}^{(2)} = \hat{\boldsymbol{U}}_2^{[\mathrm{s}]} \cdot \hat{\boldsymbol{T}}_2$
10: $\hat{\boldsymbol{F}}^{(2)} = [\boldsymbol{\mathcal{X}}]_{(2)} \cdot \left(\hat{\boldsymbol{F}}^{(3)} \diamond \hat{\boldsymbol{F}}^{(1)}\right)^{+\mathrm{T}}$	10: $\hat{\bar{\boldsymbol{F}}}^{(3)}(k,:) = \mathrm{diag}\left(\hat{\boldsymbol{D}}_{3,k}\right)^{\mathrm{T}}$

Table 9.1.: SECSI Algorithm: Factor matrix estimates resulting from the 2 JEVD construction from Eq. (13). The whole SECSI framework is shown in Fig. 9.1
.

9.3.2. Perturbation of the JEVD Estimates

For a 3-way array, we can construct up to 6 JEVD problems in the SECSI framework [RH13] that are obtained from

$$\hat{\boldsymbol{\mathcal{S}}}_1^{[\mathrm{s}]} = \hat{\boldsymbol{\mathcal{S}}}^{[\mathrm{s}]} \times_1 \hat{\boldsymbol{U}}_1^{[\mathrm{s}]} \in \mathbb{C}^{M_1 \times d \times d} \tag{9.10}$$

$$\hat{\boldsymbol{\mathcal{S}}}_2^{[\mathrm{s}]} = \hat{\boldsymbol{\mathcal{S}}}^{[\mathrm{s}]} \times_2 \hat{\boldsymbol{U}}_2^{[\mathrm{s}]} \in \mathbb{C}^{d \times M_2 \times d} \tag{9.11}$$

$$\hat{\boldsymbol{\mathcal{S}}}_3^{[\mathrm{s}]} = \hat{\boldsymbol{\mathcal{S}}}^{[\mathrm{s}]} \times_3 \hat{\boldsymbol{U}}_3^{[\mathrm{s}]} \in \mathbb{C}^{d \times d \times M_3}, \tag{9.12}$$

respectively. As an example, let us consider the two JEVD problems constructed from Eq. (9.12). Here the noisy estimate $\hat{\boldsymbol{\mathcal{S}}}_3^{[\mathrm{s}]}$ can be expressed as

$$\hat{\boldsymbol{\mathcal{S}}}_3^{[\mathrm{s}]} \triangleq \boldsymbol{\mathcal{S}}_3^{[\mathrm{s}]} + \Delta\boldsymbol{\mathcal{S}}_3^{[\mathrm{s}]}. \tag{9.13}$$

Using Eq. (9.12), we get

$$\boldsymbol{\mathcal{S}}_3^{[\mathrm{s}]} + \Delta\boldsymbol{\mathcal{S}}_3^{[\mathrm{s}]} = \left(\boldsymbol{\mathcal{S}}^{[\mathrm{s}]} + \Delta\boldsymbol{\mathcal{S}}^{[\mathrm{s}]}\right) \times_3 \left(\boldsymbol{U}_3^{[\mathrm{s}]} + \Delta\boldsymbol{U}_3^{[\mathrm{s}]}\right)$$

$$= \boldsymbol{\mathcal{S}}_3^{[\mathrm{s}]} + \Delta\boldsymbol{\mathcal{S}}^{[\mathrm{s}]} \times_3 \boldsymbol{U}_3^{[\mathrm{s}]} + \boldsymbol{\mathcal{S}}^{[\mathrm{s}]} \times_3 \Delta\boldsymbol{U}_3^{[\mathrm{s}]} + \mathcal{O}(\Delta^2).$$

Therefore, we have

$$\Delta\boldsymbol{\mathcal{S}}_3^{[\mathrm{s}]} = \Delta\boldsymbol{\mathcal{S}}^{[\mathrm{s}]} \times_3 \boldsymbol{U}_3^{[\mathrm{s}]} + \boldsymbol{\mathcal{S}}^{[\mathrm{s}]} \times_3 \Delta\boldsymbol{U}_3^{[\mathrm{s}]} + \mathcal{O}(\Delta^2). \tag{9.14}$$

According to [RH08a, RH13], we define the 3-mode slices of $\hat{\boldsymbol{S}}_3$ as

$$\hat{\boldsymbol{S}}_{3,k} \triangleq \hat{\boldsymbol{\mathcal{S}}}_3^{[\mathrm{s}]} \times_3 \boldsymbol{e}_{M_3,k}^{\mathrm{T}} \in \mathbb{C}^{d \times d}, \quad k = 1, 2, ... M_3, \tag{9.15}$$

where $\hat{\boldsymbol{S}}_{3,k}$ represents the k-th slice (along the third dimension) of $\hat{\boldsymbol{\mathcal{S}}}_3^{[\mathrm{s}]}$ in Eq. (9.12). As explained in [RH13], these slices satisfy

$$\mathrm{Diag}\left\{\hat{\boldsymbol{F}}^{(3)}(k,:)\right\} \approx \hat{\boldsymbol{T}}_1^{-1} \cdot \hat{\boldsymbol{S}}_{3,k} \cdot \hat{\boldsymbol{T}}_2^{-1}, \tag{9.16}$$

where $\hat{\boldsymbol{T}}_1$ and $\hat{\boldsymbol{T}}_2$ are transformation matrices obtained by solving the associated JEVD problems. In the noiseless case, the factor matrices are related to the signal subspaces via these transformation matrices as $\boldsymbol{F}^{(r)} = \boldsymbol{U}_r^{[\mathrm{s}]} \cdot \boldsymbol{T}_r$, $r = 1, 2, 3$. Defining the perturbation in the k-th slice, we get

$$\hat{\boldsymbol{S}}_{3,k} \triangleq \boldsymbol{S}_{3,k} + \Delta\boldsymbol{S}_{3,k}, \quad \forall k = 1, 2, \dots, M_3. \tag{9.17}$$

Using Eq. (9.15), this results in

$$\Delta\boldsymbol{S}_{3,k} = \Delta\boldsymbol{\mathcal{S}}_3^{[\mathrm{s}]} \times_3 \boldsymbol{e}_{M_3,k}^{\mathrm{T}} + \mathcal{O}(\Delta^2). \tag{9.18}$$

According to [RH13], we select the slice of $\hat{\boldsymbol{\mathcal{S}}}_3^{[\mathrm{s}]}$ with the lowest condition number, i.e., $\hat{\boldsymbol{S}}_{3,p}$ where $p = \mathrm{argmin}_k\left\{\mathrm{cond}\left(\hat{\boldsymbol{S}}_{3,k}\right)\right\}$ and $\mathrm{cond}(\cdot)$ denotes the condition number operator. This leads to two sets of matrices, namely the right-hand-side (rhs) set and the left-hand-side (lhs) set that are defined as

$$\hat{\boldsymbol{S}}_{3,k}^{\mathrm{rhs}} \triangleq \hat{\boldsymbol{S}}_{3,k} \cdot \hat{\boldsymbol{S}}_{3,p}^{-1}, \quad \forall k = 1, 2, \dots, M_3 \tag{9.19}$$

$$\hat{\boldsymbol{S}}_{3,k}^{\mathrm{lhs}} \triangleq \left(\hat{\boldsymbol{S}}_{3,p}^{-1} \cdot \hat{\boldsymbol{S}}_{3,k}\right)^{\mathrm{T}}, \quad \forall k = 1, 2, \dots, M_3. \tag{9.20}$$

As an example, we compute the perturbation in Eq. (9.19). To this end, let us obtain the perturbation in $\hat{\boldsymbol{S}}_{3,k}^{\mathrm{rhs}}$ as

$$\hat{\boldsymbol{S}}_{3,k}^{\mathrm{rhs}} \triangleq \boldsymbol{S}_{3,k}^{\mathrm{rhs}} + \Delta\boldsymbol{S}_{3,k}^{\mathrm{rhs}}, \quad \forall k = 1, 2, \dots, M_3. \tag{9.21}$$

Using this definition, we now expand Eq. (9.19), as

$$\boldsymbol{S}_{3,k}^{\mathrm{rhs}} + \Delta\boldsymbol{S}_{3,k}^{\mathrm{rhs}} = (\boldsymbol{S}_{3,k} + \Delta\boldsymbol{S}_{3,k})(\boldsymbol{S}_{3,p} + \Delta\boldsymbol{S}_{3,p})^{-1} + \mathcal{O}(\Delta^2)$$

Using the definition in Eq. (1.12) for the matrix inverse, we get

$$(\boldsymbol{S}_{3,p} + \Delta\boldsymbol{S}_{3,p})^{-1} = \boldsymbol{S}_{3,p}^{-1} - \boldsymbol{S}_{3,p}^{-1} \cdot \Delta\boldsymbol{S}_{3,p} \cdot \boldsymbol{S}_{3,p}^{-1} + \mathcal{O}(\Delta^2).$$

According to Eq. (9.21), the perturbation in the slices $\hat{\boldsymbol{S}}_{3,k}^{\mathrm{rhs}}, \forall k = 1, 2, \dots, M_3$ is given by

$$\Delta\boldsymbol{S}_{3,k}^{\mathrm{rhs}} = \Delta\boldsymbol{S}_{3,k} \cdot \boldsymbol{S}_{3,p}^{-1} - \boldsymbol{S}_{3,k} \cdot \boldsymbol{S}_{3,p}^{-1} \cdot \Delta\boldsymbol{S}_{3,p} \cdot \boldsymbol{S}_{3,p}^{-1} + \mathcal{O}(\Delta^2). \tag{9.22}$$

Using the results in Eq. (9.16), it is easy to show that the two sets of matrices in Eq. (9.19) and Eq. (9.20) correspond to the following JEVD problems

$$\hat{\boldsymbol{S}}_{3,k}^{\text{rhs}} \approx \hat{\boldsymbol{T}}_1 \cdot \hat{\boldsymbol{D}}_{3,k} \cdot \boldsymbol{T}_1^{-1} \quad \forall k = 1, 2, \ldots, M_3, \tag{9.23}$$

$$\hat{\boldsymbol{S}}_{3,k}^{\text{lhs}} \approx \hat{\boldsymbol{T}}_2 \cdot \hat{\boldsymbol{D}}_{3,k} \cdot \hat{\boldsymbol{T}}_2^{-1}, \quad \forall k = 1, 2, \ldots, M_3, \tag{9.24}$$

respectively, where the diagonal matrices $\hat{\boldsymbol{D}}_{3,k}$ are defined as

$$\hat{\boldsymbol{D}}_{3,k} \triangleq \text{Diag}\left\{\hat{\boldsymbol{F}}^{(3)}(k,:)\right\} \cdot \text{Diag}\left\{\hat{\boldsymbol{F}}^{(3)}(p,:)\right\}^{-1}. \tag{9.25}$$

Eqs. (9.23) and (9.24) show that $\hat{\boldsymbol{T}}_1$ and $\hat{\boldsymbol{T}}_2$ can be found via an approximate joint diagonalization of the matrix slices $\hat{\boldsymbol{S}}_{3,k}^{\text{rhs}}$ and $\hat{\boldsymbol{S}}_{3,k}^{\text{lhs}}$, respectively. Such an approximate joint diagonalization of Eq. (9.23) and Eq. (9.24) can, for instance, be achieved via joint diagonalization algorithms based on the indirect least squares (LS) cost function such as Sh-Rt [FG06], JDTM [LA10], or the coupled JEVD [RLM16]. In [BCW$^+$17], we have presented a first order perturbation analysis of JEVD algorithms that are based on the indirect LS cost function. The results are also summarized in Appendix D.1. We can use these results to obtain analytical expressions for the perturbation in the estimates $\hat{\boldsymbol{T}}_1$, $\hat{\boldsymbol{T}}_2$, and $\hat{\boldsymbol{D}}_{3,k}, \forall k = 1, 2, \ldots, M_3$. To this end, the perturbations in the $\hat{\boldsymbol{T}}_1$, $\hat{\boldsymbol{T}}_2$, and $\hat{\boldsymbol{D}}_{3,k}$ estimates are defined as

$$\hat{\boldsymbol{T}}_1 \triangleq \boldsymbol{T}_1 + \Delta\boldsymbol{T}_1 \tag{9.26}$$

$$\hat{\boldsymbol{T}}_2 \triangleq \boldsymbol{T}_2 + \Delta\boldsymbol{T}_2 \tag{9.27}$$

$$\hat{\boldsymbol{D}}_{3,k} \triangleq \boldsymbol{D}_{3,k} + \Delta\boldsymbol{D}_{3,k}, \quad \forall k = 1, 2, \ldots, M_3. \tag{9.28}$$

According to [BCW$^+$17], we also define the following matrices

$$\boldsymbol{B}_0 = \boldsymbol{J}_{(d)} \cdot \left(\boldsymbol{T}_1^{\text{T}} \otimes \boldsymbol{T}_1^{-1}\right) \tag{9.29}$$

$$\boldsymbol{s}_k = \text{vec}\left\{\Delta\boldsymbol{S}_{3,k}^{\text{rhs}}\right\} \tag{9.30}$$

$$\boldsymbol{A}_k = \boldsymbol{J}_{(d)} \cdot \left[\left(\boldsymbol{I}_M \otimes \boldsymbol{T}_1^{-1} \cdot \boldsymbol{S}_{3,k}^{\text{rhs}}\right) - \left(\boldsymbol{D}_{3,k} \otimes \boldsymbol{T}_1^{-1}\right)\right], \tag{9.31}$$

where $\boldsymbol{J}_{(d)} \in \{0, 1\}^{d^2 \times d^2}$ is a selection matrix that satisfies the relation $\text{vec}\left\{\text{Off}\left(\boldsymbol{X}\right)\right\} = \boldsymbol{J}_{(d)} \cdot \text{vec}\left\{\boldsymbol{X}\right\}$, for any given $\boldsymbol{X} \in \mathbb{C}^{d \times d}$. After defining the quantities

$$\boldsymbol{A} = \begin{bmatrix} \boldsymbol{A}_1 \\ \boldsymbol{A}_2 \\ \vdots \\ \boldsymbol{A}_{M_3} \end{bmatrix}, \quad \boldsymbol{B} = \boldsymbol{I}_{M_3} \otimes \boldsymbol{B}_0, \quad \boldsymbol{s} = \begin{bmatrix} \boldsymbol{s}_1 \\ \boldsymbol{s}_2 \\ \vdots \\ \boldsymbol{s}_{M_3} \end{bmatrix}, \tag{9.32}$$

we can use the results obtained in [BCW$^+$17]. This leads to

$$\text{vec}\left\{\Delta\boldsymbol{T}_1\right\} = -\boldsymbol{A}^+ \cdot \boldsymbol{B} \cdot \boldsymbol{s} + \mathcal{O}(\Delta^2) \tag{9.33}$$

$$\Delta \boldsymbol{D}_{3,k} = \text{Ddiag}\left(\boldsymbol{T}_1^{-1} \cdot \Delta \boldsymbol{S}_{3,k}^{\text{rhs}} \cdot \boldsymbol{T}_1\right) + \mathcal{O}(\Delta^2), \tag{9.34}$$

for the rhs JEVD problem.

9.3.3. Perturbation of the Factor Matrix Estimates

Using the SECSI framework for a 3-way tensor, we can get up to six different estimates for each factor matrix. The factor matrix $\boldsymbol{F}^{(1)}$ can be estimated from the transform matrix $\hat{\boldsymbol{T}}_1$ via $\hat{\boldsymbol{F}}^{(1)} = \hat{\boldsymbol{U}}_1^{[\text{s}]} \cdot \hat{\boldsymbol{T}}_1$ by using the result of the JEVD defined in Eq. (9.23). Expanding this equation leads to

$$\hat{\boldsymbol{F}}^{(1)} = \left(\boldsymbol{U}_1^{[\text{s}]} + \Delta \boldsymbol{U}_1^{[\text{s}]}\right) \cdot (\boldsymbol{T}_1 + \Delta \boldsymbol{T}_1) + \mathcal{O}(\Delta^2)$$
$$= \boldsymbol{F}^{(1)} + \Delta \boldsymbol{U}_1^{[\text{s}]} \cdot \boldsymbol{T}_1 + \boldsymbol{U}_1^{[\text{s}]} \cdot \Delta \boldsymbol{T}_1 + \mathcal{O}(\Delta^2).$$

Again, we express the perturbation in $\hat{\boldsymbol{F}}^{(1)}$ as

$$\hat{\boldsymbol{F}}^{(1)} \triangleq \boldsymbol{F}^{(1)} + \Delta \boldsymbol{F}^{(1)}. \tag{9.35}$$

This results in an expression for the perturbation $\Delta \boldsymbol{F}^{(1)}$ in the first factor matrix as

$$\Delta \boldsymbol{F}^{(1)} = \Delta \boldsymbol{U}_1^{[\text{s}]} \cdot \boldsymbol{T}_1 + \boldsymbol{U}_1^{[\text{s}]} \cdot \Delta \boldsymbol{T}_1 + \mathcal{O}(\Delta^2). \tag{9.36}$$

Using the result of the JEVD defined in Eq. (9.23), a scaled version of the kth row of the factor matrix $\boldsymbol{F}^{(3)}$ can be estimated from the diagonal of $\hat{\boldsymbol{D}}_{3,k}, \forall k = 1, 2, \ldots, M_3$, according to Eq. (9.25) as

$$\hat{\tilde{\boldsymbol{F}}}^{(3)}(k,:) = \text{diag}\left(\hat{\boldsymbol{D}}_{3,k}\right)^{\text{T}}$$
$$= \text{diag}\left(\boldsymbol{D}_{3,k} + \Delta \boldsymbol{D}_{3,k}\right)^{\text{T}}$$
$$= \tilde{\boldsymbol{F}}^{(3)}(k,:) + \text{diag}\left(\Delta \boldsymbol{D}_{3,k}\right)^{\text{T}} + \mathcal{O}(\Delta^2),$$

where the perturbation in $\hat{\tilde{\boldsymbol{F}}}^{(3)}(k,:)$ is defined as

$$\hat{\tilde{\boldsymbol{F}}}^{(3)}(k,:) = \tilde{\boldsymbol{F}}^{(3)}(k,:) + \Delta \tilde{\boldsymbol{F}}^{(3)}(k,:),$$

which results in

$$\Delta \tilde{\boldsymbol{F}}^{(3)}(k,:) = \text{diag}\left(\Delta \boldsymbol{D}_{3,k}\right)^{\text{T}} + \mathcal{O}(\Delta^2).$$

To get an expression of the corresponding factor matrix estimate $\hat{\boldsymbol{F}}^{(3)}$, we take into account Eq. (9.25) via $\hat{\boldsymbol{F}}^{(3)} \triangleq \hat{\tilde{\boldsymbol{F}}}^{(3)} \cdot \text{Diag}\left(\boldsymbol{F}^{(3)}(p,:)\right)$. This leads to

$$\hat{\boldsymbol{F}}^{(3)} = \boldsymbol{F}^{(3)} + \Delta \boldsymbol{F}^{(3)}, \tag{9.37}$$

where

$$\Delta \boldsymbol{F}^{(3)} = \Delta \tilde{\boldsymbol{F}}^{(3)} \cdot \operatorname{Diag}\left(\boldsymbol{F}^{(3)}(p,:)\right). \tag{9.38}$$

Using this equation, the perturbation of the kth row of $\Delta \boldsymbol{F}^{(3)}$ is obtained as

$$\Delta \boldsymbol{F}^{(3)}(k,:) = \operatorname{diag}\left(\Delta \boldsymbol{D}_{3,k}\right)^{\mathrm{T}} \cdot \operatorname{Diag}\left(\boldsymbol{F}^{(3)}(p,:)\right) + \mathcal{O}(\Delta^2). \tag{9.39}$$

The factor matrix $\boldsymbol{F}^{(2)}$ can be estimated via a LS fit. To this end, we define the LS estimate of $\boldsymbol{F}^{(2)}$ as

$$\hat{\boldsymbol{F}}^{(2)} \triangleq [\boldsymbol{\mathcal{X}}]_{(2)} \cdot \left(\hat{\boldsymbol{F}}^{(3)} \diamond \hat{\boldsymbol{F}}^{(1)}\right)^{+\mathrm{T}}.$$

Using equations (9.35) and (9.37), we get:

$$\hat{\boldsymbol{F}}^{(2)} = \left[\boldsymbol{\mathcal{X}}_0 + \boldsymbol{\mathcal{N}}\right]_{(2)} \cdot \left[\left(\boldsymbol{F}^{(3)} + \Delta \boldsymbol{F}^{(3)}\right) \diamond \left(\boldsymbol{F}^{(1)} + \Delta \boldsymbol{F}^{(1)}\right)\right]^{+\mathrm{T}}.$$

Since $\hat{\boldsymbol{F}}^{(2)} = \boldsymbol{F}^{(2)} + \Delta \boldsymbol{F}^{(2)}$, we finally calculate $\Delta \boldsymbol{F}^{(2)}$ as

$$\begin{aligned}
\Delta \boldsymbol{F}^{(2)} &= \hat{\boldsymbol{F}}^{(2)} - \boldsymbol{F}^{(2)} \\
&= \left[\boldsymbol{\mathcal{X}}_0 + \boldsymbol{\mathcal{N}}\right]_{(2)} \left[\left(\boldsymbol{F}^{(3)} + \Delta \boldsymbol{F}^{(3)}\right) \diamond \left(\boldsymbol{F}^{(1)} + \Delta \boldsymbol{F}^{(1)}\right)\right]^{+\mathrm{T}} - \boldsymbol{F}^{(2)} \\
&= [\boldsymbol{\mathcal{X}}_0]_{(2)} \cdot \left[\left(\boldsymbol{F}^{(3)} \diamond \boldsymbol{F}^{(1)}\right) + \left(\Delta \boldsymbol{F}^{(3)} \diamond \boldsymbol{F}^{(1)}\right) + \left(\boldsymbol{F}^{(3)} \diamond \Delta \boldsymbol{F}^{(1)}\right)\right]^{+\mathrm{T}} \\
&\quad + [\boldsymbol{\mathcal{N}}]_{(2)} \cdot \left[\boldsymbol{F}^{(3)} \diamond \boldsymbol{F}^{(1)}\right]^{+\mathrm{T}} - \boldsymbol{F}^{(2)} + \mathcal{O}(\Delta^2)
\end{aligned}$$

Using the definition in Eq. (1.12), we get

$$\begin{aligned}
\Delta \boldsymbol{F}^{(2)} &= [\boldsymbol{\mathcal{X}}_0]_{(2)} \cdot \left[\left(\boldsymbol{F}^{(3)} \diamond \boldsymbol{F}^{(1)}\right)^{+} - \left(\boldsymbol{F}^{(3)} \diamond \boldsymbol{F}^{(1)}\right)^{+}\right. \\
&\quad \left. \cdot \left(\left(\Delta \boldsymbol{F}^{(3)} \diamond \boldsymbol{F}^{(1)}\right) + \left(\boldsymbol{F}^{(3)} \diamond \Delta \boldsymbol{F}^{(1)}\right)\right) \cdot \left(\boldsymbol{F}^{(3)} \diamond \boldsymbol{F}^{(1)}\right)^{+}\right]^{\mathrm{T}} + [\boldsymbol{\mathcal{N}}]_{(2)} \cdot \left[\boldsymbol{F}^{(3)} \diamond \boldsymbol{F}^{(1)}\right]^{+\mathrm{T}} - \boldsymbol{F}^{(2)} \\
&\quad + \mathcal{O}(\Delta^2) \\
&= -[\boldsymbol{\mathcal{X}}_0]_{(2)} \cdot \left[\left(\boldsymbol{F}^{(3)} \diamond \boldsymbol{F}^{(1)}\right)^{+} \cdot \left(\left(\Delta \boldsymbol{F}^{(3)} \diamond \boldsymbol{F}^{(1)}\right) + \left(\boldsymbol{F}^{(3)} \diamond \Delta \boldsymbol{F}^{(1)}\right)\right) \cdot \left(\boldsymbol{F}^{(3)} \diamond \boldsymbol{F}^{(1)}\right)^{+}\right]^{\mathrm{T}} \\
&\quad + [\boldsymbol{\mathcal{N}}]_{(2)} \cdot \left[\boldsymbol{F}^{(3)} \diamond \boldsymbol{F}^{(1)}\right]^{+\mathrm{T}} + \mathcal{O}(\Delta^2) \\
&= -\boldsymbol{F}^{(2)} \cdot \left[\left(\Delta \boldsymbol{F}^{(3)} \diamond \boldsymbol{F}^{(1)}\right) + \left(\boldsymbol{F}^{(3)} \diamond \Delta \boldsymbol{F}^{(1)}\right)\right]^{\mathrm{T}} \cdot \left(\boldsymbol{F}^{(3)} \diamond \boldsymbol{F}^{(1)}\right)^{+\mathrm{T}} + [\boldsymbol{\mathcal{N}}]_{(2)} \cdot \left[\boldsymbol{F}^{(3)} \diamond \boldsymbol{F}^{(1)}\right]^{+\mathrm{T}} \\
&\quad + \mathcal{O}(\Delta^2). \tag{9.40}
\end{aligned}$$

In the same manner, another set of factor matrix estimates can be obtained by solving the lhs JEVD problem for $\hat{\boldsymbol{T}}_2$ and $\hat{\boldsymbol{D}}_{3,k}, \forall k = 1, 2 \ldots, M_3$ in Eq. (9.24). This leads to the two sets of estimates (rhs and lhs) in the third mode, as summarized in Table 9.1. Note that the obtained expressions can be directly used for the first and second mode estimates obtained from Eq. (9.10) and Eq. (9.11), respectively, since such estimates can be derived by applying the SECSI framework to a permuted version of $\boldsymbol{\mathcal{X}}$.

For example, we can obtain the first mode estimates, corresponding to Eq. (9.10), by applying the SECSI framework on the third mode of permute($\boldsymbol{\mathcal{X}}, [2, 3, 1]$), where permute($\boldsymbol{\mathcal{A}}, \text{ORDER}$) rearranges the dimensions of $\boldsymbol{\mathcal{A}}$ so that they are in the order specified by the vector ORDER (as defined in Matlab). In the same manner, the second mode estimates, corresponding to Eq. (9.11), are obtained by using the SECSI framework on the third mode of permute($\boldsymbol{\mathcal{X}}, [1, 3, 2]$). Therefore, we obtain a total of six estimates for each factor matrix (two from each mode), as shown in Fig. 9.1. To select the final estimates, we can use best matching scheme or any low-complexity heuristic alternative that has been discussed in [RH13].

9.4. Closed-Form rMSFE expressions

In this section, we present an analytical rMSFE expression for each of the factor matrices estimates. We first introduce some definitions which will be used subsequently to derive the analytical expressions. Additionally, Theorem 1 will be used to resolve the scaling ambiguity in the factor matrices of the CPD.

9.4.1. Preliminary Definitions

Let $\boldsymbol{P}_{(M_1,M_2,M_3)}^{(r)} \in \{0,1\}^{(M_1 \cdot M_2 \cdot M_3) \times (M_1 \cdot M_2 \cdot M_3)}$ be the r-to-1 mode permutation matrix of any third order tensor $\boldsymbol{\mathcal{Z}} \in \mathbb{C}^{M_1 \times M_2 \times M_3}$. This means that the permutation matrix $\boldsymbol{P}_{(M_1,M_2,M_3)}^{(r)}$ satisfies the property

$$\text{vec}\left\{[\boldsymbol{\mathcal{Z}}]_{(r)}\right\} = \boldsymbol{P}_{(M_1,M_2,M_3)}^{(r)} \cdot \text{vec}\left\{[\boldsymbol{\mathcal{Z}}]_{(1)}\right\}. \tag{9.41}$$

Note that $\boldsymbol{P}_{(M_1,M_2,M_3)}^{(1)} = \boldsymbol{I}_{(M_1 \cdot M_2 \cdot M_3)}$. In the same manner, let $\boldsymbol{Q}_{(M_1,M_2)} \in \{0,1\}^{(M_1 \cdot M_2) \times (M_1 \cdot M_2)}$ be the permutation matrix that satisfies the following relation for any $\boldsymbol{Z} \in \mathbb{C}^{M_1 \times M_2}$

$$\text{vec}\left\{\boldsymbol{Z}^{\text{T}}\right\} = \boldsymbol{Q}_{(M_1,M_2)} \cdot \text{vec}\left\{\boldsymbol{Z}\right\}. \tag{9.42}$$

Additionally, let $\boldsymbol{n}_r \triangleq \text{vec}\left\{[\boldsymbol{\mathcal{N}}]_{(r)}\right\}$ be the r-mode noise vector, with $\boldsymbol{R}_{\text{nn}}^{(r)} \triangleq \mathbb{E}\{\boldsymbol{n}_r \cdot \boldsymbol{n}_r^{\text{H}}\}$ and $\boldsymbol{C}_{\text{nn}}^{(r)} \triangleq \mathbb{E}\{\boldsymbol{n}_r \cdot \boldsymbol{n}_r^{\text{T}}\}$ being the corresponding r-mode covariance and pseudo-covariance matrices, respectively. Note that the these covariance matrices $\boldsymbol{R}_{\text{nn}}^{(r)}$ are permuted versions of $\boldsymbol{R}_{\text{nn}}^{(1)}$, since $\boldsymbol{n}_r = \boldsymbol{P}_{(M_1,M_2,M_3)}^{(r)} \cdot \boldsymbol{n}_1$. This property is also satisfied for the pseudo-covariance matrices $\boldsymbol{C}_{\text{nn}}^{(r)}$.

Let $\boldsymbol{W}_{(d)} \in \{0,1\}^{d^2 \times d^2}$ be the diagonal elements selection matrix defined as

$$\text{vec}\left\{\text{Ddiag}\left(\boldsymbol{Z}\right)\right\} = \boldsymbol{W}_{(d)} \cdot \text{vec}\left\{\boldsymbol{Z}\right\} \in \mathbb{C}^{d^2 \times 1}, \tag{9.43}$$

where $\boldsymbol{Z} \in \mathbb{C}^{d \times d}$ is a square matrix. Note that $\boldsymbol{W}_{(d)}$ is simply $\boldsymbol{I}_{d^2} - \boldsymbol{J}_{(d)}$, where $\boldsymbol{J}_{(d)}$ has already been defined below Eq. (9.31). Likewise, let $\boldsymbol{W}_{(d)}^{\text{red}} \in \{0,1\}^{d \times d^2}$ be the reduced dimensional diagonal elements selection matrix that selects only the diagonal elements i.e.,

$$\text{diag}\left(\boldsymbol{Z}\right) = \boldsymbol{W}_{(d)}^{\text{red}} \cdot \text{vec}\left\{\boldsymbol{Z}\right\} \in \mathbb{C}^{d \times 1} \tag{9.44}$$

for any square matrix $\boldsymbol{Z} \in \mathbb{C}^{d \times d}$.

Theorem 1. *Let $\boldsymbol{Z} \in \mathbb{C}^{d \times d}$ and $\Delta \boldsymbol{Z} \in \mathbb{C}^{d \times d}$ be two matrices where the norm of each column in $\Delta \boldsymbol{Z}$ is much smaller than the corresponding column in $\boldsymbol{Z}$. Let $\tilde{\boldsymbol{P}} \in \mathbb{C}^{d \times d}$ be a diagonal matrix that introduces a scaling ambiguity in $(\boldsymbol{Z} + \Delta \boldsymbol{Z})$. Then, a diagonal matrix $\boldsymbol{P}_{\mathrm{opt}}$ that resolve this scaling ambiguity can be expressed as*

$$\boldsymbol{P}_{\mathrm{opt}} = \operatorname*{argmin}_{\boldsymbol{P} \in \mathcal{M}_D(d)} \left\| \boldsymbol{Z} - (\boldsymbol{Z} + \Delta \boldsymbol{Z}) \cdot \tilde{\boldsymbol{P}} \cdot \boldsymbol{P} \right\|_{\mathrm{F}}^2,$$

where $\mathcal{M}_D(d)$ is the set of $d \times d$ diagonal matrices. Thus, the following relation holds

$$\boldsymbol{Z} - (\boldsymbol{Z} + \Delta \boldsymbol{Z}) \cdot \tilde{\boldsymbol{P}} \cdot \boldsymbol{P}_{\mathrm{opt}} = \boldsymbol{Z} \cdot \mathrm{Ddiag}\left(\boldsymbol{Z}^{\mathrm{H}} \cdot \Delta \boldsymbol{Z}\right) \cdot \boldsymbol{K}^{-1} - \Delta \boldsymbol{Z} + \mathcal{O}(\Delta^2),$$

where $\boldsymbol{K} = \mathrm{Ddiag}(\boldsymbol{Z}^{\mathrm{H}} \cdot \boldsymbol{Z}) \in \mathbb{R}^{d \times d}$ is a diagonal matrix.

Proof. cf. Appendix D.2 □

9.4.2. Factor Matrices rMSFE Expressions

In this section, we derive closed-form rMSFE expressions for the three factor matrices. As an example, we consider these closed-form rMSFE expressions using the JEVD of the rhs tensor slices in Eq. (9.23). In Section 9.5.1, we also present the results for the lhs tensor slices in Eq. (9.24). The rMSFE in the r-th factor matrix is defined as

$$\mathrm{rMSFE}^{(r)} = \mathbb{E} \left\{ \min_{\boldsymbol{P}^{(r)} \in \mathcal{M}_{\mathrm{PD}}(d)} \left(\frac{\left\| \boldsymbol{F}^{(r)} - \hat{\boldsymbol{F}}^{(r)} \cdot \boldsymbol{P}^{(r)} \right\|_{\mathrm{F}}^2}{\left\| \boldsymbol{F}^{(r)} \right\|_{\mathrm{F}}^2} \right) \right\}, \tag{9.45}$$

where $\mathcal{M}_{\mathrm{PD}}(d)$ is the set of $d \times d$ permuted diagonal matrices (also called monomial matrices), i.e., the matrices $\boldsymbol{P}^{(r)}$ correct the permutation and scaling ambiguity that is inherent in the estimation of the loading matrices [RH13] and $\boldsymbol{F}^{(r)}$ is the true factor matrix. The goal of the SECSI framework is to estimate these factor matrices up to the inevitable ambiguities, and our goal in the performance analysis is to predict the resulting relative errors, assuming (for the sake of the analysis) that the true matrices are known and that these ambiguities are resolved. Consequently, the rMSFE measures how accurately the actual canonical polyadic model can be estimated from the noisy observations. After correcting the permutation ambiguity, the factor matrix estimates that we get from Monte-Carlo simulations [RH13] can be approximated as

$$\hat{\boldsymbol{F}}^{(r)} = (\boldsymbol{F}^{(r)} + \Delta \boldsymbol{F}^{(r)}) \cdot \tilde{\boldsymbol{P}}^{(r)},$$

where $\Delta \boldsymbol{F}^{(r)}$ represents the perturbation that can be obtained from the performance analysis and $\tilde{\boldsymbol{P}}^{(r)}$ is a diagonal matrix modeling the scaling ambiguity. By using this relation, we rewrite the rMSFE definition in Eq. (9.45) as

$$\mathrm{rMSFE}^{(r)} = \mathbb{E} \left\{ \frac{\left\| \boldsymbol{F}^{(r)} - (\boldsymbol{F}^{(r)} + \Delta \boldsymbol{F}^{(r)}) \cdot \tilde{\boldsymbol{P}}^{(r)} \cdot \boldsymbol{P}_{\mathrm{opt}}^{(r)} \right\|_{\mathrm{F}}^2}{\left\| \boldsymbol{F}^{(r)} \right\|_{\mathrm{F}}^2} \right\}, \tag{9.46}$$

where $\boldsymbol{P}_{\text{opt}}^{(r)}$ is the optimal column scaling matrix, since the scaling ambiguity is only relevant for the perturbation analysis. To derive closed-form rMSFE$^{(r)}$ expressions, we first vectorize $\boldsymbol{F}^{(r)} - (\boldsymbol{F}^{(r)} + \Delta\boldsymbol{F}^{(r)}) \cdot \tilde{\boldsymbol{P}}^{(r)} \cdot \boldsymbol{P}_{\text{opt}}^{(r)}$, use Theorem 1, and the definitions in Eq. (9.43) and Eq. (9.42), to get

$$
\begin{aligned}
\text{vec}\left\{\boldsymbol{F}^{(r)} - (\boldsymbol{F}^{(r)} + \Delta\boldsymbol{F}^{(r)}) \cdot \tilde{\boldsymbol{P}}^{(r)} \cdot \boldsymbol{P}_{\text{opt}}^{(r)}\right\} &\approx \text{vec}\left\{\boldsymbol{F}^{(r)} \cdot \text{Ddiag}\left(\boldsymbol{F}^{(r)\text{H}} \cdot \Delta\boldsymbol{F}^{(r)}\right) \cdot \boldsymbol{K}_r^{-1} - \Delta\boldsymbol{F}^{(r)}\right\} \\
&= \left(\boldsymbol{I}_d \otimes \boldsymbol{F}^{(r)}\right) \cdot \left(\boldsymbol{K}_r^{-1} \otimes \boldsymbol{I}_d\right) \cdot \boldsymbol{W}_{(d)} \cdot \text{vec}\left\{\boldsymbol{F}^{(r)\text{H}} \cdot \Delta\boldsymbol{F}^{(r)}\right\} - \text{vec}\left\{\Delta\boldsymbol{F}^{(r)}\right\} \\
&= \left(\boldsymbol{I}_d \otimes \boldsymbol{F}^{(r)}\right) \cdot \left(\boldsymbol{K}_r^{-1} \otimes \boldsymbol{I}_d\right) \cdot \boldsymbol{W}_{(d)} \cdot \left(\boldsymbol{I}_d \otimes \boldsymbol{F}^{(r)\text{H}}\right) \cdot \text{vec}\left\{\Delta\boldsymbol{F}^{(r)}\right\} - \text{vec}\left\{\Delta\boldsymbol{F}^{(r)}\right\},
\end{aligned}
\tag{9.47}
$$

where $\boldsymbol{K}_r = \text{Ddiag}\left(\boldsymbol{F}^{(r)\text{H}} \cdot \boldsymbol{F}^{(r)}\right)$. Note that the resulting expression contains the vectorization of the perturbation in the respective factor matrix estimates. As shown in Section 9.3.3, the perturbations in the three factor matrix estimates (Eq. (9.36), Eq. (9.40), and Eq. (9.38)) are a function of different perturbations, i.e., $\Delta\boldsymbol{U}_r^{[\text{s}]}$ in Eq. (9.8), $\Delta\boldsymbol{\mathcal{S}}^{[\text{s}]}$ in Eq. (9.9), $\Delta\boldsymbol{\mathcal{S}}_3^{[\text{s}]}$ in Eq. (9.14), $\Delta\boldsymbol{S}_{3,k}$ in Eq. (9.18), $\Delta\boldsymbol{S}_{3,k}^{\text{rhs}}$ in Eq. (9.22), and $\Delta\boldsymbol{D}_{3,k}$ in Eq. (9.34). Therefore, to get final closed-form rMSFE expressions for the three factor matrices in Eq. (9.47), we vectorize all of the perturbation expressions. We start by applying the vectorization operator to $\Delta\boldsymbol{U}_r^{[\text{s}]}$ in Eq. (9.8) and use the r-to-1 mode permutation matrix in Eq. (9.41) to get

$$
\begin{aligned}
\text{vec}\left\{\Delta\boldsymbol{U}_r^{[\text{s}]}\right\} &= \left(\boldsymbol{\Sigma}_r^{[\text{s}]^{-1}} \boldsymbol{V}_r^{[\text{s}]\text{T}} \otimes \boldsymbol{\Gamma}_r^{[\text{n}]}\right) \cdot \boldsymbol{n}_r + \mathcal{O}(\Delta^2) \\
&= \left(\boldsymbol{\Sigma}_r^{[\text{s}]^{-1}} \boldsymbol{V}_r^{[\text{s}]\text{T}} \otimes \boldsymbol{\Gamma}_r^{[\text{n}]}\right) \cdot \boldsymbol{P}_{(M_1,M_2,M_3)}^{(r)} \cdot \boldsymbol{n}_1 + \mathcal{O}(\Delta^2).
\end{aligned}
\tag{9.48}
$$

Next, we vectorize the 1-mode unfolding of $\Delta\boldsymbol{\mathcal{S}}^{[\text{s}]}$ in Eq. (9.9), by using the definition in Eq. (9.41) to obtain

$$
\begin{aligned}
\text{vec}\left\{[\Delta\boldsymbol{\mathcal{S}}^{[\text{s}]}]_{(1)}\right\} &= \text{vec}\left\{\left[\boldsymbol{\mathcal{N}}\bigtimes_{r=1}^{3}\boldsymbol{U}_r^{[\text{s}]\text{H}}\right]_{(1)}\right\} + \mathcal{O}(\Delta^2) \\
&= \underbrace{\left(\boldsymbol{U}_2^{[\text{s}]\text{H}} \otimes \boldsymbol{U}_3^{[\text{s}]\text{H}} \otimes \boldsymbol{U}_1^{[\text{s}]\text{H}}\right)}_{\boldsymbol{L}_0} \cdot \boldsymbol{n}_1 + \mathcal{O}(\Delta^2).
\end{aligned}
\tag{9.49}
$$

In the same manner, we expand $\text{vec}\left\{[\Delta\boldsymbol{\mathcal{S}}_3^{[\text{s}]}]_{(1)}\right\}$ using Eq. (9.48) and Eq. (9.49) to get

$$
\begin{aligned}
\text{vec}\left\{[\Delta\boldsymbol{\mathcal{S}}_3^{[\text{s}]}]_{(1)}\right\} &= \text{vec}\left\{[\Delta\boldsymbol{\mathcal{S}}^{[\text{s}]} \times_3 \boldsymbol{U}_3^{[\text{s}]} + \boldsymbol{\mathcal{S}}^{[\text{s}]} \times_3 \Delta\boldsymbol{U}_3^{[\text{s}]}]_{(1)}\right\} + \mathcal{O}(\Delta^2) \\
&= \boldsymbol{P}_{(d,d,M_3)}^{(3)\text{T}} \cdot \text{vec}\left\{[\Delta\boldsymbol{\mathcal{S}}^{[\text{s}]} \times_3 \boldsymbol{U}_3^{[\text{s}]} + \boldsymbol{\mathcal{S}}^{[\text{s}]} \times_3 \Delta\boldsymbol{U}_3^{[\text{s}]}]_{(3)}\right\} + \mathcal{O}(\Delta^2) \\
&= \boldsymbol{P}_{(d,d,M_3)}^{(3)\text{T}} \cdot \left(\boldsymbol{I}_{d^2} \otimes \boldsymbol{U}_3^{[\text{s}]}\right) \cdot \text{vec}\left\{[\Delta\boldsymbol{\mathcal{S}}^{[\text{s}]}]_{(3)}\right\} \\
&\quad + \boldsymbol{P}_{(d,d,M_3)}^{(3)\text{T}} \cdot \left([\boldsymbol{\mathcal{S}}^{[\text{s}]}]_{(3)}^{\text{T}} \otimes \boldsymbol{I}_{M_3}\right) \cdot \text{vec}\left\{\Delta\boldsymbol{U}_3^{[\text{s}]}\right\} + \mathcal{O}(\Delta^2) \\
&= \boldsymbol{P}_{(d,d,M_3)}^{(3)\text{T}} \cdot \left(\boldsymbol{I}_{d^2} \otimes \boldsymbol{U}_3^{[\text{s}]}\right) \cdot \boldsymbol{P}_{(d,d,d)}^{(3)} \cdot \text{vec}\left\{[\Delta\boldsymbol{\mathcal{S}}^{[\text{s}]}]_{(1)}\right\}
\end{aligned}
$$

$$+ \boldsymbol{P}_{(d,d,M_3)}^{(3)^{\mathrm{T}}} \cdot \left([\Delta\boldsymbol{\mathcal{S}}^{[\mathrm{s}]}]_{(3)}^{\mathrm{T}} \otimes \boldsymbol{I}_{M_3}\right) \cdot \left(\boldsymbol{\Sigma}_3^{[\mathrm{s}]^{-1}} \boldsymbol{V}_3^{[\mathrm{s}]^{\mathrm{T}}} \otimes \boldsymbol{\Gamma}_3^{[\mathrm{n}]}\right) \cdot \boldsymbol{P}_{(M_1,M_2,M_3)}^{(3)} \cdot \boldsymbol{n}_1 + \mathcal{O}(\Delta^2)$$

$$= \boldsymbol{P}_{(d,d,M_3)}^{(3)^{\mathrm{T}}} \cdot \left(\boldsymbol{I}_{d^2} \otimes \boldsymbol{U}_3^{[\mathrm{s}]}\right) \cdot \boldsymbol{P}_{(d,d,d)}^{(3)} \cdot \boldsymbol{L}_0 \cdot \boldsymbol{n}_1$$

$$+ \boldsymbol{P}_{(d,d,M_3)}^{(3)^{\mathrm{T}}} \cdot \left([\Delta\boldsymbol{\mathcal{S}}^{[\mathrm{s}]}]_{(3)}^{\mathrm{T}} \cdot \boldsymbol{\Sigma}_3^{[\mathrm{s}]^{-1}} \boldsymbol{V}_3^{[\mathrm{s}]^{\mathrm{T}}} \otimes \boldsymbol{\Gamma}_3^{[\mathrm{n}]}\right) \cdot \boldsymbol{P}_{(M_1,M_2,M_3)}^{(3)} \cdot \boldsymbol{n}_1 + \mathcal{O}(\Delta^2)$$

$$= \boldsymbol{L}_1 \cdot \boldsymbol{n}_1 + \mathcal{O}(\Delta^2)\,, \tag{9.50}$$

where

$$\boldsymbol{L}_1 \triangleq \boldsymbol{P}_{(d,d,M_3)}^{(3)^{\mathrm{T}}} \cdot \left(\boldsymbol{I}_{d^2} \otimes \boldsymbol{U}_3^{[\mathrm{s}]}\right) \cdot \boldsymbol{P}_{(d,d,d)}^{(3)} \cdot \boldsymbol{L}_0 + \boldsymbol{P}_{(d,d,M_3)}^{(3)^{\mathrm{T}}} \cdot \left([\boldsymbol{\mathcal{S}}^{[\mathrm{s}]}]_{(3)}^{\mathrm{T}} \cdot \boldsymbol{\Sigma}_3^{[\mathrm{s}]^{-1}} \boldsymbol{V}_3^{[\mathrm{s}]^{\mathrm{T}}} \otimes \boldsymbol{\Gamma}_3^{[\mathrm{n}]}\right) \cdot \boldsymbol{P}_{(M_1,M_2,M_3)}^{(3)} \tag{9.51}$$

Furthermore, we can use this result to obtain an expression for the vectorization of each slice $\Delta\boldsymbol{S}_{3,k}$ $\forall k = 1, 2, \ldots, M_3$ of $\Delta\boldsymbol{\mathcal{S}}_3^{[\mathrm{s}]}$. Using Eq. (9.18) and Eq. (9.50), we derive an expression for $\mathrm{vec}\left\{\Delta\boldsymbol{S}_{3,k}\right\}$ as

$$\mathrm{vec}\left\{\Delta\boldsymbol{S}_{3,k}\right\} = \mathrm{vec}\left\{\Delta\boldsymbol{\mathcal{S}}_3^{[\mathrm{s}]} \times_3 \boldsymbol{e}_{M_3,k}^{\mathrm{T}}\right\}$$

$$= \mathrm{vec}\left\{[\Delta\boldsymbol{\mathcal{S}}_3^{[\mathrm{s}]} \times_3 \boldsymbol{e}_{M_3,k}^{\mathrm{T}}]_{(1)}\right\}$$

$$= \mathrm{vec}\left\{[\Delta\boldsymbol{\mathcal{S}}_3^{[\mathrm{s}]}]_{(1)} \cdot (\boldsymbol{I}_d \otimes \boldsymbol{e}_{M_3,k}^{\mathrm{T}})^{\mathrm{T}}\right\} + \mathcal{O}(\Delta^2)$$

$$= (\boldsymbol{I}_d \otimes \boldsymbol{e}_{M_3,k}^{\mathrm{T}} \otimes \boldsymbol{I}_d) \cdot \mathrm{vec}\left\{[\Delta\boldsymbol{\mathcal{S}}_3^{[\mathrm{s}]}]_{(1)}\right\}$$

$$= (\boldsymbol{I}_d \otimes \boldsymbol{e}_{M_3,k}^{\mathrm{T}} \otimes \boldsymbol{I}_d) \cdot \boldsymbol{L}_1 \cdot \boldsymbol{n}_1$$

$$= \boldsymbol{L}_2^{(k)} \cdot \boldsymbol{n}_1 + \mathcal{O}(\Delta^2)\,, \tag{9.52}$$

where

$$\boldsymbol{L}_2^{(k)} \triangleq (\boldsymbol{I}_d \otimes \boldsymbol{e}_{M_3,k}^{\mathrm{T}} \otimes \boldsymbol{I}_d) \cdot \boldsymbol{L}_1 \tag{9.53}$$

for $k = 1, 2, \ldots, M_3$. Next, we use this result and Eq. (9.9) to expand the vectorization of Eq. (9.22). This leads to

$$\mathrm{vec}\left\{\Delta\boldsymbol{S}_{3,k}^{\mathrm{rhs}}\right\} = \mathrm{vec}\left\{\Delta\boldsymbol{S}_{3,k} \cdot \boldsymbol{S}_{3,p}^{-1} - \boldsymbol{S}_{3,k} \cdot \boldsymbol{S}_{3,p}^{-1} \cdot \Delta\boldsymbol{S}_{3,p} \cdot \boldsymbol{S}_{3,p}^{-1}\right\} + \mathcal{O}(\Delta^2)$$

$$= (\boldsymbol{S}_{3,p}^{-\mathrm{T}} \otimes \boldsymbol{I}_d) \cdot \mathrm{vec}\left\{\Delta\boldsymbol{S}_{3,k}\right\} - (\boldsymbol{S}_{3,p}^{-\mathrm{T}} \otimes \boldsymbol{S}_{3,k} \cdot \boldsymbol{S}_{3,p}^{-1}) \cdot \mathrm{vec}\left\{\Delta\boldsymbol{S}_{3,p}\right\} + \mathcal{O}(\Delta^2)$$

$$= (\boldsymbol{S}_{3,p}^{-\mathrm{T}} \otimes \boldsymbol{I}_d) \cdot \boldsymbol{L}_2^{(k)} \cdot \boldsymbol{n}_1 - (\boldsymbol{S}_{3,p}^{-\mathrm{T}} \otimes \boldsymbol{S}_{3,k} \cdot \boldsymbol{S}_{3,p}^{-1}) \cdot \boldsymbol{L}_2^{(p)} \cdot \boldsymbol{n}_1 + \mathcal{O}(\Delta^2)$$

$$= \boldsymbol{L}_3^{(k)} \cdot \boldsymbol{n}_1 + \mathcal{O}(\Delta^2)\,, \tag{9.54}$$

where

$$\boldsymbol{L}_3^{(k)} \triangleq (\boldsymbol{S}_{3,p}^{-\mathrm{T}} \otimes \boldsymbol{I}_d) \cdot \boldsymbol{L}_2^{(k)} - (\boldsymbol{S}_{3,p}^{-\mathrm{T}} \otimes \boldsymbol{S}_{3,k} \cdot \boldsymbol{S}_{3,p}^{-1}) \cdot \boldsymbol{L}_2^{(p)}. \tag{9.55}$$

Next, we stack the column vectors $\boldsymbol{s}_k = \mathrm{vec}\left\{\Delta\boldsymbol{S}_{3,k}^{\mathrm{rhs}}\right\}$ into the vector $\boldsymbol{s}$, as defined in Eq. (9.32), and use

the previous result to obtain

$$s = L_3 \cdot n_1 + \mathcal{O}(\Delta^2), \tag{9.56}$$

where $L_3 = \begin{bmatrix} L_3^{(1)} & L_3^{(2)} \dots L_3^{(M_3)} \end{bmatrix}^T$. This expression for s is used to expand Eq. (9.33) into

$$
\begin{aligned}
\operatorname{vec}\left\{\Delta T_1\right\} &= -A^+ \cdot B \cdot s + \mathcal{O}(\Delta^2) \\
&= \underbrace{-A^+ \cdot B \cdot L_3}_{L_4} \cdot n_1 + \mathcal{O}(\Delta^2).
\end{aligned}
\tag{9.57}
$$

Since $\operatorname{diag}\left(\operatorname{Ddiag}\left(Z\right)\right) = \operatorname{diag}\left(Z\right)$ for any matrix Z, we use the matrix $W_{(d)}^{\mathrm{red}}$ (defined in Eq. (9.44)) and Eq. (9.34) to vectorize Eq. (9.39) as

$$
\begin{aligned}
\operatorname{vec}\left\{\Delta F^{(3)}(k,:)\right\} &= \operatorname{vec}\left\{\operatorname{diag}\left(\Delta D_{3,k}\right)^{\mathrm{T}} \cdot \operatorname{Diag}\left(F^{(3)}(p,:)\right)\right\} \\
&= \operatorname{vec}\left\{\operatorname{diag}\left(\operatorname{Ddiag}\left(T_1^{-1} \cdot \Delta S_{3,k}^{\mathrm{rhs}} \cdot T_1\right)\right)^{\mathrm{T}} \operatorname{Diag}\left(F^{(3)}(p,:)\right)\right\} + \mathcal{O}(\Delta^2) \\
&= \operatorname{vec}\left\{\operatorname{diag}\left(T_1^{-1} \cdot \Delta S_{3,k}^{\mathrm{rhs}} \cdot T_1\right)^{\mathrm{T}} \cdot \operatorname{Diag}\left(F^{(3)}(p,:)\right)\right\} + \mathcal{O}(\Delta^2) \\
&= \operatorname{vec}\left\{\operatorname{diag}\left[T_1^{-1} \cdot \Delta S_{3,k}^{\mathrm{rhs}} \cdot T_1 \cdot \operatorname{Diag}\left(F^{(3)}(p,:)\right)\right]\right\} + \mathcal{O}(\Delta^2) \\
&= W_{(d)}^{\mathrm{red}} \cdot \operatorname{vec}\left\{T_1^{-1} \cdot \Delta S_{3,k}^{\mathrm{rhs}} \cdot T_1 \cdot \operatorname{Diag}\left(F^{(3)}(p,:)\right)\right\} + \mathcal{O}(\Delta^2) \\
&= W_{(d)}^{\mathrm{red}} \cdot \left(\operatorname{diag}\left(F^{(3)}(p,:)\right) \cdot T_1^{\mathrm{T}} \otimes T_1^{-1}\right) \cdot \operatorname{vec}\left\{\Delta S_{3,k}^{\mathrm{rhs}}\right\} + \mathcal{O}(\Delta^2) \\
&= W_{(d)}^{\mathrm{red}} \left(\operatorname{diag}\left(F^{(3)}(p,:)\right) \cdot T_1^{\mathrm{T}} \otimes T_1^{-1}\right) \cdot L_3^{(k)} \cdot n_1 + \mathcal{O}(\Delta^2) \\
&= L_4^{(k)} \cdot n_1 + \mathcal{O}(\Delta^2),
\end{aligned}
\tag{9.58}
$$

where

$$L_4^{(k)} \triangleq W_{(d)}^{\mathrm{red}} \cdot \left(\operatorname{diag}\left(F^{(3)}(p,:)\right) \cdot T_1^{\mathrm{T}} \otimes T_1^{-1}\right) \cdot L_3^{(k)}. \tag{9.59}$$

The expression for each row of $\Delta F^{(3)}$ in Eq. (9.58) can be used to obtain an expression for the vectorization of $\Delta F^{(3)}$. To this end, we use the permutation matrix $Q_{(M_3,d)}$, defined in Eq. (9.42), to express $\operatorname{vec}\left\{\Delta F^{(3)}\right\}$ as

$$
\begin{aligned}
\operatorname{vec}\left\{\Delta F^{(3)}\right\} &= Q_{(M_3,d)}^{\mathrm{T}} \cdot \operatorname{vec}\left\{\Delta F^{(3)^{\mathrm{T}}}\right\} \\
&= Q_{(M_3,d)}^{\mathrm{T}} \cdot \begin{bmatrix} \operatorname{vec}\left\{\Delta F^{(3)}(1,:)\right\} \\ \operatorname{vec}\left\{\Delta F^{(3)}(2,:)\right\} \\ \vdots \\ \operatorname{vec}\left\{\Delta F^{(3)}(M_3,:)\right\} \end{bmatrix}
\end{aligned}
$$

$$= \boldsymbol{Q}_{(M_3,d)}^{\mathrm{T}} \cdot \begin{bmatrix} \boldsymbol{L}_4^{(1)} \\ \boldsymbol{L}_4^{(2)} \\ \vdots \\ \boldsymbol{L}_4^{(M_3)} \end{bmatrix} \cdot \boldsymbol{n}_1 + \mathcal{O}(\Delta^2)$$

$$= \boldsymbol{L}_5 \cdot \boldsymbol{n}_1 + \mathcal{O}(\Delta^2) , \tag{9.60}$$

where

$$\boldsymbol{L}_5 = \boldsymbol{Q}_{(M_3,d)}^{\mathrm{T}} \cdot \begin{bmatrix} \boldsymbol{L}_4^{(1)} \\ \boldsymbol{L}_4^{(2)} \\ \vdots \\ \boldsymbol{L}_4^{(M_3)} \end{bmatrix} . \tag{9.61}$$

Then we insert Eq. (9.60) in Eq. (9.47) to get

$$\mathrm{vec}\left\{ \boldsymbol{F}^{(3)} - (\boldsymbol{F}^{(3)} + \Delta\boldsymbol{F}^{(3)}) \cdot \tilde{\boldsymbol{P}}^{(3)} \cdot \boldsymbol{P}_{\mathrm{opt}}^{(3)} \right\} \approx \boldsymbol{L}_{\boldsymbol{F}_3} \cdot \boldsymbol{n}_1, \tag{9.62}$$

where

$$\boldsymbol{L}_{\boldsymbol{F}_3} = \left(\boldsymbol{I}_d \otimes \boldsymbol{F}^{(3)} \right) \cdot \left(\boldsymbol{K}_3^{-1} \otimes \boldsymbol{I}_d \right) \cdot \boldsymbol{W}_{(d)} \cdot \left[\left(\boldsymbol{I}_d \otimes \boldsymbol{F}^{(1)\mathrm{H}} \right) \cdot \boldsymbol{L}_5 \right] - \boldsymbol{L}_5 . \tag{9.63}$$

The final closed-form rMSFE$_{\boldsymbol{F}_3}$ expression can be approximated to

$$\mathrm{rMSFE}_{\boldsymbol{F}_3} = \frac{\mathrm{tr}\left(\boldsymbol{L}_{\boldsymbol{F}_3} \cdot \boldsymbol{R}_{\mathrm{nn}}^{(1)} \cdot \boldsymbol{L}_{\boldsymbol{F}_3}^{\mathrm{H}} \right)}{\left\| \boldsymbol{F}^{(3)} \right\|_{\mathrm{F}}^2} . \tag{9.64}$$

Similarly, vectorization of the perturbation in the first factor matrix estimate $\Delta\boldsymbol{F}^{(1)}$ is performed by using Eq. (9.36), Eq. (9.57), and Eq. (9.48) as

$$\begin{aligned}
\mathrm{vec}\{\Delta\boldsymbol{F}^{(1)}\} &= \mathrm{vec}\left\{ \Delta\boldsymbol{U}_1^{[\mathrm{s}]} \cdot \boldsymbol{T}_1 + \boldsymbol{U}_1^{[\mathrm{s}]} \cdot \Delta\boldsymbol{T}_1 \right\} + \mathcal{O}(\Delta^2) \\
&= \left(\boldsymbol{I}_d \otimes \boldsymbol{U}_1^{[\mathrm{s}]} \right) \cdot \mathrm{vec}\left\{ \Delta\boldsymbol{T}_1 \right\} + \left(\boldsymbol{T}_1^{\mathrm{T}} \otimes \boldsymbol{I}_{M_1} \right) \cdot \mathrm{vec}\left\{ \Delta\boldsymbol{U}_1^{[\mathrm{s}]} \right\} + \mathcal{O}(\Delta^2) \\
&= \left(\boldsymbol{I}_d \otimes \boldsymbol{U}_1^{[\mathrm{s}]} \right) \cdot \boldsymbol{L}_4 \cdot \boldsymbol{n}_1 + \left(\boldsymbol{T}_1^{\mathrm{T}} \otimes \boldsymbol{I}_{M_1} \right) \cdot \left(\boldsymbol{\Sigma}_1^{[\mathrm{s}]^{-1}} \boldsymbol{V}_1^{[\mathrm{s}]^{\mathrm{T}}} \otimes \boldsymbol{\Gamma}_1^{[\mathrm{n}]} \right) \cdot \boldsymbol{n}_1 + \mathcal{O}(\Delta^2) \\
&= \boldsymbol{L}_6 \cdot \boldsymbol{n}_1 + \mathcal{O}(\Delta^2) , \tag{9.65}
\end{aligned}$$

where

$$\boldsymbol{L}_6 = \left(\boldsymbol{I}_d \otimes \boldsymbol{U}_1^{[\mathrm{s}]} \right) \cdot \boldsymbol{L}_4 + \left(\boldsymbol{T}_1^{\mathrm{T}} \cdot \boldsymbol{\Sigma}_1^{[\mathrm{s}]^{-1}} \boldsymbol{V}_1^{[\mathrm{s}]^{\mathrm{T}}} \otimes \boldsymbol{\Gamma}_1^{[\mathrm{n}]} \right) . \tag{9.66}$$

By inserting Eq. (9.65) in Eq. (9.47), we get

$$\mathrm{vec}\left\{ \boldsymbol{F}^{(1)} - (\boldsymbol{F}^{(1)} + \Delta\boldsymbol{F}^{(1)}) \cdot \tilde{\boldsymbol{P}}^{(1)} \cdot \boldsymbol{P}_{\mathrm{opt}}^{(1)} \right\} \approx \boldsymbol{L}_{\boldsymbol{F}_1} \cdot \boldsymbol{n}_1, \tag{9.67}$$

where

$$\boldsymbol{L}_{\boldsymbol{F}_1} = \left(\boldsymbol{I}_d \otimes \boldsymbol{F}^{(1)}\right) \cdot \left(\boldsymbol{K}_1^{-1} \otimes \boldsymbol{I}_d\right) \cdot \boldsymbol{W}_{(d)} \cdot \left[\left(\boldsymbol{I}_d \otimes \boldsymbol{F}^{(1)\mathrm{H}}\right) \cdot \boldsymbol{L}_6\right] - \boldsymbol{L}_6. \tag{9.68}$$

Now we get the closed-form expression for the first factor matrix rMSFE$_{\boldsymbol{F}_1}$ by

$$\mathrm{rMSFE}_{\boldsymbol{F}_1} = \frac{\mathrm{tr}\left(\boldsymbol{L}_{\boldsymbol{F}_1} \cdot \boldsymbol{R}_{\mathrm{nn}}^{(1)} \cdot \boldsymbol{L}_{\boldsymbol{F}_1}^{\mathrm{H}}\right)}{\left\|\boldsymbol{F}^{(1)}\right\|_{\mathrm{F}}^2}. \tag{9.69}$$

Finally, the vectorization of the perturbation in the second factor matrix estimate $\Delta\boldsymbol{F}^{(2)}$ is achieved by using the obtained expressions for the vectorization of $\Delta\boldsymbol{F}^{(1)}$ (Eq. (9.65)) and $\Delta\boldsymbol{F}^{(3)}$ (Eq. (9.60)) to vectorize $\Delta\boldsymbol{F}^{(2)}$ as

$$
\begin{aligned}
\mathrm{vec}\left\{\Delta\boldsymbol{F}^{(2)}\right\} &= \mathrm{vec}\Big\{[\boldsymbol{\mathcal{N}}]_{(2)} \cdot \left[\boldsymbol{F}^{(3)} \diamond \boldsymbol{F}^{(1)}\right]^{+\mathrm{T}} - \boldsymbol{F}^{(2)} \cdot \Big[\left(\Delta\boldsymbol{F}^{(3)} \diamond \boldsymbol{F}^{(1)}\right) \\
&\quad + \left(\boldsymbol{F}^{(3)} \diamond \Delta\boldsymbol{F}^{(1)}\right)\Big]^{\mathrm{T}} \cdot \left(\boldsymbol{F}^{(3)} \diamond \boldsymbol{F}^{(1)}\right)^{+\mathrm{T}}\Big\} + \mathcal{O}(\Delta^2) \\
&= \left(\left(\boldsymbol{F}^{(3)} \diamond \boldsymbol{F}^{(1)}\right)^+ \otimes \boldsymbol{I}_{M_2}\right) \cdot \boldsymbol{P}_{(M_1,M_2,M_3)}^{(2)} \cdot \boldsymbol{n}_1 \\
&\quad - \left(\left(\boldsymbol{F}^{(3)} \diamond \boldsymbol{F}^{(1)}\right)^+ \otimes \boldsymbol{F}^{(2)}\right) \cdot \boldsymbol{Q}_{(M_1 \cdot M_2, d)} \cdot \left[\mathrm{vec}\left\{\Delta\boldsymbol{F}^{(3)} \diamond \boldsymbol{F}^{(1)}\right\} + \mathrm{vec}\left\{\boldsymbol{F}^{(3)} \diamond \Delta\boldsymbol{F}^{(1)}\right\}\right] \\
&\quad + \mathcal{O}(\Delta^2).
\end{aligned}
\tag{9.70}
$$

The following relation for two matrices $\boldsymbol{X} = [\boldsymbol{x}_1, \boldsymbol{x}_2, \ldots, \boldsymbol{x}_d] \in \mathbb{C}^{M_1 \times d}$ and $\boldsymbol{Y} = [\boldsymbol{y}_1, \boldsymbol{y}_2, \ldots, \boldsymbol{y}_d] \in \mathbb{C}^{M_2 \times d}$ can easily be verified for the vectorization of Khatri-Rao products.

$$\mathrm{vec}\left\{\boldsymbol{X} \diamond \boldsymbol{Y}\right\} = \boldsymbol{G}(\boldsymbol{X}, M_2) \cdot \mathrm{vec}\{\boldsymbol{Y}\} = \boldsymbol{H}(\boldsymbol{Y}, M_1) \cdot \mathrm{vec}\{\boldsymbol{X}\}, \tag{9.71}$$

where

$$
\boldsymbol{G}(\boldsymbol{X}, M_2) \triangleq \begin{bmatrix} (\boldsymbol{x}_1 \otimes \boldsymbol{I}_{M_2}) \cdot \left(\boldsymbol{e}_{d,1}^{\mathrm{T}} \otimes \boldsymbol{I}_{M_2}\right) \\ (\boldsymbol{x}_2 \otimes \boldsymbol{I}_{M_2}) \cdot \left(\boldsymbol{e}_{d,2}^{\mathrm{T}} \otimes \boldsymbol{I}_{M_2}\right) \\ \vdots \\ (\boldsymbol{x}_d \otimes \boldsymbol{I}_{M_2}) \cdot \left(\boldsymbol{e}_{d,d}^{\mathrm{T}} \otimes \boldsymbol{I}_{M_2}\right) \end{bmatrix}
$$

$$
\boldsymbol{H}(\boldsymbol{Y}, M_1) \triangleq \begin{bmatrix} (\boldsymbol{I}_{M_1} \otimes \boldsymbol{y}_1) \cdot \left(\boldsymbol{e}_{d,1}^{\mathrm{T}} \otimes \boldsymbol{I}_{M_1}\right) \\ (\boldsymbol{I}_{M_1} \otimes \boldsymbol{y}_2) \cdot \left(\boldsymbol{e}_{d,2}^{\mathrm{T}} \otimes \boldsymbol{I}_{M_1}\right) \\ \vdots \\ (\boldsymbol{I}_{M_1} \otimes \boldsymbol{y}_d) \cdot \left(\boldsymbol{e}_{d,d}^{\mathrm{T}} \otimes \boldsymbol{I}_{M_1}\right) \end{bmatrix}.
$$

In order to apply the relation in Eq. (9.71) to Eq. (9.70), we define $\boldsymbol{f}_l^{(r)}$ to be the l-th column of the r-th factor matrix $\boldsymbol{F}^{(r)}$ which implies that $\boldsymbol{f}_l^{(r)} = \boldsymbol{F}^{(r)}(:, l)$. Therefore, by applying the relation in Eq. (9.71)

to vec $\left\{ \Delta \boldsymbol{F}^{(3)} \diamond \boldsymbol{F}^{(1)} \right\}$ we get

$$\text{vec}\left\{\Delta \boldsymbol{F}^{(3)} \diamond \boldsymbol{F}^{(1)}\right\} = \boldsymbol{H}(\boldsymbol{F}^{(1)}, M_3) \cdot \text{vec}\left\{\Delta \boldsymbol{F}^{(3)}\right\}. \tag{9.72}$$

In the same manner, we apply the relation in Eq. (9.71) to vec $\left\{ \boldsymbol{F}^{(3)} \diamond \Delta \boldsymbol{F}^{(1)} \right\}$, leading to

$$\text{vec}\left\{\boldsymbol{F}^{(3)} \diamond \Delta \boldsymbol{F}^{(1)}\right\} = \boldsymbol{G}(\boldsymbol{F}^{(3)}, M_1) \cdot \text{vec}\left\{\Delta \boldsymbol{F}^{(1)}\right\}. \tag{9.73}$$

Furthermore, we use the results from Eq. (9.72) and Eq. (9.73), as well as from Eq. (9.65) and Eq. (9.60), in Eq. (9.70) to get

$$\text{vec}\left\{\Delta \boldsymbol{F}^{(2)}\right\} = \boldsymbol{L}_7 \cdot \boldsymbol{n}_1 + \mathcal{O}(\Delta^2), \tag{9.74}$$

where

$$\boldsymbol{L}_7 = \left(\left(\boldsymbol{F}^{(3)} \diamond \boldsymbol{F}^{(1)} \right)^{+} \otimes \boldsymbol{I}_{M_2} \right) \cdot \boldsymbol{P}^{(2)}_{(M_1, M_2, M_3)}$$

$$\quad - \left(\left(\boldsymbol{F}^{(3)} \diamond \boldsymbol{F}^{(1)} \right)^{+} \otimes \boldsymbol{F}^{(2)} \right) \cdot \boldsymbol{Q}_{(M_1 \cdot M_3, d)} \cdot \left(\boldsymbol{H}(\boldsymbol{F}^{(1)}, M_3) \cdot \boldsymbol{L}_5 + \boldsymbol{G}(\boldsymbol{F}^{(3)}, M_1) \cdot \boldsymbol{L}_6 \right). \tag{9.75}$$

By using the obtained expressions for Eq. (9.74) in Eq. (9.47), we get

$$\text{vec}\left\{\boldsymbol{F}^{(2)} - (\boldsymbol{F}^{(2)} + \Delta \boldsymbol{F}^{(2)}) \cdot \tilde{\boldsymbol{P}}^{(2)} \cdot \boldsymbol{P}^{(2)}_{\text{opt}}\right\} \approx \boldsymbol{L}_{\boldsymbol{F}_2} \cdot \boldsymbol{n}_1, \tag{9.76}$$

where

$$\boldsymbol{L}_{\boldsymbol{F}_2} = \left(\boldsymbol{I}_d \otimes \boldsymbol{F}^{(2)} \right) \cdot \left(\boldsymbol{K}_2^{-1} \otimes \boldsymbol{I}_d \right) \cdot \boldsymbol{W}_{(d)} \cdot \left[\left(\boldsymbol{I}_d \otimes \boldsymbol{F}^{(2)\text{H}} \right) \cdot \boldsymbol{L}_7 \right] - \boldsymbol{L}_7. \tag{9.77}$$

Finally, the closed-form expression for the second factor matrix rMSFE$_{\boldsymbol{F}_2}$ is approximated by

$$\text{rMSFE}_{\boldsymbol{F}_2} = \frac{\text{tr}\left(\boldsymbol{L}_{\boldsymbol{F}_2} \cdot \boldsymbol{R}^{(1)}_{\text{nn}} \cdot \boldsymbol{L}^{\text{H}}_{\boldsymbol{F}_2} \right)}{\left\| \boldsymbol{F}^{(2)} \right\|^2_{\text{F}}}. \tag{9.78}$$

Note that we have performed this first order perturbation analysis on the 3-mode rhs solution as shown in Table 9.1, where rMSFE$^{(1)} \approx$ rMSFE$_{\boldsymbol{F}_1}$, rMSFE$^{(2)} \approx$ rMSFE$_{\boldsymbol{F}_2}$, and rMSFE$^{(3)} \approx$ rMSFE$_{\boldsymbol{F}_3}$. Nevertheless, the 1-mode and 2-mode rhs estimates can be obtained by applying the SECSI framework on the 3-mode (i.e., Table 9.1) to the permuted versions of the input tensor $\boldsymbol{\mathcal{X}}$. In the same manner, the rMSFE$^{(r)}$ for the 1-mode and 2-mode rhs estimates can also be approximated, by applying this performance analysis framework on the permuted versions of the noiseless input tensor $\boldsymbol{\mathcal{X}}_0$, as shown in Table 9.2.

	3-mode	2-mode	1-mode
input	$\boldsymbol{\mathcal{X}}$	$\mathrm{perm}(\boldsymbol{\mathcal{X}}, [2,3,1])$	$\mathrm{perm}(\boldsymbol{\mathcal{X}}, [1,3,2])$
$\mathrm{rMSFE}^{(1)}$	$\mathrm{rMSFE}_{\boldsymbol{F}_1}$	$\mathrm{rMSFE}_{\boldsymbol{F}_3}$	$\mathrm{rMSFE}_{\boldsymbol{F}_1}$
$\mathrm{rMSFE}^{(2)}$	$\mathrm{rMSFE}_{\boldsymbol{F}_2}$	$\mathrm{rMSFE}_{\boldsymbol{F}_1}$	$\mathrm{rMSFE}_{\boldsymbol{F}_3}$
$\mathrm{rMSFE}^{(3)}$	$\mathrm{rMSFE}_{\boldsymbol{F}_3}$	$\mathrm{rMSFE}_{\boldsymbol{F}_2}$	$\mathrm{rMSFE}_{\boldsymbol{F}_2}$

Table 9.2.: $\mathrm{rMSFE}^{(r)}$ from Eq. (9.45) approximation, using eqs. (9.69) (9.78) (9.64), for the different r-modes of SECSI

9.5. Extensions

9.5.1. Extension to the 3-mode LHS

In this section, we extend the obtained results for the rhs estimates to the lhs estimates. We first describe the main differences between the rhs and lhs third mode estimates, and later redefine the performance analysis framework accordingly. Note that, since there are no significant changes for computing the lhs estimates, when compared to the rhs case, we can reuse most of the expressions obtained in Section 9.4 for this extension to the lhs.

For computing the lhs estimates, the matrices $\boldsymbol{S}_{3,k}^{\mathrm{lhs}}$ from Eq. (9.24) are used as input to the JEVD problem, instead of the matrices $\boldsymbol{S}_{3,k}^{\mathrm{rhs}}$ from Eq. (9.23). This leads to a redefinition of the matrices $\boldsymbol{K}_3^{(k)}$ and $\boldsymbol{L}_3^{(k)}$ that appear in the vectorization of $\boldsymbol{S}_{3,k}^{\mathrm{rhs}}$ (Eq. (9.54)), in the rhs case, and now are used to express the vectorization of $\boldsymbol{S}_{3,k}^{\mathrm{lhs}}$ as $\mathrm{vec}\left\{\boldsymbol{S}_{3,k}^{\mathrm{lhs}}\right\} = \boldsymbol{L}_{3,\mathrm{lhs}}^{(k)} \cdot \boldsymbol{n}_1$, where

$$\boldsymbol{L}_{3,\mathrm{lhs}}^{(k)} = \boldsymbol{Q}_{d,d}^T \cdot (\boldsymbol{I}_d \otimes \boldsymbol{S}_{3,p}^{-1}) \cdot \boldsymbol{L}_2^{(k)} - (\boldsymbol{S}_{3,k}^T \cdot \boldsymbol{S}_{3,p}^{-\mathrm{T}} \otimes \boldsymbol{S}_{3,p}^{-1}) \cdot \boldsymbol{L}_2^{(p)}. \tag{9.79}$$

The calculation of a JEVD for the slices $\hat{\boldsymbol{S}}_{3,k}^{\mathrm{lhs}}$ in Eq. (9.24) results in the estimation of the transformation matrix $\boldsymbol{T}_2$, instead of $\boldsymbol{T}_1$. Therefore, this leads to a different way of estimating the factor matrices, as defined in Table 9.1. For instance, $\boldsymbol{F}^{(1)}$ is estimated via a LS-fit and $\boldsymbol{F}^{(2)}$ is now estimated from $\boldsymbol{T}_2$. These changes lead to a redefinition of $\boldsymbol{L}_6$ that is similar to the definition of $\boldsymbol{L}_7$ for the rhs (Eq. (9.75)). Therefore, we refer to it as

$$\boldsymbol{L}_{7,\mathrm{lhs}} = \left(\boldsymbol{I}_d \otimes \boldsymbol{U}_2^{[\mathrm{s}]}\right) \cdot \boldsymbol{L}_4 + \left(\boldsymbol{T}_2^{\mathrm{T}} \cdot \boldsymbol{\Sigma}_2^{[\mathrm{s}]^{-1}} \boldsymbol{V}_2^{[\mathrm{s}]^{\mathrm{T}}} \otimes \boldsymbol{\Gamma}_2^{[\mathrm{n}]}\right). \tag{9.80}$$

In the same manner, $\boldsymbol{L}_7$ for the rhs is also redefined for the lhs as

$$\begin{aligned}
\boldsymbol{L}_{6,\mathrm{lhs}} =& \left(\left(\boldsymbol{F}^{(2)} \diamond \boldsymbol{F}^{(3)}\right)^+ \otimes \boldsymbol{I}_{M_1}\right) \cdot \boldsymbol{P}_{(M_1,M_2,M_3)}^{(1)} \\
&- \left(\left(\boldsymbol{F}^{(2)} \diamond \boldsymbol{F}^{(3)}\right)^+ \otimes \boldsymbol{F}^{(1)}\right) \cdot \boldsymbol{Q}_{(M_2 \cdot M_3, d)} \cdot \left(\boldsymbol{G}(\boldsymbol{F}^{(2)}, M_3) \cdot \boldsymbol{L}_5 + \boldsymbol{H}(\boldsymbol{F}^{(3)}, M_2) \cdot \boldsymbol{L}_7\right). \quad (9.81)
\end{aligned}$$

Finally, a summary of the third mode rhs and lhs performance analysis is shown in Table 9.3 and Table 9.4, respectively. Note that only steps 4 ($\boldsymbol{L}_3^{(k)}$), 8 ($\boldsymbol{L}_6$), and 9 ($\boldsymbol{L}_7$) are changed from the rhs to the lhs performance analysis. Once the matrices $\boldsymbol{L}_5$, $\boldsymbol{L}_6$, and $\boldsymbol{L}_7$ have been calculated, then the matrices $\boldsymbol{L}_{\boldsymbol{F}_1}$, $\boldsymbol{L}_{\boldsymbol{F}_1}$, $\boldsymbol{L}_{\boldsymbol{F}_1}$ are calculated for both lhs and rhs by using Eq. (9.67), Eq. (9.76), and Eq. (9.62), respectively.

Finally, the rMSFE expressions for the lhs and rhs factor matrices are calculated by using Eq. (9.69), Eq. (9.78), and Eq. (9.64). Moreover the lhs rMSFE$^{(r)}$ expressions in the other modes (i.e., 1-mode and 2-mode) can be approximated in the same manner as in Section 9.4 by applying this first order performance analysis to permuted versions of the noiseless tensor $\boldsymbol{\mathcal{X}}_0$, as shown in Table 9.2.

9.5.2. Extension to the underdetermined (degenerate) case

In this work, we have assumed the non-degenerate case, but the results can also be applied to the underdetermined (degenerate) case. The decomposition is underdetermined in mode n if $d > M_n$. The SECSI framework is still applicable if the problem is underdetermined in up to one mode [RH13]. For example, let the tensor rank of the noiseless tensor be greater than any one of the dimension, i.e., $M_1 < d \leq \min\{M_2, M_3\}$. In this case, $\boldsymbol{F}^{(1)} \in \mathbb{C}^{M_1 \times d}$ is a flat matrix. But $\boldsymbol{U}_1$ has the dimension of $M_1 \times M_1$. Therefore, $\boldsymbol{T}_1$ does not exist. However, the diagonalization problems $\boldsymbol{S}_{1,k}^{\mathrm{rhs}}$ and $\boldsymbol{S}_{1,k}^{\mathrm{lhs}}$ in Fig. 9.1 can still be solved and yield two estimates for $\boldsymbol{F}^{(1)}$, one for $\boldsymbol{F}^{(2)}$, and one for $\boldsymbol{F}^{(3)}$.

9.6. A Performance Analysis based Factor Matrix Estimates Selection Scheme

In this section we propose a new estimates selection scheme for the SECSI framework. We refer to this new scheme as Performance Analysis based Selection (PAS). Unlike other selection schemes for the final matrix estimates proposed in [RH13], such as CON-PS (conditioning number - paired solutions), REC-PS (reconstruction error - paired solutions), and BM (best matching), which perform a heuristic selection or an exhaustive search (BM) to select the final estimates, this new selection scheme allows us to directly select one estimate per factor matrix (instead of performing a search among all the possible estimate combinations). For instance, the BM scheme tests all possible combinations of the estimates of the loading matrices in an exhaustive search. It therefore requires the reconstruction of $(R \cdot (R-1))^R$ tensors [RH13], which grows rapidly with R and already reaches 216 for $R = 3$, whereas the PAS scheme requires only 18 estimates for $R = 3$.

All the analytical expressions in the performance analysis are computed from the noiseless estimates (such as $\boldsymbol{\mathcal{X}}_0, \boldsymbol{U}_r^{[\mathrm{s}]}, \boldsymbol{S}^{[\mathrm{s}]}$, etc.). For the PAS scheme, we approximate the noiseless quantities with the noisy ones as $\boldsymbol{\mathcal{X}}_0 \approx \hat{\boldsymbol{\mathcal{X}}}, \boldsymbol{U}_r^{[\mathrm{s}]} \approx \hat{\boldsymbol{U}}_r^{[\mathrm{s}]}, \boldsymbol{S}^{[\mathrm{s}]} \approx \hat{\boldsymbol{S}}^{[\mathrm{s}]}$, etc. Then, we use the corresponding performance analysis and assume perfect knowledge of the second order moments of the noise (i.e., $\boldsymbol{R}_{\mathrm{nn}}^{(r)}$ and $\boldsymbol{C}_{\mathrm{nn}}^{(r)}$), to estimate rMSFE$^{(r)}$ for all $r = 1, 2, 3$, in all the r-mode lhs and rhs solutions. Finally, we select the estimates that correspond to the smallest estimated rMSFE$^{(r)}$ values, for all $r = 1, 2, 3$. Note that estimating the noise variance has no effect on this scheme, since all the estimated rMSFE$^{(r)}$ values are multiplied by the same σ_N^2 factor.

vec{·}	compute
$[\Delta \mathcal{S}^{[s]}]_{(1)}$	$\mathbf{L}_0 = \left(\mathbf{U}_2^{[s]\mathrm{H}} \otimes \mathbf{U}_3^{[s]\mathrm{H}} \otimes \mathbf{U}_1^{[s]\mathrm{H}} \right)$
$[\Delta \mathcal{S}_3^{[s]}]_{(1)}$	$\mathbf{L}_1 = \mathbf{P}_{(d,d,M_3)}^{(3)\mathrm{T}} \cdot \left(\mathbf{I}_{d^2} \otimes \mathbf{U}_3^{[s]} \right) \cdot \mathbf{P}_{(d,d,d)}^{(3)} \cdot \mathbf{L}_0 + \mathbf{P}_{(d,d,M_3)}^{(3)} \cdot \left([\mathbf{S}^{[s]}]_{(3)}^{\mathrm{T}} \cdot \mathbf{\Sigma}_3^{[s]^{-1}} \mathbf{V}_3^{[s]\mathrm{T}} \otimes \mathbf{\Gamma}_3^{[n]\mathrm{T}} \right) \cdot \mathbf{P}_{(M_1,M_2,M_3)}^{(3)}$
$\Delta \mathbf{S}_{3,k}$	$\mathbf{L}_2^{(k)} = \left(\mathbf{I}_d \otimes \mathbf{e}_{M_3,k}^{\mathrm{T}} \otimes \mathbf{I}_d \right) \cdot \mathbf{L}_1$
$\Delta \mathbf{S}_{3,k}^{\mathrm{rhs}}$	$\mathbf{L}_3^{(k)} = \left(\mathbf{S}_{3,p}^{-\mathrm{T}} \otimes \mathbf{I}_d \right) \cdot \mathbf{L}_2^{(k)} - \left(\mathbf{S}_{3,p}^{-\mathrm{T}} \otimes \mathbf{S}_{3,k} \cdot \mathbf{S}_{3,p}^{-1} \right) \cdot \mathbf{L}_2^{(p)}$
Stack $\mathbf{s}_k$	$\mathbf{L}_3 = \left[\mathbf{L}_3^{(1)} \; \mathbf{L}_3^{(2)} \ldots \mathbf{L}_3^{(M_3)} \right]^T$
$\Delta \mathbf{T}_1$	$\mathbf{L}_4 = -\mathbf{A}^+ \cdot \mathbf{B} \cdot \mathbf{L}_3$
$\Delta \mathbf{F}^{(3)}(k,:)$	$\mathbf{L}_4^{(k)} = \mathbf{W}_{(d)}^{\mathrm{red}} \cdot \left(\mathrm{diag}\left(\mathbf{F}^{(3)}(p,:) \right) \cdot \mathbf{T}_1^{\mathrm{T}} \otimes \mathbf{T}_1^{-1} \right) \cdot \mathbf{L}_3^{(k)}$
$\Delta \mathbf{F}^{(3)}$	$\mathbf{L}_5 = \mathbf{Q}_{(M_3,d)}^{\mathrm{T}} \cdot \begin{bmatrix} \mathbf{L}_4^{(1)} \\ \vdots \\ \mathbf{L}_4^{(M_3)} \end{bmatrix} \qquad \forall k = 1, 2, \cdots, M_3$
$\Delta \mathbf{F}^{(1)}$	$\mathbf{L}_6 = \left(\mathbf{I}_d \otimes \mathbf{U}_1^{[s]} \right) \cdot \mathbf{L}_4 + \left(\mathbf{T}_1^{\mathrm{T}} \cdot \mathbf{\Sigma}_1^{[s]^{-1}} \mathbf{V}_1^{[s]\mathrm{T}} \otimes \mathbf{\Gamma}_1^{[n]} \right)$
$\Delta \mathbf{F}^{(2)}$	$\mathbf{L}_7 = \left(\left(\mathbf{F}^{(3)} \diamond \mathbf{F}^{(1)} \right)^+ \otimes \mathbf{I}_{M_2} \right) \cdot \mathbf{P}_{(M_1,M_2,M_3)}^{(2)} \cdot \mathbf{Q}_{(M_1 \cdot M_3, d)} \cdot \left(\mathbf{H}(\mathbf{F}^{(1)}, M_3) \cdot \mathbf{L}_5 + \mathbf{G}(\mathbf{F}^{(3)}, M_1) \cdot \mathbf{L}_6 \right)$

Table 9.3.: 3-mode rhs performance analysis of SECSI.

vec{·}	compute
$[\Delta\bm{S}^{[\mathrm{s}]}]_{(1)}$	$\bm{L}_0 = \left(\bm{U}_2^{[\mathrm{s}]\mathrm{H}} \otimes \bm{U}_3^{[\mathrm{s}]\mathrm{H}} \otimes \bm{U}_1^{[\mathrm{s}]\mathrm{H}}\right)$
$[\Delta\bm{S}_3^{[\mathrm{s}]}]_{(1)}$	$\bm{L}_1 = \bm{P}_{(d,d,M_3)}^{(3)\mathrm{T}} \cdot \bm{P}_{(d,d,d)}^{(3)} \cdot \bm{L}_0 + \bm{P}_{(d,d,M_3)}^{(3)\mathrm{T}} \cdot \left([\bm{S}^{[\mathrm{s}]}]_{(3)}^{\mathrm{T}} \cdot \bm{\Sigma}_3^{[\mathrm{s}]-1} \bm{V}_3^{[\mathrm{s}]\mathrm{T}} \otimes \bm{\Gamma}_3^{[\mathrm{n}]}\right) \cdot \bm{P}_{(M_1,M_2,M_3)}^{(3)}$
$\Delta\bm{S}_{3,k}$	$\bm{L}_2^{(k)} = \left(\bm{I}_d \otimes \bm{e}_{M_3,k}^{\mathrm{T}} \otimes \bm{I}_d\right) \cdot \bm{L}_1$
$\Delta S_{3,k}^{\mathrm{lhs}}$	$\bm{L}_3^{(k)} = \bm{Q}_{d,d}^{\mathrm{T}} \cdot \left(\bm{I}_d \otimes \bm{S}_{3,p}^{-1}\right) \cdot \bm{L}_2^{(k)} - \left(\bm{S}_{3,k}^{\mathrm{T}} \cdot \bm{S}_{3,p}^{-\mathrm{T}} \otimes \bm{S}_{3,p}^{-1}\right) \cdot \bm{L}_2^{(p)}$
Stack $\bm{s}_k$	$\bm{L}_3 = \left[\bm{L}_3^{(1)} \ \ \bm{L}_3^{(2)} \ldots \bm{L}_3^{(M_3)}\right]^{\mathrm{T}}$
$\Delta\bm{T}_1$	$\bm{L}_4 = -\bm{A}^+ \cdot \bm{B} \cdot \bm{L}_3$
$\Delta\bm{F}^{(3)}(k,:)$	$\bm{L}_4^{(k)} = \bm{W}_{(d)}^{\mathrm{red}} \cdot \left(\mathrm{diag}\left(\bm{F}^{(3)}(p,:)\right) \cdot \bm{T}_1^{\mathrm{T}} \otimes \bm{T}_1^{-1}\right) \cdot \bm{L}_3^{(k)}$
$\Delta\bm{F}^{(3)}$	$\bm{L}_5 = \bm{Q}_{(M_3,d)}^{\mathrm{T}} \cdot \begin{bmatrix} \bm{L}_4^{(1)} \\ \vdots \\ \bm{L}_4^{(M_3)} \end{bmatrix} \qquad \forall k = 1,2,\cdots,M_3$
$\Delta\bm{F}^{(1)}$	$\bm{L}_6 = \left(\left(\bm{F}^{(2)} \diamond \bm{F}^{(3)}\right)^+ \otimes \bm{I}_{M_1}\right) \cdot \bm{P}_{(M_1,M_2,M_3)}^{(1)} - \left(\left(\bm{F}^{(2)} \diamond \bm{F}^{(3)}\right)^+ \otimes \bm{F}^{(1)}\right) \cdot \bm{Q}_{(M_2\cdot M_3,d)} \cdot \left(\bm{G}(\bm{F}^{(2)}, M_3) \cdot \bm{L}_5 + \bm{H}(\bm{F}^{(3)}, M_2) \cdot \bm{L}_7\right)$
$\Delta\bm{F}^{(2)}$	$\bm{L}_7 = \left(\bm{I}_d \otimes \bm{U}_2^{[\mathrm{s}]}\right) \cdot \bm{L}_4 + \left(\bm{T}_2^{\mathrm{T}} \cdot \bm{\Sigma}_2^{[\mathrm{s}]-1} \bm{V}_2^{[\mathrm{s}]\mathrm{T}} \otimes \bm{\Gamma}_2^{[\mathrm{n}]}\right)$

Table 9.4.: 3-mode lhs performance analysis of SECSI. The matrix $\bm{L}_6$ is always used for $\Delta\bm{F}^{(1)}$. Similarly $\bm{L}_7$ is always used for $\Delta\bm{F}^{(2)}$. Note that only matrices $\bm{L}_3^{(k)}$, $\bm{L}_6$, and $\bm{L}_7$ are changed from the rhs to the lhs performance analysis.

9.7. Simulation Results

In this section, we validate the resulting analytical expressions with empirical simulations. First we compare the results for the proposed analytical framework to the empirical results. Then, we compare the performance of the PAS selection scheme with other estimates selection schemes.

9.7.1. Performance Analysis Simulations

We define three simulation scenarios, where the properties of the noiseless tensor $\boldsymbol{\mathcal{X}}_0$ and the number of trials used for every point of the simulation are stated in Table 9.5.

Scenario	Size	d	$\boldsymbol{F}^{(r)}$ Correlation	Trials
I	$5 \times 5 \times 5$	4	(none)	$10{,}000$
II	$5 \times 8 \times 7$	4	$r = 1$	$10{,}000$
III	$3 \times 15 \times 70$	3	(none)	$5{,}000$

Table 9.5.: Scenarios for varying SNR simulations.

In scenario I and scenario III, we have used real-valued tensors while complex-valued tensors are used for scenario II. Moreover, to further illustrate the robustness of our performance analysis results, we have used different JEVDs algorithms for both scenarios. We employ the JDTM algorithm [LA10] for scenario I while the coupled JEVD [RLM16] is employed for scenario II. Note that both algorithms are based on the indirect LS cost function [BCW$^+$17]. For every trial, the noise tensor $\boldsymbol{\mathcal{N}}$ is randomly generated and has zero-mean Gaussian entries of variance $\sigma_N^2 = \|\boldsymbol{\mathcal{X}}_0\|_{\mathrm{H}}^2/(\mathrm{SNR}{\cdot}M)$. Moreover, the noiseless tensor $\boldsymbol{\mathcal{X}}_0$ is fixed in each the experiment and has zero-mean uncorrelated Gaussian entries on its factor matrices $\boldsymbol{F}^{(r)}$. We plot several realizations of the experiments (therefore different $\boldsymbol{\mathcal{X}}_0$) on top of each other, to provide better insights about the performance of the tested algorithms. This simulation setup is selected, since the derived analytical expression depicts the rMSFE for a known noiseless tensor $\boldsymbol{\mathcal{X}}_0$ over several noise trials. Moreover, every realization of the noiseless tensor $\boldsymbol{\mathcal{X}}_0$ is given by $\boldsymbol{\mathcal{X}}_0 = \boldsymbol{\mathcal{I}}_{3,d} \times_1 \boldsymbol{F}^{(1)} \times_2 \boldsymbol{F}^{(2)} \times_3 \boldsymbol{F}^{(3)}$, where the factor matrices $\boldsymbol{F}^{(r)} \in \mathbb{R}^{M_r \times d}$ have uncorrelated Gaussian entries for all $r = 1, 2, 3$ for scenario I. Furthermore, for scenario II, we also introduce correlation in the factor matrix $\boldsymbol{F}^{(1)}$. In this scenario, the factor matrices $\boldsymbol{F}^{(2)}$ and $\boldsymbol{F}^{(3)}$ are randomly drawn but $\boldsymbol{F}^{(1)}$ is fixed along the experiments as

$$\boldsymbol{F}^{(1)} = \begin{bmatrix} 1 & 1 & 1 & 1 \\ 1 & 0.95 & 0.95 & 0.95 \\ 1 & 0.95 & 1 & 1 \\ 1 & 1 & 0.95 & 1 \\ 0.95 & 1 & 1 & 1 \end{bmatrix}. \tag{9.82}$$

We depict the results in the form of the Total rMSFE (TrMSFE) since it reflects the total factor matrix estimation accuracy of the tested algorithms. The TrMSFE is defined as $\mathrm{TrMSFE} = \sum_{r=1}^{3} \mathrm{rMSFE}^{(r)}$ where $\mathrm{rMSFE}^{(r)}$ is the same as in Eq. (9.45).

It is evident from the results in Fig. 9.2 that the analytical results from the proposed first-order

perturbation analysis match well with the Monte-Carlo simulations for both real and complex-valued tensors. Moreover, the results also show an excellent match to the empirical simulations for scenario II where we have an asymmetric tensor and also have high correlation in the first factor matrix.

In Fig. 9.3, we show the analytical and empirical results for the asymmetric scenario III where the results are shown for 6 estimates of each factor matrix obtained by solving all of the r-modes for a SNR = 50 dB. The estimates are arranged according to Fig. 9.1. The results show an excellent match for emiprical and analytical results for all of 6 estimates for each factor matrix. Moreover, the estimates $\boldsymbol{F}_{\mathrm{IV}}^{(1)}$, $\boldsymbol{F}_{\mathrm{V}}^{(1)}$, $\boldsymbol{F}_{\mathrm{IV}}^{(2)}$, $\boldsymbol{F}_{\mathrm{V}}^{(2)}$, $\boldsymbol{F}_{\mathrm{I}}^{(3)}$, and $\boldsymbol{F}_{\mathrm{II}}^{(3)}$ are the best estimates for each of the factor matrices. Note that all of these estimates are obtained by solving the JEVD problem for the 3-mode in Eq. (9.23) and Eq. (9.24). This results from the fact that JEVD for this mode has the highest number of slices (70) which results in a better accuracy.

9.7.2. SECSI framework based on PAS scheme

In this section, we compare the performance of the PAS scheme with other selection schemes, such as the CON-PS, REC-PS, and BM schemes from [RH13] for two simulation scenarios in Table 9.6.

Scenario	Size	SNR	d	$\boldsymbol{F}^{(r)}$ Correlation	Trials
IV	$5 \times 5 \times 5$	50 dB	3	(none)	$10,000$
V	$3 \times 15 \times 70$	40 dB	3	(none)	$5,000$

Table 9.6.: Scenarios for fixed SNR simulations.

In these simulation setups, the noise tensor $\boldsymbol{\mathcal{N}}$ as well as the noiseless tensor $\boldsymbol{\mathcal{X}}_0$ are randomly generated at every trial. Since the noise variance has no effect on the selected estimate, for the real-valued uncorrelated noise with equal variance scenario, we use $\boldsymbol{R}_{\mathrm{nn}}^{(r)} = \boldsymbol{I}_M$ and $\boldsymbol{C}_{\mathrm{nn}}^{(r)} = \boldsymbol{I}_M$, for all $r = 1, 2, 3$, as input for this PAS scheme, regardless of the value of σ_N^2. Moreover, to provide more insights about the performance, we also define a naive selection scheme denoted as DUMMYR, where the final estimates are randomly selected among the 6 possible estimates available per factor matrix. We use the complementary cumulative density function (CCDF) of the TrMSFE to illustrate the robustness of the selected strategy [RH13].

The results are shown in Fig. 9.4 for two scenarios with different tensor sizes. The results show that the proposed PAS scheme outperforms the other schemes especially in scenario IV where the tensor size is small and the SNR is also high. This is to be expected, since the expressions used to build the PAS scheme are based on the high SNR assumption. Nevertheless, we also observe that even with the higher dimensional tensor and relatively low SNR, as shown in Fig. 9.4(b), we observe that the PAS scheme performs slightly better than the CON-PS, REC-PS, and BM schemes.

9.8. Conclusion

In this chapter, a first-order perturbation analysis of the SECSI framework for the approximate CPD of 3-D noise-corrupted low-rank tensors is presented, where we provide closed-form expressions for the relative

mean square error for each of the estimated factor matrices. The derived expressions are formulated in terms of the second-order moments of the noise, such that apart from a zero-mean, no assumptions on the noise statistics are required. The simulation results depict the excellent match between the closed-form expressions and the empirical results for both real-valued and complex-valued data. Moreover, these expressions can also be used for an enhancement in the factor matrix estimates selection step of the SECSI framework. The new PAS selection scheme outperforms the existing schemes especially at high SNR values.
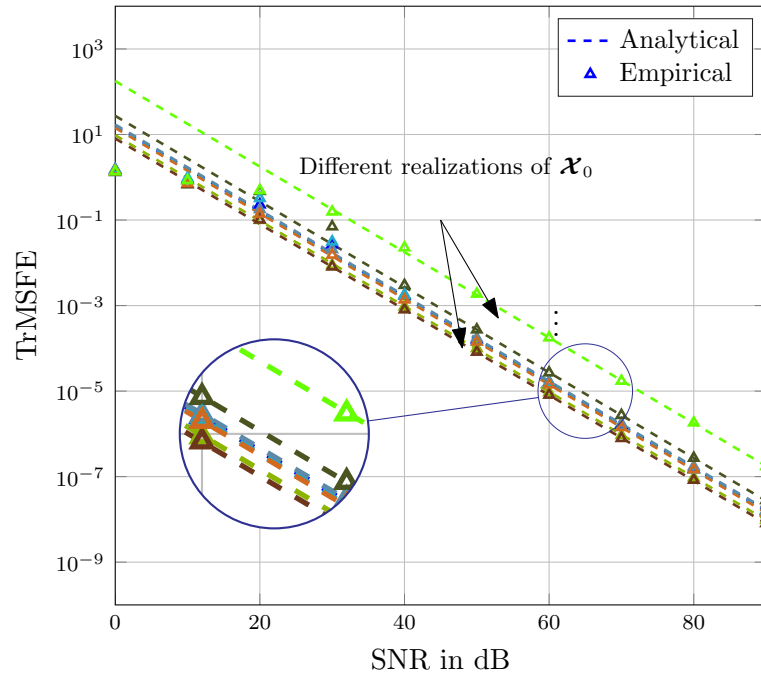
(a) Scenario I
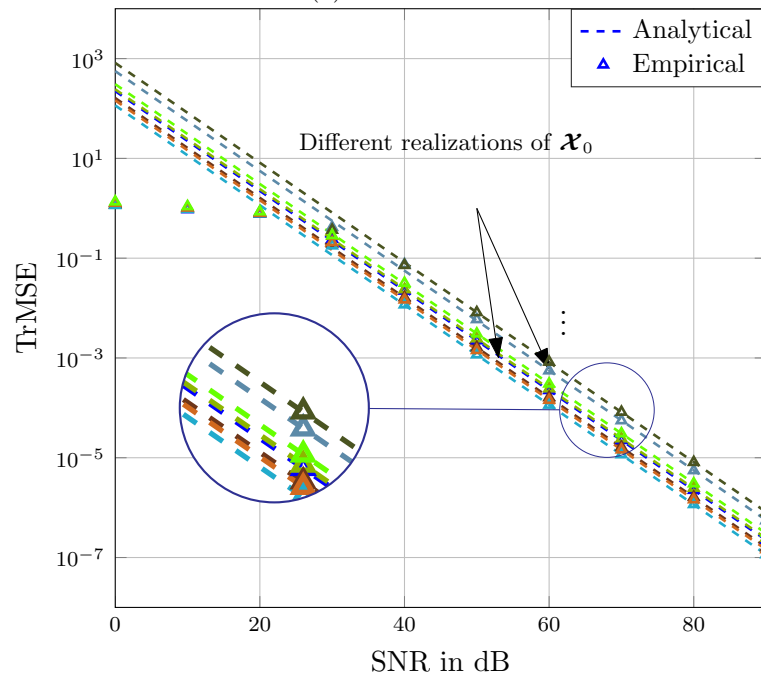
(b) Scenario II

Figure 9.2.: TrMSFE of the 3-mode rhs estimates using the SECSI framework in scenarios I and II
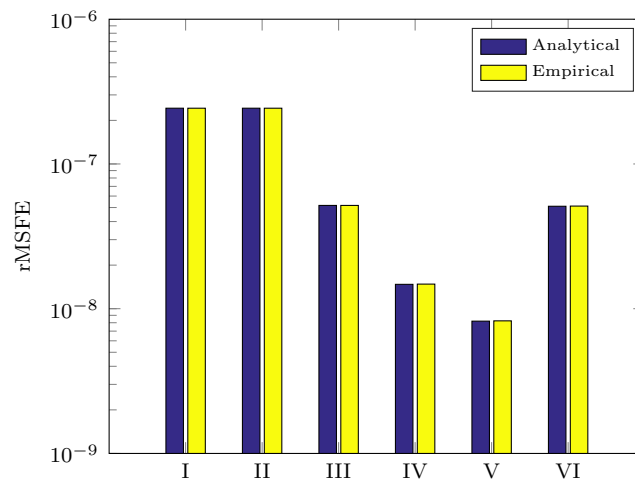
(a) 6 estimates of $\boldsymbol{F}^{(1)}$
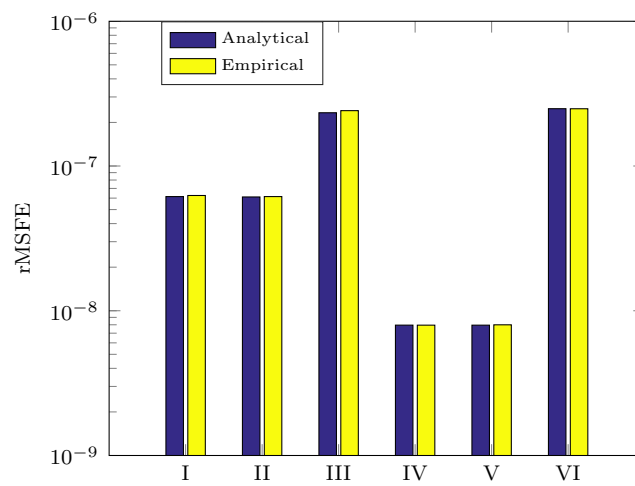
(b) 6 estimates of $\boldsymbol{F}^{(2)}$
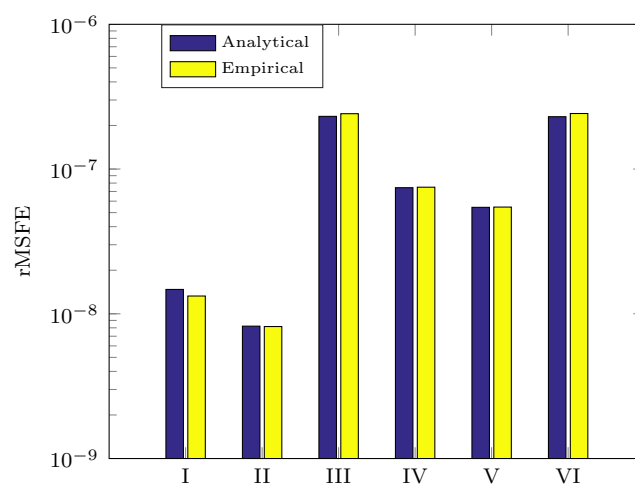
(c) 6 estimates of $\boldsymbol{F}^{(3)}$

Figure 9.3.: 6 estimates for each of the factor matrix for scenario III and for a SNR = 50 dB.
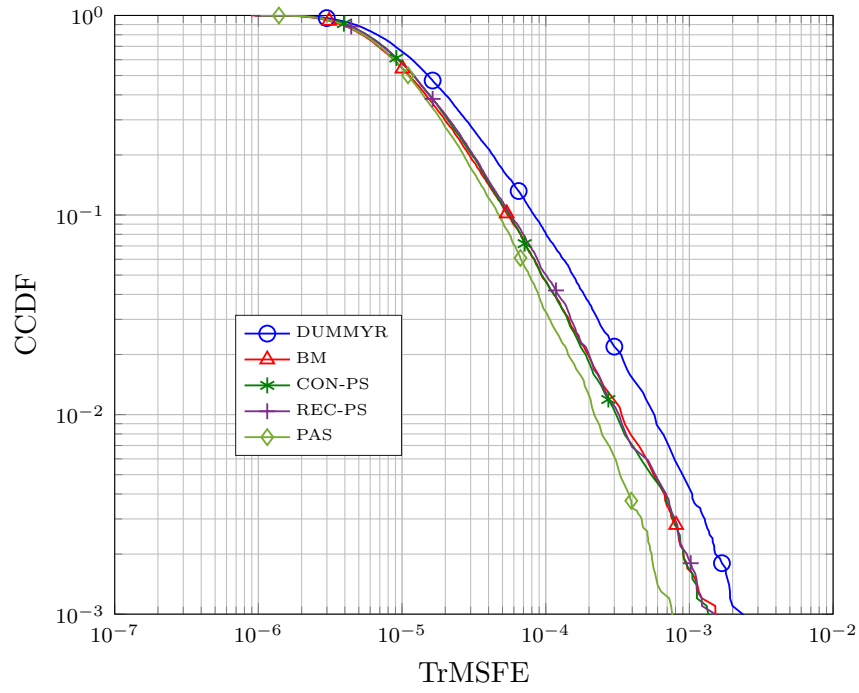
(a) Scenario IV
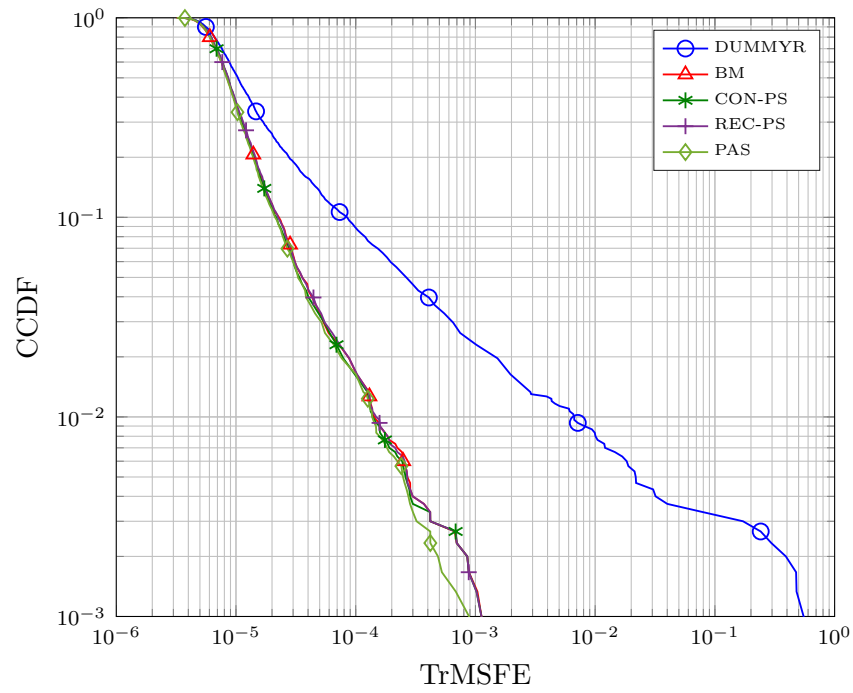
(b) Scenario V

Figure 9.4.: CCDF of the TrMSFE for Scenarios IV and V.

Part IV.

Conclusions and Outlook

10. Conclusions and future work

In this thesis, we develop novel and advanced signal processing algorithms for multi-dimensional areas of future communication systems. The main goal is to fulfill the ever-growing demand for new innovations that require an enhanced performance, a higher efficiency, a greater flexibility, etc. With this aim in mind, we have discussed signal processing aspects for three application areas, i.e., MIMO concepts for waveforms to be used in 5G communications systems and beyond, efficient transceiver designs for optical systems employing intensity modulation and direct detection, and a first-order perturbation analysis of tensor decomposition methods. Moreover, since we address a broad spectrum of topics in the thesis, it opens up many exciting directions for future research.

In the first part of thesis, we discuss MIMO concepts for UW-OFDM systems. UW-OFDM is a novel signaling schemes that has been introduced in 2010 [HHH10b, OH10]. In contrast to the other CP based schemes, a known deterministic sequence is inserted in the time domain inside the IDFT interval. This is achieved by introducing redundancy in the frequency domain which is added with the help of a code generator matrix. This code generator matrix has to be applied on all data subcarriers and introduces correlation among the data symbols. This correlation can be exploited at the receiver by designing sophisticated receivers. For SISO systems, it has been shown that a design based on joint detection exploits this correlation in an efficient manner and results in a superior BER performance over CP-OFDM [HOH11, Oni13]. Note that joint detection refers to a detection scheme where channel equalization and code generator demodulation is performed in a single step. We have extended these investigations to MIMO UW-OFDM systems. We start by proposing two linear detection schemes. In the first approach, the joint detection based design for SISO systems is extended to a MIMO UW-OFDM system. This approach outperforms CP-OFDM significantly but also results in receivers with very high computational complexity, thus making it unsuitable for practical applications. Therefore, an alternative low complexity scheme is proposed where the detection is performed in two steps. In the first step, a subcarrier-wise linear equalization is performed, and in the second step an LMMSE based demodulation is performed. This scheme results practically in the same performance as the joint detection scheme, but has a much lower computational complexity. After discussing the linear detection schemes, we expand our investigations to SIC receivers. The SIC receivers for UW-OFDM can only be designed based on the joint detection approach. Using this technique, we have proposed ZF and QR decomposition based SIC detection schemes. UW-OFDM with these SIC detection schemes shows a high performance gain in terms of the BER, but at the cost of a much higher computational complexity. Therefore, we have proposed a novel hybrid detection scheme that is based on a two step approach. In this scheme, a linear equalization is performed in the first step and a SIC code generator demodulation is used in the second step. This scheme results in a better BER performance than the linear detection schemes but slightly worse than the QR SIC scheme. On the other hand, it has a much lower computational complexity, thus offering a trade-off between performance and computational complexity. In Chapter 3, we have further extended these investigations to space-time block coded UW-OFDM system. We have aimed to provide methods to use existing OSTBCs for UW-OFDM. For this purpose, we have proposed two approaches.

In the first approach, we have followed the technique employed for CP-OFDM and apply OSTBCs in the frequency domain. But unlike CP-OFDM, this approach results in a non-orthogonal effective channel matrix at the receiver. Thus it demands for computationally complex receivers, since the performance of MRC based detection is not good enough, as shown in Fig. 3.5. In the second approach, we have applied OSTBCs on the time domain samples. This requires a slight modification of the conventional UW-OFDM frame structure to correctly use this approach. This approach not only yields a similar performance as the first approach but also results in receivers with a very low computational complexity. Specifically, we have shown that we can use a two step detection method where in the first step, an MRC based detection is performed on each subcarrier and in the second step, an MF based demodulation is performed. This combination has a slightly higher computational complexity than for CP-OFDM but outperforms CP-OFDM with the corresponding OSTBCs significantly. We have compared the performance of this space-time block coded UW-OFDM systems with other 5G air interface proposals such as GFDM, FBMC, and UFMC in Chapter 4. Only for GFDM and FBMC waveforms, techniques to apply STBCs have already been proposed in the literature [MMF14, MMG+15, ZL13]. Therefore, we have first proposed different space-time coding concepts for UFMC waveforms. Similar to space-time block coded UW-OFDM systems, we can either use the STBCs on the data carriers in the frequency domain or on the time domain samples (TR-STC). However, the decoding complexity depends on the type of receive filtering technique. We have shown that if an FFT based receiver is employed, the use of a STBC encoder in the frequency domain is a feasible solution. However, TR-STCs are recommended for all filtering techniques such as matched filtering, ZF, and MMSE filtering. After describing the methods to use STBCs with UFMC waveforms, we have compared the performance of space-time block coded UW-OFDM, UFMC, GFDM, and FBMC systems using the LTE-A parameters. Our simulations show that UW-OFDM has not only the best performance especially over highly frequency selective channels but also has a lower decoding complexity. This is due to the fact that we can efficiently employ an MF based demodulation for UW-OFDM if the channel matrix is orthogonal. However, for other waveforms, a MF based demodulation cannot efficiently resolve the interference, even if the effective channel matrix is orthogonal.

In this work, we have proposed novel concepts for MIMO UW-OFDM systems. These results emphasize the potential of UW-OFDM over currently utilized multicarrier techniques. However, there are still many aspects which require further and intense research to fully assess the potential of MIMO UW-OFDM. In the presented work, we have assumed a single user MIMO (SU-MIMO) case with no CSI at the transmitter. We have also assumed the use of the same code generator matrix for all transmit antennas. Moreover, the code generator matrices to produce UW-OFDM symbols have been optimized assuming an AWGN channel [HHH12]. This allows for designing the generator matrix independently of instantaneous channel conditions, thus avoiding the implementation of a side information channel from the receiver to the transmitter for selecting the proper matrix. Despite this simplification, UW-OFDM systems show an impressive performance especially in a frequency selective environment. However, a code generator design exploiting CSI is still an open issue. Specifically for MIMO UW-OFDM systems, a separate code generator matrix can be designed for each transmit antenna. Such code generator matrices can yield a better performance for UW-OFDM but at the expense of a higher complexity of the system. Therefore, the main challenge of the design is to achieve a trade-off between the performance and the computational

complexity. Another open issue is the design of precoding and beamforming techniques for MIMO UW-OFDM systems when CSI is available at the transmitter. The main challenge is to design a subcarrier-wise precoding matrix for each spatial stream. However, this may require a new code generator design based on the precoding matrix for each channel realization. Such designs will significantly increase the computational complexity at the transmitter and hence are not the best choices. A suboptimal solution to this problem can be a code-book based precoding design where different precoding matrices along with different code genrator matrices are stored for different channel conditions. So far we have focused on some of the SU-MIMO aspects of UW-OFDM. The extension to multi-user MIMO (MU-MIMO) is still an open problem. This opens a vast range of research challenges that address efficient STBCs and spatial multiplexing transmission and reception schemes with reasonable complexity for the MU-MIMO uplink and downlink scenarios. We have also assumed a perfect synchronization and channel estimation in our work. However, the impact of synchronization and channel estimation errors on the performance of MIMO UW-OFDM systems still needs to be investigated. The open question is that whether the inherent nature of UW-OFDM provides some benefits in an asynchronous environment compared to CP-OFDM and other waveforms. Moreover, the efficient utilization of the UW in the channel estimation process for MIMO UW-OFDM is another research direction.

The second part of the thesis is devoted to the transmission strategies for optical systems that employ intensity modulation and direct detection (IM/DD). Such systems demand for real-valued and positive signals at the transmitter. Therefore, the transmission strategies used for RF communication systems cannot be directly used. The CP-DMT schemes (real-valued version of CP-OFDM from RF) are widely recommended schemes for these optical systems. However, in these schemes a Hermitian symmetry is applied to obtain a real-valued signal. This results in a reduced bandwidth efficiency of these schemes. Therefore, in Chapter 5, we have discussed various alternative transmission schemes and have compared their performance with the CP-DMT schemes and other state-of-the-art schemes. Specifically, we have shown that PAM block transmission with FDE is an efficient scheme for these optical systems. We have investigated this scheme from various aspects. We have also proposed some novel SSC block transmission schemes such as OPAM schemes. Moreover, we have presented a simple transceiver architecture for SSC schemes where we have shown how these scheme can benefit from block transmission and FDE. The performance of all of these schemes is evaluated for two optical systems, i.e., POFs and VLC. Since VLC systems require a DC-balance scheme, we have proposed novel DC-balance techniques for PAM block transmission. The results suggest that PAM block transmission with FDE is a very good alternative to CP-DMT schemes. Especially, PAM block transmission with a 50 % RZ-rectangular pulse shows a much superior performance as compared to all other schemes, as shown in Section 5.4. Under the constraint of a low-pass channel with a Gaussian profile for POF systems, it has been shown that there is no performance gain for CP-DMT schemes over PAM block transmission with FDE. Even with full CSI at the transmitter, bit-loading enhanced CP-DMT schemes do not match the performance of adaptive PAM block transmission. Note that bit-loading requires the knowledge of full CSI at the transmitter but adaptive PAM block transmission requires only information about the modulation order and the symbol interval. Moreover, there is a negligible performance difference between the optimal bit-loading Hughes-Hartogs algorithm and the suboptimal Fischer-Huber algorithm. For VLC systems, we have considered only DC-balanced schemes. We have used a scenario where four LED lamps are placed

in a medium sized room at different locations, as explained in Section 5.2.2. We have calculated the channel impulse response using up to 8 reflections. The results show that the impact of the diffuse part disappears at higher frequencies, whereas it provides additional power in the lower frequency range. Although, line codes add more redundancy, PAM block transmission shows a superior performance than the DC-biased CP-DMT, even if bit-loading is used in the latter case. DC-biased single-subcarrier modulation or orthogonal PAM are not attractive choices, since the spectral centroid of the signal is shifted to the bandpass range that results in their inferior performance. Another widely recommended scheme for VLC systems is carrier-less amplitude and phase modulation (CAP). However, we have shown that the performance of CAP is worse than the PAM block transmission and DC-biased DMT schemes. Moreover, the CAP scheme requires long FIR filters and has high PAPR, thus making it less suitable for VLC systems. Although PAM block transmission has shown superior performance over all other schemes, but still PAM does not achieve the best performance, if linear equalization is used. Therefore, we have further extended these investigations to non-linear precoding and equalization techniques in Chapter 6. We have discussed DFE and THP techniques that can be used with PAM transmission. These techniques result in a much superior performance of PAM transmission in dispersive optical channels. However, such techniques increase the computational complexity of the system significantly. Moreover, DFE suffers from the error propagation problem, while THP requires full CSI at the transmitter. These factors make these techniques less suitable for practical application. Alternatively, we have suggested to use a hybrid equalization scheme with PAM block transmission. In this scheme, a frequency domain equalizer is still used while an additional feedback filter is added in the time domain to eliminate the residual ISI. Such a hybrid equalizer requires fewer feedback filter taps as compared to the DFE. Moreover, instead of using a CP, we have used a UW to resolve the error propagation problem of the DFE. We have shown that PAM block transmission with this hybrid scheme has the same performance as the DFE, but on the other side it has a significantly lower computational complexity. We have shown that even with a 2 PAM-RZ (OOK) modulation combined with this hybrid equalization scheme, data rates up to 2 Gbps can be achieved for 10m of step-index POF with a reasonable power penalty, as shown in Fig. 6.12b. Therefore, this transceiver design offers the best performance for the dispersive optical systems with a reasonable system complexity. In the last chapter of this part, we have proposed three novel UW-DMT schemes that are derived from the UW-OFDM concept. Since optical systems with IM/DD require real-valued signals, this puts an extra constraint on the design of the code generator matrix. We have shown that the design of the code generator is different for complex-valued and real-valued constellation formats. We have designed systematic and non-systematic code generator matrices and proposed two solutions, as discussed in Section 7.2. The design based on the solution 2 outperforms the solution 1. Moreover, UW-DMT schemes with non-systematic code generator matrices outperforms the UW-DMT schemes with systematic code generator matrices. Specifically we have shown that all UW-DMT schemes outperform their counterpart CP-DMT schemes significantly.

In this part of the thesis, we have discussed various transmission schemes. We have shown that PAM block transmission can be a serious alternate to the widely recommended CP-DMT schemes. Although we have investigated PAM block transmission from various aspects, there are still many open problems. For instance, we have used 5B6B codes to guarantee a constant brightness for VLC systems. However, better line codes can be designed by extending the existing 5B6B codes to general $XBYM$ codes meaning

where X Bits are mapped to Y M-level symbols. We have also recommended to use a UW instead of a CP for PAM block transmission, especially with a hybrid equalizer. The UW can be additionally used for the clock-frequency offset tracking which needs to be investigated. For VLC systems, we have investigated the performance of all the schemes assuming a single-user and a single-cell. The use of a single-cell or multi-cell multi-user VLC technique is a primary method for boosting the network throughput for indoor VLC wireless systems. In multi-user scenarios the intra-cell or inter-cell interference will limit the performance and therefore the interference mitigation tasks becomes critical. Recent studies on single-cell or multi-cell multi-user VLC networks are either only based on DMT waveforms or do not consider the illumination constraints. Therefore, interference mitigation techniques such as space division multiple access for PAM block transmission based VLC system with illumination constraints need to be investigated. In Chapter 7, we have proposed three novel UW-DMT schemes that are designed using the UW-OFDM concept. We have designed the systematic and non-systematic code generator matrices for these schemes. We have also demonstrated that the UW-DMT schemes using non-systematic code generator matrices outperform the UW-DMT schemes with systematic code generator matrices. These non-systematic code generator matrices contain an orthonormal basis of the null space that are computed by the SVD of the desired matrices. However, for UW-OFDM systems, the optimum code generator matrices are derived by minimizing the trace of the error covariance matrices of the BLUE or LMMSE estimator in the AWGN channel and for a fixed signal-to-noise ratio. Such code generator matrices can also be designed for UW-DMT schemes which may further improve their performance.

In the last part of the thesis, we have performed a first-order perturbation analysis of some of the multi-linear (tensor) algebraic concepts. The most widely employed tensor decompositions methods are the truncated HOSVD and the CPD. These methods are used in a variety of scientific application fields ranging from telecommunications to quantum chemistry. The performance of these tensor decomposition methods is usually evaluated by performing time-expensive Monte-Carlo trials. However, an analytical perturbation analysis of these algorithms could predict the performance of these algorithms for different noisy conditions in advance. This has motivated us to perform the first-order perturbation analysis. A first-order perturbation analysis of the truncated HOSVD is presented in Chapter 8. For this purpose, we have derived closed-form expressions for the subspace estimation error and the tensor estimation error. For the derivation of these closed-form expressions, we have only assumed that the noise is zero-mean. However, to provide a better insight into the truncated HOSVD performance, we have further simplified the obtained expression for the special case of uncorrelated noise with equal variance. We have evaluated the performance of the derived expressions using computer generated data and also using images. The simulations results show that the proposed solutions (MSE of the subspace estimation error and the reconstruction error) depicts an excellent match to the empirical results for both data sets. There exist many methods to compute the CPD of a low-rank noisy tensor. However, the semi-algebraic approaches are widely recommended in the literature due to their better performance and comparatively low complexity. In particular, the semi-algebraic framework for the approximate canonical polyadic decomposition via simultaneaous matrix diagonalization (SECSI) is an efficient and flexible framework for the computation of the CPD. We have performed a first-order perturbation analysis of the SECSI framework for the approximate CPD of 3-D noise-corrupted low-rank tensors in Chapter 9. The SECSI framework performs three distinct steps to estimate the factor matrices. Thus, to compute a performance

analysis of the SECSI framework, a perturbation analysis of each of the steps is required. In the first step, the truncated HOSVD is used to suppress the noise. For this purpose, the results derived in Chapter 8 have been used. In the second step, the whole sets of JEVDs are constructed from the truncated core tensor. In the SECSI framework, the JEVD algorithms that are based on the indirect LS cost function are used. We have performed a first order perturbation analysis of such JEVDs algorithms, i.e., JDTM [LA10], Sh-Rt [FG06], and coupled JEVD [RLM16], in [BCW$^+$17]. These results are also summarized in Appendix D.1. Using these results, we have performed a first-order performance analysis of the SECSI framework. Specifically, we have presented the closed-form analytical expressions for the rMSFE for each of the estimates of the factor matrices. The derived expressions are formulated in terms of second-order moment of the noise, where we have only assumed that the noise is zero-mean. We have evaluated the performance of the proposed results for real-valued and complex-valued tensors. We have also shown results using different JEVD algorithms. The results show an excellent match between the analytical closed-form expressions and the empirical results for both real-valued and complex-valued data. Note that, solving all JEVDs result in several estimates of the factor matrices. The best factor matrices are estimated from these estimates using an exhaustive search based best matching scheme or by using heuristic selection schemes with a reduced computational complexity, as proposed in [RH13]. Alternatively, we have also proposed a new selection scheme that is based on the performance analysis results. We have shown that the new PAS scheme outperforms the existing schemes especially at high SNR values.

Although we have proposed the first-order perturbation analysis of the truncated HOSVD and the SECSI framework, there are many open problems. For example, the SECSI framework can be extended for tensors with symmetries and Hermitian symmetries along with the corresponding performance analysis. In such cases, we do not need to multiply with the inverse of the pivot slice to render the diagonalizations symmetric. Therefore, we can use diagonalization by congruence algorithms such as ACDC. However, it needs to be investigated that such a formulation will result in an improved performance or not. If it results in an improved performance, then the perturbation analysis can be modified accordingly. This will require to perform a perturbation analysis of diagonalization by congruence algorithms. A truncated version of SECSI (i.e., T-SECSI) has been introduced recently in [NHT$^+$16]. In this approach, the diagonalizing of the slices of the estimated core tensor is performed that leads to complexity reduction. Based on the performance analysis results, a first-order perturbation analysis of the T-SECSI can also be performed. In [NH16], the SECSI framework has been extended for coupled tensors. The coupled SECSI framework exploits the fact that the tensors have at least one factor matrix in common and guarantees that even in noisy scenarios the common mode will have the same factor matrix for the different tensors. Such a tensor structure is present in many combined signal processing applications such as the joint processing of EEG and MEG data. A performance analysis of the coupled SECSI framework can be performed in future using the performance analysis results for the SECSI framework.

Part V.

Appendices

Appendix A.

Glossary of Acronyms, Symbols and Notation

A.1. Acronyms

4G	Fourth Generation
5G	Fifth Generation
AWGN	Additive White Gaussian Noise
BER	Bit Error Rate
BLUE	Best Linear Unbiased Estimator
BPSK	Binary Phase Shift Keying
CAP	Carrier-less Amplitude and Phase modulation
CCDF	Complementary Cumulative Distribution Function
CP	Cyclic Prefix
CPD	Canonical Polyadic Decomposition
CSI	Channel State Information
CTF	Channel Transfer Function
DFT	Discrete Fourier Transform
DFT	Decision Feedback Equalization
DSL	Dynamic Subscriber Line
DVB-T	Digital Video Broadcasting Terrestrial
EPA	Extended Pedestrian A
EVA	Extended Vehicular A
FDE	Frequency Division Equalization
FFT	Fast Fourier Transform
FBMC	Filter Bank Multicarrier
FH	Fischer-Huber
GFDM	Generalized Frequency Division Multiplex
HH	Hughes-Hartogs
HOSVD	Higher Order Singular Value Decomposition
ICI	Inter Carrier Interference
IDFT	Inverse Discrete Fourier Transform
IFFT	Inverse Fast Fourier Transform
ISI	Inter Symbol Interference
JEVD	Joint Eigen Value Decomposition
KS	Known Symbol
KSP	Known Symbol Padding
LED	Light Emitting Diode
LS	Least Squares
LTE	Long Term Evolution
LTI	Linear Time Invariant
M2M	Machine-to-Machine
MF	Matched Filter
MIMO	Multiple Input Multiple Output
MOST	Media Oriented System Transport
MRC	Maximum Ratio Combining
MSE	Mean Square Error

MMSE	Minimum Mean Squared Error
NLoS	Non Line Of Sight
NRZ	Non Return to Zero
OFDM	Orthogonal Frequency Division Multiplexing
OOB	out-of-band
OOK	On Off Keying
OSTBC	Orthogonal Space-Time Block Code
PAS	Performance Analysis based Selection
PAM	Pulse Amplitude Modulation
PAPR	Peak to Average Power Ratio
POF	Plastic Optical Fiber
QAM	Quadrature Amplitude Modulation
RF	Radio Frequency
RRC	Root-Raised Cosine
RS	Relay Station
SECSI	Semi-Algebraic CPD via Simultaneous Matrix Diagonalization
SMD	Simultaneous Matrix Diagonalization
SNR	Signal to Noise Ratio
SIC	Successive Interference cancellation
SISO	Single Input Single Output
SSC	Single Subcarrier
SVD	Singular Value Decomposition
THP	Tomlinson Harashima Precoding
TR-STC	Time Reversal Space-Time Code
UFMC	Universal Filtered Multicarrier
UE	User Equipment
UT	User Terminal
UW	Unique Word
VLC	Visible Light Communication
ZF	Zero Forcing
ZMCSCG	Zero Mean Circularly Symmetric Complex Gaussian

A.2. Symbols and Notation

$\mathbb{R}$	Set of real numbers
$\mathbb{C}$	Set of complex numbers
a, b, c	Scalars
$\boldsymbol{a}$, $\boldsymbol{b}$, $\boldsymbol{c}$	Column vectors
$\boldsymbol{A}$, $\boldsymbol{B}$, $\boldsymbol{C}$	Matrices
$\mathrm{Re}\{x\}$	Real part of complex variable x
$\mathrm{Im}\{x\}$	Imaginary part of complex variable x
x^*	Complex conjugate of x
$\boldsymbol{0}_{M \times N}$	Matrix of zeros of size $M \times N$
$\boldsymbol{I}_M$	Identity matrix of size $M \times M$
$\boldsymbol{\Pi}_M$	Exchange of size $M \times M$ with ones on its anti-diagonal and zeros elsewhere
$(\cdot)^{\mathrm{T}}$	Matrix transpose
$(\cdot)^{\mathrm{H}}$	Hermitian transpose
$\|\cdot\|_2$	Euclidean (two-) norm

$\|\cdot\|_{\mathrm{F}}$	Frobenius norm
$\|\cdot\|_{\mathrm{H}}$	Higher-Order (Frobenius) norm
$\boldsymbol{A} \otimes \boldsymbol{B}$	Kronecker product between $\boldsymbol{A} \in \mathbb{C}^{M \times N}$ and $\boldsymbol{B} \in \mathbb{C}^{P \times Q}$ defined as

$$\boldsymbol{A} \otimes \boldsymbol{B} = \begin{bmatrix} a_{1,1} \cdot \boldsymbol{B} & a_{1,2} \cdot \boldsymbol{B} & \cdots & a_{1,N} \cdot \boldsymbol{B} \\ a_{2,1} \cdot \boldsymbol{B} & a_{2,2} \cdot \boldsymbol{B} & \cdots & a_{2,N} \cdot \boldsymbol{B} \\ \vdots & \vdots & \vdots & \vdots \\ a_{M,1} \cdot \boldsymbol{B} & a_{M,2} \cdot \boldsymbol{B} & \cdots & a_{M,N} \cdot \boldsymbol{B} \end{bmatrix}.$$

$\boldsymbol{A} \diamond \boldsymbol{B}$	Khatri-Rao (column-wise Kronecker) product between $\boldsymbol{A} \in \mathbb{C}^{M \times N}$ and $\boldsymbol{B} \in \mathbb{C}^{P \times N}$
$\mathrm{vec}\{\cdot\}$	Vec-operator: stack elements of a matrix/tensor into a column vector, begin with first (row) index, then proceed to second (column), third, etc.
$\mathrm{unvec}\{\cdot\}$	Inverse vec-operator: reshape elements of a vector back into a matrix/tensor of the indicated size
$\mathrm{tr}\{\cdot\}$	Trace of a matrix (sum of diagonal elements = sum of eigenvalues)
$\mathrm{rank}\{\cdot\}$	Rank of a matrix
$\boldsymbol{A}^{+}$	Moore-Penrose pseudo inverse of a matrix $\boldsymbol{A} \in \mathbb{C}^{M \times N}$, which we can compute via

- $\boldsymbol{A}^{+} = \boldsymbol{V}_{\mathrm{s}} \cdot \boldsymbol{\Sigma}_{\mathrm{s}}^{-1} \cdot \boldsymbol{U}_{\mathrm{s}}^{\mathrm{H}}$, where $\boldsymbol{A} = \boldsymbol{U}_{\mathrm{s}} \cdot \boldsymbol{\Sigma}_{\mathrm{s}} \cdot \boldsymbol{V}_{\mathrm{s}}^{\mathrm{H}}$ represents the economy-size SVD of $\boldsymbol{A}$.

- $\boldsymbol{A}^{+} = (\boldsymbol{A}^{\mathrm{H}} \cdot \boldsymbol{A})^{-1} \cdot \boldsymbol{A}^{\mathrm{H}}$ if $\mathrm{rank}\{\boldsymbol{A}\} = N$ (full column rank)

- $\boldsymbol{A}^{+} = \boldsymbol{A}^{\mathrm{H}} \cdot (\boldsymbol{A} \cdot \boldsymbol{A}^{\mathrm{H}})^{-1}$ if $\mathrm{rank}\{\boldsymbol{A}\} = M$ (full row rank).

$\mathbb{E}\{X\}$	Expectation operator, i.e., mean of the random variable X

Appendix B.

An example illustrating the cyclic convolution

Let us assume a system where a block of data samples $\boldsymbol{x} \in \mathbb{C}^{N \times 1}$ of length N is transmitted. The received signal is given by

$$\boldsymbol{y} = \boldsymbol{H}\boldsymbol{x} + \boldsymbol{n} \in \mathbb{C}^{(N+N_{\text{ch}}-1) \times 1}, \tag{B.1}$$

where $\boldsymbol{H}$ is the channel convolution matrix containing the channel impulse response. The channel convolution matrix has the following structure

$$\boldsymbol{H} = \begin{bmatrix} h_1 & 0 & 0 & 0 & 0 \\ h_2 & h_1 & 0 & 0 & 0 \\ h_3 & h_2 & h_1 & 0 & 0 \\ 0 & h_3 & h_2 & h_1 & 0 \\ 0 & 0 & h_3 & h_2 & h_1 \\ 0 & 0 & 0 & h_3 & h_2 \\ 0 & 0 & 0 & 0 & h_3 \end{bmatrix} \in \mathbb{C}^{(N+N_{\text{ch}}-1) \times N}, \tag{B.2}$$

where, for simplicity, we have assumed that the length of channel impulse response is $N_{\text{ch}} = 3$.

Next we assume a system where a CP/UW is prepended to the block of data samples $\boldsymbol{x} \in \mathbb{C}^{N \times 1}$ before transmission. Then the received signal after removing the CP/UW in the time domain is given as

$$\boldsymbol{y} = \hat{\boldsymbol{H}}\boldsymbol{x} + \boldsymbol{n} \in \mathbb{C}^{N \times 1}. \tag{B.3}$$

In this case, $\hat{\boldsymbol{H}}$ is a circulant matrix that contains the channel impulse response of length $N_{\text{ch}} = 3$ in the following way

$$\hat{\boldsymbol{H}} = \begin{bmatrix} h_1 & 0 & 0 & h_3 & h_2 \\ h_2 & h_1 & 0 & 0 & h_3 \\ h_3 & h_2 & h_1 & 0 & 0 \\ 0 & h_3 & h_2 & h_1 & 0 \\ 0 & 0 & h_3 & h_2 & h_1 \end{bmatrix} \in \mathbb{C}^{N \times N}. \tag{B.4}$$

Appendix C.

Derivation of the decision feedback equalizer filters

The cost function as defined by Eq. (6.15) is,

$$J(\boldsymbol{f}, \bar{\boldsymbol{b}}) = \mathbb{E}\left\{|\bar{\boldsymbol{b}}^H \boldsymbol{x} - \boldsymbol{f}^H \boldsymbol{y}|^2\right\} \tag{C.1}$$

The task is to determine the filter vectors $\boldsymbol{f}^H$ and $\bar{\boldsymbol{b}}^H$ that minimize this cost function. This goal is accomplished by firstly minimizing the cost function over one of the vectors, and then determining the other one [Say03]. We first fix the vector $\bar{\boldsymbol{b}}$ and minimize the error variance over $\boldsymbol{f}$. To do so, a scalar $\alpha = \bar{\boldsymbol{b}}^H \boldsymbol{x}$ is introduced such that

$$J(\boldsymbol{f}) = \mathbb{E}\left\{|\alpha - \boldsymbol{f}^H \boldsymbol{y}|^2\right\}. \tag{C.2}$$

This cost function is a standard linear least-mean-squares estimation problem and results in the optimal choice of $\boldsymbol{f}$ as,

$$\boldsymbol{f}_{\text{opt}}^H = \boldsymbol{R}_{\alpha y} \boldsymbol{R}_{yy}^{-1}, \tag{C.3}$$

where $\boldsymbol{R}_{\alpha y} = \mathbb{E}\left\{\alpha \boldsymbol{y}^H\right\} = \mathbb{E}\left\{\bar{\boldsymbol{b}}^H \boldsymbol{x} \boldsymbol{y}^H\right\} = \bar{\boldsymbol{b}}^H \boldsymbol{R}_{xy}$. This implies that

$$\boldsymbol{f}_{\text{opt}}^H = \bar{\boldsymbol{b}}^H \boldsymbol{R}_{xy} \boldsymbol{R}_{yy}^{-1}. \tag{C.4}$$

Substituting this expression into the cost function (Eq. (C.2)), we get

$$\begin{aligned} J(\bar{\boldsymbol{b}}) &= \mathbb{E}\left\{|\alpha - \boldsymbol{f}_{\text{opt}}^H \boldsymbol{y}|^2\right\} \\ &= \boldsymbol{R}_{\alpha\alpha} - \boldsymbol{R}_{\alpha y} \boldsymbol{R}_{yy}^{-1} \boldsymbol{R}_{y\alpha} \\ &= \bar{\boldsymbol{b}}^H \boldsymbol{R}_{xx} \bar{\boldsymbol{b}} - \bar{\boldsymbol{b}}^H \boldsymbol{R}_{xy} \boldsymbol{R}_{yy}^{-1} \boldsymbol{R}_{yx} \bar{\boldsymbol{b}} \\ &= \bar{\boldsymbol{b}}^H \left(\boldsymbol{R}_{xx} - \boldsymbol{R}_{xy} \boldsymbol{R}_{yy}^{-1} \boldsymbol{R}_{yx}\right) \bar{\boldsymbol{b}} \\ &= \bar{\boldsymbol{b}}^H \mathbf{R}_{\delta} \bar{\boldsymbol{b}}, \end{aligned} \tag{C.5}$$

where $\mathbf{R}_{\delta} = \mathbf{R}_{xx} - \mathbf{R}_{xy} \mathbf{R}_{yy}^{-1} \mathbf{R}_{yx}$.

Note that the first entry of $\bar{\mathbf{b}}$ is unity, so that the constrained problem in Eq. (C.5), i.e., $J(\bar{\mathbf{b}}) = \bar{\mathbf{b}}^H \mathbf{R}_{\delta} \bar{\mathbf{b}}$ is minimized subject to $\bar{\mathbf{b}}^H \mathbf{e}_1 = 1$. Here $\mathbf{e}_1 = \begin{bmatrix} 1 & 0 & 0 & \cdots & 0 \end{bmatrix}^T \in \mathbb{R}^{(B+1)\times 1}$ is the first basis column vector. To solve this problem, we benefit from the results of Gauss-Markov Theorem. Using this theorem, the optimal filter coefficients for $\bar{\mathbf{b}}$ result in,

$$\bar{\mathbf{b}}_{\text{opt}}^H = \frac{\mathbf{e}_1^T \mathbf{R}_{\delta}^{-1}}{\mathbf{e}_1^T \mathbf{R}_{\delta}^{-1} \mathbf{e}_1}. \tag{C.6}$$

And by substituting Eq. (C.6) into Eq. (C.4), optimum feedforward filter coefficients are

$$\boldsymbol{f}_{\text{opt}}^{H} = \bar{\boldsymbol{b}}_{\text{opt}}^{H} \boldsymbol{R}_{xy} \boldsymbol{R}_{yy}^{-1}. \tag{C.7}$$

Appendix D.

Proofs and derivations for Part 3

D.1. Perturbations in indirect LS JEVD Algorithms

Computing the JEVD of a given set of K jointly diagonalizable matrices $\boldsymbol{S}_k \in \mathbb{C}^{M \times M}, \quad \forall k = 1, 2, \dots, K$ consists of finding the matrix $\boldsymbol{T}$ such that

$$\boldsymbol{S}_k = \boldsymbol{T} \cdot \boldsymbol{D}_k \cdot \boldsymbol{T}^{-1}, \quad \forall k = 1, 2, \dots, K, \tag{D.1}$$

where $\boldsymbol{T} \in \mathbb{C}^{M \times M}$ is an invertible matrix and $\boldsymbol{D}_k \in \mathbb{C}^{M \times M}$ are diagonal matrices for $k = 1, 2, \dots, K$. The algorithms such as JDTM, Sh-Rt, and coupled JEVD aim to find the $\hat{\boldsymbol{T}}$ that minimizes the indirect LS cost function

$$J = \sum_{k=1}^{K} \left\| \mathrm{Off} \left(\hat{\boldsymbol{T}}^{-1} \cdot \hat{\boldsymbol{S}}_k \cdot \hat{\boldsymbol{T}} \right) \right\|_{\mathrm{F}}^2. \tag{D.2}$$

This implies that, ideally, these algorithms estimate $\boldsymbol{T}$ iteratively by solving

$$\hat{\boldsymbol{T}} = \underset{\hat{\boldsymbol{T}}}{\arg\min} \left(\sum_{k=1}^{K} \left\| \mathrm{Off} \left(\hat{\boldsymbol{T}}^{-1} \cdot \hat{\boldsymbol{S}}_k \cdot \hat{\boldsymbol{T}} \right) \right\|_{\mathrm{F}}^2 \right). \tag{D.3}$$

and the estimates $\hat{\boldsymbol{D}}_k$ are computed as

$$\hat{\boldsymbol{D}}_k = \mathrm{Ddiag} \left(\hat{\boldsymbol{T}}^{-1} \cdot \hat{\boldsymbol{S}}_k \cdot \hat{\boldsymbol{T}} \right), \quad \forall k = 1, 2, \dots, K. \tag{D.4}$$

Note that in the case of the JEVD algorithms based on the direct LS cost function, the matrix $\boldsymbol{T}$ is estimated by solving

$$\hat{\boldsymbol{T}} = \underset{\hat{\boldsymbol{T}}}{\arg\min} \left(\sum_{k=1}^{K} \left\| \hat{\boldsymbol{S}}_k - \hat{\boldsymbol{T}} \cdot \hat{\boldsymbol{D}}_k \cdot \hat{\boldsymbol{T}}^{-1} \right\|_{\mathrm{F}}^2 \right). \tag{D.5}$$

In this appendix, we solve for the perturbations to compute the JEVDs using indirect LS cost function. We expand the term $\hat{\boldsymbol{T}}^{-1} \cdot \hat{\boldsymbol{S}}_k \cdot \hat{\boldsymbol{T}}$, inside equation (D.2), to

$$
\begin{aligned}
\hat{\boldsymbol{T}}^{-1} \cdot \hat{\boldsymbol{S}}_k \cdot \hat{\boldsymbol{T}} &= (\boldsymbol{T} + \Delta \boldsymbol{T})^{-1} \cdot (\boldsymbol{S}_k + \Delta \boldsymbol{S}_k) \cdot (\boldsymbol{T} + \Delta \boldsymbol{T}) \\
&= \left(\boldsymbol{T}^{-1} - \boldsymbol{T}^{-1} \cdot \Delta \boldsymbol{T} \cdot \boldsymbol{T}^{-1} \right) \cdot (\boldsymbol{S}_k + \Delta \boldsymbol{S}_k) \cdot (\boldsymbol{T} + \Delta \boldsymbol{T}) + \mathcal{O}(\Delta^2) \\
&= \boldsymbol{T}^{-1} \cdot \boldsymbol{S}_k \cdot \boldsymbol{T} + \boldsymbol{T}^{-1} \cdot \Delta \boldsymbol{S}_k \cdot \boldsymbol{T} + \boldsymbol{T}^{-1} \cdot \boldsymbol{S}_k \cdot \Delta \boldsymbol{T} - \boldsymbol{T}^{-1} \cdot \Delta \boldsymbol{T} \cdot \boldsymbol{T}^{-1} \cdot \boldsymbol{S}_k \cdot \boldsymbol{T} + \mathcal{O}(\Delta^2) \\
&= \boldsymbol{D}_k + \boldsymbol{T}^{-1} \cdot \Delta \boldsymbol{S}_k \cdot \boldsymbol{T} + \boldsymbol{T}^{-1} \cdot \boldsymbol{S}_k \cdot \Delta \boldsymbol{T} - \boldsymbol{T}^{-1} \cdot \Delta \boldsymbol{T} \cdot \boldsymbol{D}_k + \mathcal{O}(\Delta^2).
\end{aligned}
\tag{D.6}
$$

Since $\mathrm{Off}\left(\boldsymbol{D}_k\right) = \boldsymbol{0}$, we compute

$$\mathrm{Off}\left(\hat{\boldsymbol{T}}^{-1} \cdot \hat{\boldsymbol{S}}_k \cdot \hat{\boldsymbol{T}}\right) = \mathrm{Off}\left(\boldsymbol{D}_k + \boldsymbol{T}^{-1} \cdot \Delta\boldsymbol{S}_k \cdot \boldsymbol{T} + \boldsymbol{T}^{-1} \cdot \boldsymbol{S}_k \cdot \Delta\boldsymbol{T} - \boldsymbol{T}^{-1} \cdot \Delta\boldsymbol{T} \cdot \boldsymbol{D}_k + \mathcal{O}(\Delta^2)\right)$$

$$= \mathrm{Off}\left(\boldsymbol{T}^{-1} \cdot \Delta\boldsymbol{S}_k \cdot \boldsymbol{T}\right) + \mathrm{Off}\left(\boldsymbol{T}^{-1} \cdot \boldsymbol{S}_k \cdot \Delta\boldsymbol{T}\right) - \mathrm{Off}\left(\boldsymbol{T}^{-1} \cdot \Delta\boldsymbol{T} \cdot \boldsymbol{D}_k\right) + \mathcal{O}(\Delta^2). \tag{D.7}$$

Next we vectorise the result from equation (D.7) to find

$$\mathrm{vec}\left\{\left(\mathrm{Off}\left(\hat{\boldsymbol{T}}^{-1} \cdot \hat{\boldsymbol{S}}_k \cdot \hat{\boldsymbol{T}}\right)\right\} = \mathrm{vec}\left\{\mathrm{Off}\left(\boldsymbol{T}^{-1} \cdot \Delta\boldsymbol{S}_k \cdot \boldsymbol{T} + \boldsymbol{T}^{-1} \cdot \boldsymbol{S}_k \cdot \Delta\boldsymbol{T} - \boldsymbol{T}^{-1}\Delta\boldsymbol{T} \cdot \boldsymbol{D}_k + \mathcal{O}(\Delta^2)\right)\right\}$$

$$= \boldsymbol{Q} \cdot \mathrm{vec}\left\{\boldsymbol{T}^{-1} \cdot \Delta\boldsymbol{S}_k \cdot \boldsymbol{T}\right\} + \boldsymbol{Q} \cdot \mathrm{vec}\left\{\boldsymbol{T}^{-1} \cdot \boldsymbol{S}_k \cdot \Delta\boldsymbol{T}\right\}$$

$$- \boldsymbol{Q} \cdot \mathrm{vec}\left\{\boldsymbol{T}^{-1} \cdot \Delta\boldsymbol{T} \cdot \boldsymbol{D}_k\right\} + \mathcal{O}(\Delta^2)$$

$$= \boldsymbol{Q} \cdot \left(\boldsymbol{T}^{\mathrm{T}} \otimes \boldsymbol{T}^{-1}\right) \cdot \mathrm{vec}\left\{\Delta\boldsymbol{S}_k\right\} + \boldsymbol{Q} \cdot \left(\boldsymbol{I} \otimes \boldsymbol{T}^{-1} \cdot \boldsymbol{S}_k\right) \cdot \mathrm{vec}\left\{\Delta\boldsymbol{T}\right\}$$

$$- \boldsymbol{Q} \cdot \left(\boldsymbol{D}_k \otimes \boldsymbol{T}^{-1}\right) \cdot \mathrm{vec}\left\{\Delta\boldsymbol{T}\right\} + \mathcal{O}(\Delta^2), \tag{D.8}$$

where $\boldsymbol{Q} \in \{0,1\}^{M^2 \times M^2}$ is a selection matrix that satisfies the relation $\mathrm{vec}\left\{(\mathrm{Off}\left(\boldsymbol{X}\right)\right\} = \boldsymbol{Q} \cdot \mathrm{vec}\left\{\boldsymbol{X}\right\}$ and can be constructed as $\boldsymbol{Q} = \boldsymbol{I}_{M^2} - \mathrm{diag}\left(\mathrm{vec}\left\{\boldsymbol{I}_M\right\}\right)$.

Let us define $\boldsymbol{B}_0 \in \mathbb{C}^{M^2 \times M^2}$, $\boldsymbol{n}_k \in \mathbb{C}^{M^2 \times 1}$, $\boldsymbol{A}_k \in \mathbb{C}^{M^2 \times M^2}$, and $\boldsymbol{w} \in \mathbb{C}^{M^2 \times 1}$ as

$$\boldsymbol{B}_0 = \boldsymbol{Q} \cdot \left(\boldsymbol{T}^{\mathrm{T}} \otimes \boldsymbol{T}^{-1}\right) \tag{D.9}$$

$$\boldsymbol{n}_k = \mathrm{vec}\left\{\Delta\boldsymbol{S}_k\right\} \tag{D.10}$$

$$\boldsymbol{A}_k = \boldsymbol{Q} \cdot \left[\left(\boldsymbol{I}_M \otimes \boldsymbol{T}^{-1} \cdot \boldsymbol{S}_k\right) - \left(\boldsymbol{D}_k \otimes \boldsymbol{T}^{-1}\right)\right] \tag{D.11}$$

$$\boldsymbol{w} = \mathrm{vec}\left\{\Delta\boldsymbol{T}\right\}. \tag{D.12}$$

This notation allows us to reformulate equation (D.8) as

$$\mathrm{vec}\left\{\mathrm{Off}\left(\hat{\boldsymbol{T}}^{-1} \cdot \hat{\boldsymbol{S}}_k \cdot \hat{\boldsymbol{T}}\right)\right\} = \boldsymbol{B}_0 \cdot \boldsymbol{n}_k + \boldsymbol{A}_k \cdot \boldsymbol{w} + \mathcal{O}(\Delta^2). \tag{D.13}$$

Now, by substituting the values of equation (D.13) in equation (D.2) and neglecting the terms that contain $\mathcal{O}(\Delta^2)$, we approximate the indirect LS cost function to

$$J = \sum_{k=1}^{K} \left\|\mathrm{Off}\left(\hat{\boldsymbol{T}}^{-1} \cdot \hat{\boldsymbol{S}}_k \cdot \hat{\boldsymbol{T}}\right)\right\|_{\mathrm{F}}^{2}$$

$$\approx \sum_{k=1}^{K} \left\|\boldsymbol{B}_0 \cdot \boldsymbol{n}_k + \boldsymbol{A}_k \cdot \boldsymbol{w}\right\|^{2}$$

$$= \left\|\boldsymbol{B} \cdot \boldsymbol{n} + \boldsymbol{A} \cdot \boldsymbol{w}\right\|^{2}, \tag{D.14}$$

where

$$\boldsymbol{A} = \begin{bmatrix} \boldsymbol{A}_1 \\ \boldsymbol{A}_2 \\ \vdots \\ \boldsymbol{A}_K \end{bmatrix}, \qquad \boldsymbol{B} = \begin{bmatrix} \boldsymbol{B}_0 & \boldsymbol{0} & \cdots & \boldsymbol{0} \\ \boldsymbol{0} & \boldsymbol{B}_0 & \cdots & \boldsymbol{0} \\ \vdots & \vdots & \vdots & \vdots \\ \boldsymbol{0} & \boldsymbol{0} & \cdots & \boldsymbol{B}_0 \end{bmatrix}, \qquad \boldsymbol{n} = \begin{bmatrix} \boldsymbol{n}_1 \\ \boldsymbol{n}_2 \\ \vdots \\ \boldsymbol{n}_K \end{bmatrix}. \tag{D.15}$$

Since we have approximated equation (D.2) by a conventional LS problem in equation (D.14), the $\boldsymbol{w} = \boldsymbol{w}_{\mathrm{opt}}$ that approximately minimizes J is given by

$$\boldsymbol{w}_{\mathrm{opt}} = -\boldsymbol{A}^{+} \cdot \boldsymbol{B} \cdot \boldsymbol{n}, \tag{D.16}$$

which means that

$$\Delta \boldsymbol{T} \approx \underset{M \times M}{\mathrm{unvec}} \left\{ \boldsymbol{w}_{\mathrm{opt}} \right\}. \tag{D.17}$$

Next, we substitute equation (D.6) into (D.4) that leads to

$$\boldsymbol{D}_k + \Delta \boldsymbol{D}_k = \mathrm{Ddiag} \left(\hat{\boldsymbol{T}}^{-1} \cdot \hat{\boldsymbol{S}}_k \cdot \hat{\boldsymbol{T}} \right) \approx \boldsymbol{D}_k + \mathrm{Ddiag} \left(\boldsymbol{T}^{-1} \cdot \Delta \boldsymbol{S}_k \cdot \boldsymbol{T} \right)$$
$$+ \mathrm{Ddiag} \left(\boldsymbol{T}^{-1} \cdot \boldsymbol{S}_k \cdot \Delta \boldsymbol{T} - \boldsymbol{T}^{-1} \cdot \Delta \boldsymbol{T} \cdot \boldsymbol{D}_k \right). \tag{D.18}$$

We now rewrite the last term of equation (D.18) as

$$\mathrm{Ddiag} \left(\boldsymbol{T}^{-1} \cdot \boldsymbol{S}_k \cdot \Delta \boldsymbol{T} - \boldsymbol{T}^{-1} \cdot \Delta \boldsymbol{T} \cdot \boldsymbol{D}_k \right)$$
$$= \underset{M \times M}{\mathrm{unvec}} \left\{ \boldsymbol{P} \cdot \mathrm{vec} \left(\boldsymbol{T}^{-1} \cdot \boldsymbol{S}_k \cdot \Delta \boldsymbol{T} - \boldsymbol{T}^{-1} \cdot \Delta \boldsymbol{T} \cdot \boldsymbol{D}_k \right) \right\}$$
$$= \underset{M \times M}{\mathrm{unvec}} \left\{ \boldsymbol{P} \cdot \left[\left(\boldsymbol{I}_M \otimes \boldsymbol{T}^{-1} \cdot \boldsymbol{S}_k \right) - \left(\boldsymbol{D}_k \otimes \boldsymbol{T}^{-1} \right) \right] \cdot \mathrm{vec} \left(\Delta \boldsymbol{T} \right) \right\}$$
$$= \underset{M \times M}{\mathrm{unvec}} \left\{ \boldsymbol{P} \cdot \left[\left(\boldsymbol{I}_M \otimes \boldsymbol{D}_k \cdot \boldsymbol{T}^{-1} \right) - \left(\boldsymbol{D}_k \otimes \boldsymbol{T}^{-1} \right) \right] \cdot \mathrm{vec} \left(\Delta \boldsymbol{T} \right) \right\}$$
$$= \underset{M \times M}{\mathrm{unvec}} \left\{ \boldsymbol{P} \cdot \boldsymbol{R}_k \cdot \mathrm{vec} \left(\Delta \boldsymbol{T} \right) \right\}, \tag{D.19}$$

where $\boldsymbol{P}$ is a selection matrix defined as $\boldsymbol{P} = \mathrm{diag}(\mathrm{vec}\{\boldsymbol{I}_M\})$. Furthermore, the structure present in $\boldsymbol{R}_k$ as discussed above ensures that $\boldsymbol{P} \cdot \boldsymbol{R}_k$ is always equal to zero. This leads to equation (D.19) being equal to zero and, therefore, equation (D.18) leads to

$$\Delta \boldsymbol{D}_k \approx \mathrm{Ddiag} \left(\boldsymbol{T}^{-1} \cdot \Delta \boldsymbol{S}_k \cdot \boldsymbol{T} \right). \tag{D.20}$$

D.2. Proof of Theorem 1

The term $(\boldsymbol{Z} + \Delta \boldsymbol{Z}) \cdot \tilde{\boldsymbol{P}}$ can be interpreted as the estimate of $\boldsymbol{Z}$ up to a scaling of its column, given by

$$\hat{\boldsymbol{Z}} = (\boldsymbol{Z} + \Delta \boldsymbol{Z}) \cdot \tilde{\boldsymbol{P}} = \tilde{\boldsymbol{Z}} + \Delta \tilde{\boldsymbol{Z}}.$$

Therefore, $\tilde{\boldsymbol{P}}$ can be expressed as $\tilde{\boldsymbol{P}} = \text{Ddiag}\left(\boldsymbol{Z}^{\text{H}} \cdot \tilde{\boldsymbol{Z}} \cdot \boldsymbol{K}^{-1}\right)$. To resolve the scaling ambiguity, we compute a diagonal matrix $\boldsymbol{P}_{\text{opt}}$ that satisfies $\boldsymbol{P}_{\text{opt}} = \text{Ddiag}(\boldsymbol{Z}^{\text{H}} \cdot \hat{\boldsymbol{Z}} \cdot \boldsymbol{K}^{-1})^{-1}$. This result leads to

$$
\begin{aligned}
\tilde{\boldsymbol{P}} \cdot \boldsymbol{P}_{\text{opt}} &= \tilde{\boldsymbol{P}} \cdot \text{Ddiag}\left(\boldsymbol{Z}^{\text{H}} \cdot \hat{\boldsymbol{Z}} \cdot \boldsymbol{K}^{-1}\right)^{-1} \\
&= \tilde{\boldsymbol{P}} \cdot \text{Ddiag}\left(\boldsymbol{Z}^{\text{H}} \cdot (\boldsymbol{Z} + \Delta\boldsymbol{Z}) \cdot \tilde{\boldsymbol{P}} \cdot \boldsymbol{K}^{-1}\right)^{-1} \\
&= \left(\boldsymbol{I}_d + \text{Ddiag}(\boldsymbol{Z}^{\text{H}} \cdot \Delta\boldsymbol{Z}) \cdot \boldsymbol{K}^{-1}\right)^{-1}
\end{aligned}
$$

Let us define the diagonal matrix $\boldsymbol{U} \triangleq \text{Ddiag}\left(\boldsymbol{Z}^{\text{H}} \cdot \Delta\boldsymbol{Z}\right) \cdot \boldsymbol{K}^{-1}$ of size $d \times d$ with diagonal elements $\boldsymbol{U}(i,i)$ for all $i = 1, 2, \ldots, d$. Therefore, $(\boldsymbol{I}_d + \boldsymbol{U})^{-1}$ is also a diagonal matrix, with diagonal elements $(1 + \boldsymbol{U}(i,i))^{-1}$ for all $i = 1, 2, \ldots, d$. Since the elements $\boldsymbol{U}(i,i)$ are first-order terms, we use the well known Taylor's expansion $(1 + x)^{-1} = 1 - x + \mathcal{O}(\Delta^2)$ which holds for any first-order scalar term x. This leads to $(\boldsymbol{I}_d + \boldsymbol{U})^{-1} = (\boldsymbol{I}_d - \boldsymbol{U}) + \mathcal{O}(\Delta^2)$. Therefore, we get

$$
\left(\boldsymbol{I}_d + \text{Ddiag}(\boldsymbol{Z}^{\text{H}} \cdot \Delta\boldsymbol{Z}) \cdot \boldsymbol{K}^{-1}\right)^{-1} = \boldsymbol{I}_d - \text{Ddiag}\left(\boldsymbol{Z}^{\text{H}} \cdot \Delta\boldsymbol{Z}\right) \cdot \boldsymbol{K}^{-1} + \mathcal{O}(\Delta^2),
$$

and thus

$$
\begin{aligned}
\boldsymbol{Z} - (\boldsymbol{Z} + \Delta\boldsymbol{Z}) \cdot \tilde{\boldsymbol{P}} \cdot \boldsymbol{P}_{\text{opt}} &= \boldsymbol{Z} - (\boldsymbol{Z} + \Delta\boldsymbol{Z}) \cdot \left[\boldsymbol{I}_d - \text{Ddiag}\left(\boldsymbol{Z}^{\text{H}} \cdot \Delta\boldsymbol{Z}\right) \cdot \boldsymbol{K}^{-1}\right] + \mathcal{O}(\Delta^2) \\
&= \boldsymbol{Z} \cdot \text{Ddiag}\left(\boldsymbol{Z}^{\text{H}} \cdot \Delta\boldsymbol{Z}\right) \cdot \boldsymbol{K}^{-1} - \Delta\boldsymbol{Z} + \mathcal{O}(\Delta^2),
\end{aligned}
$$

which proves this theorem.

Bibliography

Publications and Technical Documents as Co- or First Author

[ACC+18]   M. Attar, Y. Chen, S. A. Cheema, T. Wild, and M. Haardt, "NOCA versus IDMA using UFMC for 5G multiple access," in *Proceedings of 22nd International ITG Workshop on Smart Antennas, WSA 2018, submitted*, March 2018.

[BCS+16]   E. R. Balda, S. A. Cheema, J. Steinwandt, M. Haardt, A. Weiss, and A. Yeredor, "First-order perturbation analysis of low-rank tensor approximations based on the truncated HOSVD," in *Proceedings of the 50th Asilomar Conference on Signals, Systems and Computers (ASILOMAR)*, November 2016.

[BCW+17]   E. R. Balda, S. A. Cheema, A. Weiss, A. Yeredor, and M. Haardt, "Perturbation analysis of joint eigenvalue decomposition algorithms," in *Proceedings of IEEE Int. Conference on Acoustics, Speech, and Signal Processing (ICASSP)*, March 2017.

[CBC+17]   S. A. Cheema, E. R. Balda, Y. Cheng, M. Haardt, A. Weiss, and A. Yeredor, "First-order perturbation analysis of the SECSI framework for the approximate CP decomposition of 3-D noise-corrupted low-rank tensors," *IEEE Transactions on Signal Processing, submitted*, 2017.

[CBW+17]   S. A. Cheema, E. R. Balda, A. Weiss, A. Yeredor, and M. Haardt, "Analytical performance analysis of the semi-algebraic framework for approximate CP decompositions via simultaneous matrix diagonalizations (SECSI)," in *Proceedings of 51st Asilomar Conf. on Signals, Systems, and Computers*, Pacific Grove, CA, November 2017.

[CBWH17]   S. A. Cheema, E. R. Balda, M. Wolf, and M. Haardt, "Unique word DMT schemes for optical systems with intensity modulation and direct detection," *Journal of Lightwave Technology*, vol. 35, no. 18, pp. 3862–3869, September 2017.

[CCB+16]   O. D. Candido, S. A. Cheema, L. G. Baltar, M. Haardt, and J. A. Nossek, "Downlink precoder and equalizer designs for multi-user MIMO FBMC/OQAM," in *Proceedings of 20th International ITG Workshop on Smart Antennas (WSA 2016)*, Munich, Germany, March 2016.

[CCH+17]   Y. Cheng, S. A. Cheema, M. Haardt, A. Weiss, and A. Yeredor, "Performance analysis of least-squares Khatri-Rao factorization," in *Proceedings of IEEE 7th Int. Workshop on Computational Advances in Multi-Sensor Adaptive Processing (CAMSAP)*, Curacao, Dutch Antilles, December 2017.

[CCH+18]   ——, "First-order perturbation analysis of SECSI with generalized unfoldings," in *Proceedings of IEEE Int. Conference on Acoustics, Speech, and Signal Processing (ICASSP), submitted*, March 2018.

[CGLdG14]   S. A. Cheema, M. Grossmann, M. Landmann, and G. del Galdo, "Link adaptation for LTE-A systems employing MMSE turbo equalization," in *Proceedings of 18th International ITG Workshop on Smart Antennas, WSA 2014*, March 2014, pp. 1–7.

[CNA⁺16] S. A. Cheema, K. Naskovska, M. Attar, B. Zafar, and M. Haardt, "Performance comparison of space time block codes for different 5G air interface proposals," in *Proceedings of 20th International ITG Workshop on Smart Antennas WSA 2016*, March 2016, pp. 1–7.

[CWHH17] S. A. Cheema, M. Wolf, M. Huemer, and M. Haardt, "Unique word DMT schemes using real-valued constellations for IM/DD optical systems," *IEEE Photonics Technology Letters, submitted*, 2017.

[CWTH15] S. A. Cheema, M. Wolf, Ö. Tolay, and M. Haardt, "Efficient Techniques for Multi-Gigabits/s Transmission over Plastic Optical Fiber," in *Proceedings of 17th International Conference on Transparent Optical Networks (ICTON), 2015*, July 2015, pp. 1–5.

[CZHH16] S. A. Cheema, J. Zhang, M. Huemer, and M. Haardt, "Linear detection schemes for MIMO UW-OFDM," in *Proceedings of 50th Asilomar Conf. on Signals, Systems, and Computers*, Pacific Grove, CA, November 2016.

[CZHH17a] ——, "Design of space-time block coded unique word OFDM systems," in *Proceedings of IEEE Int. Conference on Acoustics, Speech, and Signal Processing (ICASSP)*, LA, USA, March 2017.

[CZHH17b] ——, "Successive interference cancellation for MIMO UW-OFDM," in *Proceedings of 21st International ITG Workshop on Smart Antennas, WSA 2017*, March 2017, pp. 1–5.

[KRD⁺15] K.Saleh, R.Jaeger, D.Ammon, M.Specht, A.Henkel, D.Laqua, P.Husar, M.Wolf, K.Blau, S.A.Cheema, M. V.Busch, Th.Linnert, M.Nass, and J.Pospiech, "Prototypical implementation of a novel tagging system for safe localization of devices in medical environments," in *Proceedings of 49th DGBMT Annual Conference (BMT 2015)*, Lbeck, Germany, September 2015.

[LOC⁺16] G. A. Lodi, A. Ott, S. A. Cheema, M. Haardt, and T. Freitag, "Power line communication in automotive harness on the example of local interconnect network," in *Proceedings of 20th IEEE International Symposium on Power Line Communications and its Applications (ISPLC) 2016 (IEEE ISPLC 2016)*, Bottrop, Germany, March 2016.

[NCE⁺17] K. Naskovska, S. A. Cheema, Y. Evdokimov, M. Haardt, and B. Valeev, "Iterative GFDM receiver based on the PARATUCK2 tensor decomposition," in *Proceedings of 21th International ITG Workshop on Smart Antennas, WSA 2017*, March 2017, pp. 1–7.

[WCH16a] M. Wolf, S. A. Cheema, and M. Haardt, "Block transmission with frequency domain equalization for VLC," in *Optical Wireless Communications: An Emerging Technology*, M. Uysal, C. Capsoni, Z. Ghassemlooy, A. Boucouvalas, and E. Udvary, Eds. Cham: Springer International Publishing, 2016, pp. 299–323.

[WCH16b] ——, "Synchronization and channel estimation for optical block-transmission systems with IM/DD," in *Proceedings of 18th International Conference on Transparent Optical Networks ICTON 2016*, Trento, Italy, July 2016.

[WCH17] ——, "PAM-transmission with optimal detection for dispersive optical channels with intensity modulation and direct detection," in *Proceedings of 19th International Conference on Transparent Optical Networks ICTON 2017*, Girona, Spain, July 2017.

[WCHG14] M. Wolf, S. A. Cheema, M. Haardt, and L. Grobe, "On the Performance of Block Transmission Schemes in Optical Channels with a Gaussian Profile," in *Proceedings of 16th International Conference on Transperent Optical Networks (ICTON) 2014*, Graz, July 2014.

[WCKL15]   M. Wolf, S. A. Cheema, M. A. Khalighi, and S. Long, "Transmission Schemes for Visible Light Communications in Multipath Environments," in *Proceedings of 17th International Conference on Transparent Optical Networks (ICTON), 2015*, July 2015, pp. 1–7.

[WYCH17a] A. Weiss, A. Yeredor, S. A. Cheema, and M. Haardt, "The extended "sequentially drilled" joint congruence transformation and its application in Gaussian independent vector analysis," *IEEE Transactions on Signal Processing*, vol. PP, no. 99, pp. 1–1, 2017.

[WYCH17b] ——, "A maximum likelihood "identification-correction" scheme of sub-optimal "sedjoco" solutions for semi-blind source separation," in *Proceedings of IEEE Int. Conference on Acoustics, Speech, and Signal Processing (ICASSP)*, LA, USA, March 2017.

[WYCH18]   ——, "On consistency and asymptotic uniqueness in quasi-maximum likelihood blind separation of temporally-diverse sources," in *Proceedings of IEEE Int. Conference on Acoustics, Speech, and Signal Processing (ICASSP), submitted*, March 2018.

References by Other Authors

[ABNW11]   K. Acolatse, Y. Bar-Ness, and S. Wilson, "Novel Techniques of Single-Carrier Frequency-Domain Equalization for Optical Wireless Communications," *EURASIP Journal on Advances in Signal Processing*, pp. 1–13, 2011.

[AD01]   N. Al-Dhahir, "Single-carrier frequency-domain equalization for space-time block-coded transmissions over frequency-selective fading channels," *IEEE Communications Letters,*, vol. 5, no. 7, pp. 304–306, July 2001.

[AG13]   S. Afra and E. Gildin, "Permeability parametrization using higher order singular value decomposition (HOSVD)," in *Proceedings of 12th International Conference on Machine Learning and Applications (ICMLA)*, vol. 2, December 2013, pp. 188–193.

[AHF+14]   M. R. Ameri, M. Haji, A. Fischer, D. Ponson, and T. D. Bui, "A feature extraction method for cursive character recognition using higher-order singular value decomposition," in *Proceedings of 14th International Conference on Frontiers in Handwriting Recognition (ICFHR)*, September 2014, pp. 512–516.

[AS08]   J. Armstrong and B. J. C. Schmidt, "Comparison of asymmetrically clipped optical OFDM and DC-biased optical OFDM in AGWN," *IEEE Communications Letters*, vol. 12, pp. 343–345, May 2008.

[ASN13]   J. Armstrong, Y. A. Sekercioglu, and A. Neild, "Visible light positioning: a roadmap for international standardization," *IEEE Communications Magazine*, vol. 51, no. 12, pp. 68–73, 2013.

[BCA+10]   H. Becker, P. Comon, L. Albera, M. Haardt, and I. Merlet, "Multiway space-time-wave-vector analysis for source localization and extraction," in *18th European Signal Processing Conference*, August 2010, pp. 1349–1353.

[BCS10]   P. Brgisser, M. Clausen, and M. A. Shokrollahi, *Algebraic Complexity Theory*, 1st ed. Springer Publishing Company, Incorporated, 2010.

[BDH99]   H. Bolcskei, P. Duhamel, and R. Hleiss, "Design of pulse shaping OFDM/OQAM systems for high data-rate transmission over wireless channels," in *Proceedings of IEEE International Conference on Communications*, vol. 1, 1999, pp. 559–564 vol.1.

[Bel10a]   M. Bellanger, "FBMC physical layer: A primer," *Available: http://www.ict-phydyas.org/ teamspace/internal-folder/FBMC-Primer_06-2010.pdf*, June 2010.

[Bel10b]   ——, "Physical layer for future broadband radio systems," in *Proceedings of IEEE Radio and Wireless Symposium (RWS), 2010*, January 2010, pp. 436–439.

[BGPF12]   M. Boizard, G. Ginolhac, F. Pascal, and P. Forster, "A new tool for multidimensional low-rank STAP filter: Cross HOSVDs," in *Proceedings of the 20th European Signal Processing Conference (EUSIPCO)*, August 2012, pp. 1324–1328.

[BK$^+$93]   J. R. Barry, J. M. Kahn *et al.*, "Simulation of Multipath Impulse Response for Indoor Wireless Optical Channels," *IEEE Journal on Selected Areas in Comm.*, vol. 11, no. 3, pp. 367–379, April 1993.

[BP00]   H. Boelcskei and A. Paulraj, "Space-frequency coded broadband OFDM systems," in *Proceedings of IEEE Wireless Communications and Networking Confernce, 2000. WCNC. 2000*, vol. 1, 2000, pp. 1–6 vol.1.

[BST$^+$14] H. Burchardt, N. Serafimovski, D. Tsonev, S. Videv, and H. Haas, "VLC: Beyond point-to-point communication," *IEEE Communications Magazine*, vol. 52, no. 7, pp. 98–105, July 2014.

[CB10]   A. Csapo and P. Baranyi, "A tensor algebraic framework for the intuitive exploration of sensory substitution spaces," in *Proceedings of 8th International Symposium on Intelligent Systems and Informatics (SISY)*, September 2010, pp. 547–552.

[CB11]   ——, "An adaptive tuning model for cognitive info-communication channels," in *Proceedings of IEEE 9th International Symposium on Applied Machine Intelligence and Informatics (SAMI)*, January 2011, pp. 231–236.

[CC70]   J. Carroll and J. Chang, "Analysis of individual differences in multidimensional scaling via an N-way generalization of Eckart-Young decomposition," *Psychometrika*, vol. 35, no. 3, pp. 283–319, 1970.

[CCC14]   G. Cossu, R. Corsini, and E. Ciaramella, "Proceedings of Indoor High-Speed Optical Wireless Communications: Recent Developments," in *ICTON'14*, Graz, July 2014.

[Cha66]   R. W. Chang, "Synthesis of band-limited orthogonal signals for multichannel data transmission," *The Bell System Technical Journal*, vol. 45, no. 10, pp. 1775–1796, Dec 1966.

[Cic13]   A. Cichocki, "Tensor decompositions: A new concept in brain data analysis?" *CoRR*, vol. abs/1305.0395, 2013. [Online]. Available: http://arxiv.org/abs/1305.0395

[CJ10]   P. Comon and C. Jutten, *Handbook of Blind Source Separation: Independent Component Analysis and Applications*, 1st ed.   Academic Press, 2010.

[CK94]   J. B. Carruthers and J. M. Kahn, "Multiple-subcarrier modulation for non-directed wireless infrared communication," in *Proceedings of IEEE GLOBECOM*, vol. 2, November 1994, pp. 1055–1059 vol.2.

[CK96]   ——, "Multiple-subcarrier modulation for nondirected wireless," *IEEE Journal on Selected Areas in Communications*, vol. 14, no. 3, pp. 538–546, 1996.

[CM01]   R. Cendrillon and M. Moonen, "Efficient equalizers for single and multi-carrier environments with known symbol padding," in *Proceedings of Sixth International Symposium on Signal Processing and its Applications*, vol. 2, 2001, pp. 607–610 vol.2.

[CMdL+15]   A. Cichocki, D. Mandic, L. de Lathauwer, G. Zhou, Q. Zhao, C. Caiafa, and H. A. PHAN, "Tensor decompositions for signal processing applications: From two-way to multiway component analysis," *IEEE Signal Processing Magazine*, vol. 32, no. 2, pp. 145–163, March 2015.

[CS14]   B. Cyganek and K. Socha, "Novel parallel algorithm for object recognition with the ensemble of classifiers based on the higher-order singular value decomposition of prototype pattern tensors," in *Proceedings of International Conference on Computer Vision Theory and Applications (VISAPP)*, vol. 2, January 2014, pp. 648–653.

[CSBM06]   J. Coon, M. Sandell, M. Beach, and J. McGeehan, "Channel and noise variance estimation and tracking algorithms for unique-word based single-carrier systems," *IEEE Transactions on Wireless Communications*, vol. 5, no. 6, pp. 1488–1496, June 2006.

[CZPA09]   A. Cichocki, R. Zdunek, A. H. Phan, and S.-i. Amari, *Nonnegative Matrix and Tensor Factorizations: Applications to Exploratory Multi-way Data Analysis and Blind Source Separation.*   Wiley Publishing, 2009.

[DA13]   S. D. Dissanayake and J. Armstrong, "Comparison of ACO-OFDM, DCO-OFDM and ADO-OFDM in IM/DD systems," *Journal of Lightwave Technology*, vol. 31, no. 7, pp. 1063–1072, April 2013.

[dAFM07]   A. L. de Almeida, G. Favier, and J. C. M. Mota, "PARAFAC-based unified tensor modeling for wireless communication systems with application to blind multiuser equalization," *Signal Processing*, vol. 87, no. 2, pp. 337 – 351, 2007, tensor Signal Processing.

[dL04]   L. de Lathauwer, "First-order perturbation analysis of the best rank-(R1,R2,R3) approximation in multilinear algebra," *Journal of Chemometrics*, vol. 18, pp. 2–11, 2004.

[dL05]   ——, "Parallel factor analysis by means of simultaneous matrix decompositions," in *Proceedings of 1st IEEE International Workshop on Computational Advances in Multi-Sensor Adaptive Processing*, December 2005, pp. 125–128.

[dL06]   ——, "A link between the canonical decomposition in multilinear algebra and simultaneous matrix diagonalization," *SIAM Journal on Matrix Analysis and Applications*, vol. 28, no. 3, pp. 642–666, 2006.

[dLC07]   L. de Lathauwer and J. Castaing, "Tensor-based techniques for the blind separation of DSCDMA signals," *Signal Processing*, vol. 87, no. 2, pp. 322 – 336, 2007, tensor Signal Processing. [Online]. Available: http://www.sciencedirect.com/science/article/pii/S0165168406001745

[dLdMV00a] L. de Lathauwer, B. de Moor, and J. Vandewalle, "On the best rank-1 and rank-(R1,R2, . . . , Rn) approximation of higher-order tensors," *SIAM Journal of Matrix Analysis and Applications*, vol. 21, no. 4, pp. 1324–1342, 2000.

[dLdMV00b] ——, "A multilinear singular value decomposition," *SIAM Journal on Matrix Analysis and Applications*, vol. 21, no. 4, pp. 1253–1278, 2000.

[DLS⁺15] W. Dong, G. Li, G. Shi, X. Li, and Y. Ma, "Low-rank tensor approximation with Laplacian scale mixture modeling for multiframe image denoising," in *Proceedings of IEEE International Conference on Computer Vision (ICCV)*, December 2015, pp. 442–449.

[DMLF12] R. Datta, N. Michailow, M. Lentmaier, and G. Fettweis, "GFDM interference cancellation for flexible cognitive radio PHY design," in *IEEE Vehicular Technology Conference (VTC Fall), 2012*, September 2012, pp. 1–5.

[Dol46] C. L. Dolph, "A current distribution for broadside arrays which optimizes the relationship between beam width and side-lobe level," *Proceedings of the IRE*, vol. 34, no. 6, pp. 335–348, June 1946.

[EMH09] H. Elgala, R. Mesleh, and H. Haas, "Indoor broadcasting via white LEDs and OFDM," *IEEE Transactions on Consumer Electronics*, vol. 55, no. 3, pp. 1127–1134, August 2009.

[FA⁺02] D. Falconer, S. L. Ariyavisitakul *et al.*, "Frequency Domain Equalization for Single-Carrier Broadband Wireless Systems," *IEEE Communications Magazine*, vol. 40, pp. 58–66, 2002.

[FABSE02] D. Falconer, S. L. Ariyavisitakul, A. Benyamin-Seeyar, and B. Eidson, "Frequency domain equalization for single-carrier broadband wireless systems," *IEEE Communications Magazine*, vol. 40, no. 4, pp. 58–66, April 2002.

[FB09] G. Favier and T. Bouilloc, "Parametric complexity reduction of volterra models using tensor decompositions," in *Proceedings of 17th European Signal Processing Conference*, August 2009, pp. 2288–2292.

[FG06] T. Fu and X. Gao, "Simultaneous diagonalization with similarity transformation for nondefective matrices," in *Proceedings of IEEE International Conference on Acoustics Speech and Signal Processing Proceedings*, vol. 4, 2006, pp. IV–IV.

[FG14] H. Fanaee-T and J. Gama, "Eigenevent: An algorithm for event detection from complex data streams in syndromic surveillance," *CoRR*, vol. abs/1406.3496, 2014. [Online]. Available: http://arxiv.org/abs/1406.3496

[FH96] F. Fischer and J. Huber, "A new loading algorithm for discrete multitone transmission," in *Proceedings of GLOBECOM 96*, November 1996, p. 724728.

[FKC⁺12] Z. H. Feng, J. Kittler, W. Christmas, X. J. Wu, and S. Pfeiffer, "Automatic face annotation by multilinear AAM with missing values," in *Proceedings of 21st International Conference on Pattern Recognition (ICPR)*, November 2012, pp. 2586–2589.

[Gan80] W. Gander, "Algorithms for the QR-decomposition," in *Resesrch Report No. 80-82*, 1980, pp. 1–27.

[GB79] F. Gfeller and U. Bapst, "Wireless in-house data communication via diffuse infrared radiation," *Proceedings of the IEEE*, vol. 67, no. 11, pp. 1474–1486, November 1979.

[GCS⁺05] R. Gaudino, D. Cardenas, P. Spalla *et al.*, "A novel DC-balancing line coding for multilevel transmission over POF," in *POF'2005*, September 2005, pp. 2007–210.

[GL10] J. Grubor and K.-D. Langer, "Efficient signal processing in OFDM-based indoor optical wireless links," *Journal of Networks*, vol. 5, no. 2, pp. 197–211, 2010.

[GL13]   L. Grobe and K.-D. Langer, "Block-Based PAM with Frequency Domain Equalization in Visible Light Communications," in *Proceedings of IEEE Globecom*, Atlanta, Georgia, USA, December 2013.

[GMM⁺14]   I. Gaspar, L. Mendes, M. Matth, N. Michailow, A. Festag, and G. Fettweis, "LTE-compatible 5G phy based on generalized frequency division multiplexing," in *Proceedings of 11th International Symposium on Wireless Communications Systems (ISWCS)*, August 2014, pp. 209–213.

[Grz11]   A. Grzemba, *MOST: The Automotive Multimedia Network ; from MOST25 to MOST150*, ser. Electronics library.   Franzis, 2011.

[GVL13]   G. Golub and C. Van Loan, *Matrix Computations*, ser. Johns Hopkins Studies in the Mathematical Sciences.   Johns Hopkins University Press, 2013.

[Hac12]   W. Hackbusch, *Tensor Spaces and Numerical Tensor Calculus*, ser. Springer Series in Computational Mathematics.   Springer Berlin Heidelberg, 2012.

[Har70]   R. Harshman, *Foundations of the PARAFAC procedure: Models and conditions for an" explanatory" multi-modal factor analysis*.   University of California Los Angeles, 1970.

[Hay01]   S. Haykin, *Communication Systems*, 4th ed.   John Wiley & Sons, 2001.

[HC15]   M. Haardt and A. T. Cemgil, "Matrix and tensor decompositions." *Summer School of the 12-th International Conference on Latent Variable Analysis and Signal Separation (LVA / ICA)*, 2015.

[HH89]   D. Hughes-Hartgogs, "Ensemble modern structure for imperfect transmission media," U.S. Patent 4,679,227 (July 1987), 4,731,816 (March 1988), and 4,883,706 (May 1989), 1989.

[HHH10a]   M. Huemer, C. Hofbauer, and J. B. Huber, "Complex number RS coded OFDM with systematic noise in the guard interval," in *Proceedings of the Asilomar Conference on Signals, Systems, and Computers*, Pacific Grove, USA, November 2010.

[HHH10b]   ——, "The potential of unique words in OFDM," in *Proceedings of the International OFDM-Workshop*, Hamburg, Germany, September 2010.

[HHH12]   ——, "Non-systematic complex number RS coded OFDM by unique word prefix," *IEEE Transactions on Signal Processing*, vol. 60, no. 1, pp. 285–299, Janaury 2012.

[HHOH14]   M. Huemer, C. Hofbauer, A. Onic, and J. B. Huber, "Design and analysis of UW-OFDM signals," *AEÜ - International Journal of Electronics and Communications*, vol. 68, no. 10, pp. 958 – 968, 2014.

[Hir81]   B. Hirosaki, "An orthogonally multiplexed QAM system using the discrete Fourier transform," *IEEE Transactions on Communications*, vol. 29, no. 7, pp. 982–989, July 1981.

[HOH11]   M. Huemer, A. Onic, and C. Hofbauer, "Classical and bayesian linear data estimators for unique word OFDM," *IEEE Transactions on Signal Processing*, vol. 59, no. 12, pp. 6073–6085, December 2011.

[Hos09]   E. Hossain, "Dynamic spectrum access and management in cognitive radio," *Cambridge University Press*, 2009.

[HRdG08]   M. Haardt, F. Roemer, and G. del Galdo, "Higher-order SVD-based subspace estimation to improve the parameter estimation accuracy in multidimensional harmonic retrieval problems," *IEEE Transactions on Signal Processing*, vol. 56, no. 7, pp. 3198–3213, July 2008.

[HT10]   Z. Y. Huang and P. Y. Tsai, "High-throughput QR decomposition for MIMO detection in OFDM systems," in *Proceedings of 2010 IEEE International Symposium on Circuits and Systems*, May 2010, pp. 1492–1495.

[HX14]   A. Hajiloo and W. F. Xie, "Multi-objective control design of the nonlinear systems using genetic algorithm," in *Proceedings of IEEE International Symposium on Innovations in Intelligent Systems and Applications (INISTA) Proceedings*, June 2014, pp. 27–34.

[HYWC16]   H. Haas, L. Yin, Y. Wang, and C. Chen, "What is LiFi?" *IEEE Communications Survey and Tutorials*, vol. 34, pp. 1533–154, 2016.

[IKN+15]   C. Ibars, U. Kumar, H. Niu, H. Jung, and S. Pawar, "A comparison of waveform candidates for 5G millimeter wave systems," in *Proceedings of 49th Asilomar Conference on Signals, Systems and Computers*, November 2015, pp. 1747–1751.

[Jaf01]   H. Jafarkhani, "A quasi-orthogonal space-time block code," *IEEE Transactions on Communications*, vol. 49, no. 1, pp. 1–4, Jan 2001.

[JSI+07]   F. Janoos, S. Singh, O. Irfanoglu, R. Machiraju, and R. Parent, "Activity analysis using spatio-temporal trajectory volumes in surveillance applications," in *Proceedings of IEEE Symposium on Visual Analytics Science and Technology (VAST)*, October 2007, pp. 3–10.

[Kam08]   K. D. Kammeyer, *Nachrichtenübertragung*, 4th ed.   Teubner Verlag, 2008.

[Kay93]   S. Kay, *Fundamentals of Statistical Signal Processing: Estimation Theory*.   Englewood Cliffs, NJ: Prentice-Hall, 1993.

[KB97]   J. Kahn and J. Barry, "Wireless Infrared Communications," *Proceedings of the IEEE*, pp. 265–298, February 1997.

[KB09]   T. G. Kolda and B. W. Bader, "Tensor decompositions and applications," *SIAM Review*, vol. 51, no. 3, pp. 455–500, 2009.

[Kei08]   G. Keiser, *Optical Fiber Communications*, 2nd ed.   McGraw-Hill Education Pvt Limited, 2008.

[KI89]   D. Kreß and R. Irmer, *Angewandte Systemtheorie: Kontinuierliche und zeitdiskrete Signalverarbeitung*.   1. edition, Berlin: Verlag Technik, 1989.

[Kim14]   T. H. Kim, "Low-complexity sorted QR decomposition for MIMO systems based on pairwise column symmetrization," in *Proceedings of IEEE Wireless Communications and Networking Conference (WCNC)*, April 2014, pp. 1281–1286.

[Kru77]   J. B. Kruskal, "Three-way arrays: rank and uniqueness of trilinear decompositions, with application to arithmetic complexity and statistics," *Linear Algebra and its Applications*, vol. 18, no. 2, pp. 95 – 138, 1977. [Online]. Available: http://www.sciencedirect.com/science/article/pii/0024379577900696

[KY+98]   J. Kahn, R. You *et al.*, "Imaging Diversity Receivers for High-Speed Infrared Wireless Communication," *IEEE Communication Magazine*, pp. 88–94, December 1998.

[LA10]   X. Luciani and L. Albera, "Joint eigenvalue decomposition using polar matrix factorization," in *Proceedings of International Conference on Latent Variable Analysis and Signal Separation.*   Springer, 2010, pp. 555–562.

[LA11]   ——, "Semi-algebraic canonical decomposition of multi-way arrays and joint eigenvalue decomposition," in *IEEE International Conference on Acoustics, Speech and Signal Processing (ICASSP)*, 2011, pp. 4104–4107.

[LA15]   ——, "Joint eigenvalue decomposition of non-defective matrices based on the LU factorization with application to ICA," *IEEE Transactions on Signal Processing*, vol. 63, no. 17, pp. 4594–4608, 2015.

[LKW+14]   S. Long, M. Khalighi, M. Wolf, S. Bourennane, and Z. Ghassemlooy, "Channel Characterization for Indoor Visible Light Communications," in *Proceedings of Int. Workshop on Optical Wireless Communications (IWOW), Madeira (Portugal)*, September 2014.

[LLV93]   F. Li, H. Liu, and R. J. Vaccaro, "Performance analysis for DOA estimation algorithms: unification, simplification, and observations," *IEEE Transactions on Aerospace and Electronic Systems*, vol. 29, no. 4, pp. 1170–1184, October 1993.

[LPB11]   K. Lee, H. Park, and J. Barry, "Indoor channel characteristics for visible light communications," *Communications Letters, IEEE*, vol. 15, no. 2, pp. 217–219, February 2011.

[LRBV09]   S. C. J. Lee, S. Randel, F. Breyer, and J. Vucic, "PAM-DMT for intensity-modulated and direct-detection optical communication systems," *IEEE Photonics Technology Letterrs*, vol. 21, no. 23, December 2009.

[LW00]   B. Lu and X. Wang, "Space-time code design in OFDM systems," in *Proceedings of IEEE Global Telecommunications Conference, 2000. GLOBECOM '00.*, vol. 2, 2000, pp. 1000–1004 vol.2.

[LWS02]   Y. G. Li, J. H. Winters, and N. R. Sollenberger, "MIMO-OFDM for wireless communications: signal detection with enhanced channel estimation," *IEEE Transactions on Communications*, vol. 50, no. 9, pp. 1471–1477, September 2002.

[LXG02]   Z. Liu, Y. Xin, and G. B. Giannakis, "Space-time-frequency coded OFDM over frequency-selective fading channels," *IEEE Transactions on Signal Processing*, vol. 50, no. 10, pp. 2465–2476, October 2002.

[LYD+15]   J. Li, Y. Yan, W. Duan, S. Song, and M. H. Lee, "Tensor decomposition of Toeplitz Jacket matrices for big data processing," in *Proceedings of International Conference on Big Data and Smart Computing (BigComp)*, February 2015, pp. 11–14.

[LZH09a]   C. Liu, J. Zhou, and K. He, "Image compression based on truncated HOSVD," in *Proceedings of International Conference on Information Engineering and Computer Science*, December 2009, pp. 1–4.

[LZH+09b]   C. Liu, J. Zhou, K. He, Y. Zhu, D. Wang, and J. Xia, "Supervised locally linear embedding in tensor space," in *Proceedings of Third International Symposium on Intelligent Information Technology Application (IITA)*, vol. 3, November 2009, pp. 31–34.

[LZY+05]   N. Liu, B. Zhang, J. Yan, Z. Chen, W. Liu, F. Bai, and L. Chien, "Text representation: from vector to tensor," in *Proceedings of Fifth IEEE International Conference on Data Mining*, November 2005, pp. 4 pp.–.

[MHH+06]   M. Mørup, L. K. Hansen, C. S. Herrmann, J. Parnas, and S. M. Arnfred, "Parallel factor analysis as an exploratory tool for wavelet transformed event-related EEG," *NeuroImage*, vol. 29, no. 3, pp. 938 – 947, 2006. [Online]. Available: http://www.sciencedirect.com/science/article/pii/S1053811905005896

[MMF14]   M. Matthe, L. L. Mendes, and G. Fettweis, "Space-time coding for generalized frequency division multiplexing," in *Proceedings of 20th European Wireless Conference*, May 2014, pp. 1–5.

[MMG+14]   N. Michailow, M. Matthe, I. Gaspar, A. Caldevilla, L. Mendes, A. Festag, and G. Fettweis, "Generalized frequency division multiplexing for 5th generation cellular networks," *IEEE Transactions on Communications,*, vol. 62, no. 9, pp. 3045–3061, September 2014.

[MMG+15]   M. Matthe, L. Mendes, I. Gaspar, N. Michailow, D. Zhang, and G. Fettweis, "Multi-user time-reversal STC-GFDMA for future wireless networks," *EURASIP Journal on Wireless Communications and Networking*, vol. 2015, no. 1, 2015.

[MNM11]   H. Y. Mesri, M. K. Najafabadi, and T. McKelvey, "A multidimensional signal processing approach for classification of microwave measurements with application to stroke type diagnosis," in *Proceedings of Annual International Conference of the IEEE Engineering in Medicine and Biology Society, EMBC*, August 2011, pp. 6465–6469.

[Mør11]   M. Mørup, "Applications of tensor (multiway array) factorizations and decompositions in data mining," *Wiley Interdisciplinary Reviews: Data Mining and Knowledge Discovery*, vol. 1, no. 1, pp. 24–40, 2011. [Online]. Available: http://dx.doi.org/10.1002/widm.1

[MOS10]   "MOST150 PHY Automotive Physical Layer Sub-Specification, Rev.1.1." *MOST Cooperation*, 2010.

[MPG09]   S. Manna, Z. Petres, and T. Gedeon, "Tensor term indexing: an application of HOSVD for document summarization," in *Proceedings of 4th International Symposium on Computational Intelligence and Intelligent Informatics*, October 2009, pp. 135–141.

[MV13]   N. I. Miridakis and D. D. Vergados, "A Survey on the Successive Interference Cancellation Performance for Single-Antenna and Multiple-Antenna OFDM Systems," *IEEE Communications Surveys Tutorials*, vol. 15, no. 1, pp. 312–335, First 2013.

[Neu77]   C. Neumann, "Zur Theorie des Logarithmischen und des Newton'schen Potentials," *Mathematische Annalen*, vol. 11, no. 4, pp. 558–566, 1877.

[NH16]   K. Naskovska and M. Haardt, "Extension of the semi-algebraic framework for approximate CP decompositions via simultaneous matrix diagonalization to the efficient calculation of coupled CP decompositions," in *2016 50th Asilomar Conference on Signals, Systems and Computers*, Nov 2016, pp. 1728–1732.

[NHT+16]   K. Naskovska, M. Haardt, P. Tichavsky, G. Chabriel, and J. Barrer, "Extension of the semi-algebraic framework for approximate CP decompositions via non-symmetric simultaneous matrix diagonalization," in *IEEE International Conference on Acoustics, Speech and Signal Processing (ICASSP)*, March 2016, pp. 2971–2975.

[OH10]   A. Onic and M. Huemer, "Direct vs. two-step approach for unique word generation in UW-OFDM," in *Proceedings of the International OFDM-Workshop*, Hamburg, Germany, September 2010.

[Oni13]   A. Onic, "Receiver concepts for unique word OFDM," Ph.D. dissertation, Institute of Networked and Embedded Systems, Alpen-Adria-Universität Klagenfurt, Klagenfurt, Austria, 2013.

[ORV11]   G. Orbn, A. Rövid, and P. Vrlaki, "Control model for loading systems using higher order singular value decomposition," in *Proceedings of IEEE International Conference on Computer Science and Automation Engineering (CSAE)*, vol. 3, June 2011, pp. 754–758.

[PB95]   H. Park and J. R. Barry, "Modulation analysis for wireless infrared communications," in *Proceedings of IEEE International Conference on Communications. ICC '95 Seattle*, vol. 2, June 1995, pp. 1182–1186 vol.2.

[PFHM15]   P. H. Pathak, X. Feng, P. Hu, and P. Mohapatra, "Visible light communication, networking, and sensing: a survey, potential, and challenges," *IEEE Communications Survey and Tutorials*, vol. 17, pp. 2047–2077, 2015.

[PHH13]   L. Peng, M. Hélard, and S. Haese, "On bit-loading for discrete multi-tone transmission over short range POF systems," *J. Lightwave Technol.*, vol. 31, no. 24, pp. 4155–4165, December 2013.

[PNCZ$^+$16]   A. I. Pérez-Neira, M. Caus, R. Zakaria, D. L. Ruyet, E. Kofidis, M. Haardt, X. Mestre, and Y. Cheng, "MIMO signal processing in offset-QAM based filter bank multicarrier systems," *IEEE Transactions on Signal Processing*, vol. 64, no. 21, pp. 5733–5762, Nov 2016.

[RBHW09]   F. Roemer, H. Becker, M. Haardt, and M. Weis, "Analytical performance evaluation for HOSVD-based parameter estimation schemes," in *Proceedings of 3rd IEEE International Workshop on Computational Advances in Multi-Sensor Adaptive Processing (CAMSAP)*, December 2009, pp. 77–80.

[RD13]   D. Rafailidis and P. Daras, "The TFC model: Tensor factorization and tag clustering for item recommendation in social tagging systems," *IEEE Transactions on Systems, Man, and Cybernetics: Systems*, vol. 43, no. 3, pp. 673–688, May 2013.

[RH08a]   F. Roemer and M. Haardt, "A closed-form solution for multilinear PARAFAC decompositions," in *Proceedings of 5th IEEE Sensor Array and Multichannel Signal Processing Workshop*, 2008, pp. 487–491.

[RH08b]   ——, "A closed-form solution for parallel factor (PARAFAC) analysis," in *Proceedings of IEEE International Conference on Acoustics, Speech and Signal Processing 2008*, March 2008.

[RH13]   ——, "A semi-algebraic framework for approximate CP decompositions via simultaneous matrix diagonalizations (SECSI)," *Signal Processing*, vol. 93, no. 9, pp. 2722 – 2738, 2013. [Online]. Available: http://www.sciencedirect.com/science/article/pii/S0165168413000704

[RHDG14]   F. Roemer, M. Haardt, and G. Del Galdo, "Analytical performance assessment of multidimensional matrix- and tensor-based ESPRIT-type algorithms," *IEEE Transactions on Signal Processing*, vol. 62, no. 10, pp. 2611–2625, May 2014.

[RIS10]   M. Renfors, T. Ihalainen, and T. Stitz, "A block-Alamouti scheme for filter bank based multicarrier transmission," in *Proceedings of European Wireless Conference (EW),*, April 2010, pp. 1031–1037.

[RKS14]   M. Rajabzadeh, H. Khoshbin, and H. Steendam, "Sidelobe suppression for non-systematic coded UW-OFDM in cognitive radio networks," in *Proceedings of 20th European Wireless Conference*, May 2014, pp. 1–6.

[RLM16]   A. Remi, X. Luciani, and E. Moreau, "A coupled joint eigenvalue decomposition algorithm for canonical polyadic decomposition of tensors," in *2016 IEEE Sensor Array and Multichannel Signal Processing Workshop (SAM)*, 2016.

[RNSK14]   M. Rajabzadeh, N. Noels, H. Steendam, and H. Khoshbin, "Sidelobe suppression for non-systematic coded UW-OFDM in cognitive radio networks," in *Proceedings of European Wireless Conference (EW2014)*, Barcelona, Spain, May 2014.

[Roe12]   F. Roemer, "Advanced algebraic concepts for efficient multi-channel signal processing," Ph.D. dissertation, Universitätsbibliothek Ilmenau, 2012.

[RRB13]   A. Rajwade, A. Rangarajan, and A. Banerjee, "Image denoising using the higher order singular value decomposition," *IEEE Trans. Pattern Anal. Mach. Intell.*, vol. 35, no. 4, pp. 849–862, Apr. 2013. [Online]. Available: http://dx.doi.org/10.1109/TPAMI.2012.140

[RSH12]   F. Roemer, C. Schroeter, and M. Haardt, "A semi-algebraic framework for approximate CP decompositions via joint matrix diagonalization and generalized unfoldings," in *Proceedings of Forty Sixth Asilomar Conference on Signals, Systems and Computers (ASILOMAR)*, 2012, pp. 2023–2027.

[RSK13]   M. Rajabzadeh, H. Steendam, and H. Khoshbin, "Power spectrum characterization of systematic coded UW-OFDM systems," in *Proceedings of IEEE 78th Vehicular Technology Conference (VTC Fall)*, September 2013, pp. 1–5.

[RSR13]   R. Rath, C. Schmidt, and W. Rosenkranz, "Is Tomlinson-Harashima precoding suitable for fiber-optic communication systems?" *Photonic Networks, ITG Symposium*, 2013.

[RSSV13]   A. Rövid, L. Szeidl, S. Sergyn, and P. Varlaki, "HOSVD-wavelet based framework for multidimensional data approximation," in *Proceedings of IEEE 9th International Conference on Computational Cybernetics (ICCC)*, July 2013, pp. 29–33.

[RSV13]   A. Rövid, L. Szeidl, and P. Vrlaki, "Data representation in HOSVD-DCT based domain," in *Proceedings of IEEE 17th International Conference on Intelligent Engineering Systems (INES)*, June 2013, pp. 103–106.

[Sal67]   B. Saltzberg, "Performance of an efficient parallel data transmission system," *IEEE Transactions on Communication Technology*, vol. 15, no. 6, pp. 805–811, December 1967.

[Say03]   A. H. Sayed, *Fundamentals of Adaptive Filtering*.   Wiley, 2003.

[SBG05]   A. Smilde, R. Bro, and P. Geladi, *Multi-way Analysis: Applications in the Chemical Sciences*, ser. Wiley InterScience online books.   Wiley, 2005.

[SdLF+17] N. D. Sidiropoulos, L. de Lathauwer, X. Fu, K. Huang, E. E. Papalexakis, and C. Faloutsos, "Tensor decomposition for signal processing and machine learning," *IEEE Transactions on Signal Processing*, vol. 65, no. 13, pp. 3551–3582, July 2017.

[SGB00]   N. D. Sidiropoulos, G. B. Giannakis, and R. Bro, "Blind PARAFAC receivers for DS-CDMA systems," *IEEE Transactions on Signal Processing*, vol. 48, no. 3, pp. 810–823, March 2000.

[SPSH04]   Q. H. Spencer, C. B. Peel, A. L. Swindlehurst, and M. Haardt, "An introduction to the multi-user MIMO downlink," *IEEE Communications Magazine*, vol. 42, no. 10, pp. 60–67, October 2004.

[Ste13a]   H. Steendam, "On the diversity order of UW-OFDM," in *IFIP TC7 2013 Conference on System Modeling and Optimization*, Klagenfurt, Austria, September 2013.

[Ste13b]   ——, "On the selection of the redundant carrier positions in UW-OFDM," *IEEE Transactions on Signal Processing*, vol. 61, no. 5, pp. 1112–1120, March 2013.

[Ste14]   ——, "Design and analysis of the UW-OFDM signal," in *Proceedings of ISCCSP'14*, Athens, Greece, May 2014, pp. 511–515.

[SWC14]   F. Schaich, T. Wild, and Y. Chen, "Waveform contenders for 5G - suitability for short packet and low latency transmissions," in *Proceedings of 79th IEEE Vehicular Technology Conference (VTC Spring)*, May 2014, pp. 1–5.

[TJC99]   V. Tarokh, H. Jafarkhani, and A. R. Calderbank, "Space-time block codes from orthogonal designs," *IEEE Transactions on Information Theory*, vol. 45, no. 5, pp. 1456–1467, Jul 1999.

[Tuc64]   L. R. Tucker, "The extension of factor analysis to three-dimensional matrices," in *Contributions to mathematical psychology.*, H. Gulliksen and N. Frederiksen, Eds. New York: Holt, Rinehart and Winston, 1964, pp. 110–127.

[Tuc66]   ——, "Some mathematical notes on three-mode factor analysis," *Psychometrika*, vol. 31, no. 3, pp. 279–311, Sep 1966. [Online]. Available: https://doi.org/10.1007/BF02289464

[TVH15]   D. Tsonev, S. Videv, and H. Haas, "Towards a 100 Gb/s visible light wireless access network," *Opt. Express*, vol. 23, no. 2, pp. 1627–1637, Jan 2015. [Online]. Available: http://www.opticsexpress.org/abstract.cfm?URI=oe-23-2-1627

[VdLV+07]   M. D. Vos, L. de Lathauwer, B. Vanrumste, V. Huffel, and W. V. Paesschen, "Canonical decomposition of ictal scalp EEG and accurate source localisation: Principles and simulation study," *Computational Intelligence and Neuroscience*, 2007.

[VFea10]   J. Vucic, L. Fernandez, and et al, "Implemeation of a real-time DMT based 100 Mbit/s visible light link," in *Proceedings of 36th European Conference and Exhibition on Optical Communication (ECOC)*, September 2010, pp. 1–5.

[WBKK03]   D. Wubben, R. Bohnke, V. Kuhn, and K. D. Kammeyer, "MMSE extension of V-BLAST based on sorted QR decomposition," in *Proceedings of 58th Vehicular Technology Conference. VTC 2003-Fall (IEEE Cat. No.03CH37484)*, vol. 1, October 2003, pp. 508–512 Vol.1.

[WCLM99]   C. Y. Wong, R. S. Cheng, K. B. Lataief, and R. D. Murch, "Multiuser OFDM with adaptive subcarrier, bit, and power allocation," *IEEE Journal on Selected Areas in Communications*, vol. 17, no. 10, pp. 1747–1758, October 1999.

[WE71]   S. Weinstein and P. Ebert, "Data transmission by frequency-division multiplexing using the discrete Fourier transform," *IEEE Transactions on Communication Technology*, vol. 19, no. 5, pp. 628–634, October 1971.

[WF83]   A. X. Widmer and P. A. Franaszek, "A DC-Balanced, Partitioned-block, 8B/10B Transmission Code," *IBM Journal of research and development*, vol. 27, September 1983.

[WGR⁺10]   M. Wolf, L. Grobe, M. R. Rieche, A. Koher, and J. Vucic, "Block transmission with linear frequency domain equalization for dispersive optical channels with direct detection," in *Proceedings of 12th International Conference on Transperent Optical Networks (ICTON) 2010*, Munich, Germany, June 2010.

[WH11]   M. Wolf and M. Haardt, "Block transmission with frequency domain equalization in the presence of colored noise," in *Proceedings of 13th International Conference on Transperent Optical Networks (ICTON) 2011*, Stockholm, SW, June 2011.

[WH12]   ——, "Comparison of OFDM and frequency domain equalization for dispersive optical channels with direct detection," in *Proceedings of 14th International Conference on Transperent Optical Networks (ICTON) 2012*, Coventry, UK, July 2012.

[WL⁺12]   F.-M. Wu, C.-T. Lin *et al.*, "1.1-Gb/s white-LED-based visible light communication employing carrier-less amplitude and phase modulation," *IEEE Photonics Technology Letters*, pp. 1730 – 1732, October 2012.

[WMP⁺03]   H. Witschnig, T. Mayer, M. Petit, H. Hutzelmann, A. Springer, and R. Weigel, "The advantages of a unique word for synchronisation and channel estimation in a SC/FDE system," in *Proceedings of 5th European Personal Mobile Communications Conference*, April 2003, pp. 436–440.

[WMS13]   Y. Wang, J. Muller, and J. Speidel, "3Gbit/s transmission over plastic optical fiber with adaptive Tomlinson-Harashima Precoded systems," in *Proceedings of IEEE International Conference on Consumer Electronics (ICCE), 2013*, January 2013, pp. 629–632.

[WRH⁺09]   M. Weis, F. Roemer, M. Haardt, D. Jannek, and P. Husar, "Multi-dimensional space-time-frequency component analysis of event related EEG data using closed-form PARAFAC," in *IEEE International Conference on Acoustics, Speech and Signal Processing*, April 2009, pp. 349–352.

[YA10]   S. Yamazaki and D. Asano, "Single-carrier transmission frequency-domain equalization based on a Wiener filter," in *Proceedings of IEEE ISCIT 2010, Tokyo*, 2010, pp. 683–688.

[ZKZD02]   O. Ziemann, J. Krauser, P. Zamzow, and W. Daum, *POF - Polymer Optical Fibers for Data Communication*, ser. Engineering online library.   Springer Berlin Heidelberg, 2002.

[ZL13]   R. Zakaria and D. Le Ruyet, "On interference cancellation in Alamouti coding scheme for filter bank based multicarrier systems," in *Proceedings of the Tenth International Symposium on Wireless Communication Systems (ISWCS 2013),*, August 2013, pp. 1–5.

[ZT03]   L. Zheng and D. N. C. Tse, "Diversity and multiplexing: a fundamental tradeoff in multiple-antenna channels," *IEEE Transactions on Information Theory*, vol. 49, no. 5, pp. 1073–1096, May 2003.